

A Thesis Submitted for the Degree of PhD at the University of Warwick

Permanent WRAP URL:

<http://wrap.warwick.ac.uk/114456/>

Copyright and reuse:

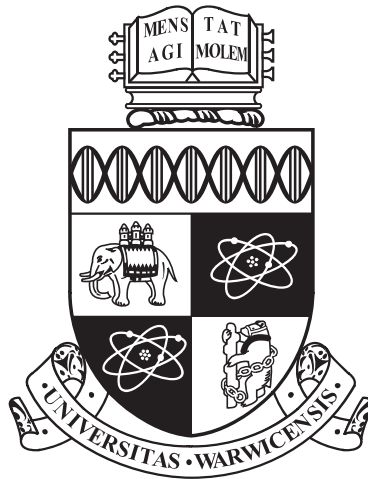
This thesis is made available online and is protected by original copyright.

Please scroll down to view the document itself.

Please refer to the repository record for this item for information to help you to cite it.

Our policy information is available from the repository home page.

For more information, please contact the WRAP Team at: wrap@warwick.ac.uk



**Enhanced EMAT Techniques for the
Characterisation of Hidden Defects**

by

C. B. Thring

Thesis

Submitted to the University of Warwick

for the degree of

Doctor of Philosophy

Department of Physics

January 2019

THE UNIVERSITY OF
WARWICK

Contents

Acknowledgments	iv
Declarations	v
Abstract	vi
Abbreviations	viii
Chapter 1 Introduction	1
1.1 Surface Breaking Defects	1
1.1.1 Rolling Contact Fatigue Cracks	1
1.1.2 Stress Corrosion Cracking	3
1.2 Non-Destructive Evaluation Methods	5
1.2.1 Dye Penetrant Inspection	5
1.2.2 Magnetic Particle Inspection	5
1.2.3 Radiography	6
1.2.4 Eddy Current Testing	6
1.2.5 Alternating Current Potential Drop	8
1.2.6 Ultrasound	9
1.3 Summary	21
Chapter 2 Theory	22
2.1 Ultrasound	22
2.1.1 Wave generation and Propagation	22
2.1.2 Bulk Wave Interface Interactions	25
2.1.3 Surface Wave Propagation	28
2.1.4 Rayleigh Wave Defect Interaction	34
2.2 EMAT Mechanisms	37
2.2.1 Generation of Ultrasound using EMATs	39

2.2.2	Detection of Ultrasound using EMATs	45
2.3	Summary	46
Chapter 3 Methodology		47
3.1	EMAT Designs	47
3.1.1	Coil designs developed for operation in pulse-echo mode . . .	47
3.1.2	Coil designs developed for operation in pitch-catch mode . .	52
3.2	Wavefield Imaging	56
3.3	Defect Detection	56
3.4	Signal Processing	60
3.5	Finite Element Analysis	61
3.6	EMAT Construction	63
3.6.1	Coil Construction	63
3.6.2	Impedance Matching	67
3.7	Summary	71
Chapter 4 The Effect of EMAT Coil Geometry on the Frequency of Generated and Detected Rayleigh Waves		72
4.1	Analytical Solutions	73
4.2	Experimental Results	77
4.3	Modelling	83
4.3.1	Lift-off Behaviour	83
4.3.2	Spatial Frequency Model	85
4.3.3	Time Evolution	86
4.3.4	Finite Element Modelling	93
4.4	Conclusion	95
Chapter 5 Characterisation and Defect Detection Capabilities of Fo- cused and Unfocused Pseudo-Pulse-Echo Meanderline EMAT De- signs		97
5.1	Wavefield Imaging	97
5.2	Aperture Effect	101
5.3	Defect Detection	109
5.4	Conclusion	113
Chapter 6 Characterisation and Defect Detection Capabilities of Fo- cused and Unfocused Pitch-Catch Racetrack EMAT Designs		115
6.1	Unfocused Racetrack Coil Designs	116

6.2	Focused Racetrack Coil Designs	118
6.2.1	Wavefield Imaging	118
6.2.2	Defect Detection	119
6.2.3	Frequency Depth Calibration	123
6.3	Focused Four Coil Racetrack Design	125
6.4	Conclusion	131
Chapter 7 Scanning Real Defects		132
7.1	Surface Cracked Samples	133
7.2	EMAT Scanning on Cracked Aluminium Billet Sample	139
7.3	EMAT scanning on Thermal Fatigue Cracked Samples	145
7.3.1	W1128	149
7.3.2	W1129	153
7.3.3	W1130	153
7.3.4	W1131	156
7.3.5	W1133	156
7.4	Conclusion	158
Chapter 8 EMAT lift-off capabilities		162
8.1	Focused EMATs	162
8.2	Unfocused EMAT Calibration	164
8.2.1	Generator versus Detector Effects	167
8.3	Phased Linear Coils	170
8.4	Conclusion	170
Chapter 9 Conclusions and Further Work		172
9.1	Conclusions	172
9.2	Future Directions	174
9.2.1	Four Coil Phased Designs	175
9.2.2	Magnetic Edge Field Designs	176

Acknowledgments

Firstly I must give my thanks to my supervisor, Dr Rachel Edwards, whose influence was a large factor in my decision to do a PhD, and I have not regretted it. Thank you also to Charley Fan for all my initial training, and to Sam Hill, and the rest of the University of Warwick Ultrasound group, for all the assistance I have received over these last few years. A particular mention must also be given to my father, Rob Thring, for very patiently reading everything I have ever written, and my mother for all her baking. The University of Warwick Pole and Aerial Arts society must also be mentioned, as without dancing (and my cat) I would have gone insane many years ago. Thanks to all of my friends and family for putting up with my constant complaints, especially my dancer partner Katherine Hewitt for repeatedly fixing me when my clumsiness got the better of me, and my friend Harry Austin for repeatedly fixing my computer. I wish I could list everyone who has supported me in some way, but the list would get too long.

Thanks also goes to EPSRC for funding this studentship, and to David Wright at Rolls Royce for providing samples and equipment funding.

Declarations

The research presented in this thesis is my original work, produced under the supervision of Dr Rachel Edwards in the Department of Physics at the University of Warwick, UK, between October 2014 and March 2018. No part of this work has been previously submitted to the University of Warwick, nor to any other academic institution for the purposes of obtaining a higher degree. Some parts of the work have been published as journal submissions:

1. C. B. Thring, S. J. Hill, S. Dixon, R. S. Edwards, ‘The effect of EMAT coil geometry on the Rayleigh wave frequency behaviour’, Under Review, 2018.
2. C. B. Thring, W. E. Somerset, R. S. Edwards, ‘Enhanced surface defect detection using focused electromagnetic acoustic transducers (EMATs)’, Proceedings of Meetings on Acoustics, 6ICU **32** (1), 045001, 2017.
3. C. B. Thring, Y. Fan, R. S. Edwards, ‘Multi-coil focused EMAT for characterisation of surface-breaking defects of arbitrary orientation’, NDT&E International, **88**, 1-7, 2017.
4. C. B. Thring, Y. Fan, R. S. Edwards, ‘Multiple focused EMAT designs for improved surface breaking defect characterization’, AIP Conference Proceedings, 1806 (1), 020019, 2017.
5. C. B. Thring, Y. Fan, R. S. Edwards, ‘Focused Rayleigh wave EMAT for characterisation of surface-breaking defects’, NDT&E International, **81**, 20-27, 2016.

Abstract

There is an industrial drive for the improved detection of sub-mm sized surface breaking defects using non-destructive evaluation (NDE) methods [1]. Electromagnetic acoustic transducers (EMATs) are a non-contact NDE technique that utilise the generation and detection of Ultrasound using primarily Lorentz force mechanisms [2]. They are relatively safe and inexpensive, however, they suffer from low generation efficiency. The precise industrial drive for this work is improved ultrasonic crack detection of surface defects hidden by a thin metallic paint coating. The majority of standard ultrasonic techniques are not applicable as they require direct contact to the sample surface. Laser techniques, while non-contact, are still impeded by the coating, and eddy current techniques are difficult to implement due to interference from the metallic coating. EMATs are applicable, however their low generation efficiency limits the minimum defect that can be detected.

This work presents improved resolution surface wave EMATs using geometric focusing for the detection of sub-mm sized surface breaking defects. Three main design types have been presented: a pseudo-pulse-echo focused meander-line EMAT, a pitch-catch focused racetrack EMAT and a pitch-catch focused linear EMAT. The first two designs have been fully characterised, finding the relations between coil geometry, focal point location and size, and the optimum operation frequencies [3, 4, 5]. Both designs have been used to size the lengths of a set of drilled calibration defects to accuracies of ± 0.5 and ± 0.4 mm respectively, and the pitch-catch design has been used to create a calibration curve for defect depth measurements. In addition, both designs have been used to map a pair of real surface breaking cracks

in an aluminium billet sample to sub-mm resolution. The pitch-catch design has been used to detect a set of mm-size real thermal fatigue cracks in steel through a 40 – 60 μm thick metallic paint coating. A four-coil EMAT design based on the pitch-catch focused racetrack EMAT has been built and demonstrated to detect surface breaking defects regardless of their surface orientation.

Finally, the meander-line, racetrack, and linear coil design types have been compared based on their signal strength and their performance at lift-off from a sample surface. The meander-line designs have the strongest signal to noise ratios (SNR), with over 40 dB found when in contact with the sample, but the largest SNR loss with increased lift-off, reducing to 0 dB by 0.3 mm lift-off. The linear designs have the weakest SNRs, under 30 dB when in direct contact, but the smallest SNR loss with increased lift-off, dropping to 0 dB by around 1 mm, depending on the frequency of operation. This makes the linear coil designs optimal for situations requiring higher lift-off. Lower frequency designs are shown to perform better with increased lift-off regardless of the coil design, however, lower frequencies have less spatial resolution capabilities. A proposed linear-meander-line phased EMAT design is presented to generate 1 MHz signals but with the improved lift-off capabilities of the linear designs.

This proves that surface wave EMATs can be optimised for surface wave detection of sub-mm defects through a metallic paint coating. While pseudo-pulse-echo focused meander-line EMATs are already in existence, there was previously no published work on their capabilities and full characterisation. The other focused designs presented here are new designs in the field.

Abbreviations

AC : alternating current

ACPD : alternating potential drop.

B-scan : brightness scan.

CHOTs : cheap optical transducers.

DC : direct current.

DCPD : direct current potential drop.

EDM : electro-discharge machined.

EMAT : electromangetic acoustic transducer.

FDM : fused deposition modeling

FEA : finite element analysis.

FFT : fast Fourier transform.

NDE : non-destructive evaluation.

NDT : non-destructive testing.

RCF : rolling contact fatigue.

SCC : stress corrosion cracking.

SNR : signal to noise ratio.

Symbols

Latin

A : arbitrary amplitude constant.

B : arbitrary amplitude constant, Chapter 2, section 1.
: magnitude of magnetic flux density elsewhere.

\mathbf{B} : magnetic flux density.

\mathcal{B}_1 : first order Bessel function

C : elastic stiffness constant(s) in Chapter 2, section 1 only.
: Capacitance elsewhere.

c : phase velocity.

c_L : longitudinal phase velocity.

c_T : shear wave phase velocity.

D : lens diameter, Chapter 2, section 1 only.

\mathbf{D} : electric flux density.

dS : surface integral.

dV : volume integral.

\mathbf{E} : electric field.

e : charge of an electron, Chapter 2, section 2. : Euler's number elsewhere.

F : focal length.

f : frequency.

g : constant, used for Lamb wave definitions, where $g^2 = (\omega/c_T)^2 - k^2$.
H : magnetic field.
 h : thickness.
I : electric current magnitude.
J : electric current density.
 j : imaginary number, $\sqrt{-1}$.
 k : wave number (unless in index notation).
 L : inductance in Chapter 3.
: racetrack coil width in Chapter 4.
 l_1 : Lamé parameter, often represented as μ .
 l_2 : Lamé parameter, often represented as λ .
M : magnetisation.
 m : density unless otherwise specified.
 m_e : mass of an electron.
 N_i : ion density.
 $\hat{\mathbf{n}}$: unit vector normal to the surface S .
 n_e : electron density.
 p : constant, used for Lamb wave definitions, where $p^2 = (\omega/c_L)^2 - k^2$.
 q : constant, used for Rayleigh wave definitions, where $q^2 = 1 - (c/c_L)^2$.
 R : reflection coefficient in Chapter 2, section 1.
: resistance in Chapter 2, section 2.
 Re : taking the real part of the function.
 r : constant, used for Rayleigh wave definitions, where $r = 2 - (c/c_T)^2$, in Chapter 2. : radial distance, in Chapter 4.
 s : constant, used for Rayleigh wave definitions, where $s^2 = 1 - (c/c_T)^2$.
 T : Transmission coefficient.

t : time.

u : displacement.

V : wave velocity.

\mathbf{v}_e : mean electron velocity.

\mathbf{v}_i : mean ion velocity.

$\dot{\mathbf{v}}_e$: mean electron acceleration.

X : reactance.

Z_i : charge on an ion.

x, y, z : Cartesian co-ordinates.

i, j, k, l : integer indices when used in index notation.

Greek

α : $\sqrt{a^2 + j\omega\mu\sigma}$

Γ_{ij} : Christoffel matrix.

δ : electromagnetic skin depth.

δ_{ij} : Kronecker delta (1 for $i = j$, 0 otherwise).

ϵ : strain in Chapter 2, section 1 only.

 : material permittivity elsewhere.

ϵ_0 : permittivity of free space.

ϵ_r : relative permittivity. $\epsilon = \epsilon_0\epsilon_r$.

η : constant, where $\eta = (c/c_T)$.

θ : angular measurement.

λ : wavelength.

μ : material permeability.

μ_0 : permeability of free space.

μ_r : relative permeability. $\mu = \mu_0\mu_r$.

ν : Poisson ratio.

ν_R : Poisson ratio for a Rayleigh wave.

ξ : constant, used for Rayleigh wave definitions, where $\xi = (c_T/c_L)$.

ρ : charge density.

\sum_i : summation over i .

σ : stress in Chapter 2, section 1.

 : material conductivity elsewhere.

τ : mean time between electron-ion collisions.

ϕ : scalar potential.

χ_e : electric susceptibility.

χ_m : magnetic susceptibility.

$\boldsymbol{\psi}$: vector potential.

ω : angular frequency.

Miscellaneous

∇ : gradient operator.

$\nabla \cdot$: divergence operator.

$\nabla \times$: curl operator.

Chapter 1

Introduction

With an ageing infrastructure, detection of smaller defects and identification of the start of cracking is becoming a higher priority industrial requirement [1]. This work investigates ways to improve the ability of electromagnetic acoustic transducers (EMATs) to detect smaller surface breaking defects, and to characterise the capability of these improved designs for working in a non-contact manner at higher lift-offs from the sample.

1.1 Surface Breaking Defects

Two important types of surface cracking that can occur in industry are rolling contact fatigue (RCF) and stress corrosion cracking (SCC).

1.1.1 Rolling Contact Fatigue Cracks

Rolling contact fatigue (RCF) is a surface initiated, directional cracking caused by a rolling contact between two surfaces [6, 7]. It can occur in systems containing two metals in rolling contact, such as twin discs, ball bearings and in railway tracks. Its importance was brought to the forefront after a fatal train disaster in Hatfield, October 2000, highlighted its dangers [8, 9, 10]. The cracks initiate at a shallow angle ($\sim 10\text{-}25^\circ$ [11]) to the surface, propagating in the direction of the rolling contact, but can branch deeper into the sample as they grow (figure 1.1). For early stage detection of RCF, defects as small as 0.5 mm need to be identified [12]. The current advice to treat this early stage cracking in railway tracks is to regularly grind off the top layer of the rail head as they are too small to be detected and this prevents them from propagating deep into the rail head, but this is not a sustainable policy [8, 10].

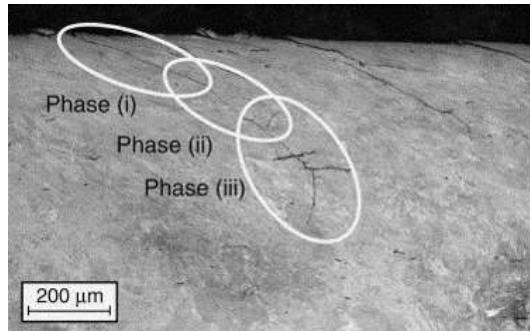


Figure 1.1: Rolling contact fatigue cracking found in a sectioned disc after laboratory controlled rolling contact with another disc. Image reproduced from Ringsberg et al. [7].

RCF cracking was originally found by visual inspection. The current detection system for RCF cracking consists of a wheel probe using a bulk wave piezoelectric ultrasound transducer that looks for reflections returned from defects [13]. This method requires continuous application of couplant during scanning, usually spray on water, and the pulse-echo system requires a scanning speed which allows detection of the reflections returning to the probe from the sample bulk, making the system inherently slow, 40-70 km/h [10]. The use of surface wave instead of bulk wave analysis allows for a pitch-catch detection method, analysing the signal transmitted along the material surface [14, 15]. This means the theoretical limit to the detection is limited by the speed of the ultrasound velocity (~ 3000 m/s depending on the type of steel [16]). As long as the scanning speed is less than the ultrasound velocity the surface wave generated at one position in the scan will always catch up with the detection probe as it is scanned along the surface. Surface waves are also most sensitive to the deepest surface cracks, which will block most of the wave transmission, whereas bulk waves can encounter masking of larger cracks by smaller cracks due to the angled beam geometry of the set up, shown in figure 1.2 [10, 13]. EMAT probe systems have been designed to work with an unloaded, flexible contact to the surface, with the EMAT magnet at a much larger lift-off than the coil, allowing for fast movement without couplant [15]. EMATs can also directly induce surface waves, unlike piezoelectric transducers which have to use an angled wedge to convert the ultrasound reducing their efficiency, [17], and are usually used for bulk waves instead. An alternative surface technique is the use of lasers, and/or air coupled transducers [18], which are discussed later.

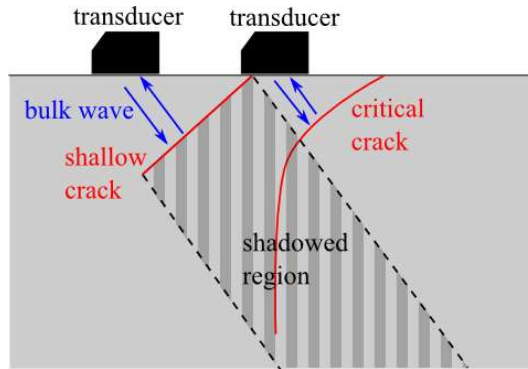


Figure 1.2: Schematic of how shallow RCF cracks can shadow deeper RCF cracks when inspected using bulk waves [10, 13].

1.1.2 Stress Corrosion Cracking

Stress corrosion cracking (SCC) originates from non-cyclic tensile stress in a corrosive environment [12, 19, 20, 21, 22]. The cracking process is complex and varied, often resulting in complex geometry branching cracks propagating inwards from the surface (figure 1.3). Depth gauging of these defects using ultrasonics is complex due to this branching nature, but feasible [22], with branching cracks potentially shadowing deeper vertical sections of cracks when using bulk waves, as shown in figure 1.4. SCC detection is of high importance in many situations in industry, notably in the nuclear power plant industry [20], where in-service inspection at high temperatures is desirable to avoid the need to shut down the plant. SCC has also been observed in buried pipelines, notably in the oil and gas industry [23].

Crack growth and branching is very difficult to predict as SCC describes a whole range of different variations depending on the different mechanical and chemical environments [12, 19]. In some cases the crack is largely due to the effect of local stresses, and only marginally exacerbated by a corrosive environment, and in some cases the cracking is created largely by corrosion as the chemical composition of the material is altered, with only minor contributions from the stress. The dominant factor may not be clear, with chemical changes causing changes in the local stresses, and local stresses opening up cracks causing exposure of further material to the corrosive environment. A report written by the National Physical Laboratory lists three main SCC mechanisms: active path dissolution, hydrogen embrittlement, and film-induced cleavage [24]. Active path growth is slow, around 1 mm in three years, whereas hydrogen embrittlement can be as fast as 1 mm in 1 second. While there are many standards in place to test materials to different SCC risk environments, such as exposure to boiling 42% MgCl_2 solution to test austenitic steels for chloride

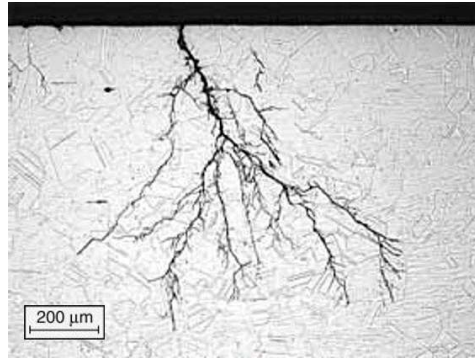


Figure 1.3: Stress corrosion cracking in type 316L stainless steel, reproduced from Mathers [26].

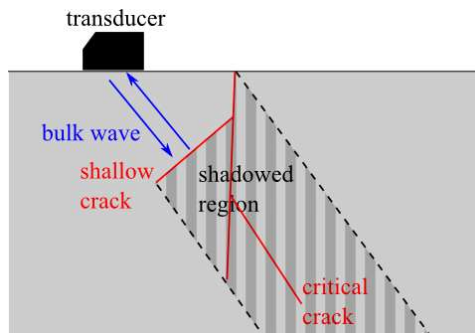


Figure 1.4: Schematic of how shallow crack branches can mask the real depth of a crack when inspected using bulk waves.

SCC [25], the mechanisms are not well understood. This makes early stage detection and monitoring of such defects key to better understanding their nature, giving a need for higher resolution imaging and depth detection [12].

1.2 Non-Destructive Evaluation Methods

Defect detection in industrial components, without damage to the component, is called on for a variety of reasons. It can be for inspection at the manufacturing stage, to ensure components are created as expected, for in service monitoring to watch for component degradation, or for routine checking, taking a component out of service to see if it is still fit for purpose. A great variety of techniques have been employed for this, the simplest of which is unassisted visual inspection. This has clear limitations in that it is difficult to automate, the software requirements for computer recognition of defects from optical images are currently impractical, and it is also restricted to defects which are open at the surface, and hence visible with optical light. A variety of other techniques for surface breaking defect detection are briefly reviewed here, however there are more techniques available.

1.2.1 Dye Penetrant Inspection

This is a type of visual inspection. Coloured or fluorescent liquid dye is spread over the surface to be inspected and is drawn into any surface breaking defects by capillary action. As the dye is often then hidden inside the defects a developer can be used to draw the dye back out of the cracks and provide image contrast. The defect locations are then observed by eye [27, 28]. This technique is quick, cheap and simple. However, the surface has to be clean and completely dry for the capillary action to work. Porous surfaces also prevent detection. The technique is mostly qualitative, gives no depth information, requires a highly trained operator, requires clean up of the dye after inspection, and is low resolution [17].

1.2.2 Magnetic Particle Inspection

This is another type of visual inspection. Magnetic particle inspection (MPI) runs on the principle that cracks in a magnetised sample will disrupt the flow of the magnetic field lines. This disruption causes concentrations of the magnetic field at a defect. The magnetic field can be measured directly using e.g. Helmholtz coils, which is known as Magnetic Flux Leakage (MFL) inspection [29]. Alternatively, a faster and simpler way is to inspect the magnetic field visually by using particles such as iron filings, or iron particles suspended in a fluid, which then concentrate at these spikes in the magnetic field. A white contrast paint is often applied to increase the visibility of the particles used. A device such as a yoke is used to apply a magnetic field through the sample at the area of interest, the contrast paint is applied, and then the particles. Some indication is given of the defect size from the surface extent

of the particles, however, it is again largely qualitative, with no indication of defect depth. This is a simple, cheap, and quick to use technique, especially when large areas need to be studied, but it is messy, low resolution, qualitative, it needs direct access to the surface, and only works on magnetic materials [28, 30].

1.2.3 Radiography

Radiography inspects materials by exposing them to an x-ray or γ -ray source and detecting the transmission on the other side of the sample [28]. The input rays spread out from the source uniformly, but variations in the density of the material cause corresponding variations in the attenuation of the rays, creating an image on the detection surface. X-ray sources are typically created by bombarding a material (often Tungsten) with electrons. Varying the electron energy by changing the voltage drop over which they are accelerated varies the x-ray spectrum created. The total attenuation of the x-rays through a material is a combination of material absorption and scattering, which varies depending on how different x-ray energies interact with the materials, and so an appropriate x-ray source and energy is needed for a good image contrast. Sometimes other related techniques using electrons, protons, or neutrons can give better images depending on the material and defects being imaged [28, 31]. The image detection mechanism was originally x-ray sensitive photographic paper that darkens when the x-rays make contact, but is being replaced by digitized detection plates.

Many different effects can lead to variations in the radiographic image, such as variations in material density. In some ways, this then becomes a type of visual inspection to interpret the images, although it is no longer surface limited and computer algorithms are often employed [32]. Radiography is non-contact, can image any defect type (although some types are more difficult and orientation dependent), simple, and fast, imaging large areas very quickly. However, it is relatively high cost, uses hazardous radiation, needs a highly trained operator to interpret the images, and access is needed to the whole surface on both sides. A single source cannot be used for all materials, and so systems have to be varied dependent on the individual inspection.

1.2.4 Eddy Current Testing

When an alternating electric current, typically carried by a wire solenoid coil, is present in proximity to a conductive material, the effect of its associated alternating magnetic field generates an eddy current within the conductive material in

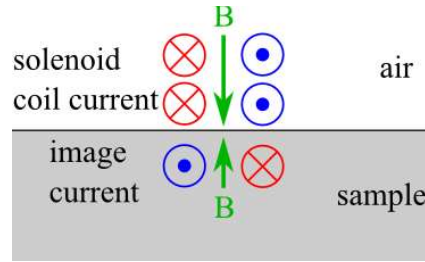


Figure 1.5: Schematic of the cross-section through an eddy current solenoid coil and the corresponding image current and magnetic fields in the proximity of a metallic sample

opposition to the initial current [33, 34]. In turn this new current creates its own alternating magnetic field, shown in figure 1.5. The behavior of this eddy current and its field depends upon the properties of the material, such as its electrical conductivity and magnetic permeability, and also upon the shape of the surface of the material. Flaws within the range of the eddy current alter its path and therefore change the magnetic field that it creates [35].

Eddy Current testing can be done using a continuous wave excitation of the generation coil, or using excitation pulses [36]. The response from the sample can be measured by directly measuring the magnetic field, for example with Hall effect sensors [37], at the sample surface. Alternatively, the changes in magnetic field in turn induce current changes back in the original conductor, and these variations can be detected. A single coil can be used to generate the eddy currents and then detect the sample response [38], but often a separate passive coil, or set of coils, is used for detection to isolate the generation and detection systems. Whole arrays of coils can also be used to map large areas at once [39, 40]. The variations of current in the coils are small so the electronics have to be well isolated against noise. The depth range of the eddy current within the sample depends upon the electro-magnetic skin depth, δ , of the input signal, which is predominantly dependent on the frequency,

$$\delta = \sqrt{\frac{2}{\omega\mu\sigma}}, \quad (1.1)$$

where ω is the angular frequency, μ is the material permeability, and σ is the material conductivity [41]. This is explained in more detail in section 2.2 in the context of EMATs. Consequently, lower frequencies extend deeper into the sample, and higher frequencies are more surface sensitive. Very small size coils (1 mm or less) can be used to give high spatial resolution of the defect surface profile, however, the data is often qualitative and complex to interpret [35].

Eddy currents can be used for surface defect depth gauging with careful calibration, depending on the material properties. However, the technique is very sensitive to many sample parameters such as the conductivity and magnetic permeability, making depth gauging impossible without complex sample characterisation. Eddy current probes are also sensitive to variations in lift-off, so variations in the sample surface roughness can affect the depth measurements made. High frequency operation for the detection of small surface breaking defects becomes sensitive to surface roughness creating more noise in the signals. This can be improved by performing a frequency sweep and then using data fusion to couple all the data, although this becomes time consuming [38, 42]. Data fusion with thermal imaging has also been performed [43], improving imaging resolution. Operation at electrical resonance has been investigated to improve the SNR [44]. Both techniques, [43, 44], have shown defect detection capabilities down to cracks in the sub-mm range. A distinct advantage over ultrasonic techniques is the ability to perform defect detection on materials with grain structures close to the size of typical ultrasound wavelengths, causing ultrasound signals to be highly scattered, such as the titanium and composite materials often used in aerospace [44]. Eddy currents are a non-contact technique and can therefore work through some coatings, however, their strong surface sensitivity makes it difficult to find small cracks beneath some metallic coatings which can block operation in the sample under the coating at typical test frequencies, where non-contact ultrasonic methods can be advantageous. The disadvantages of needing a calibration, sensitivity to roughness, and difficulty operating through some coatings, means that ultrasonic inspection is also useful.

1.2.5 Alternating Current Potential Drop

The alternating current potential drop (ACPD) technique also relies on the electromagnetic skin depth effect to deep size cracks [35, 45, 46], but instead of using induction, the current is applied directly into a metal sample. It is an extension of the direct current potential drop (DCPD) technique which sends a direct electrical current through a metal sample and measures changes in the detected voltage. If the voltage is reduced, there is likely a defect in the material. The DCPD measurement, however, had no depth sensitivity. Both ACPD and DCPD can be done as two or four point measurements. Two point measurements simply monitor the voltage drop between two electrodes. Four point measurements applies the AC between two contact points, and the second two contact points are used to detect current flow in the sample. DCPD usually uses currents of around 30 Amps, whereas ACPD uses currents of around 1 Amp, making it safer and less likely to cause sample

heating. By varying the frequency of the AC between the first two contact points, different depth sensitivities can be achieved, in accordance with equation 1.1. This technique, however, has the same problems as eddy currents for the depth measurements, as it is sensitive to changes in material conductivity and permeability, this can be exploited to make stress and strain measurements, and to study closed cracking [46]. The main noise source in ACPD is induction from the driving current wires to the receiving wires, however this can be removed digitally, or using careful isolation. Another disadvantage of these techniques is the requirement for direct surface contact.

1.2.6 Ultrasound

Ultrasonic testing methods rely on the general principal that the material in which an ultrasonic wave travels affects the wave propagation. A measurement of the time of flight for an ultrasonic wave gives the distance it has traveled if the sound velocity in the material is known. This can be used to locate defects by observing reflections from a defect and measuring their arrival times, or to look for variations in material thickness by measuring changes in reflection arrival time for applications such as looking for thinning in pipe walls [17, 47]. Longer wavelengths can usually penetrate further into a sample (depending on the material and the wave mode), whereas shorter wavelengths tend to attenuate faster [48]. The attenuation of bulk wave ultrasound is dependent on two main factors: the energy absorbed by the material, and the scattering of the ultrasound. In polycrystalline metals, scattering is typically caused by their granular structure, and ultrasound waves which have a similar wavelength or smaller with respect to the average grain boundary size are highly scattered [49]. A problematic material for typical ultrasound measurements is Titanium as it has a large granular structure, causing most ultrasound signals to be highly attenuated. However, shorter wavelengths typically provide better time resolution as shorter wave pulses can be created, allowing reflections which are closer together in arrival time to be individually resolved. Resolution capabilities will be discussed further in the theory chapter.

Surface wave techniques can be used to locate surface cracks by observing the enhancement of an ultrasonic wave at a defect as the incident and reflected waves undergo constructive interference [50, 51]. When defects are smaller than the ultrasonic surface wavelength a significant proportion of the wave will transmit underneath and around the defect. This transmitted wave can be detected, and variations in amplitude and frequency can be used to size the defect, further discussed in section 2.1.4.

All ultrasonic techniques are quantitative, although scans can take longer than visual inspections, and the ultrasonic waves are safe, thus avoiding the health hazards of radiography. Implementation of the most common technique, using piezoelectric transducers, is relatively simple and inexpensive.

Piezoelectric Transducers

Piezoelectric transducers are the most well known type of ultrasonic transducer due to their wide use in medical diagnostics and therapy. A typical material used to make piezoelectric transducers is Lead Zirconate Titanate, or PZT, shown in figure 1.6 [52, 53]. It is both pyroelectric and piezoelectric. Pyroelectricity means that while the material is below a critical (Curie) temperature the crystal structure distorts with temperature, as shown in figure 1.6. However, the central Ti/Zr atom does not move uniformly with the rest of the structure, causing an electrical polarisation of the crystal which varies with temperature. This polarisation causes a voltage drop between the top and the bottom face of the structure in figure 1.6b), which can be measured, allowing them to be used as heat sensors. Piezoelectricity means that when the material is distorted in shape by an applied stress the same type of distortion is seen, creating a measurable voltage change, allowing them to be used as vibration sensors. The reverse process can also be used to create vibrations, where an applied external electric field causes the material to distort to create a polarisation in alignment with the external field, and so an alternating current causes the crystal to vibrate longitudinally. This is the property that is exploited to generate ultrasonic bulk waves. Piezoelectric materials are often employed in inchworm actuators [54, 55, 56], for instance in atomic force and scanning tunneling microscopy, as controlled voltages can be used to create very accurate step sizes from the piezoelectric material distortion.

PZT is a common material for ultrasound sensors as it has a large physical distortion for a small applied field, however, it is not the only material. Sodium Bismuth Titanate, Bismuth Titanate and Lithium Niobate are being developed for higher temperature applications of ultrasound, and also due to the environmental concerns associated with the use of lead [52, 57, 58]. Bismuth Titanate has a Curie temperature of around 675°C and Lithium Niobate around 1142-1210°C, however, they are much less efficient. For example, Baba et al. [58] managed steel wall thickness measurements up to 1000°C using a Lithium Niobate transducer but 256 averages were needed to obtain usable signals.

Another difficulty is the transfer of the piezoelectric vibrations from the material to the sample of interest. In room temperature applications coupling fluids

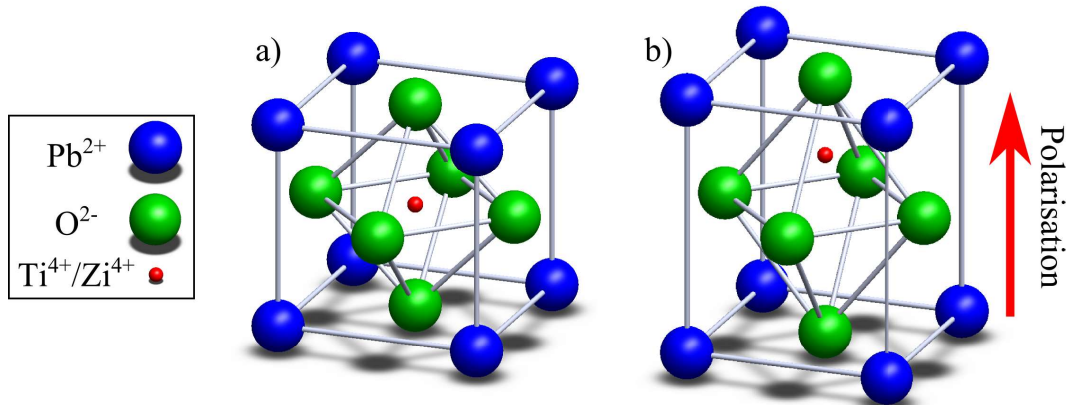


Figure 1.6: Schematic of an example lead zirconate titanate (PZT) configuration (a) above the critical temperature, with no applied forces or electric fields (b) the distortion seen below the Curie temperature, in a vertical applied electric field, or under an applied stress.

such as water or gel are used to reduce the acoustic impedance mismatch (see section 2.1) between the piezoelectric material and the sample, and also filling in any air gaps which add a strong acoustic impedance mismatch. However, few of these couplants remain liquid at such high temperatures. The study by Baba et. al [58], coupled the transducer directly to the steel, making it immovable, so only a point measurement could be taken. Burrows et al. [57] managed steel wall thickness measurements with a movable Bismuth Titanate transducer, however it was limited by the 300°C boiling point of the Pyrogel 100 couplant used, and measurements were made at 225°C . Even outside of high temperature applications, the need for contact and a coupling medium makes scanning slow. Additionally, piezoelectric transducers are efficient at generating longitudinal bulk waves, and can also be used for shear wave generation. However, they cannot generate shear horizontal waves easily, and can only generate surface waves with the use of angled matching wedges, reducing their efficiency [17].

Air coupled Transducers

Transmission of ultrasound through air is desirable for non-contact measurements in an air environment. Coupling ultrasound into air is intrinsically difficult for piezoelectric transducers due to the large impedance mis-match, however it can be done for Lamb wave generation with careful alignment, electronics, and post-processing for the low SNR [59, 60]. One way to circumvent this is submersion in water, however this can be impossible for in-situ measurements. Flexural transducers circumvent

this by using the physical push from the bending modes of a vibrating plate, such as a metal cap, or a membrane, to initiate ultrasonic vibrations into a fluid. The cap or membrane can be vibrated using a piezoelectric material [61], however it can also be done using micromachined capacitance transducers [62], and EMATs [63]. This is needed as coupling ultrasound from a piezoelectric material into fluids such as air is inherently poor due to their mismatched impedances (see section 2.1) although matching layers can be used to improve this [64].

A widely known application of flexural transducers is car parking sensors, however there are multiple applications for them where ultrasound propagation is through air or liquids, such as fluid flow measurements in pipes [65]. Air-coupled transducers have also been used for NDT [59, 60], although the interaction with typical inspection materials such as steel is weak. They are inherently non-contact, however for NDT purposes they need very careful alignment, but their non-contact nature makes them simple to automate for robotic scanning [60, 66].

Laser Induced Ultrasound

Laser ultrasonic generation can be done in two main regimes. The first is the thermoelastic regime, where the laser powers are kept low enough that the material being inspected is usually not damaged. This relies on the principle of thermal expansion and contraction [67]. A high powered, pulsed laser such as a Ruby or Neodymium doped yttrium-aluminium-garnet (Nd:YAG) is fired at a sample and the local area of the sample undergoes thermal expansion during the pulse, and relaxation between pulses, initiating a vibration. This can generate both bulk waves and surface waves [68]. If the power is high enough to damage the surface of the sample this is known as the ablative regime. This generates ultrasound by ablating the sample surface. A shock wave is created from the ablation, and it is no longer non-destructive, typically rendering it undesirable. However, the ablative regime can be utilised if a separate, disposable material is used, protecting the sample of interest, and then the ultrasound is actually generated by the plasma created from this ablation [69]. This plasma and the high power of the laser increase the safety hazards of the technique.

There are multiple ways of detecting ultrasound using lasers. Laser detection systems can be safer than generation as lower powers can be used, although this is not always the case. One detection method is interferometry. This method reflects the laser beam off the surface and mixes it with a reference signal that has traveled a known distance. The variations in the interference between the two waves gives a measure of the displacement of the sample surface. These can measure the

absolute out-of-plane displacement. Early versions of these, such as the Michelson interferometer, could only be used on highly reflective surfaces, requiring sample polishing. However, techniques have improved greatly and crystal diffraction techniques have been used to perform the interferometry measurements on much rougher surfaces [70]. These rely on a measured calibration, making them less accurate than the Michelson interferometer, but much more practical. Heterodyne interferometers, or ‘vibrometers’, use a reference wave that has been shifted in frequency, which is equivalent to a modulation by the wave velocity rather than the displacement. This can be used to directly measure the velocity, and also the displacement independently [67]. Knife-edge techniques can be used to measure both out-of-plane and in-plane motion, using a glancing angle to the surface and measuring the angle of the reflected wave which oscillates with the surface below. Some techniques have also measured in-plane motion using two laser beams incident on the surface and observing their interference patterns [71].

Laser techniques can be used at very large distances, completely remotely, and can be operated at very high frequencies, [72]. Very small beam spot sizes give very good resolution [67]. However, they are expensive, need access to the surface, and most laser generation systems have serious safety hazards. Safety hazards can often be mitigated by sufficient beam confinement and lower powers, and the systems can be fully automated for simple scanning.

EMATs

EMATs are a robust and inexpensive alternative to piezoelectric and laser ultrasonics, and are fairly safe when appropriate precautions are taken around the high currents and magnetic fields used [2]. They can work without direct physical contact to the samples, although have to be within a few mm, with no coupling gel required, allowing them to be utilised in a variety of situations where standard piezoelectric ultrasonics are not viable, such as on moving, hot, rough, coated, or rusted surfaces [73, 74, 72, 15].

EMATs as generators consist in their simplest form as a coil of wire through which an alternating current is pulsed [2]. Their generation and detection mechanism will be discussed in more detail in section 2.2, however, in brief, this current creates an alternating magnetic field around the coil elements which, when close to a conductive sample, creates an image current from the sample’s delocalised electrons, shown in figure 1.7. These image currents then experience a Lorentz force as a moving charge in a magnetic field. The electrons in the image current transfer their momentum by elastic collision causes their parent ions to move with them. This

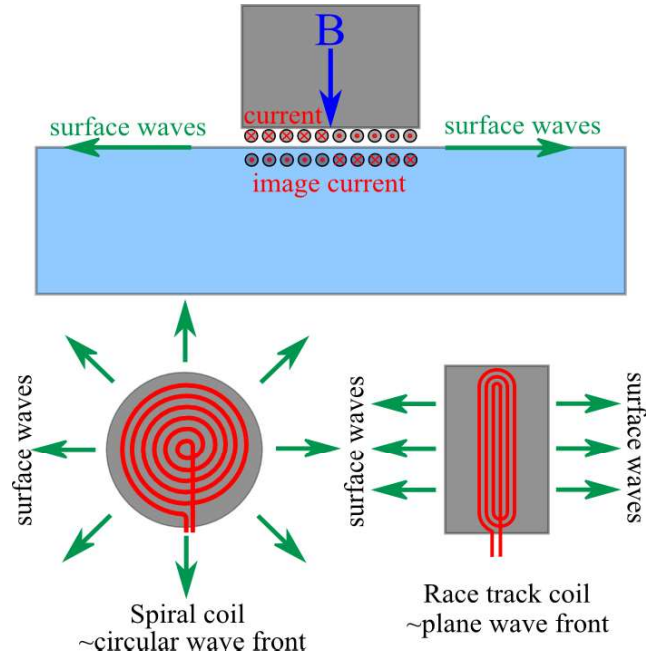


Figure 1.7: EMAT schematics showing the set-up of wire direction and magnetic field for surface wave generation, and the variation in wave fronts created from different coil profiles.

can be done without the external magnetic field, however this field typically creates strong ultrasound waves. The configuration of the magnetic field direction and the coil shape alters the wavemodes that are generated. Figure 1.7 shows the configurations for two types of EMATs as examples which can generate surface waves, and figure 1.8 shows the three main designs relevant to this work. EMAT detection works similarly, however, it is more efficient than the generation method as the sample ions are already moving, causing the motion of the electrons which are much lighter and so the energy transfer is more efficient, and the electron motion can be detected by the coils [75]. The presence of a permanent magnet is a necessity for detection as the ultrasound wave had no net charge movement due to the motion of both the ions and the electrons,. Magnetisation and magnetostrictive forces are also present when EMATs are used on ferromagnetic materials which can enhance their performance [2, 73]. The mechanisms are covered in more detail in section 2.2.

One application of EMATs is in power plants due to their high temperature capabilities, either in conjunction with water cooling around the magnet to prevent it from rising above the magnetic Curie temperature [76], or using high temperature magnets [77]. Another application is in the railway industry where the non-contact ability has the potential for scanning speeds of up to 100 mph [13, 15], whereas

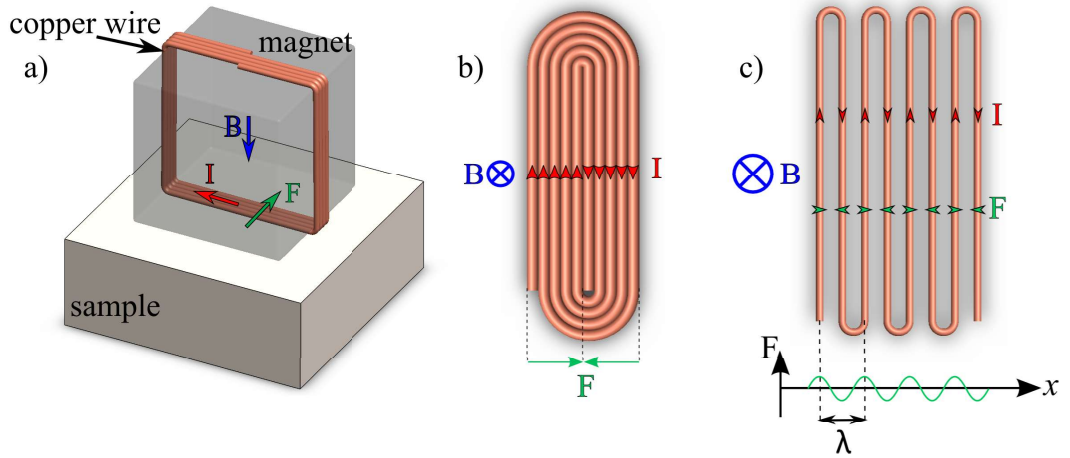


Figure 1.8: EMAT schematics showing the set-up of wire direction and magnetic field for the three main surface wave generation designs applicable to this work. a) shows a linear design with all wire elements in parallel, b) shows a racetrack design with two halves of the coil having current flow in opposing directions, and c) shows a meanderline design with alternating current directions.

most current systems operate around 20-30 mph. Another application is the steel industry, where inspection of hot steel up to temperatures of 800° is required to monitor the integrity of the steel as it is rolled [72]. They have also been used in the food inspection industry for the inspection of the level of drink in cans after production [78]. EMATs do introduce some hazards as the driving currents used are often high, and some designs hold large magnets, however, system automation reduces the human risk.

Phased Arrays

Phased array techniques offer one type of ultrasonic beam focusing (discussed further in the following section) [39]. Phased array transducers consist of a set of identical ultrasound transducers arranged in an array forming a single unit. The individual elements of the array can be excited to produce ultrasound with controlled time delays with respect to each other [79]. Using the correct time delays creates different shape wave-fields from the unit. The ultrasound waves excited by the elements experience different constructive and destructive interference with the waves from the other elements depending on the times at which they are incident with each other. It is therefore possible to fire the elements so that there only is a strong constructive interference of the waves in a small volume of the sample to be inspected. This allows for high resolution inspection of small areas with stronger

signals. Detection can be performed using the same array as the transmitter [79], or another array if transmission measurements are desired. When the same array is used, the exact origin of an ultrasonic wave reflection can be determined, as it has a different arrival time at each array element depending on its origin. Full sample images can be generated this way, however, the data processing is complex, and computer algorithms are being developed to distinguish different defect types from this imaging [80].

There are three typical array configurations: linear arrays, annular arrays, and 2D grid arrays, shown in figure 1.9 [39], although there are more. A linear array is comprised of a set of elements in a single line. This only allows for a variable angle, but planar, wavefront, or line focusing into the bulk, in the image plane shown in figure 1.9a). Annular arrays typically consist of a set of concentric annular elements, allowing for variable depth point focusing, but no other directional variation without scanning the unit [81]. 2D grid arrays give the most variability but they are also the most complex to build. An ideal array would have infinitely small elements with no gaps between them allowing for perfect focusing. The finite size of elements and the pitch between them creates a diffraction grating effect, causing side lobes in the profiles [82].

Phased array techniques have largely been pioneered using piezoelectric transducers, however they have also been implemented using EMATs [83, 84] and flexural transducers [66, 60, 65]. Ohara et al. [85] have implemented a Rayleigh wave piezoelectric focused array with a central frequency of 5 MHz to image a variety of long (5-30 mm) surface breaking fatigue cracks and SCC type defects in aluminium, reporting a length measurement accuracy of ± 0.5 mm. Exact defect depths were not reported, but appear to be above 1 mm. Deutsch et al. have used a similar array to identify holes drilled through an aluminium sample with diameters of 2 and 1 mm [86]. Scanning of phased arrays requires sophisticated electronics and computation to deal with the volumes of data being returned [39]. Piezoelectric phased arrays also experience all the draw backs associated with the ultrasound generation mechanism such as continuous applicant of couplant, or submersion in water for scanning, and the need for surface access. EMAT phased array techniques have had little use so far due to the difficulty in construction, and large sizes (typical single EMATs being 30 mm or more in dimensions, although much smaller ones are now possible).

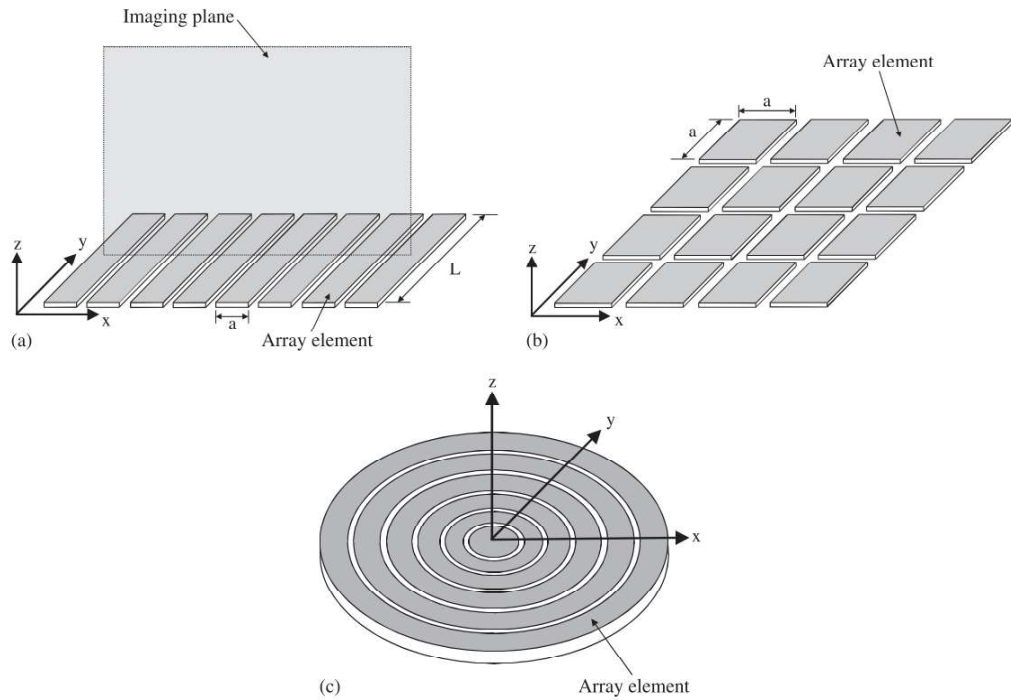


Figure 1.9: The three main types of phased array, a) linear, b) 2-D array, c) annular. Image reproduced from Drinkwater et al. [39]

Ultrasonic Beam Focusing

Ultrasonic beam focusing offers part of the solution to the industrial need to image small defects [1]. This allows the usage of large transducers, or whole arrays of transducers to create a strong signal, but a detailed spatial resolution is achieved through the focusing [39]. This also concentrates the signal power into the area of interest, further increasing the capability to detect small defects. Focusing of Rayleigh surface waves is therefore desirable for the improved detection of small surface breaking defects such as RCF cracking and SCC.

Piezoelectric elements only generate bulk waves. Surface waves can be created if the bulk waves are then mode converted through wedge shaped contact ‘lenses’. This gives additional attenuation as some energy is converted to different mode types, and some is reflected, decreasing efficiency. For Lamb waves (plate waves, see section 2.1.3) and different materials this also requires a different wedge angle for exciting different modes. Rayleigh wave focusing has previously been implemented using shaped piezoelectric elements and wedges [87] (figure 1.10a)) and with piezoelectric phased arrays, as discussed in the previous section [86, 88, 85] (figure 1.10b)). Single piezoelectric focused transducers have been produced with

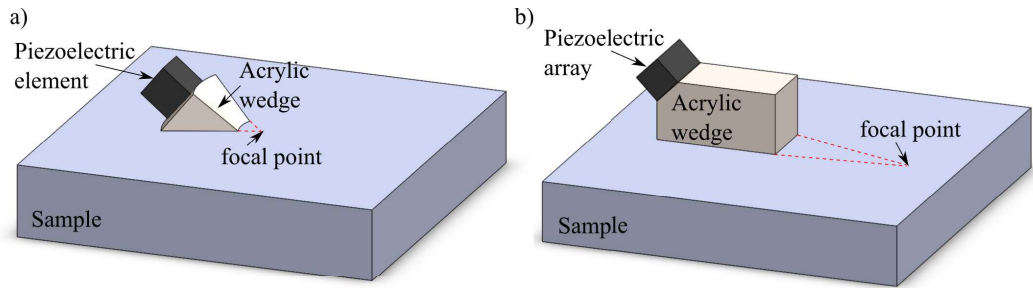


Figure 1.10: Rayleigh wave focusing using piezoelectric elements. (a) shows the complex geometry wedge used to focus the beam from a single piezoelectric element [87], (b) shows the focus created by using time delays from a piezoelectric array [86, 88].

a beam width of 1.2 mm at 3.3 MHz [87]. Phased arrays allow for variable focusing and can therefore perform multiple different inspections without having to be scanned in detail over large areas. Single transducers are simpler and cheaper, however, these techniques focus to a fixed point and so have to be scanned over whole surface areas, and suffer from the sound equivalent of the optical phenomenon known as chromatic aberration [17]. Different wavelengths of a wave (optical or sound), will refract by different angles when entering and leaving a focal lens or block as the different wavelengths have different refractive indexes in a material (see section 2.1). This causes different wavelengths to focus to slightly different locations, leading to blurred images [17].

The use of non-contact ultrasonic methods for generating focused ultrasound beams offers many advantages in terms of implementation of inspection, despite the reduced efficiency of the techniques, and fixed focal points. The use of optical components when generating ultrasound with a laser can give a ring shaped beam, (figure 1.11a)), which when incident on a sample surface creates an inward traveling wave that becomes focused at the ring center. This focused point has much higher intensity than is possible with a direct incidence laser beam while staying in the thermoelastic (non-destructive) regime of laser generation [68, 89, 90]. A ring focused beam has been used to detect a 1 mm deep, 0.1 mm width, electro-discharge machined (EDM) slot in aluminium (length not reported), but this measurement required the defect length to be larger than the ring diameter [89]. Sample surface deposits or screens can also be employed to shape the laser footprint on the sample surface, changing the frequency bandwidth of the generated ultrasound waves and creating a focus, (figure 1.11b)) [91, 92, 93, 94]. This has been developed into a commercial technique called Cheap Optical Transducers (CHOTs) [91, 92]. How-

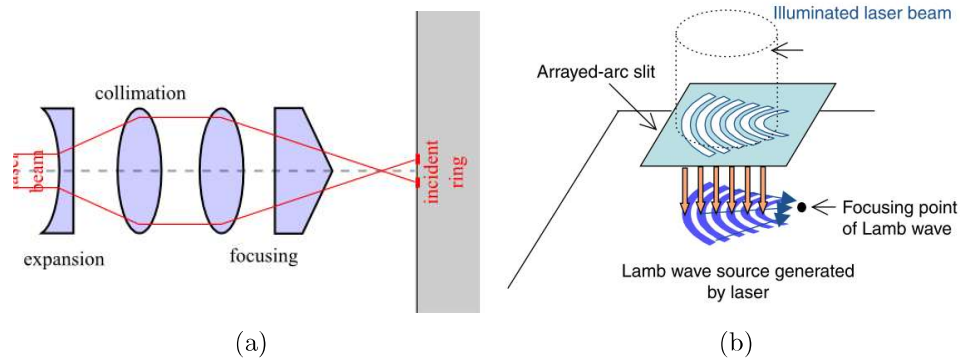


Figure 1.11: (a) the lenses used to focus a laser source into a ring [68], (b) surface wave focusing using laser surface patterning, image from Kim et. al. [94].

ever, laser generation is not always viable for regular machine testing in a factory setting due to their high costs and potentially serious safety implications.

The majority of previous work on focused EMAT techniques have concentrated on shear wave generation [2, 95, 96, 97, 98]. A straight meander line EMAT can generate shear waves which propagate into the sample bulk, and varying the meander spacings causes constructive interference of the beam to form a focal line [2, 96] (figure 1.12a) and c)). Curving this design adds a geometric focus for constructive interference at a point location (figure 1.12b) and c)), and this has been employed for detection of slits deeper than 0.05 mm on the opposite surface of a 20 mm thick stainless steel sample [97]. A curved EMAT design for Rayleigh waves has been shown in EMAT testing standards [99], but this has not been the focus of any concentrated research effort to understand and improve the EMAT behaviour until now. This design is mentioned only briefly as complimentary to a patented technique for finding weld defects [100, 101]. These designs are highly promising, offering increased resolution, depth gauging, operation through some coatings and high temperature operation, however more work is needed to understand their behaviour and capabilities.

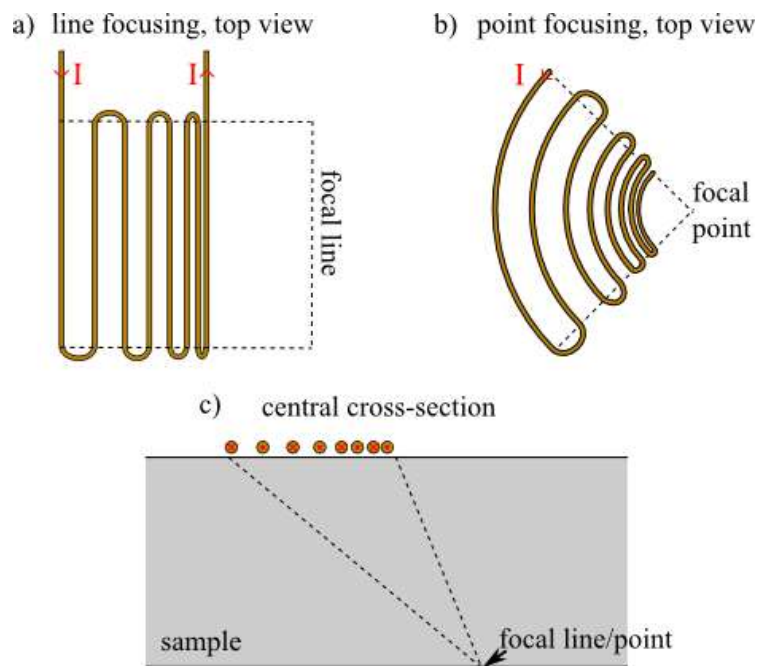


Figure 1.12: (a) the top view of the coil path used to create a line focused shear wave into the sample bulk. (b) the top view of the coil path used to create a point focused shear wave into the sample bulk. (c) the central cross-section of both (a) and (b), showing how the beam converges through the sample bulk. The background magnetic field used is into the sample surface.

1.3 Summary

The NDE industry is a long established field, however changing safety requirements demands improved techniques, especially for complex component assesment. For the direct application of this work, EMATs were chosen as the most viable testing device for inspecting a metal substrate through a thin metallic coating due to their non-contact nature and ability to function through a coating, and their quantitative measurements, including depth gauging. The main challenge is improvement of their intensity and resolution to find sub-mm surface breaking defects.

This work addresses a need for improved EMAT techniques for the inspection of sub-mm sized surface defects by using geometric focusing to increase the scanning resolution as well as the signal strength. Coil designs are modelled and characterised to find the optimum geometry for the increased frequencies required for these small defects. The different capabilities of different types of designs are compared, especially considering their ability to work at lift-off from the sample. Further design improvements are also suggested.

Chapter 2

Theory

This chapter outlines the well established theory on which the experiments in this work are built. Section 2.1 outlines the principals of ultrasonic wave propagation in materials, the constraint of a material surface, and the wave interaction with surface breaking defects. Section 2.2 outlines the electro-magnetic interactions which allow EMATs to generate elastic waves in a test material, and how these can then be detected.

2.1 Ultrasound

Ultrasonic waves are vibrations of individual atoms or particles oscillating about their equilibrium position at a frequency higher than the audible range, which ends at roughly 18 kHz [17]. They can create standing waves where the maximum oscillation amplitude of each atom does not change, or they can form travelling waves, where the motion propagates through a material, passed from atom to atom. The atoms themselves do not have a net movement, and return to their equilibrium position once the wave has passed. These travelling waves can be exploited for ultrasonic NDE.

2.1.1 Wave generation and Propagation

When a stress, σ , is applied to a material, there is a deformation of the material, which can be described by a material strain, ϵ . Where this stress is below the elastic limit of the material, Hooke's Law applies; this strain is linearly proportional to the applied stress. The general relation is:

$$\sigma_{ij} = C_{ijkl}\epsilon_{kl} \tag{2.1}$$

where i, j, k , and l correspond to positions in the tensors, and the summing convention over repeated subscripts is implemented. σ_{ij} the strain from a force applied in the i direction, on a face perpendicular to j . ϵ_{kl} gives deformation in the l direction, and the type of deformations is given by k , where y is a compressive deformation, and x and z are shear deformations. C_{ijkl} is a 4th rank tensor, often referred to as the elastic constant(s), or the elastic stiffness constant(s) [102, 103]. For NDE ultrasonic waves it can be assumed that all forces are below the material elastic limit, as otherwise the technique becomes damaging, and so Hooke's law holds [48]. This represents nine different equations each containing nine coefficients of C , making 81 coefficients in total.

This general form of Hooke's law can be greatly simplified if some assumptions are made [103]. Firstly, if it is assumed that the applied stress does not cause a net material acceleration or rotation (i.e. the sample overall remains static), the tensors σ and ϵ contain diagonal symmetry. This means that $C_{ijkl} = C_{kijl} = C_{iklj}$. This reduces the number of coefficients to 36. Secondly, if it is assumed that strain is a function of the material state, and not dependent on how the strain was created, then $C_{ikjl} = C_{jlik}$. This is a valid assumption for any material behaving elastically [104]. This reduces the number of independent coefficients to 21. Together these assumptions allow the number of indices for C to be reduced, and Hooke's law reduces to six equations which can be written as:

$$\begin{bmatrix} \sigma_{11} \\ \sigma_{22} \\ \sigma_{33} \\ \sigma_{23} \\ \sigma_{31} \\ \sigma_{12} \end{bmatrix} = \begin{bmatrix} C_{11} & C_{12} & C_{13} & C_{14} & C_{15} & C_{16} \\ C_{12} & C_{22} & C_{23} & C_{24} & C_{25} & C_{26} \\ C_{13} & C_{23} & C_{33} & C_{34} & C_{35} & C_{36} \\ C_{14} & C_{24} & C_{34} & C_{44} & C_{45} & C_{46} \\ C_{15} & C_{25} & C_{35} & C_{45} & C_{55} & C_{56} \\ C_{16} & C_{26} & C_{36} & C_{46} & C_{56} & C_{66} \end{bmatrix} \begin{bmatrix} \epsilon_{11} \\ \epsilon_{22} \\ \epsilon_{33} \\ \epsilon_{23} \\ \epsilon_{31} \\ \epsilon_{12} \end{bmatrix} \quad (2.2)$$

A C index of 1 now stands for 11, 2 for 22, 3 for 33, 4 for 23 and 32 (now equivalent), 5 for 13, 31, and 6 for 12, 21. This is the most general form of Hooke's Law for an elastic material. If the material can also be assumed to be isotropic (i.e. the xy , xz and yz cartesian co-ordinate planes are equivalent) then $C_{12} = C_{13} = C_{23} = l_1$, $C_{44} = C_{55} = C_{66} = l_2$, $C_{11} = C_{22} = C_{33}$, and all the other co-efficients become 0. l_1 and l_2 are known as the Lamé parameters [105], and are related using $C_{11} + C_{22} + C_{33} = l_1 + 2l_2$. This means Hooke's law (equation 2.1) can be written as:

$$\sigma_{ij} = l_1 \epsilon_{11} \delta_{ij} + 2l_2 \epsilon_{ij} \quad (2.3)$$

where δ_{ij} is the Kronecker delta. However, isotropy can only be assumed for cubic structure crystals. There are other simplifications that can be used for other systems which contain isotropy in some directions (e.g. a hexagonal system can be reduced to six co-efficients), but are not relevant to this work [103]. The cubic assumption can be used for the Rayleigh wave systems involved in this work as aluminium is a face-centered cubic structure, and steel is a body-centered cubic structure. However, it must be noted that this neglects effects from variations in grain structures. Extruded and rolled metals often show distinct variations in ultrasound velocity between the different rolling axes [106] due to changes in the grain structure, and so isotropy cannot be assumed, but this work concentrated on machined samples.

The displacement of a material particle, u_i , that is caused by an applied stress can be found using Newton's second law ($F = ma$ where m is mass) [48]. The force associated with a stress is the stress multiplied by the area over which that stress is applied. The instantaneous force is the differential of the stress, and then all the different stresses must be summed giving a force equation,

$$\sum_i \frac{\partial \sigma_{ij}}{\partial x_j} = m \frac{\partial^2 u_i}{\partial t^2}, \quad (2.4)$$

where m is now representing the mass density, and x_i are the particle locations. Equation 2.3 can then be substituted into equation 2.4, and using the definition of material strain as a small particle displacement,

$$\epsilon_{ij} = \frac{1}{2} \left(\frac{\partial u_i}{\partial x_j} + \frac{\partial u_j}{\partial x_i} \right), \quad (2.5)$$

this gives an equation of motion for the material particles,

$$m \frac{\partial^2 u_i}{\partial t^2} = C_{12} \frac{\partial}{\partial x_j} \left(\frac{\partial u_1}{\partial x_1} \right) \delta_{ij} + C_{44} \frac{\partial^2 u_i}{\partial x_j^2} + C_{44} \frac{\partial}{\partial x_j} \left(\frac{\partial u_j}{\partial x_i} \right). \quad (2.6)$$

The plane wave solution to this equation of motion is known as the Christoffel equation [48],

$$k^2 \Gamma_{ij} u_j - m \omega^2 u_i = 0 \quad (2.7)$$

where k is the wave number ($k = \frac{2\pi}{\lambda}$ where λ is the wavelength), ω is the angular frequency, and Γ_{ij} is the Christoffel matrix, which is given by:

$$\Gamma = \begin{bmatrix} C_{44} & 0 & 0 \\ 0 & C_{44} & 0 \\ 0 & 0 & C_{11} \end{bmatrix} \quad (2.8)$$

for an isotropic material. The derivation of this is detailed by Achenbach [105] and Rose [48]. This represents three equations:

$$k^2 C_{44} u_i = m \omega^2 u_i, \quad (2.9)$$

$$k^2 C_{44} u_j = m \omega^2 u_j, \quad (2.10)$$

$$k^2 C_{11} u_k = m \omega^2 u_k. \quad (2.11)$$

Equations 2.9 and 2.10 are degenerate, and describe the motion of shear waves where the particle motion is perpendicular to the wave propagation direction. The two equations represent different types of shear wave, with the perpendicular particle motion taking different polarisations. Equation 2.11 describes the motion of longitudinal waves where the particle motion and the wave propagation are in the same direction. The phase velocity of each wave type is calculated by rearranging equations 2.9-2.11 to find ω/k :

$$c_L = \sqrt{\frac{C_{11}}{m}}, \quad (2.12)$$

$$c_T = \sqrt{\frac{C_{22}}{m}}, \quad (2.13)$$

where c_L is the longitudinal phase velocity, and c_T is the shear wave phase velocity.

If isotropy is not assumed, equation 2.2 can be substituted into equation 2.4 instead, creating a more complex equation of motion. The solution to this is the Christoffel equation in anisotropic media:

$$(m \omega^2 \delta_{il} - C_{ijkl} k_j k_k) u_l = 0, \quad (2.14)$$

where k_j and k_k are the different wave numbers associated with different orientations, and C retains 21 independent coefficients. This correspondingly solves to give directional dependencies for c_L and c_T .

2.1.2 Bulk Wave Interface Interactions

When a travelling wave, such as the bulk waves outlined in the previous section, encounters a sudden change in material properties, such as an interface between

two different materials, a variety of interactions can occur. Some of the wave energy can transfer through to the new material (transmission), some of the wave energy can be reflected at the boundary, and sometimes wave energy can be converted into a different type of wave (mode conversion) [48]. This latter behaviour is specific to the interaction geometry and the wave type. Taking the simplest scenario of a longitudinal bulk wave in normal incidence on a material interface, only the former two interactions (transmission and reflection) will occur. In this case, the amount of wave energy that is transmitted and reflected is given by the transmission and reflection coefficients, T and R respectively:

$$T = -\frac{2m_2c_2}{m_1c_1 + m_2c_2}, \quad (2.15)$$

$$R = \frac{m_1c_1 - m_2c_2}{m_1c_1 + m_2c_2}, \quad (2.16)$$

where m is the material density, c is the bulk wave velocity in the material, an index of 1 indicates the material the wave is initially travelling in, and an index of 2 indicates the new material that it encounters at the interface [48]. mc is referred to as the acoustic impedance of a material. It can be seen from these equations that when the two materials have very similar acoustic impedances the transmission coefficient will tend towards -1, so all the wave is transmitted, and the reflection coefficient correspondingly tends towards 0. Conversely, when the acoustic impedances are very disparate the reflection coefficient tends towards 1 or -1 while the transmission coefficient tends towards 0. This gives rise to the term ‘impedance matching’, which is needed when transmission is desired between two materials. Solid-air boundaries typically have very mis-matched impedances [48], and so coupling gels are often used between contact transducers and solid samples. These coupling gels are typically chosen with an acoustic impedance between that of the transducer and the solid sample to give maximum transmission between the two. An alternative is submersion of the transducer and sample in water.

When a bulk wave meets a material interface at an angle, the transmitted wave can change in angle as well as intensity, dependent on the angle of incidence and the change in wave velocity between materials. This relation is given by Snell’s Law:

$$c_1 \sin(\theta_2) = c_2 \sin(\theta_1) \quad (2.17)$$

where the respective angles are shown in figure 2.1a). This is analogous to the effect seen with other types of waves, such as light waves, refracting at a material

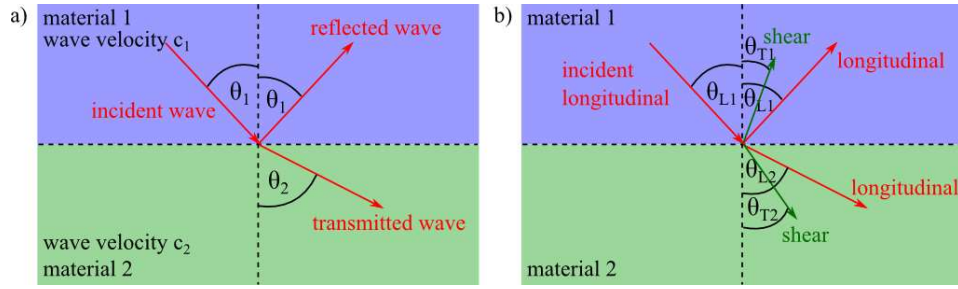


Figure 2.1: Graphical interpretation of Snell's Law, showing a wave interacting with a material boundary with a change in acoustic impedance, for a) a general case with no mode conversions, b) a longitudinal incident wave and including potential shear wave mode conversions.

boundary due to the change in wave speed in the new material.

When an angled incidence occurs, such as shown in figure 2.1, mode conversion can also occur. For instance, if the incident wave is a longitudinal wave, on incidence with the material interface the wave displacement can be considered as having two components, one which is perpendicular to the interface, and one which is parallel. This parallel component can give rise to motion that is not in the direction of wave propagation, leading to a shear wave mode. The shear wave has a different velocity, c_{T2} , in the new material to the transmitted longitudinal wave, c_{L2} , and therefore it travels at a different angle to the transmitted longitudinal wave, governed by $c_{L1} \sin(\theta_{T2}) = c_{T2} \sin(\theta_{L1})$ and $c_{L1} \sin(\theta_{L2}) = c_{L2} \sin(\theta_{L1})$, where the subscript L indicates a longitudinal wave, and the subscript T indicates a shear wave. Similarly, this shear wave created at the interface can also travel away from the boundary back into the original material. This example is shown in figure 2.1b) for an incident longitudinal wave, but an incident shear wave gives a similar pattern. When either θ_{L2} or θ_{T2} is equal to 90° it can be seen from figure 2.1b) that one transmitted wave direction will be directly along the interface between the two materials. This creates two critical angles, one for the longitudinal wave, and one for the shear wave, at which interface waves are generated.

These bulk wave interactions with interfaces are exploited for some NDE methods. If the wave velocity in the material is known, interface reflections can be used to measure the distance to the interface by measuring the arrival time of the reflection. This technique is often used to look for wall thinning in pipes by measuring the pipe thickness using reflections [47]. It can also be used to scan for defects, such as voids in rolled steel and welds, as the pockets of air return reflections [107]. However, if the void is smaller than the ultrasound wavelength it will act as a point scatterer of the wave rather than a reflector. While these

scatterings are detectable, in accordance with the Rayleigh criterion, it is typically said to be unresolvable [108]. The Rayleigh criterion was originally found in optics as the image resolution achievable by an optical lens:

$$\Delta x = 1.220 \frac{F\lambda}{D}, \quad (2.18)$$

where Δx is the smallest distance between two objects that can be resolved, F is the focal length of the optical lens, λ is the wavelength of the light being used, and D is the diameter of the lens [109]. In ultrasonics there is no optical lens present and the Rayleigh criterion is often quoted as $\Delta x = \lambda / 2$, approximately the full width at half maximum (FWHM) of the Airy disk created by a point scatterer [110]. This means that, while a sub-wavelength size object can be detected from scattering an ultrasonic field, its size, shape and orientation cannot be imaged. This also means that systems where voids or cracks are closer together than the inspection wavelength cannot be resolved as separate defects. However, some sub-wavelength ultrasonic imaging has been performed by Simonetti et. al., extracting sub-wavelength information that is encoded in the far field pattern of the scattered waves to distinguish multiple reflections [111, 112].

2.1.3 Surface Wave Propagation

When the shear and longitudinal wave motions described in the previous sections come into contact with a surface or surfaces this adds additional constraints to the wave equations. When a surface is encountered but the relative refractive index between the two materials is similar, interface waves known as Stoneley and Scholte waves can arise [48]. When a single surface is encountered, and there is a very large mismatch between the acoustic impedance of the two materials, such as between metal and air, the surface can be considered free. This system is called a half-space as the wave energy is contained entirely within one material with only one surface, with the rest of the material assumed as infinite in depth, and the associated surface wave is known as a Rayleigh wave. When two parallel free surfaces are encountered, such as in a plate, the associated guided wave is known as a Lamb wave. Rayleigh and Lamb waves are in fact extensions of each other, often referred to as Rayleigh-Lamb waves, with Rayleigh waves taking the far limit where the two surfaces are infinitely far apart. In reality a distance of more than approximately 10 wavelengths apart is sufficient to neglect one surface and consider a wave to be Rayleigh in nature, and in some cases 2-3 wavelengths can be sufficient.

This section will largely concentrate on Rayleigh wave behaviour as the most

relevant to this work, with a small amount on Lamb waves to demonstrate that the Rayleigh-Lamb waves used in this work can be approximated as Rayleigh waves. A third surface wave must also be acknowledged for this work, known as sub-surface longitudinal waves, or surface skimming longitudinal waves (SSL) [48]. These are longitudinal waves very close to the critical angle at the surface so that they almost travel along the surface (around 10 to 20° below it), and their far edge is incident with the surface. They travel into the sample bulk with the same phase velocity as a longitudinal wave, however, the speed along the surface itself is very slightly slower. They can be used for NDT, [113], however, they are dispersive and relatively weak in the EMAT generation systems used in this work and so have not been utilized for any NDE, but they are detectable in some experiments.

Rayleigh Wave Motion

A solid material (e.g. aluminium or steel) surface interface with air can be assumed to be a free surface [48]. This gives the boundary condition that the stresses at the surface must be zero, so $\sigma_{zz} = \sigma_{xz} = 0$ at $z = 0$. Rayleigh waves can be defined considering only a 2D plane of z and x with positive z into the sample and negative z as ‘free’, assuming symmetry in the y direction. Following the classical derivation given by Viktorov [104], a plane wave equation for the particle displacement vector, \mathbf{u} , is defined in terms of a scalar potential ϕ , and a vector potential $\boldsymbol{\psi}$ by:

$$\mathbf{u} = \nabla\phi + \nabla \times \boldsymbol{\psi}. \quad (2.19)$$

Here, ϕ corresponds to longitudinal particle motion in the direction of wave propagation (x), and $\boldsymbol{\psi}$ corresponds to the shear particle motion, perpendicular to the wave propagation direction (z). The particle displacement components can be expressed by:

$$u_{in} = \frac{\partial\phi}{\partial x} - \frac{\partial\boldsymbol{\psi}}{\partial z}, \quad (2.20)$$

$$u_{out} = \frac{\partial\phi}{\partial x} + \frac{\partial\boldsymbol{\psi}}{\partial z}. \quad (2.21)$$

u_{in} is the component of \mathbf{u} in the x direction, in-plane with the surface, and u_{out} is the component of \mathbf{u} in the z direction, out-of-plane to the surface. The potentials must also satisfy the wave equations, and hence:

$$\frac{\partial^2\phi}{\partial x^2} + \frac{\partial^2\phi}{\partial z^2} + \left(\frac{\omega}{c_L}\right)^2 \phi = 0, \quad (2.22)$$

$$\frac{\partial^2 \psi}{\partial x^2} + \frac{\partial^2 \psi}{\partial z^2} + \left(\frac{\omega}{c_T} \right)^2 \psi = 0. \quad (2.23)$$

Assuming an isotropic material, Hooke's law takes the reduced form given in equation 2.3. ϵ can be written in terms of the potentials ϕ and ψ by substituting the expressions for \mathbf{u} , equations 2.20 and 2.21, into the expression for ϵ given by equation 2.5. Substituting these expressions for ϵ into the reduced Hooke's law (equation 2.3) gives:

$$\sigma_{xx} = l_1 \left(\frac{\partial^2 \phi}{\partial x^2} + \frac{\partial^2 \psi}{\partial z^2} \right) + 2l_2 \left(\frac{\partial^2 \phi}{\partial x^2} - \frac{\partial^2 \psi}{\partial x \partial z} \right), \quad (2.24)$$

$$\sigma_{zz} = l_1 \left(\frac{\partial^2 \phi}{\partial x^2} + \frac{\partial^2 \psi}{\partial z^2} \right) + 2l_2 \left(\frac{\partial^2 \phi}{\partial x^2} - \frac{\partial^2 \psi}{\partial x \partial z} \right), \quad (2.25)$$

$$\sigma_{xz} = l_1 \left(2 \frac{\partial^2 \phi}{\partial x \partial z} + \frac{\partial^2 \psi}{\partial x^2} - \frac{\partial^2 \psi}{\partial z^2} \right). \quad (2.26)$$

Seeking plane wave solutions for ϕ and ψ of the form $e^{j(kx-j\omega t)}$, and using the wave equations given by equations 2.22 and 2.23, the potentials can be expressed as:

$$\phi = A e^{-qz} e^{j(kx-\omega t)}, \quad (2.27)$$

$$\psi = B e^{-sz} e^{j(kx-\omega t)}, \quad (2.28)$$

where t is time, A and B are arbitrary amplitude constants, k is the wavenumber, ω is the angular frequency, and q and s are constants defined in terms of the shear (c_T) and longitudinal velocities (c_L): $q^2 = 1 - (c/c_L)^2$ and $s^2 = 1 - (c/c_T)^2$. The additional constraint of the half-space, $\sigma_{zz} = \sigma_{xz} = 0$ at $z = 0$, gives rise to relations between A , B , and k , [48, 104], leading to the solutions:

$$\phi = -A e^{j(kx-\omega t)-qz}, \quad (2.29)$$

$$\psi = jA \frac{2kq}{k^2 + s^2} e^{j(kx-\omega t)-sz}. \quad (2.30)$$

As $c_{phase} = \omega / k$, k can be used to find an expression for the phase velocity. This gives rise to the characteristic equation:

$$\eta^6 - 8\eta^4 + 8(3 - 2\xi^2)\eta^2 - 16(1 - \xi^2) = 0, \quad (2.31)$$

where $\eta = c / c_T$ and $\xi = c^T / c_L$. There are six roots to this equation. Only one root, however, corresponds to a real material solution; this is the root for η that lies between 0 and 1, η_R . This root gives a value of c that corresponds to the Rayleigh

wave phase velocity. This cannot be solved directly, however, Viktorov [104] gives an approximate solution of

$$\eta_R = \frac{0.87 + 1.12\nu}{1 + \nu}, \quad (2.32)$$

where ν is the Poisson ratio for the material and varies from 0 to 0.5. Poissons ratio represents the relative distortions seen in a material when a stress is applied, comparing the distortion in the direction of the applied stress and perpendicular to it. There is no frequency dependence in this equation for phase velocity, showing that Rayleigh waves are non-dispersive.

The solutions found in equations 2.29 and 2.30 can be substituted into the particle motion expressions, equations 2.20 and 2.21. This gives rise to an elliptical particle motion for the Rayleigh wave, shown in figure 2.2a), and described by:

$$u_{in} = A(re^{-kqz} - 2sqe^{-ksz}) \cos(k(x - ct)), \quad (2.33)$$

$$u_{out} = Aq(re^{-kqz} - 2e^{-ksz}) \sin(k(x - ct)), \quad (2.34)$$

where $c = \omega / k$ (the phase velocity) and $r = 2 - (c/c_T)^2$ [104, 48]. Figure 2.2 illustrates how the components of \mathbf{u} change with respect to each other the further into the sample the motion is, with the out-of-plane component decreasing faster than the in-plane component, changing the ratios of the elliptical motion, and eventually reversing the direction of the elliptical motion after a certain depth. It should be noted that Rose [48] loses the factor of k in each of the exponential terms. The correct equations are given here, and also by Viktorov [104], where Viktorov has used different definitions of q and s to include a factor of k . Equations 2.33 and 2.34 have been used to plot the maximum displacement of a particle for a Rayleigh wave in aluminium (Poisson's ratios $\nu = 0.345$, $c_L = 6374$ m/s, $c_T = 3111$ m/s [16]). The cosine and sine terms have both been set equal to 1 to show the maximum displacement, and the drop off with z is given with respect to λ by converting $k = 2\pi / \lambda$. The result is shown in figure 2.2b), with both components normalised with respect to their values at $z = 0$. It can be seen that oscillations are almost entirely confined within one wavelength of the surface.

Lamb Wave Motion

Extending the previous discussion to a Lamb wave scenario with two parallel free surfaces gives the constraint $\sigma_{zz} = \sigma_{xz} = 0$ at $z = \pm h$ as the boundary conditions for an infinite plate of thickness $2h$. Using a similar method to the one shown

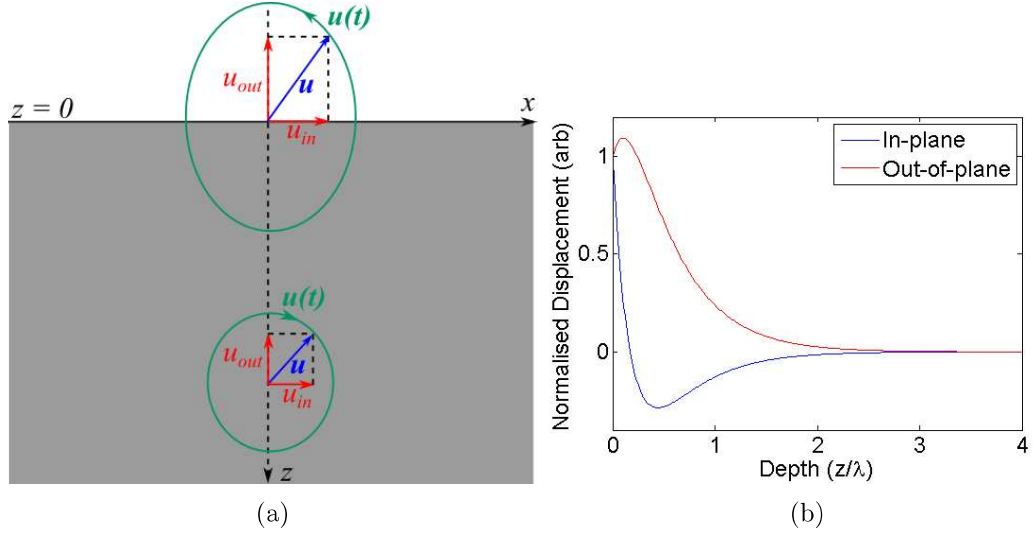


Figure 2.2: a) Schematic of the Rayleigh wave particle motion (green, \mathbf{u}) dependency on the depth into the sample (z) and the elliptical motion seen with time, as governed by equations 2.33, and 2.34. b) plots of the in-plane and out-of-plane particle maximum displacement from a Rayleigh wave.

for Rayleigh waves [48, 104] leads to two different types of wave motion, which are symmetric about $z = 0$ or anti-symmetric about $z = 0$. The in-plane particle motion for the symmetric modes is given by:

$$u_{in} = ikA_2 \cos(pz) + gB_1 \cos(gz), \quad (2.35)$$

and the out-of-plane is given by:

$$u_{out} = -pA_2 \sin(pz) - ikB_1 \sin(gz). \quad (2.36)$$

The corresponding components for the anti-symmetric modes are given by:

$$u_{in} = ikA_1 \sin(pz) - gB_2 \sin(gz), \quad (2.37)$$

$$u_{out} = pA_1 \cos(pz) - ikB_2 \cos(gz) \quad (2.38)$$

where A_1, A_2, B_1 and B_2 are arbitrary amplitude constants, $p^2 = \omega^2 / c_L^2 - k^2$, and $g^2 = \omega^2 / c_T^2 - k^2$.

The dependence of the wave phase velocity on the frequency of the wave and the thickness of the sample ($2h$) (the dispersion relation) is governed by:

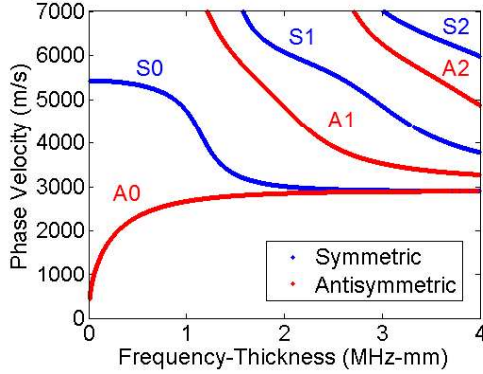


Figure 2.3: The phase velocity dispersion curves for Lamb waves in aluminium. The solutions found to equation 2.39 are shown in blue, and the solutions found to equation 2.40 are shown in red.

$$\frac{\tan(gh)}{\tan(ph)} = -\frac{4k^2pg}{(g^2 - k^2)^2}, \quad (2.39)$$

for solutions which are symmetric about $z = 0$ and

$$\frac{\tan(gh)}{\tan(ph)} = -\frac{(g^2 - k^2)^2}{4k^2pg}, \quad (2.40)$$

for solutions which are anti-symmetric about $z = 0$.

This shows that the phase velocity of ω/k is dependent on both the thickness of the plate and the frequency of the wave. Equations 2.39 and 2.40 cannot be solved directly, but solutions can be found numerically. This is done by defining a matrix of frequency \times thickness values to evaluate, and choosing an arbitrary start value for the phase velocity. Equations 2.39 and 2.40 are rearranged by subtracting the left side of the equations from the right, so as to give two equations that should evaluate to zero. These are then evaluated with the arbitrary phase velocity. If the equations are positive then the phase velocity estimate is reduced by a small increment, and if they are negative it is increased by a small increment. When the value of the equations changes from positive to negative or vice-versa then either a root or a discontinuity must be located between those values. Discontinuities can be checked for by finding the gradient either side of the zero crossing; if there is a change in the sign of the gradient then it is likely to be a discontinuity and should be discarded. If the gradients have the same sign (both positive or both negative) then a root of the equation must lie between the two values. The root can be estimated as half way between the two phase velocities calculated, or a more detailed sweep

of possible phase velocity values can be done over the narrower range. There are multiple roots for one frequency-thickness and so the possible values of the phase velocity must be swept over a large range to look for all the roots.

The results of this numerical calculation using the material parameters for Aluminium [16] are shown in figure 2.3. The x-axis shows the frequency multiplied by the thickness to combine the effect of both parameters. There are multiple different wave modes, but it can be seen from the figure that even in the range shown the two first symmetric and anti-symmetric modes (labeled S0 and A0) have converged to the same phase velocity by approximately 3 MHz.mm. Similarly, all the other wave modes converge at higher frequency-thicknesses, leaving only the Rayleigh, longitudinal and shear wave phase velocities at higher frequency-thicknesses. The A0 and S0 modes of a 1 MHz wave will appear almost Rayleigh-like for samples of 3 mm thick. This corresponds to samples thicker than the Rayleigh wavelength, which is 3 mm for a 1 MHz wave in Aluminium. This corresponds with the Rayleigh wave displacement calculations made in the previous section which shows that particle displacement has mostly dropped off after one wavelength depth into a sample, and so having an interface at that depth will have only a small effect on the wave. At 2-3 wavelengths it will essentially appear as a Rayleigh wave.

2.1.4 Rayleigh Wave Defect Interaction

Ultrasonic surface waves can be used to look for surface breaking cracks such as RCF and SCC (section 1.1). Similar to the bulk wave scenario detailed in section 2.1.2, when a surface wave encounters a sudden change in material properties, such as a small inclusion of air created by a surface breaking crack, some of the wave can be transmitted, some can be reflected, and some can be mode converted. An additional point of consideration is also the depth of the surface breaking crack [114]. As shown in figure 2.2, Rayleigh waves decrease in amplitude with depth into the material. Therefore, if the surface breaking defect is very shallow with respect to the depth of penetration of the Rayleigh wave then the majority of the wave will be unaffected by it. It also means that Rayleigh waves become highly attenuated if they encounter a surface with variations (or roughness) that are a significant percentage of the wavelength [104].

The theory behind Rayleigh wave interactions with simulated surface breaking defects have been extensively studied by many authors [104, 115, 116, 117, 118, 119, 120]. These types of interaction are typically studied using finite element analysis (FEA, section 3.5) instead of direct calculations due to their complex nature. When a Rayleigh wave encounters a corner on a sample surface some of the wave

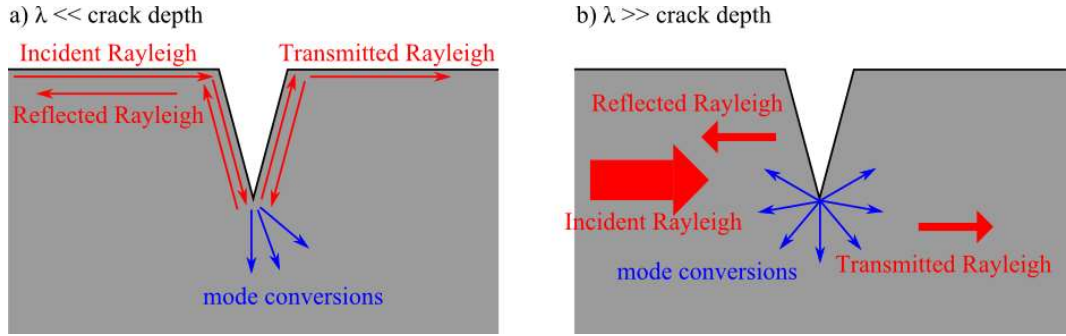


Figure 2.4: Approximate Rayleigh wave interactions with a surface breaking defect when a) the defect depth is much larger than the Rayleigh wave length, and b) the defect depth is much smaller than the Rayleigh wave length.

can travel around the corner to continue along the new surface, however some of the wave energy carries on into the bulk of the material, mode converting into longitudinal and shear waves [117, 119]. Extending this to a Rayleigh wave encountering a surface breaking crack the Rayleigh wave shows multiple effects, illustrated in figure 2.4. There are two main regimes of interaction, a) where the defect depth is much greater than the Rayleigh wavelength, and b) where the defect depth is much smaller than the Rayleigh wavelength. In reality, a combination of the interactions from both a) and b) of figure 2.4 are seen in both regimes, but one mode tends to dominate.

When the defect depth is much greater than the Rayleigh wavelength the dominant effects are as shown in figure 2.4a). Some components of the wave will be directly reflected on encountering the opening of the crack. Some components will travel down the length of the crack to the crack tip. At the crack tip some of this wave component will mode convert into shear and longitudinal bulk waves [121]. Some of the wave will be reflected back up the crack length from the crack tip creating another reflected Rayleigh wave. Some of the Rayleigh wave may also transmit up the far side of the crack to create a transmitted Rayleigh wave, although for a crack much deeper than the Rayleigh wave length this is negligible. Additionally, real cracks tend to have rough and irregular inner surfaces, attenuating any transmitted Rayleigh wave along the crack surface [104].

When the crack is much smaller than the wavelength of the Rayleigh wave, figure 2.4b), the wave can no longer be thought of as following the crack surface. The crack tip now acts as a point scatterer with respect to the wave, making shear and bulk wave circular wave fronts. Additionally, as the surface ‘depth’ of the wave is largely within one wavelength of the surface, higher frequency waves will have

a larger proportion of the wave reflected, whereas lower frequency waves will be able to transmit below the defect more easily. However, most wave fronts contain a bandwidth of frequencies and therefore wavelengths. High frequency content can still behave closer to the depiction in figure 2.4a), while lower frequency content behaves closer to that depicted in b). When a broadband wave is incident at a crack this means that the reflected wave has a higher proportion of the high frequencies, and the transmitted wave has a higher proportion of the lower frequencies [114, 121, 50].

Defect depths can be measured simply by comparing the amplitude of either or both the transmitted signal and the reflected signal. Shallower defects give weaker reflections and stronger transmissions. Viktorov [104] calculated the effect of a notch defect on a transmitted Rayleigh wave, and predicted oscillations in the transmission and reflection coefficients at the defect with an approximate periodicity of $\lambda/2$, however he assumed a narrow band signal, which is not typical of most real ultrasound transducers, although some piezoelectrics are narrow band.

Edwards et al. [114] have experimentally found real calibration curves relating slot depth to the frequency profile of the transmitted ultrasound generated by a broadband EMAT. The FFT of the transmitted signal at a defect is found. This is then divided by the FFT of the transmitted signal found with no defect present. The resulting data is linearly fitted over the frequency range in which there is significant amplitude from the original two profiles, so ignoring discontinuity spikes and zeros. The frequency at which this linear fit intersects the x-axis, giving a zero amplitude, is named the ‘cut-off’ frequency and was found to show a strong relation with the defect depth when tested with a range of machined defects. A similar technique has been reported by Ochiai et al. [122] using laser generation and detection. This cut-off frequency measurement is independent of variable parameters such as the EMAT generation efficiency which can vary with lift-off, and crack breadth.

A crack which is narrow with respect to the incident Rayleigh wave front, or oriented such that it appears narrow, also interacts less with the wavefront than one which is broader, giving an increased transmission without necessarily being any shallower [123], however, the effect on the frequency domain in theory remains unchanged, although it will affect the FFT analysis. The amplitude of reflected signals is additionally affected by the roughness of the defect, and whether it contains branches [22], leading to a weaker reflected signal for the crack depth when compared to a smoother defect, again giving an underestimate of the defect depth. Furthermore, if a defect is angled into the sample surface, as opposed to propagating perpendicularly into the surface, this again changes the reflection and transmission co-efficients without any changes in defect severity [124].

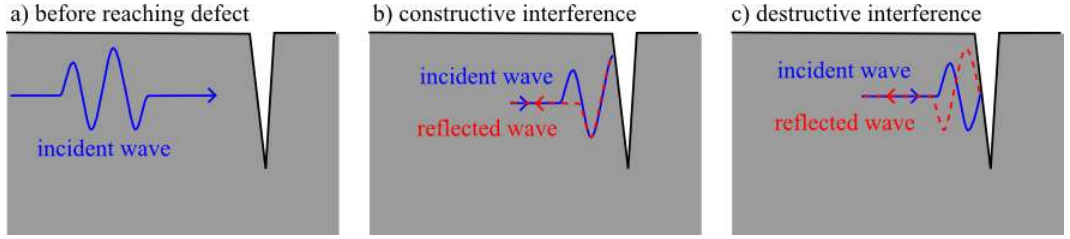


Figure 2.5: Rayleigh wave signal enhancement close to a defect showing a) the wave before it reaches the defect b) constructive interference and c) destructive interference.

An additional effect that can be seen when measuring ultrasonic waves near a surface crack opening is signal enhancement. This is due to the interference between the incident surface wave, and the reflected surface wave, causing an increase in the signals when they interfere coherently, and a decrease when they destructively interfere, as shown in figure 2.5 [50, 125]. An additional enhancement can also be seen if the crack is angled into the surface, as the Rayleigh wave can mode convert inside the wedge shape into a Lamb wave, changing in phase velocity as the wedge narrows [124, 126, 127].

2.2 EMAT Mechanisms

EMATs generate and detect ultrasound via electro-magnetic interactions with the material of interest [2]. The electro-magnetic fields are generated using pulsed AC through a coil of wire, often enhanced by a background magnetic field from a permanent magnet or electromagnet, as outlined previous in the introduction, section 1.2.6, and figure 1.7. Delocalised electrons in a metallic sample are susceptible to forces from external electro-magnetic fields due to their mobility within the parent material. The main governing equations for EMATs are Maxwell's equations [128]. The first arises from Gauss' Law and states that the electric flux density, \mathbf{D} , leaving a closed surface is proportional to the charge density within the surface, ρ :

$$\nabla \cdot \mathbf{D} = \rho. \quad (2.41)$$

The second arises from Gauss's law of magnetism and states that the net magnetic flux density, \mathbf{B} , through a closed surface is zero, i.e. there are no magnetic monopoles so magnetic field lines are always continuous:

$$\nabla \cdot \mathbf{B} = 0. \quad (2.42)$$

The third is the Maxwell-Faraday law, and arises from Faraday's law of induction. This states that any time-varying electric field, \mathbf{E} , will generate a time varying magnetic field, and vica-verca:

$$\nabla \times \mathbf{E} = -\frac{\partial \mathbf{B}}{\partial t}. \quad (2.43)$$

The fourth is the Maxwell-Ampère law, arising from Ampère's law, and states an electric current, or moving electric charge, will induce a magnetic field, \mathbf{H} , in a closed loop around it. The curl of the magnetic field loop will be proportional to the electric current density within the loop, \mathbf{J} , plus the variation in the electric flux density:

$$\nabla \times \mathbf{H} = \mathbf{J} + \frac{\partial \mathbf{D}}{\partial t}. \quad (2.44)$$

The constitutive relation between the magnetic flux density and the magnetic field is:

$$\mathbf{B} = \mu_0(\mathbf{H} + \mathbf{M}), \quad (2.45)$$

where \mathbf{M} is the magnetisation, which describes how a material reacts to an applied magnetic field, and μ_0 is the permeability of free space. The equation can often be simplified if the relation between \mathbf{M} and \mathbf{H} is known for the material in which the field is present. This is often approximated as $\mathbf{M} = \chi_m \mathbf{H}$, where χ_m is the magnetic susceptibility tensor, determined empirically. In a vacuum $\mathbf{M} = 0$. If the material is assumed to be isotropic and homogeneous this can be simplified further by defining a single constant, the permeability of the material, $\mu_r = \chi_m + 1$:

$$\mathbf{B} = \mu_0 \mu_r \mathbf{H}. \quad (2.46)$$

Similarly, the constitutive relation between the electric flux density and the electric field is:

$$\mathbf{D} = \epsilon_0 \mathbf{E} + \mathbf{P}, \quad (2.47)$$

where ϵ_0 is the permittivity of free space, and \mathbf{P} is the polarisation field, which describes how a material reacts to an applied electric field. Once again, this can be simplified if a relation between the polarisation and the electric field is known, often determined as $\mathbf{P} = \epsilon_0 \chi_e \mathbf{E}$ where χ_e is the empirical, material dependent, electric susceptibility tensor. In a vacuum $\mathbf{P} = 0$. Similarly, if the material is isotropic and homogeneous this can be approximated to:

$$\mathbf{D} = \epsilon_0 \epsilon_r \mathbf{E}, \quad (2.48)$$

where $\epsilon_r = \chi_e + 1$ is the material permittivity.

Finally, the current density in a material, \mathbf{J} , within a conductor can be related to the electric field by Ohms law:

$$\mathbf{J} = \sigma \mathbf{E}, \quad (2.49)$$

where σ is the material conductivity. While this does not hold for some materials, such as semi-conductors, the materials of interest to this work are copper (the EMAT coils), aluminium, and steel, which obey Ohms law. It must also be noted that at high frequencies σ is no longer a constant and has a frequency dependence [128], however in this work it can be assumed to be constant within the electromagnetic skin depth of the sample, as explained in the next section.

2.2.1 Generation of Ultrasound using EMATs

EMAT generation is only possible on electrically conducting or magnetic samples, as this indicates the presence of sufficient delocalised electrons or the presence of magnetic domains [2]. Three main mechanisms come into play: Lorentz force, Magnetisation force, and Magnetostriction force. Simplified descriptions of EMATs often only consider the Lorentz force as in some materials, such as aluminium, this is the only factor, and describes the electrical energy transfer from the EMAT coil to the sample [129]. However, for ferromagnetic materials, such as some types of steel, the other two forces can have significant contributions, arising from magnetoelastic mechanisms [130, 131].

Electromagnetic Skin Depth

The alternating current pulsed through the EMAT coils, as briefly outlined in the introduction, section 1.2.6, generates a corresponding alternating magnetic field, which can be calculated using equation 2.43. The subsequent electric field created in the sample forms eddy currents, or an ‘image’ current in the sample surface, in correspondence with equations 2.43 and 2.44. This current flow also creates its own magnetic field, in opposition to the field that induced the eddy currents, in correspondence with Lenz’s law [33].

It is important to note that the eddy currents can only be induced near the surface of the material, close to the induction coils. This was first considered when

alternating currents flowing through wires were discovered to experience an uncharacteristically high resistance when the frequency of the current was increased [128]. This is because a high frequency current in a wire will begin to travel predominantly at the outer edge of the wire, or within the wire ‘skin’. An expression for the skin depth is derived by finding the solution to the electric field within the conductor, starting with the assumption that equations 2.46, 2.48 and 2.49 hold true [128]. The expressions for \mathbf{H} , \mathbf{D} , and \mathbf{J} can then be substituted into the Maxwell-Ampère law, equation 2.44, giving an equation only in terms of \mathbf{B} and \mathbf{E} :

$$\frac{1}{\mu} \nabla \times \mathbf{B} = \sigma \mathbf{E} + \epsilon \frac{\partial \mathbf{E}}{\partial t}. \quad (2.50)$$

An expression for $\nabla \times \mathbf{B}$ purely in terms of \mathbf{E} can also be found using the Maxwell-Faraday law, equation 2.43, to give an equation purely in terms of \mathbf{E} . This is done by taking the curl of both sides of the Maxwell-Faraday law, giving $\nabla \times \nabla \times \mathbf{E} = -\nabla \times \frac{\partial \mathbf{B}}{\partial t}$. The vector calculus identity $\nabla \times \nabla \times \mathbf{E} = \nabla(\nabla \cdot \mathbf{E}) - \nabla^2 \mathbf{E}$ simplifies to $\nabla \times \nabla \times \mathbf{E} = -\nabla^2 \mathbf{E}$ as Gauss’ law, equation 2.41, gives $\nabla \cdot \mathbf{E} = \rho / \epsilon = 0$ on a macroscopic level as the electron density matches the ion density in a conductor, therefore the overall charge density, ρ , is zero. Therefore:

$$\frac{\partial}{\partial t}(\nabla \times \mathbf{B}) = \nabla^2 \mathbf{E}. \quad (2.51)$$

The expression for $\nabla \times \mathbf{B}$ from the re-written Maxwell-Ampère’s law, equation 2.50, can now be substituted into equation 2.51 giving:

$$\mu \epsilon \frac{\partial^2 \mathbf{E}}{\partial t^2} + \mu \sigma \frac{\partial \mathbf{E}}{\partial t} = \nabla^2 \mathbf{E}. \quad (2.52)$$

A solution to this is:

$$\mathbf{E} = \mathbf{E}_0 e^{j(\omega t - \frac{z}{\delta})} e^{-\frac{z}{\delta}}, \quad (2.53)$$

where ω is the angular frequency of the electromagnetic field within the wire or sample, z is the depth into the material from the surface, and δ is the skin depth [128] [41],

$$\delta = \sqrt{\frac{2}{\omega \mu \sigma}}. \quad (2.54)$$

It can be seen from this solution that when $z = \delta$ the magnitude of the electric field has dropped off by $1/e$ of its surface value, \mathbf{E}_0 .

In aluminium, a frequency of 1 MHz, using $\chi_m = 0.82 \times 10^{-8}$ per kilogram at 20°C, $\mu_0 = 1.26 \times 10^{-6}$ m kg s⁻² A⁻², $\sigma = 413 \times 10^3$ Ω⁻¹m⁻¹, and $\omega =$

$2\pi \times 10^6$ rad/s [16], gives a skin depth of $78 \mu\text{m}$. This is much smaller than the Rayleigh wavelength of $\lambda = 2.92$ mm. Therefore the eddy currents can be taken to be a purely surface phenomena when compared to the depth the elastic waves propagate to. However, when considering the electric current in the EMAT coils themselves, using wires with diameters much larger than $78 \mu\text{m}$ will be inefficient, as the current flow will remain near the wire edges, and conversely using wires with diameters much smaller than $78 \mu\text{m}$ is inefficient. The wire used in this work is 0.08 mm diameter. For a 2 MHz pulse, the electromagnetic skin depth is $55 \mu\text{m}$, so slightly thinner wire would potentially be more efficient for the measurements taken at this frequency, however, coils become increasingly fragile when the wire is thinner.

Lorentz Force Generation Mechanism

The above analysis considers the magnetic field due to the current pulse. EMAT generators often have the addition of a strong background magnetic field, \mathbf{B}_0 , from a permanent magnet, such as NdFeB or SmCo, or an electromagnet [132]. The general equation for the force experienced by a moving charged particle in an electromagnetic field, or the Lorentz force, is $q(\mathbf{E} + \mathbf{v} \times \mathbf{B})$, where q is the charge on the particle and \mathbf{v} is the velocity of the particle. The component $q\mathbf{E}$ arises from the Coulomb force. With a background magnetic field present the total magnetic field comprises of both \mathbf{B}_0 and the dynamic magnetic field created by the coil alternating current (AC), \mathbf{B}_D . Rueter [133] discusses EMAT generation without a permanent magnet and even proposes an ‘active’ coil method for detection without an external magnet (normally a necessity, as discussed in the Detection section of the Theory). However, for the EMATs presented in this thesis the effect of \mathbf{B}_D is much weaker than the effect of \mathbf{B}_0 , found experimentally by attempting generation without the permanent magnet and finding no detectable signals, and so it will largely be neglected here.

The eddy currents in the sample induced by the AC through the EMAT coil indicate an overall electron movement, and therefore they experience a Lorentz force due to both the self-field of the coil, and the background magnetic field. The delocalised electrons in a sample also undergo ‘collisions’ with the sample ions on time scales dependent on the material temperature, giving rise to another force, $-m_e\mathbf{v}_e/\tau$, where m_e is the mass of an electron, \mathbf{v}_e is the mean electron velocity, and τ is the mean time between electron-ion collisions [2]. At room temperature, τ in a metal is typically of the order of 10^{-14} seconds [2]. These two forces are equal to the mass times the acceleration of the electron, $F = m\dot{\mathbf{v}}_e$:

$$m_e \dot{\mathbf{v}}_e = -e(\mathbf{E} + \mathbf{v}_e \times \mathbf{B}) - \frac{m_e \mathbf{v}_e}{\tau}, \quad (2.55)$$

where $-e$ is the charge of the electron. $\dot{\mathbf{v}}_e$ can be approximated as zero, as the electron-ion interaction is on a much shorter time scale than the oscillation of the applied AC, i.e. $\tau \ll T$ where T is the period of the AC pulse. The period is inversely proportional to the angular frequency, so $\omega\tau \ll 1$. The electron-ion energy transfer can therefore be considered a continuous process. This approximates that the electrons transfer the Lorentz force experienced to the ions via elastic collision. The equation of motion for an electron is then:

$$\frac{m_e \mathbf{v}_e}{\tau} = -e(\mathbf{E} + \mathbf{v}_e \times \mathbf{B}). \quad (2.56)$$

The total force experienced by a material ion will include a term $Z_i(\mathbf{E} + \mathbf{v}_i \times \mathbf{B})$, where Z_i is the charge on the ion, and \mathbf{v}_i is the mean ion velocity, and the collision force from the electrons, as given in equation 2.56. The total force on all the ions will then be:

$$N_i Z_i (\mathbf{E} + \mathbf{v}_i \times \mathbf{B}) - n_e e (\mathbf{E} + \mathbf{v}_e \times \mathbf{B}) \quad (2.57)$$

where N_i is the ion density, and n_e is the electron density. The net charge in a metal is neutral, therefore $N_i Z_i = n_e e$, and so the \mathbf{E} terms cancel. It can also be assumed that $\mathbf{v}_e \gg \mathbf{v}_i$ as the electrons are delocalised, whereas the ions are in the material lattice and less free to move. Therefore, the predominant force on the ions will be the collision force from the electrons, rather than the Lorentz force they experience from the magnetic field. Therefore the force on the lattice ions will be:

$$\mathbf{F} = -n_e e \mathbf{v}_e \times \mathbf{B} = \mathbf{J}_e \times \mathbf{B}. \quad (2.58)$$

where $\mathbf{J}_e = -n_e e \mathbf{v}_e$ is the eddy current density.

For the EMATs in this work, \mathbf{B} is dominated by the external magnetic field, \mathbf{B}_0 , which does not change orientation, however the eddy current density will alternate in opposition to the current density in the EMAT coils. As such, the total force on the ions will oscillate, causing a vibration. This oscillation will be at right angles to both the eddy current and the external magnetic field. The total induced current is the integral of the current density. Integrating over z gives the total current for a unit surface area. Using Ohm's law (equation 2.49) and the expression for the electric field from equation 2.53 this gives:

$$\mathbf{I} = \int_0^\infty \mathbf{J} dz = \frac{\mathbf{J}_0}{\sqrt{\omega\mu\sigma}} e^{j(\omega t - \pi/4)} \quad (2.59)$$

where $\mathbf{J}_0 = \sigma \mathbf{E}_0$. Therefore the Lorentz force in the sample is proportional to the driving current, and will oscillate at the same frequency as the current in the EMAT coils, but with a phase lag of $\pi/4$, when only considering the external magnetic field. However, when the self-field is considered instead of the static field, \mathbf{B}_D oscillates in proportion to the driving AC as well as \mathbf{J}_e . Consequently the force on the ions ($\mathbf{J}_e \times \mathbf{B}$) is proportional to I^2 , instead of just I . This creates a doubling in frequency of the ion oscillations and consequently the generated ultrasound for self-field generation [2, 133].

Magnetisation Force Generation Mechanism

When most metals are manufactured the material is cooled from a liquid, forming a crystal structure. However, nucleation into this structure occurs at multiple different locations, unless care is taken to attempt single crystal growth [134]. In ferromagnetic materials the crystal structure has a magnetic polarisation, however the different domains that form are randomly orientated with respect to each other, leading to a net magnetisation of 0. However, when an external magnetic field is applied the different domains experience a rotational force to move them into alignment with the external field. This is dependent on the degree to which a magnetic field can magnetise a material. As such, it is only significant on ferromagnetic materials which experience measurable magnetisation in an external magnetic field. The force is given by:

$$\mathbf{F} = \int_V \mathbf{M} \cdot \nabla \mathbf{H} dV + \frac{1}{2} \mu_0 \int_S \hat{\mathbf{n}} M_n^2 dS \quad (2.60)$$

where the first integral over V denotes a volume integral, the second over S denotes a surface integral, $\hat{\mathbf{n}}$ is a unit vector normal to the surface S , and M_n is the component of \mathbf{M} in the $\hat{\mathbf{n}}$ direction [2]. This body force term is called the magnetisation force. The surface term arises from the change in the electromagnetic fields at the material surface due to the change in the material properties from a magnetic material to non-magnetic (air). When the external static magnetic field is parallel to the material surface the magnetisation force out of the surface acts in opposition to the Lorentz force out of the surface, making EMATs inefficient at generating longitudinal-waves into the material bulk (requiring out-of-plane displacement) in ferromagnetic material [2].

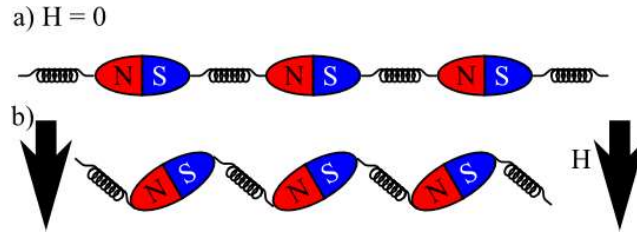


Figure 2.6: An intuitive interpretation of magnetostriction within a single crystal domain, equating atoms with spin as bar magnets, and the crystal lattice as spring connections. a) shows the domain with no applied background magnetic field, and b) shows the dimensional change due to an external magnetic field.

Magnetostriction Force Generation Mechanism

An external magnetic field creates a dimensional change to iron atoms as the $3d$ electron shell orbits are affected by the external field [2]. Within a single crystal or single magnetic domain this can be explained by equating the atoms with spins as bar magnets, as shown in figure 2.6. The change in the atoms causes a change in the shape of the magnetic domain or crystal.

In a polycrystalline material there are multiple effects. The domains closest to alignment with the magnetic field will expand, shifting the walls of neighboring domains. This creates strain between the neighboring domains. This enlarged domain then rotates to align with the external field. The presence of the oscillating self-field from an EMAT coil causes vibrations due to the expansion and contraction of the magnetic domains. This leads some materials to have much stronger ultrasonic responses to EMAT generation as this magnetostrictive effect enhances the Lorentz force and magnetisation force effects. This is difficult to predict as it is dependent on the crystal structure and magnetic phase of the individual material being used. However, a material of note is magnetite, a type of iron ore, and also a type of rust that forms on steel in a low oxygen environment, as its strong magnetostrictive response leads to much stronger EMAT signals than seen in regular steels [23, 74, 77, 135, 136]. EMATs can generate stronger signals in certain steels than non-ferromagnetic materials, such as aluminium, due to the magnetisation and magnetostrictive forces. These forces in steels have been extensively investigated by Ribichini [130, 131], however the research concludes that the Lorentz force is still dominant for most steels.

2.2.2 Detection of Ultrasound using EMATs

The propagation of ultrasound is through the crystal lattice of ions [48]. The free electrons oscillate due to the Coulomb force to maintain a net charge density of zero as the ions in the lattice oscillate [2]. The ions have greater momentum than the electrons, and so this momentum transfer is more efficient than the EMAT generation process [129]. No net electromagnetic fields are created by a propagating ultrasound wave due to the zero net charge density. However, if an external magnetic field is applied then the moving charged particles will experience a force, perturbing their motion, and creating an electric field:

$$\mathbf{E}_D \propto \frac{\partial \mathbf{u}}{\partial t} \times \mathbf{B}_0, \quad (2.61)$$

where \mathbf{u} is the particle displacement. It must be noted that while this is the Lorentz force process again, EMAT detection cannot be said to be merely the reverse of the generation due to the improved efficiency of the particle momentum transfer [129].

The motion of the particles from an ultrasonic wave is dependent on the wave mode. Rayleigh waves have both in-plane and out-of-plane components, with the individual particle motion described by an ellipse [48]. If a static background magnetic field, \mathbf{B}_0 , is applied in the $\hat{\mathbf{z}}$ direction then particle motion will only generate a dynamic electric field, \mathbf{E}_D from the in-plane motion, as the out-of-plane is parallel to the magnetic field, yielding zero from the cross-product. Using equation 2.33 for the particle motion and substituting this into equation 2.61, an in-plane dynamic electric field is created, perpendicular to both the in-plane particle motion and the out-of-plane magnet field, given by:

$$\mathbf{E}_D = \frac{\partial \mathbf{u}_{in}}{\partial t} \times \mathbf{B}_0 = Akc(re^{-qz} - 2sqe^{-sz}) \sin(k(x - ct))|B_0|. \quad (2.62)$$

If \mathbf{u}_{in} is defined to be in the component of \mathbf{u} in the $\hat{\mathbf{x}}$ direction, then \mathbf{E}_D will be in the $\hat{\mathbf{y}}$ direction. It must be noted that for a detection coil to pick up effects from \mathbf{E}_D is must be in the $\hat{\mathbf{y}}$ orientation, at right angles to both the wave propagation and the external magnetic field applied. Using Ohms law (equation 2.49) it follows that:

$$J = \frac{\sigma}{\delta} \int_0^\delta \mathbf{E}_D dz. \quad (2.63)$$

\mathbf{E}_D is integrated over the skin-depth to find the total current, as J is fully contained within $0 \leq z \leq \delta$ and this skin depth is much smaller than the ultrasonic wavelength.

Using the Rayleigh wave expression for \mathbf{E}_D (equation 2.62) equation 2.63 evaluates to:

$$J = \frac{\sigma|B_0|}{\delta} Akc \sin(k(x - ct)) \left(2q(e^{-s\delta} - 1) \frac{r}{q} (1 - e^{-q\delta}) \right). \quad (2.64)$$

The in-plane velocity of the particles at the surface is the differential of equation 2.33 evaluated for $z = 0$:

$$\frac{\partial u(0, t)}{\partial t} = Akc(r - 2sq) \sin(k(x - ct)). \quad (2.65)$$

This allows the expression for J to be re-written in terms of the particle surface velocity:

$$J = \frac{\sigma|B_0|}{\delta(r - 2sq)} \frac{\partial u(0, t)}{\partial t} \left(2q(e^{-s\delta} - 1) + \frac{r}{q}(1 - e^{-q\delta}) \right). \quad (2.66)$$

A similar effect is seen for bulk waves, and shows that the current generated is proportional to the wave velocity, making EMATs velocity sensors as opposed to displacement sensors (e.g. piezoelectrics and laser interferometry).

There is also a reverse magnetostrictive mechanism that occurs in ferromagnetic materials [2]. Ultrasonic vibrations cause distortions in the magnetic domains in the material, which causes an additional magnetic flux density, affecting the electromagnetic fields in the vicinity of the detection coil. This can be considered as the reverse of figure 2.6, where an elastic perturbation of the chain of atoms creates a net magnetic field, and so an oscillating perturbation creates an oscillating magnetic field. By Maxwells equations this can generate a current in a nearby conductor and therefore be detected. This mechanism is important in some steels, especially ones which can form the rust magnetite, as mentioned previously in the generation section. However, for all the experiments performed in this work it is either not present (aluminium) or negligible compared to the Lorentz force mechanisms.

2.3 Summary

This chapter has outlined the main theory behind the propagation of ultrasonic surface waves and their generation by EMATs. The importance of careful EMAT design, and magnetic field orientation, for the required waveform is highlighted, including consideration of the material being tested as magnetic effects can alter the waveform.

Chapter 3

Methodology

This chapter outlines the main experimental and modelling techniques used in this work. Firstly section 3.1 gives a summary of the main EMAT designs through out this work. Part 3.2 then outlines the vibrometry technique used to characterise these EMAT designs, part 3.3 outlines how these EMATs were used for defect detection, part 3.5 outlines the Finite Element Analysis techniques used to model them, and section 3.6 outlines how the EMATs were constructed and optimised. Typical EMAT set-ups employed an adapted Ritec RAM-5000 pulser to output a controlled, AC signal to the EMAT generation coil, and then the detection EMAT was connected to an oscilloscope via a separate amplifier and the voltage waveform recorded. The Ritec is adapted for improved high frequency production. It can be set to produce a sinusoidal output with a controlled number of cycles at a set frequency. The output power can be varied, but full power was used for all of this work. In some cases a 22 MHz low pass hard filter has been used, however the EMAT operating frequencies have not exceeded 8 MHz and so this should not have distorted any of the signals. The amplifiers used have not always had exactly the same gain, and so not all work is comparable for absolute voltage readings, however where direct comparisons have been made the same amplifiers have been used.

3.1 EMAT Designs

3.1.1 Coil designs developed for operation in pulse-echo mode

Meanderline Coils

As a reference point to compare later designs to, a standard meander line dual-EMAT coil, shown in figure 3.1, was designed. It is optimised to generate Rayleigh waves at 2 MHz in aluminium, corresponding to a meander line spacing of 1.5 mm.

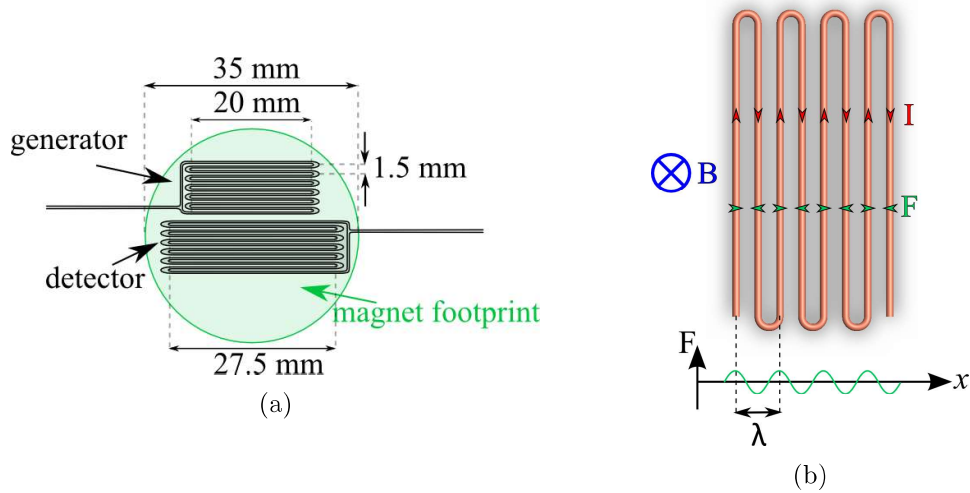


Figure 3.1: a) Meanderline EMAT coil template. b) schematic of the current, static magnetic field, and force directions in a meanderline wire leading to the wavelength of ultrasound generated

The wire is 0.08 mm in diameter and is wound three times through each of the meander line elements. Two separate coils are used, nested close together to create a pseudo pulse-echo arrangement while allowing for individual impedance matching of the coils. They are individually tuned using capacitors to create an LCR circuit with a resonant frequency of 2 MHz in order to achieve maximum signal strength [2].

2 MHz is chosen for the ultrasound frequency as it gives a wavelength suitable for detecting defects with depths in the mm range, while still allowing hand-winding of the coils to give a high current density. For comparative purposes with the later focused designs the EMAT is used with a 35 mm diameter, 20 mm height, Nd-FeB magnet, grade N45, with a maximum magnetic field of 0.5 T measured at the surface. The signal pulse used to excite the coil is a 7 cycle, 2 MHz sinusoid, for optimum signal generation, generated using an adapted Ritec RAM 5000 pulse generator. When a single wave cycle is used as the driving signal the multi-wavelength coil still creates a multi-cycle signal. This is shown in figure 3.2a); the red signal has a one cycle driving signal. Data has been digitally filtered with a bandpass butterworth filter of 0.5-4 MHz. The dead time from the initial generation noise ends at approximately $13 \mu\text{s}$ and the detected Rayleigh wave starts at approximately $30 \mu\text{s}$ for the 1 cycle data. A very weak surface skimming longitudinal wave can be seen starting at approximately $15 \mu\text{s}$ in the 1 cycle data. No bulk wave signals are seen as the meanderline coil geometry does not produce coherent bulk waves [2]. When more cycles are used the multiple impulses from each coil winding superimposes

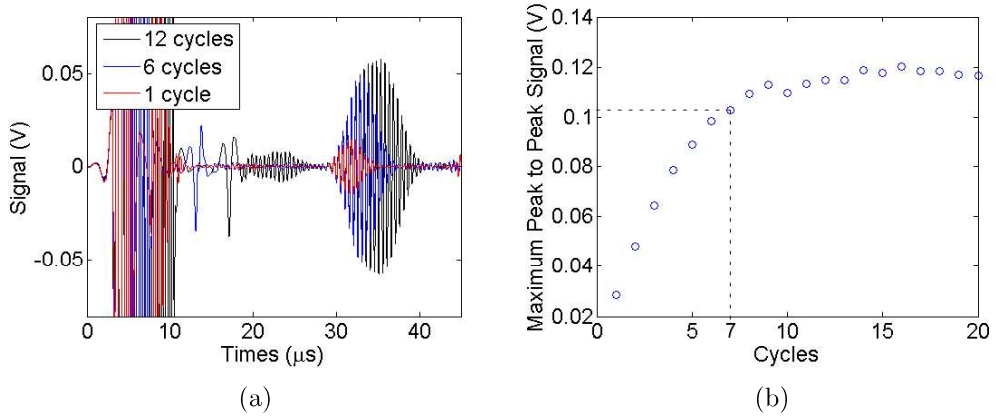


Figure 3.2: a) three example signals produced by the meanderline EMAT detailed in figure 3.1 operating in reflection against a sample edge. All three have a 2 MHz driving signal, but the number of sinusoid cycles used is varied according to the legend. b) Maximum peak-to-peak signal generated by multiple cycles.

with those from the other coil cycles, creating a stronger signal, giving the blue and black signals in figure 3.2a). However, more wave cycles increases the dead time from the initial signal generation. This can be seen in figure 3.2a) as the deadtime increases from $13 \mu\text{s}$ for the 1 cycle data, to $16 \mu\text{s}$ for the 6 cycle, and almost $20 \mu\text{s}$ for the 12 cycle data. It can also be seen that for the 12 cycle data the tail end of the surface skimming longitudinal wave is now much stronger and very close to interfering with the start of the Rayleigh wave signal. Furthermore, while all the Rayleigh waves can be seen to have the same start time at $30 \mu\text{s}$, accurately predicting the signal start is difficult as this is the weakest part of the signal packet. The signal peak is typically used to estimate the wave arrival time, and this can be seen to shift later in time with increasing cycles, and to become more difficult to identify as the peak flattens out. This means that time resolution can be lost with a higher number of cycles. Figure 3.2b) shows how the peak-to-peak signal strength of the Rayleigh waves varies with the number of driving cycles. 7 cycles was chosen as a compromise between increased signal strength, and the increased dead time and loss of resolution.

Focused Meanderline Coils

This design is the equivalent of the standard design presented in the previous section, with the addition of geometric focusing, and is shown in figure 3.3, with the focal point designed to be at 50.6 mm from the coil back edge. The coils have different aperture angles (11.4° and 20.1° as labelled in figure 3.3) as they were designed to

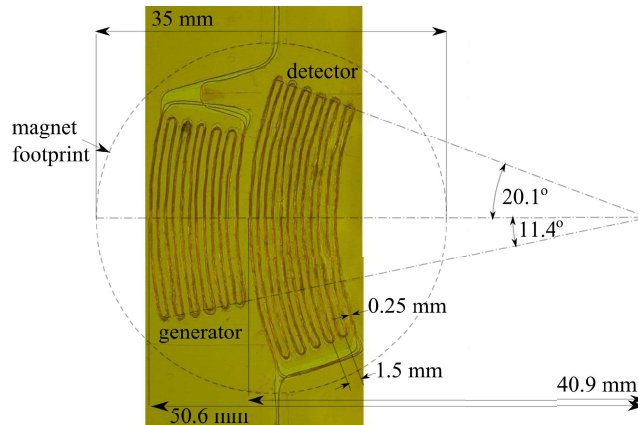


Figure 3.3: Annotated photograph of the focused meanderline EMAT coils. Dashed circle indicates magnet placement

fit under the same 35 mm diameter NdFeB magnet to facilitate simple scanning and effective alignment of the focal point with only one moving unit. The reflected signal will be weaker than the initial generated signal as it has travelled further through the attenuating sample, and reflections are often only partial depending on the size and roughness of the defect. Therefore the coil closer to the focal point was designed to be the detector coil as the reflected signal has travelled less far before detection. Furthermore the detection coil is larger. It was found in practice, however, to make marginal difference which coil is used as the generator and which as the detector. The generation coil has a designed radius of curvature, and hence focal point, of 50.6 mm when measured from the back edge of the coil. It was also used with a 35 mm diameter, 20 mm height NdFeB magnet, and excited with a 7 cycle, 2 MHz sinusoid pulse. Results and full characterisation of this coil are presented in Chapter 5.

Focused Linear Coils

Despite the disadvantages mentioned at the start of this chapter, some linear coil designs were trialled, as they have been found to give better lift-off capabilities from the sample (discussed further in chapter 4), thought to be due to their parallel and single direction currents leading to purely constructive magnetic dipoles being formed. However, to generate high frequencies the coil used has to be increasingly narrow [137], so much less wire is used for high frequency generation, decreasing the efficiency of the transducer. This is explained in more detail in section 4.1. Figure 3.4 shows a sketch of the design for the fused deposition modeling (FDM) 3D printed former used to make a linear reflection design with a focal behaviour

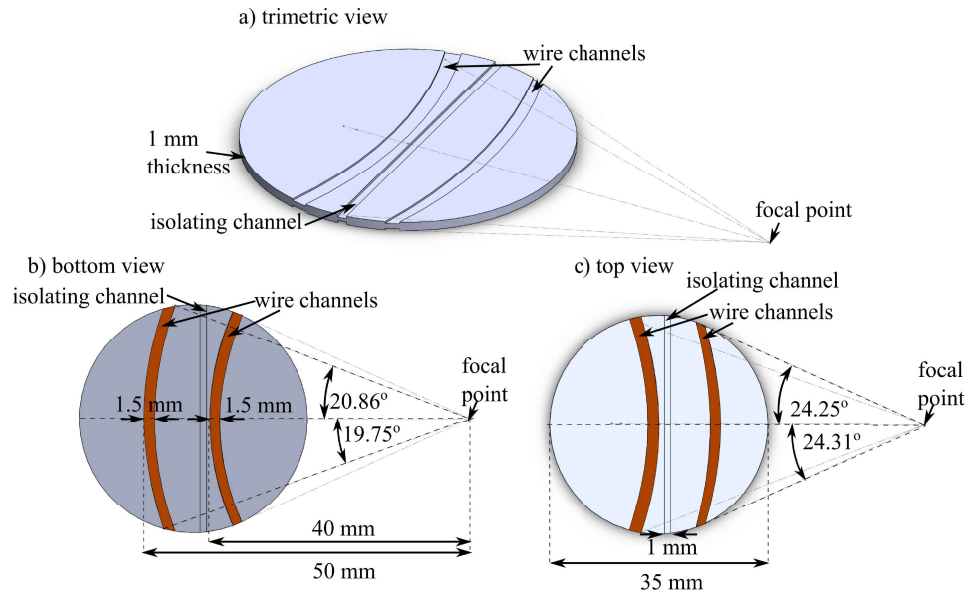


Figure 3.4: SolidWorks diagram of the former used to create the focused linear reflection EMAT

similar to the meanderline designs described in the previous paragraphs. The two curved segments of the coils were formed using a 3D printed former with insets of depth 0.2 mm to fit the wire into, with the wire looping through tracks around the back of the former. The coil path looping back behind the former was deliberately curved in the opposite direction, so that the wire paths were not directly above each other. This reduces interference as the opposing coil direction creates an opposing magnetic dipole reducing the effectiveness of the active wire beneath. A 1 mm width straight groove between the two coils is included, with a depth of 0.3 mm and a matching groove on the other side, to try and help isolate the two coils by reducing the transfer of the vibrations in the plastic former. Copper shielding was used on the back of the former, placed under the wire, again to try and improve the isolation between the coils. This design had about 40 μs of dead time with an expected signal from the focal point arriving earlier than that, making this design not practical for use. 40 μs is a much longer deadtime than expected.

An additional EMAT was used to ascertain if the generation coil was working as expected despite the deadtime by placing it at the focal point. An unfocused racetrack coil was used, with the winding shown in figure 3.5, with a separate magnet and this was sufficiently isolated that the signal could be detected, proving the generation coil design does work. A variety of isolation techniques, including using copper tape between the two linear coils, were trialled, but none were sufficient

to reduce the dead time of the incorporated detection coil. The linear designs inherently have more interference as they couple better to the sample, allowing for better lift-offs, but causing strong interference due to the coupling of the generator to the detector coil via parasitic capacitance through the sample. A solution would be to increase the size of the EMAT, moving the focal point further away from the coils so that any signals reflected from the focal point would arrive later than the dead time, however the size becomes impractical and the further the ultrasound has to travel the more the signal becomes attenuated by the material. Furthermore, the longer the focal length is the more likely there will be multiple defects within the beam path causing shadowing and making it harder to characterise the defects. However, the coils can be moved further apart without increasing their size or the distance the ultrasound has to travel in the material if the design is switched from a pseudo-pulse-echo to a transmission, or pitch-catch, design (shown later, figure 3.9).

3.1.2 Coil designs developed for operation in pitch-catch mode

Pitch-catch ultrasonic measurements, as outlined in section 3.3, detect signals which have either passed around, or transmitted underneath any defects located within the beam path. Rayleigh waves have an energy content primarily within the first wavelength of the surface, so higher frequencies travel with the majority of the wave energy closer to the surface than lower frequency waves, as explained in section 2.1.4. The frequency content of transmitted ultrasound waves compared to their original frequency content can therefore be used to measure the defect depth [138]. Transmission designs allow the two coils to be separated further apart than the pseudo-pulse-echo coils, improving the isolation between coils and therefore decreasing the noise. Operating in transmission also means that the ultrasound signal potentially has less distance to travel (depending on the design) which also helps with signal strength due to the waves suffering from less sample-based attenuation. No meanderline transmission designs were investigated as this would require two separate large magnets and a highly complex set up.

Racetrack Coils

A compromise design between meanderline, with its very close proximity alternating direction current flow, and the linear design with a single current directionality, is the racetrack design, shown in figure 3.5. The unfocused designs shown in figure 3.6 with the wire contained within the black loops, were not used for defect detection, but were built as a comparison for the behaviour of the focused designs. Two

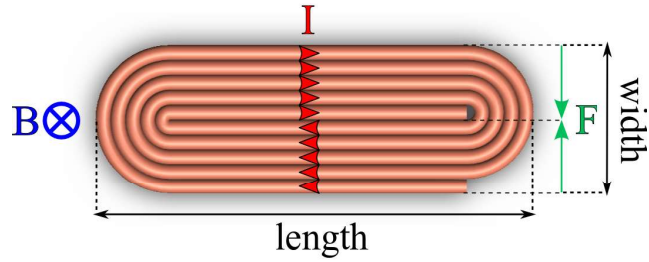


Figure 3.5: Racetrack EMAT coil design and current flow.

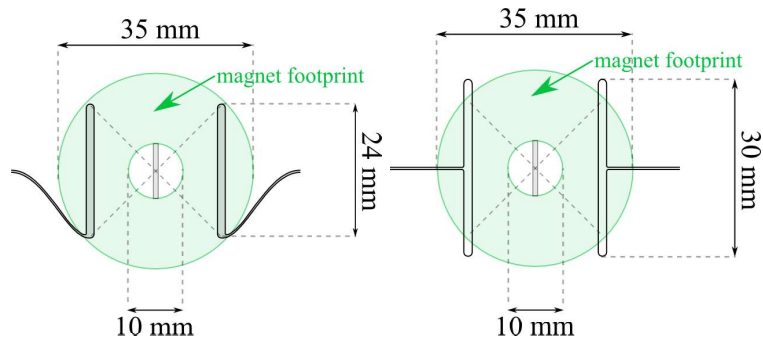


Figure 3.6: Schematics of the unfocused racetrack coils used as a comparison to the focused designs in the following section, all 1.5 mm in width.

different coil lengths were used to test the effect of the increased wire resistance of the longer design for comparison with the unfocused coils. Both were designed to fit approximately under the same cylindrical magnet for a direct comparison.

Focused Racetrack Coils

The main focused racetrack design used is shown in figure 3.7. The other related design that has been employed is identical, except that the coil widths were decreased to 0.75 mm instead of 1.5 mm to try and improve high frequency generation and detection. The simplicity of the design means that, despite using transmission, the two coils can still be fitted under one magnet, which is not possible with the meanderline designs without greatly increasing the size of the magnet. The magnet used for the majority of work was a NdFeB ring magnet, with outer diameter of 35 mm, inner diameter of 10 mm, and a height of 20 mm. It was found that the racetrack coils generate a Rayleigh-like signal in the base of the magnet with a similar wave velocity to Rayleigh waves in aluminium, creating an interfering signal arriving at the detector coil at exactly the same time as the signal of interest travelling through the sample. The magnet was changed from a cylindrical magnet to the ring magnet, with the foot print shown in the diagram 3.7, which blocks

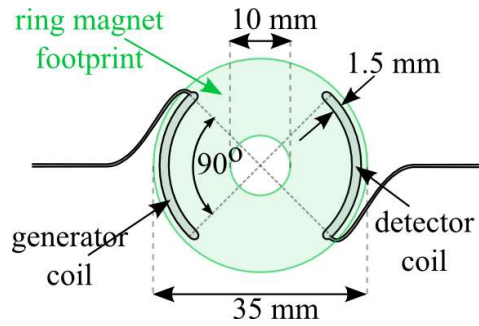


Figure 3.7: Focused racetrack diagram

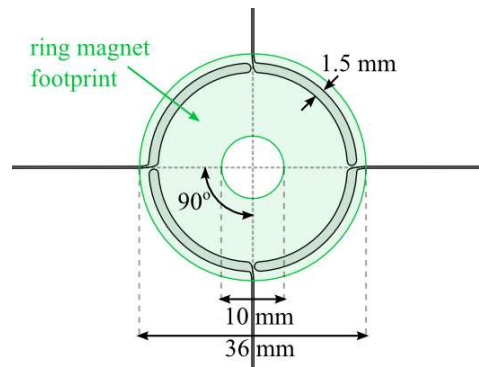


Figure 3.8: Focused racetrack diagram, extended to four confocal coils.

all noticeable signals generated in the magnet traveling through to the detector coil. The transmission designs were found to be sensitive to any direct physical connection between the coils through the focal point, with wave propagation also occurring through the plastic and kapton tape due to vibration of the wires, which resulted in slow, low frequency waves being transmitted directly from generator to detector. Cutting a 10 mm hole at the focal point (matching the ring magnet hole) was found to fix this. Both of these changes also allow direct access to the sample surface at the focal point allowing for vibrometry imaging, more accurate focal point alignment during scanning, and also does not load the surface of the sample at the focal point allowing for free vibrations.

Focused Four Racetrack Coil Set

A logical extension of the focused racetrack transmission design was to utilise the space on either side of the two coils, with the new design shown in figure 3.8. This was constructed identically except for the addition of identical confocal coils at 90° to the first pair. This design allows detection of defects which are angled relative to the direction of wave propagation, discussed fully in section 6.3.

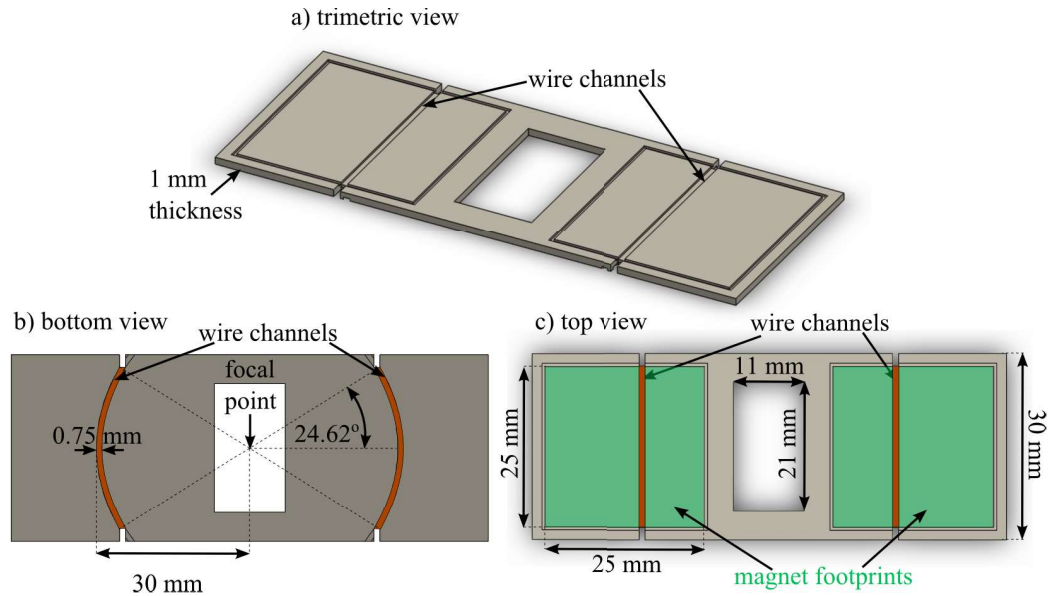


Figure 3.9: SolidWorks diagrams of the former used to create the focused linear EMAT.

Focused Linear Coils

A focused linear transmission design was trialed, attempting to match the separation of the racetrack design of section 3.1.2 to keep the two coils under one magnet, however, the close proximity of the coils was found to still cause too much interference. The two coils were then fully separated and used with entirely separate magnets. The design can be seen in figure 3.9. The central rectangle is a cut-out to access the focal point position of the design and to prevent any potential vibrations travelling through the plastic at the focal point from generator to detector, as was found to be an issue with the focused racetrack design (section 3.1.2). Part b) shows the underside of the former, with the coils wound through the curved groove lines shown, with a radial width of 0.75 mm, intended for 1 MHz signal generation. The same central rectangular cut-out can be seen over the focal point. This design has a separation of 60 mm between the outer edges of the coils giving a signal arrival time of just over $20 \mu\text{s}$. The coil separation decreased the deadtime to approximately $11 \mu\text{s}$ when driven by a three cycle, 1 MHz driving signal. A second coil set was then built with a coil separation of 47.5 mm from the outer edges of the coils, so the 30 mm measurement in figure 3.9b) was decreased to 23.75 mm, and the symmetry was retained. This gave a signal arrival time of just over $16 \mu\text{s}$, and roughly the same dead time, e.g. $11 \mu\text{s}$ for a three cycle, 1 MHz driving signal, and the closer proximity of the coils increases the strength of the detected signal.

3.2 Wavefield Imaging

To image the ultrasonic waves generated by an EMAT and how they propagate through a sample, the surface wave-field was imaged using a laser vibrometer. The vibrometer used is a Polytec OFV-5000 using an OFV-534 Compact Sensor Head, with a spot size of $250\ \mu\text{m}$, a spatial resolution of $0.5\ \text{mm}$ and a recording time resolution of $0.1\ \mu\text{s}$. This vibrometer has more than one detection capability dependent on the decoders used in conjunction with the equipment. The decoders available for this work are the VD-03 and the DD-300. The former decoder takes velocity measurements via the Doppler vibrometry, however its detection capability is limited to a maximum frequency of $1.5\ \text{MHz}$, making it impractical for this work. The latter decoder gives displacement measurements by differentiating the velocity measurements from the Doppler vibrometry. This has a frequency limit of $20\ \text{MHz}$, and was found to return stronger signals for the wavefields imaged in this work than the VD-03. The conversion quoted for the displacement decoder is $50\ \text{nm per V}$, however, the data in this work is left as a voltage signal as the signal output is very variable based on the correct alignment and focusing of the laser. Therefore the amplitude of the majority of scans are consistent during a single scan, but scans are not comparable with each other, unless the laser was carefully not altered between measurements.

The EMATs were fixed to an aluminium sample on an x-y stage and both were scanned underneath the laser, as shown in figure 3.10, to create a 2D map of the sample surface. The samples were smaller than those used in section 3.3 as the x-y stage has a weight limit, however, the depths were always at least 10 times the wavelength used to ensure the wave was still in the Rayleigh regime. The laser measures the out-of-plane displacement of the Rayleigh wave; Rayleigh waves contain significant in and out-of-plane motion and so the wave can still be imaged without considering the in-plane motion. EMAT detectors measure the velocity of the wave and not the displacement, and so these vibrometry measurements cannot be used for direct comparisons, however, coupled with finite element modelling of both the velocity and the out-of-plane displacements, the EMAT wave generation can be characterised using this method.

3.3 Defect Detection

There are multiple different ways to scan samples to detect surface breaking defects. The main distinction is whether the transducer is scanned in pulse-echo mode, look-

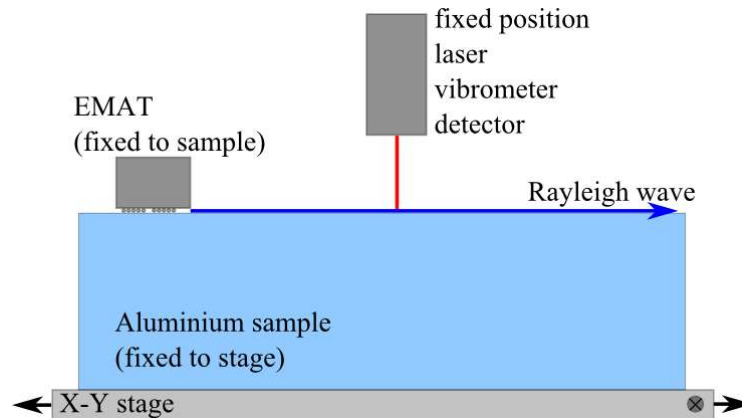


Figure 3.10: EMAT surface wave-field imaging using a laser vibrometer

ing for reflections returning from defects, typically only using a single transducer (figure 3.11 a)) or in pitch-catch mode, where variations in a transmitted signal are studied, requiring two separate transducers, one as a generator and one as a detector (figure 3.11 b)). A composite method can also be used, with either a fixed generator or a fixed detector, with the other transducer being scanned, or scanning both together but with a significant fixed distance between the two. This allows for reflections to be seen when the two transducers are in close proximity to a defect, but not between the two, transitioning to pitch-catch mode once the defect is incident between the two transducers. Both pulse-echo and pitch-catch mode scanning techniques are investigated in this work. Pulse-echo mode has the advantage that only a single transducer is needed, however, the duplexing required to both send and receive ultrasound from one transducer creates a long dead time right after sending the initial signal where reflected signals cannot be received, creating a blind spot near to the transducer. Hence, in later work, a pseudo-pitch-catch technique is used by fixing separate send and receive coils in close proximity to each other; they still suffer from some interference and dead time but the noise level is improved. Pitch-catch mode allows for complete isolation of the generator and detector which can decrease noise, and minimises this blind spot, although dead time can never be eliminated, but this can increase the complexity of the design.

Ideally, full 2D scans over an entire surface area would be made to find any surface defects, and a fully automated system would work in this way. Due to drift in the simple x-y stages used in this work 2D scans are difficult to reliably perform. However, the defect locations are known approximately for all samples in this work, and so two single line scans can be taken; a transverse scan across the sample width with the defect at the focal point, and an in-line scan down the length of the sample

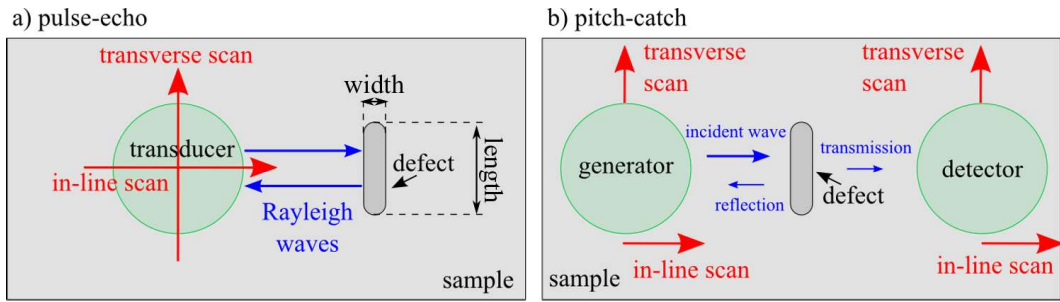


Figure 3.11: Typical surface wave scanning set ups for a) a single pulse-echo EMAT, b) a pitch-catch pair of EMATs, to detect a surface defect.

across the defect. Directions are labelled in figure 3.11. This allows for accurate sizing of the defects as they are known to pass through the focal point in both scans.

To compare the defect detection capabilities of multiple EMAT configurations, a set of 24 machined slot defects in two aluminium blocks were used, with a schematic shown in figure 3.12. They were machined using a 1 mm diameter milling piece and so are all 1 mm in width, with curved ends, and flat bottomed. The defect lengths used were 1, 3, 5, 7, 9, and 11 mm measured end to end including the rounding at the ends, as labelled in figure 3.12. The 1 mm width leads to the smallest length defect actually being a cylindrical defect of diameter 1 mm. These lengths were all created with depths of 0.5, 1, 1.5 and 2 mm, creating a total of 24 defects on two different billet samples. The defects have been staggered so no defects are directly above each other in the sample to try and avoid effects from bulk waves interacting with a defect on the lower surface. However, for the pitch-catch mode transducers, the two coils are within close enough proximity that any bulk waves arrive significantly after the Rayleigh wave, and so the waves should not interfere. The pulse-echo transducers used were meander-line coils, figure 3.1, and no measurable bulk waves were found from these. The defects on the same surface have also been spread out so that when a transducer with a focal length of 50 mm is 50 mm away from the defect of interest, the defect behind the transducer is more than 50 mm away, so that any reflections from that defect will not interfere with those from the defect at the focal point, i.e. a spacing between each defect pair of greater than 100 mm. Some defects come within 100 mm of the sample end walls, however, they were simply scanned from the other side, to avoid reflections from the end wall.

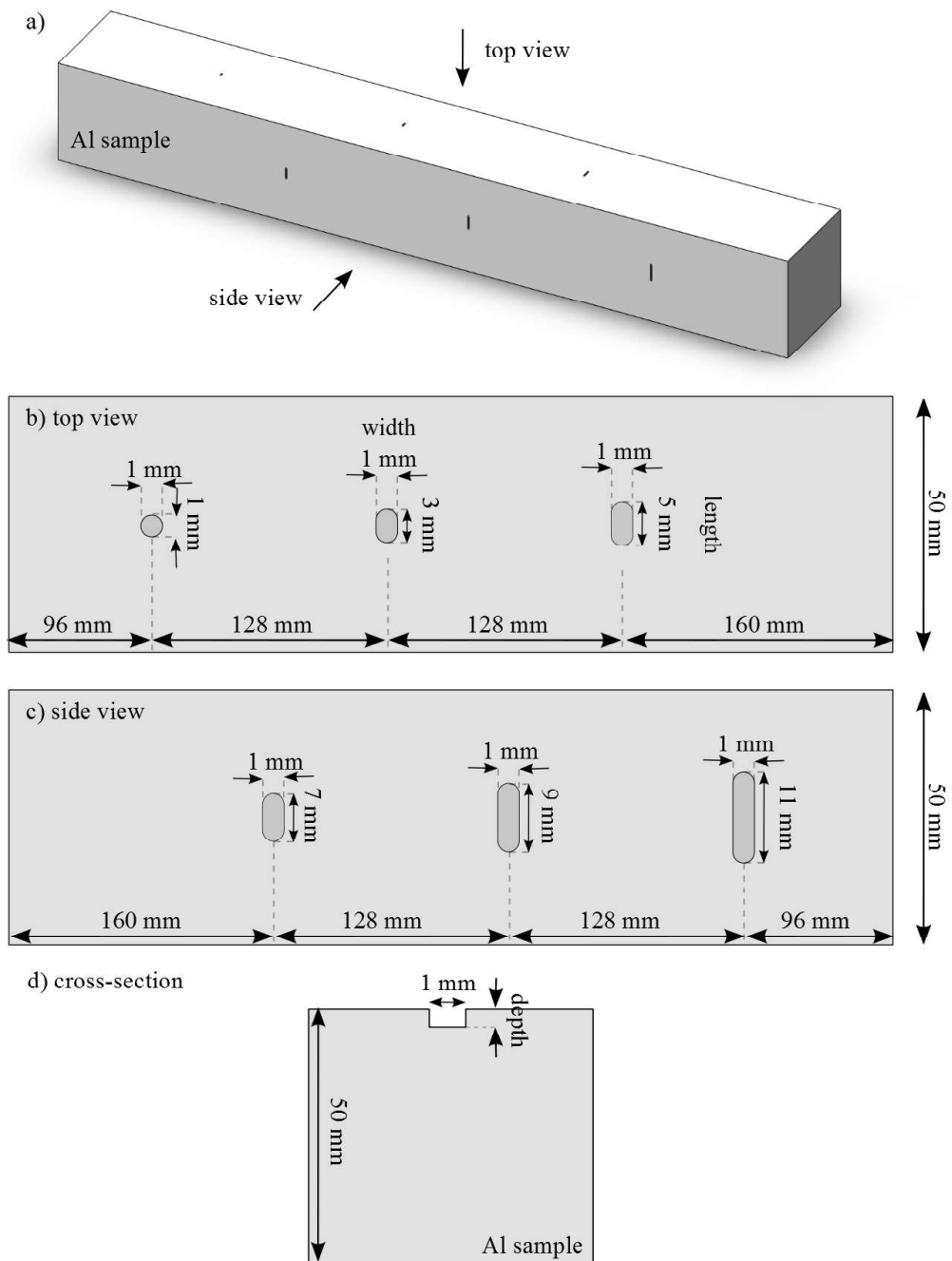


Figure 3.12: Aluminium billet samples containing defects on all sides. The two sides visible contain defects all of the same depth. The two hidden sides are identical except that the defects are a different depth, and aligned so that the defects are not directly underneath those on the opposite surface. Two such billets make up the 24 defects used for calibration.

3.4 Signal Processing

The majority of EMAT generation in this work was done using a tone burst output from an adapted Ritec RAM-5000 pulser-receiver to allow for a high level of control over the generation. A variety of different tone burst signals were used dependent on the EMAT design and the desired frequency, however, all consisted of more than one cycle of a sinusoid, creating a multi-cycle wave-packet ultrasound signal. The known shape of the signal which is generated can be utilised to improve signal detection and time resolution using a cross-correlation technique [3]. Cross-correlation is a standard signal processing technique used to compare the shapes of two wave forms using Fourier analysis. The cross-correlation of two continuous wave forms, $f(t)$ and $g(t)$, is defined as:

$$\int_{-\infty}^{\infty} f^*(t)g(t + \tau)dt, \quad (3.1)$$

where $f^*(t)$ is the complex conjugate of $f(t)$, t is time and τ is the time shift applied to signal $g(t)$ [139]. This ‘scans’ signal g past signal f using the τ time shift and compares the shape of the two signals.

To illustrate this technique the example set up shown in figure 3.11a) has been used except that the ‘defect’ is the end wall of a sample block, simulating an infinite defect, and the transducer used was the focused meanderline (figure 3.3) held at a fixed position. This generation EMAT design has optimal signal strength generation when using a seven cycle, 2 MHz, sinusoidal tone burst. Signals reflected from defects therefore return as a seven cycle, 3.5 μ s long wave packet, and therefore if no signal processing is used the spatial resolution of the technique is limited. However, cross-correlation can be used to extract the wave packet peak to allow accurate position measurements.

To extract the peak of the wave packet in an automated manner, a synthetic signal G with its real component designed to match the generated signal was created,

$$G = e^{-\frac{(t-t_0)^2}{2a^2}} e^{2i\pi f(t-t_0)}, \quad (3.2)$$

where f is the frequency, t_0 is the time offset, and a is the width of the signal in the time domain. The values were set to match those contained in the real output signal ($a=1 \mu$ s, $f=2$ MHz, $t_0=20 \mu$ s). This synthetic signal was cross-correlated with the detected waveforms and the absolute value squared returned, giving the signal power of the wave packet (effectively measuring the peak in the wave envelope), making it possible to find the maximum peak position to a higher degree of accuracy. The

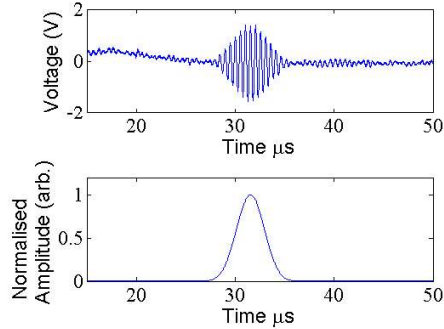


Figure 3.13: a) shows the single shot voltage data detected by an EMAT when looking for a reflection at the focal point from a large defect. b) shows the same data as a) after cross-correlation with a synthetic signal designed to mimic the generation EMAT output, and so extracting the signal wave packet.

cross-correlation process also takes advantage of data from all seven cycles of the detected wave as it compares the shape of the full signal packet with G , increasing the accuracy of the peak characteristics found, and reducing noise which has different frequency content.

To illustrate this processing, figure 3.13 shows an unprocessed, and a processed, A-scan detected by the EMAT when aligned with the focal point at the center of a defect much larger than the beam profile. The only processing that has been used on the signal in (a) is an amplifier and a 0.8-5 MHz band pass hard filter. The reflection from the defect can be seen with a peak just after 30 μs .

3.5 Finite Element Analysis

Finite Element Analysis (FEA) is a numerical technique employed for modelling of complex, dynamic systems [140, 141]. It can be used for modelling a large range of applications including structural mechanics, fluid dynamics, electromagnetic induction, and ultrasound propagation, and has the versatility to be able to model inhomogeneities, unlike most analytical solutions. The structure to be modelled is mapped using a grid of elements, with nodes at each element corner. Element shapes are typically triangular or rectangular in 2D, or tetrahedral or quadrilateral in 3D. Tetrahedral grids are more accurate for more complex geometries and have been used for the COMSOL magnet models employed in this work. The commercial ultrasound modelling software PZFlex that has also been used in this work only uses a rectangular or quadrilateral grid. A set of partial differential equations is then defined for each element, or node depending on the property being mapped, and a

set of boundary conditions imposed. This can then be numerically solved to find a solution to these equations for the entire complex geometry. For example, PZFlex maps the pressure field for each element throughout the model using the relevant wave equations, section 2.1. Care must be taken with the definition of the grid, as coarse grids lead to numerical dispersion and inaccurate models. For ultrasound modelling, the Nyquist sampling theorem [142] gives the minimum necessary grid size as two elements per wavelength. This, however, is rarely sufficient, and so for most models 15 elements per wavelength have been used, considering the shortest wavelength of interest for the model [?]. The simplest method to check the model accuracy is to gradually increase the number of elements per wavelength and once the results are identical between two numbers then it can be assumed that the model has converged.

FEA techniques are employed in this work to study the different wave-fields generated by different EMAT coil configurations. While FEA models are a computationally heavy way of building a wave-field image it allows for the comparison of in-plane velocity as detected by an EMAT, and out-of-plane displacement, as detected by a laser vibrometer. It also allows for investigation of the wave-field interaction with defects and boundaries.

PZFlex was employed for modelling the ultrasound fields generated using a pressure loading to initiate the ultrasound. It was assumed that the spatial area of the sample directly beneath an EMAT coil will receive an even pressure force at 90° to the current and the permanent magnetic field, obeying the right hand rule. For the surface wave EMATs modelled, this puts the pressure force directly along the surface of the sample. This is an over simplification, as there will be some component of the force into the sample bulk due to variations at the magnet edge field, and any contributions from the dynamic field have been neglected (see section 2.2.1), however, comparisons of the FEA models with experimental data from the laser vibrometer showed good agreement, and therefore this modelling was deemed sufficient.

For faster modelling, Huygen's principle modelling has been investigated [143]. However, traditional Huygen's principle modelling assumes the superposition of point sources, whereas EMATs work via the Lorentz force which has a strong directionality. Superpositioning of dipole point sources was investigated to try and find a faster alternative to the computationally heavy and slow FEA models for predicting EMAT focused beam profiles with moderate success.

3.6 EMAT Construction

3.6.1 Coil Construction

All the coil designs created have been produced using hand winding of wire to form the coil, as wires give greater current density than flat, printed circuit coils, and so have improved signal generation efficiency. A discussion of printed circuit techniques can be found in reference [2]. A typical EMAT coil, as discussed in section 2.2, is wound to be roughly 2D so that the majority of the wire is flat relative to the sample to be inspected, as shown in figure 3.14. This is so that the active coil is as close to the sample as possible for optimal signal generation. The exceptions in this work are the linear coil designs, detailed in sections 3.1.1 and 3.1.2, where the wire elements closest to the sample are all desired to be parallel, with the current flowing in the same direction in each element [144, 137]. The linear designs in this work were made by FDM 3D printing thin (around 1 mm thick) plastic formers with an inset groove for wire placement, so that the wire is wound around the former, leaving the bottom face with parallel wires with the same current flow direction (figure 3.15). This has the disadvantage that a large proportion of the wire is now not actively generating ultrasound while increasing the resistance of the system, wasting power. The opposing direction wire on the opposite face of the former also has the potential to interfere with the signal generation and so copper isolation is included below it. Designs where the upper former wire was deliberately staggered with respect to the active wire gave less interference as any signals picked up by the upper wire (despite the shielding) was also time staggered (e.g. figure 3.9). However, this design can increase the amount of wire without increasing the amount of active wire. A more traditional method often employed to create a linear EMAT coil is to wind the wire fully around the magnet so that the opposing wire is at large separation for the sample (figure 3.16), however, this greatly increases the amount of wire used for the same amount of active coil, and for cylindrical and ring magnets can greatly increase the complexity of building the design.

text redacted



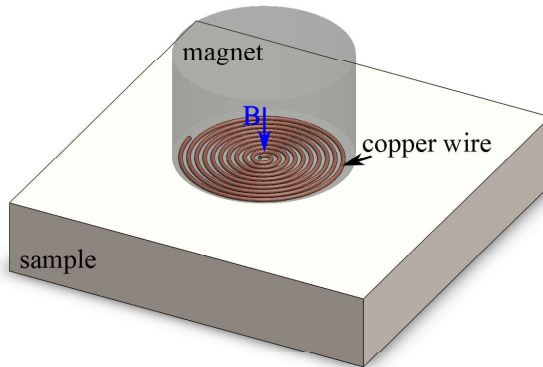


Figure 3.14: EMAT assembly with a spiral or ‘pancake’ coil, flat to the sample. A cylindrical magnet is rendered translucent for clarity.

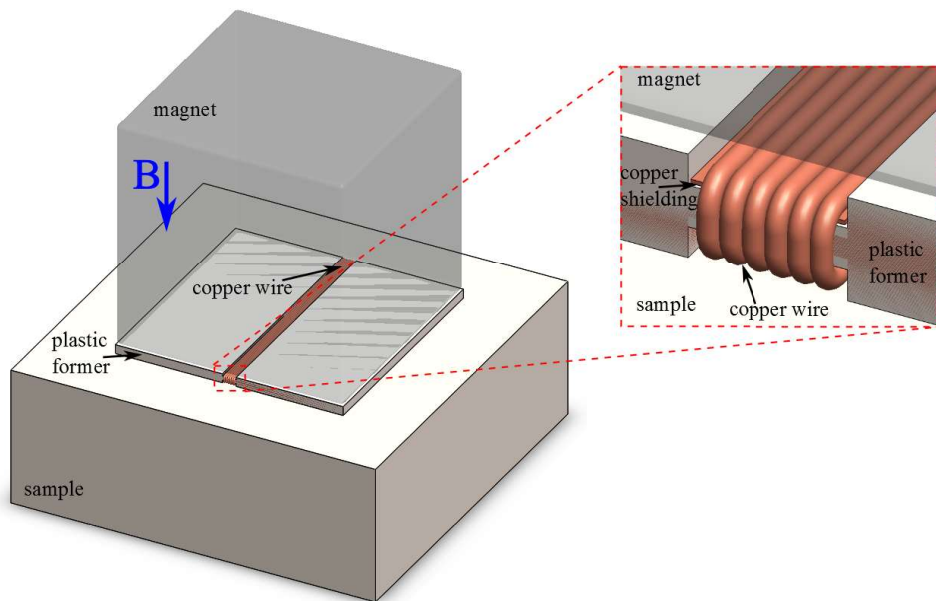


Figure 3.15: Linear EMAT made with all the wire below the magnet, wound around a plastic former. Only the lower half of the wire is actively producing ultrasound, with the upper half placed on top of copper shielding. A cube magnet is rendered translucent for clarity.

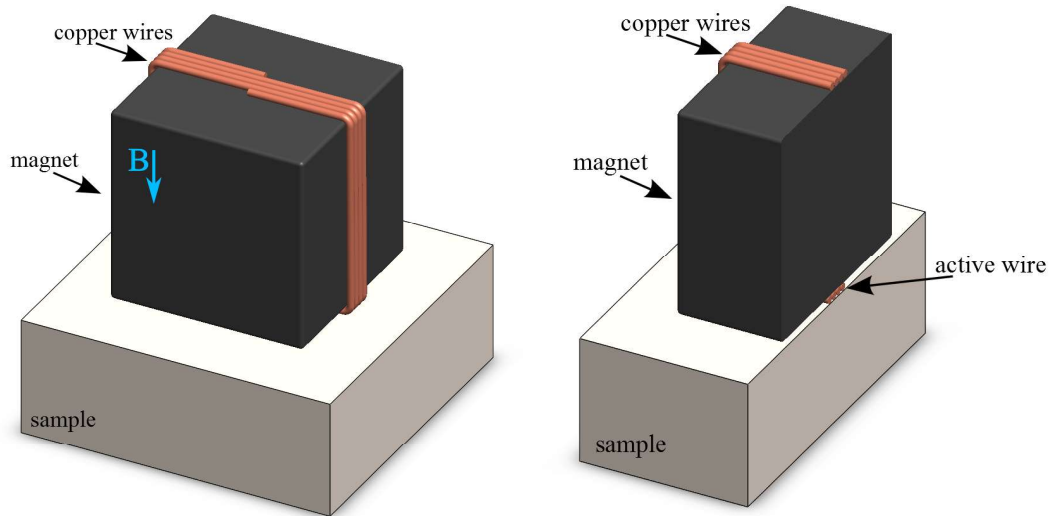
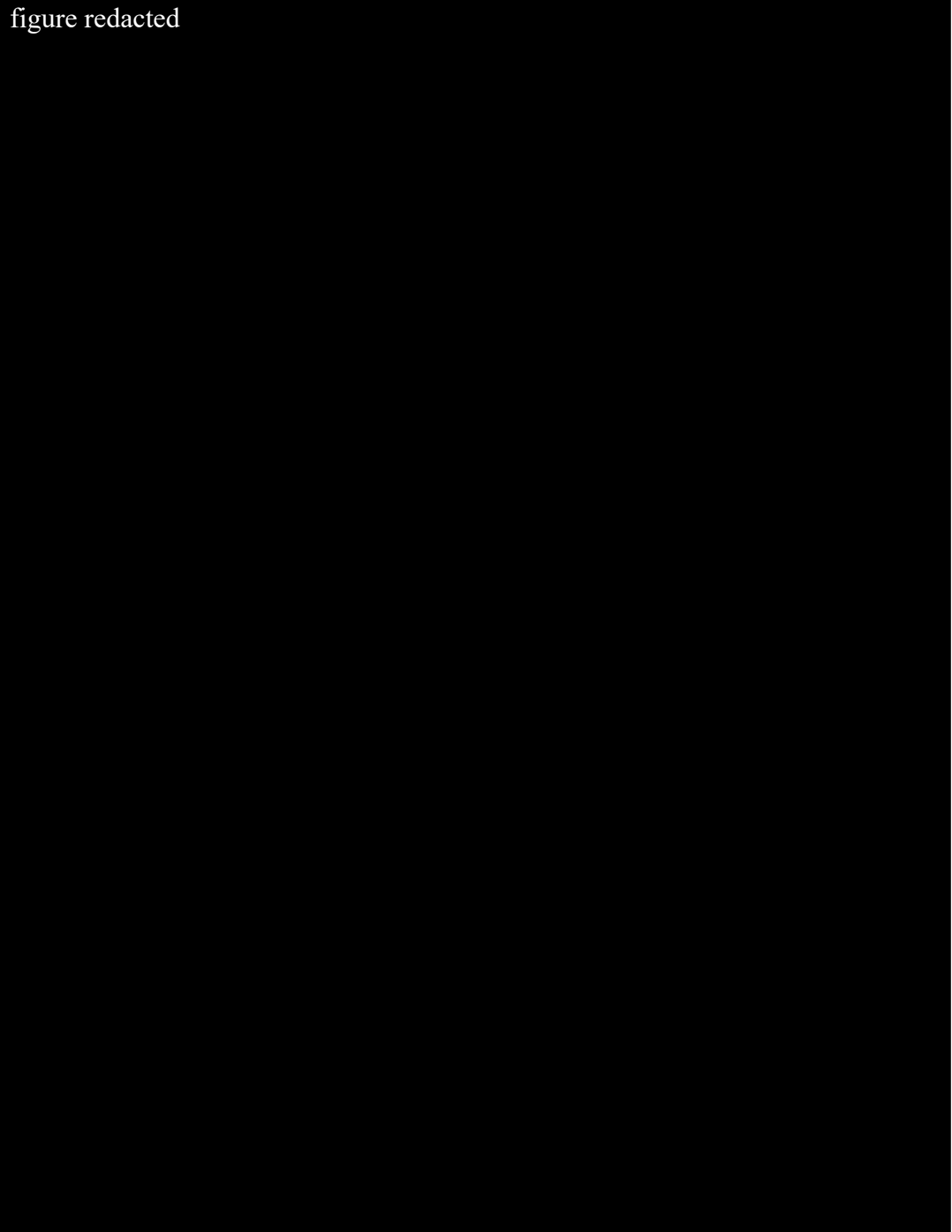


Figure 3.16: A different linear EMAT over a sample segment and the EMAT cross-section. The active wire for ultrasound generation is the wire between the magnet and the sample.

text redacted

figure redacted



text redacted



3.6.2 Impedance Matching

Ideally, an EMAT coil would be purely inductive, with no resistance or capacitance. However, the resistance of the long thin wire is not insignificant with respect to its inductance. EMAT coils also experience parasitic capacitance between the neighboring turns of wire and also between the coil and the sample. As such, a true EMAT coil behaves as an inductor in series with a resistor, both of which are in parallel with a capacitor [13]. The electrical resonance of the EMAT coils used in this work is much higher than the frequency at which the input AC is driven, typically around 40 MHz as measured with an impedance analyser, with operational frequencies of below 4 MHz. Electrical resonance is the point at which a circuit changes from behaving predominantly as a capacitor to predominately as an inductor [145]. An AC circuit with a capacitor in parallel to the current source is not affected by the

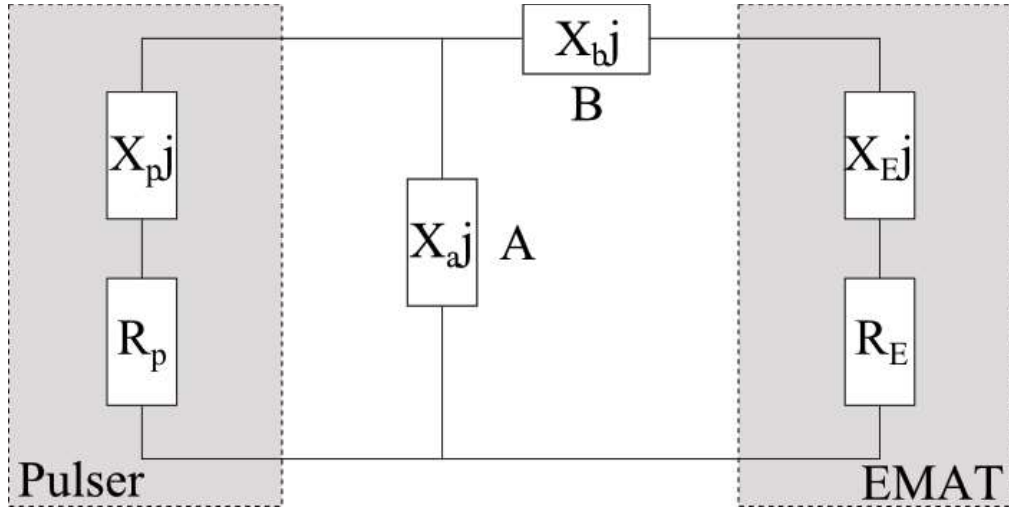


Figure 3.18: Circuit diagram of the impedance matching used between the EMAT and the pulser. X_p can usually be assumed to be negligible.

lower frequencies, and so this circuit below resonance behaves predominately as an inductor [145] and can be modelled as purely L-R.

Simple racetrack designs (figures 3.5 and 3.6) have been measured using an impedance analyser and have resistances of around $\sim 1 \Omega$, whereas the larger meanderline designs (figure 3.1) have around 5-7 Ω resistance. EMAT coils exhibit a frequency dependent delay to an applied AC signal due to their inductance, and have a total impedance of $R_E + 2\pi f L_E j$, where R_E is the resistance in Ω , f is the frequency of operation in Hz, L_E is the inductance in H and j is $\sqrt{-1}$. The term $X_E = 2\pi f L_E$ is the reactance of the coil, and is typically around 12 Ω for the coils in this work [145]. The pulsers used to drive most coils in this work have an output impedance of 50 Ω , but with negligible inductance and negligible capacitance. This is typical for most standard EMAT pulsers. This leads to a significant mismatch between the impedance of the generator and the load applied (the EMAT). Mismatch causes electrical reflectance, and so optimum power is not transferred to the coils. Such a situation is a common occurrence in any electrical set-up where a load with a lower resistance is applied to a power source.

To maximise the power transferred from a source to a load, a capacitor and an inductor can be used to match the impedance [145]. Ideally, neither of these add any resistance, and so no power is lost from the system; if the load resistance was simply increased to match the power source, power would be lost. Figure 3.18 shows the pulser-EMAT circuit diagram of the system, with two matching components, A and B, to be calculated. The total impedance, Z , from component B and the EMAT

in series is:

$$Z = R_E + j(X_b + X_E). \quad (3.3)$$

The total impedance due to the pulser and component A in parallel, setting $X_p = 0$ as the pulser has no inductive or capacitive component, can be found using $1/Z = 1/R_p + 1/jX_a$, re-arranging as:

$$Z = \frac{X_a^2 R_p + jX_a R_p^2}{R_p^2 + X_a^2}. \quad (3.4)$$

Z from equation 3.3 must equal Z from equation 3.4 to create a matched system for maximum power transfer. This can be done separately for the real components and the imaginary components of the equations. Equating the real parts gives $R_E = X_a^2 R_p / (R_p^2 + X_a^2)$. This can then be solved for X_a :

$$X_a = \pm R_p \sqrt{\frac{R_E}{R_p - R_E}}. \quad (3.5)$$

Equating the imaginary parts of equations 3.3 and 3.4 gives $X_b + X_E = X_a R_p^2 / (R_p^2 + X_a^2)$. Substituting in the solution for X_a from equation 3.5 and rearranging gives:

$$X_b = -X_E \pm R_E \sqrt{\frac{R_p}{R_E} - 1} \quad (3.6)$$

If X_p is not assumed to be negligible, solutions can also be found, and are calculated in reference [2] to be

$$X_a = \frac{R_p^2 + X_p^2}{X_p + Q R_p}, \quad (3.7)$$

$$X_b = Q R_E - X_p, \quad (3.8)$$

where

$$Q = \pm \sqrt{\frac{R_p}{R_E} \left[1 + \left(\frac{X_p}{R_p} \right)^2 \right] - 1}. \quad (3.9)$$

When $X_p = 0$, $Q = \pm \sqrt{R_p/R_E - 1}$, and $X_a = R_p / Q$ and $X_b = -X_E + Q R_E$, equivalent to equations 3.5 and 3.6.

To calculate the components needed to create an impedance matched system, the output resistance from the pulser, R_p , typically around 50 Ω , needs to be found, along with the resistance and reactance of the EMAT coil, R_E and X_E , which are measurable using an impedance analyser. The desired frequency of operation must

also be identified, as capacitors and inductors exhibit different behaviour depending on the frequency of operation. The EMAT coil will also give a different reactance dependent on the frequency of operation. It must be noted that the EMAT coil will exhibit different properties depending on its proximity to other materials, especially metals, and so the measurements should be made in situ [34]. The appropriate capacitance and inductance can be calculated using:

$$X_C = \frac{-1}{2\pi fC} \quad (3.10)$$

for a capacitor, with capacitance C in Farads, and reactance X_C in Ohms, and

$$X_L = 2\pi fL \quad (3.11)$$

for an inductor, with inductance L in Henrys, and reactance X_L in Ohms.

X_C will always be negative, while X_L is always positive, as f , C , and L are always positive. X_a and X_b therefore equate to either a capacitor or an inductor depending on whether the solutions are positive or negative. Some solutions will be physically meaningless if these values become imaginary, i.e. when Q is imaginary.

For EMATs, it is not necessarily maximum power transfer that is needed. The desired output is the alternating magnetic field, and that is at a maximum when the current is at a maximum. It can therefore be beneficial to maximise the current, rather than the power. Maximum current is transferred when the circuit is at electrical resonance, when the reactance of the pulser and the EMAT are matched, and there is no overall phase shift, or imaginary component to the circuit [145]. This can be achieved by adding a capacitor in parallel to the EMAT, so $X_b = 0$ and $X_C = X_a = X_E$. This is much simpler to calculate from setting $X_a = X_E$:

$$2\pi fL_E = \frac{1}{2\pi fC_a} \quad (3.12)$$

where L_E is the inductance of the EMAT coil, and C_a is the capacitance of the component that is added to impedance match the circuit, hence

$$C_a = \frac{1}{(2\pi f)^2 L_E}. \quad (3.13)$$

This gives the EMAT circuit a resonant frequency of f . This is also a simpler circuit to build, as all it requires is one capacitor to be soldered across the two output wires from the coil. For very thin wire the simplest way to do this is to stick two small pieces of copper tape on the edges of the EMAT design, keeping them separated by the width of the capacitor. It is simplest to do this while building the

Coil type	Receive type	Chapters	Design Parameters		
			wavelength/ width(mm)	length (mm)	aperture angle (°)
Meanderline	Reflection	3 (4) 5	1.5	20,30	unfocused
		3 (4) 5 7 8	1.5	20,30	20, 11, 15, 19
Linear	Reflection	3	1.5	28, 36	21, 20
	Transmission	3 4 8	1.5, 0.75	20	unfocused
		3 4 8	0.75	20	25
Racetrack	Transmission	3 4 6 7 8	1.5	24, 30	unfocused
		3 4 6 7 8	1.5, 0.75	20	45
	Mixed	3 6	1.5	20	45

Table 3.1: Summary table of all the EMAT designs tested in this work.

coil, before the coil is fully covered, between steps 5 and 6 in figure 3.17. One wire can then be soldered to each tab, and then the capacitor soldered on the top. It is useful if markings for the copper tab placement are included in the paper template and cut along with the EMAT coil pattern. Resonance tuning only increases the EMAT response very close to the resonant frequency, and so the signal becomes narrower in frequency band width; this method is therefore only desirable when a single frequency is of particular interest. Furthermore, the coil inductance is very susceptible to the coil environment, so for EMATs without a single specific application this matching and tuning is not possible as accurate inductance measurements cannot be made.

It must be noted that this theory assumes a continuous AC excitation. Full analysis should include transient circuit analysis at the start and end of the tone bursts used, and entirely transient analysis should be used for single pulse excitation [145].

3.7 Summary

This section describes all of the standard experimental techniques used in this work, including wavefield imaging, defect scanning, and the signal processing producers, FEA design, and coil manufacturing. In summary, the different coil designs explored are compiled in table 3.1 with a reference to the chapters in which they are detailed, if they were useful, and what testing was done with them. (Chapter labels in brackets only contain brief details on the coil, rather than extensive testing).

Chapter 4

The Effect of EMAT Coil Geometry on the Frequency of Generated and Detected Rayleigh Waves

The EMAT coil geometry, when used for surface waves puts a limitation on the upper frequency that can be generated and detected [5, 137]. This is because the coils have a spatial width, meaning that the signal gets averaged out underneath a coil in both generation and detection. If a full wavelength of a signal fits exactly underneath the full width of a linear detector coil the positive half and the negative half of the wave cancel out, making the wave undetectable no matter what phase the signal has, as pictured for $L = \lambda$ for the linear coil in figure 4.1. An infinitely thin detection coil would have a limit on the detectable wavelength of $\lambda = 0$, hence $f = \infty$, and would be sensitive to all wavelengths. However, the thinner the coil, the weaker its signal amplitude and detection capabilities. Similar wave cancellation effects are also seen from the superposition of multiple wave fronts from a finite width EMAT generation coil.

The frequency behaviour of meanderline and linear coil designs are both well understood [137, 146], however, the frequency response behaviour of the racetrack coil has not been fully characterised. It is important to understand this behaviour in order to design EMATs which will operate at a chosen frequency. This chapter discusses several mechanisms which affect this, considering geometric effects, time domain effects, pulse cycle length, and lift-off of the transducer from the sample. The work largely focuses on the effects from the detection coil, but the generation

coil effects are considered finally using FEA simulations.

The optimum driving frequency for maximum detected signal was found to range between 1.1 and 1.4 MHz on aluminium for a 1.5 mm width racetrack coil. A simple analytical model based on the instantaneous velocity of a wave predicts a maximum signal at 1.44 MHz. Modelling the detection coil as a spatial square wave agrees with this, and predicts a general relation of $f_P = 0.761v/L$ between the optimum frequency f_P , the wave velocity v , and the coil width L . A time domain model of the detection coil predicts a 1.4 to 1.5 MHz peak for continuous wave excitation, with a frequency that decreases as the length of the wavepacket is decreased, consistent with the experimental data. Linear coil modelling using the same technique is shown to be consistent with previous work, with improving detection at lower wave frequencies, and signal minima at every integer multiple of the wavelength. Finite Element Analysis (FEA) is used to model the effects of the spatial width of the racetrack generation coil and focused geometry, and no significant difference is found between the focused and the unfocused EMAT response. This highlights the importance of designing the EMAT coil for the correct lift-off and desired frequency of operation.

4.1 Analytical Solutions

Meanderline coils, as shown in figure 3.1, have a very simple relationship between the coil design and their optimum generation and detection frequency, as the meanders are designed to match the wavelength of the desired wavefront when operating with a large background magnetic field [146]. When operated using purely the self-field generation mechanism instead, the opposing coil directions generate an opposing direction magnetic field, causing the forces to always be in parallel instead of alternating, causing their optimum wavelength to halve. This is only applicable for generation EMATs, as the detection EMAT cannot work without an applied static magnetic field. This work only considers set ups with a large external magnetic field as these gave much stronger signals in the experimental work conducted, and due to the difficulties of creating very high frequency detector coils. Meanderline coils can be made to be much closer to the ideal, infinitely thin, detectors, but circumvent the problem of reduced width by having multiple meanders, spaced so that the correct wavelength will always increase the signal.

Predicting the operation frequencies for coils of more significant width is less simple. Dixon et. al [137] explore this relation for linear detection coils, with the design shown in figure 3.16, by taking the wave equation:

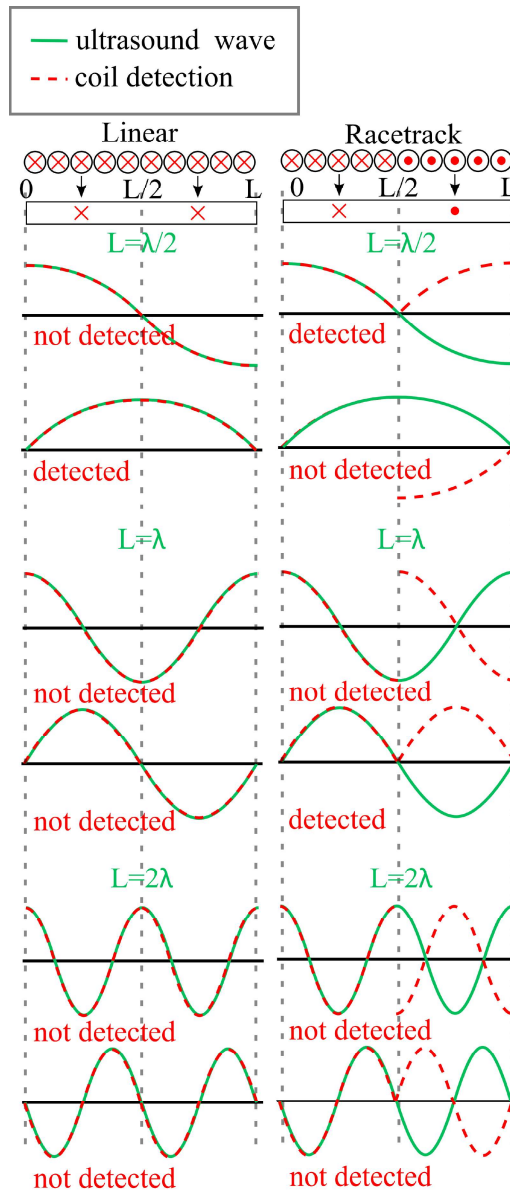


Figure 4.1: Comparisons of the detection capabilities of racetrack and linear coils for different wavelength and phase waves. In green is shown the waves to be detected, and red shows how this is seen by the coil. Notably the opposing direction of racetrack wire flips the sign of the detected wave.

$$A = A_o e^{i(\omega t - kx)}, \quad (4.1)$$

where A is the wave displacement, A_o is the maximum amplitude, ω is the angular frequency, k is the wavenumber, t is the time over which it has propagated, and x is the distance propagated. Differentiating with respect to x gives the instantaneous wave velocity:

$$V = -i\omega A_o e^{i(\omega t - kx)}. \quad (4.2)$$

Integrating this between $-L/2$ and $L/2$ gives the effect of the wave being averaged out over the spatial width of a coil width L , with 0 at its center, as EMATs are velocity sensors. This solves to give a current in the coil of:

$$I_{coil} \propto \frac{-2e^{i\omega t}}{k} \left(\sin \left(\frac{kL}{2} \right) \right). \quad (4.3)$$

Neglecting time variations, and so assuming $e^{i\omega t}$ is a non-zero constant, this gives

$$I_{coil} \propto \frac{1}{k} \sin \left(\frac{kL}{2} \right). \quad (4.4)$$

Minima in detection will occur when the sin term equates to zero. As $k = 2\pi/\lambda$, it can therefore be predicted that minima for a coil of width L will be at:

$$L = \frac{2n\pi}{k} = n\lambda, \quad (4.5)$$

where n is 0 or any integer (neglecting negative solutions as unphysical). This makes intuitive sense as shown in figure 4.1 for the $L = \lambda$, and 2λ examples; for the linear coil from symmetry the positive and negative currents generated in the coil during wave detection will always cancel out over the width of the coil, no matter what the phase of the wave is beneath the coil. Without the $1/k$ term, maxima would then be found at half integer values of the wavelength, however, the $1/k$ term cannot be ignored. As shown in figure 4.1 for the $L = \lambda/2$ example, some signal phases will be detectable as the currents in the coil add, while others will not. It was shown by Dixon et. al. [137] that the detected signal tends to a maximum at increasing wavelengths, giving a maximum at a frequency of zero, and the detected signal drops to half the maximum when the coil width is equal to twice the wavelength of the generated signal. It is therefore advisable to design detection linear EMAT coils to have a width equal to at least twice the wavelength of the signal of interest.

To extend this analysis to racetrack coils, which have two halves of the coil with opposing current directions, as shown in figure 3.5, a similar integral can be evaluated by considering first the current in the range $-L/2$ to 0 and then subtracting that from the range 0 to $L/2$ to account for the opposing current directions. Then

$$I_{coil} \propto \int_{-L/2}^0 e^{i(\omega t - kx)} dx - \int_0^{L/2} e^{i(\omega t - kx)} dx. \quad (4.6)$$

This evaluates to:

$$I_{coil} \propto \frac{2ie^{i\omega t}}{k} \left(1 - \cos\left(\frac{kL}{2}\right) \right). \quad (4.7)$$

Neglecting time variations again, the maximum current induced will be obtained when

$$I_{coil} \propto \frac{1}{k} \left(1 - \cos\left(\frac{kL}{2}\right) \right). \quad (4.8)$$

Minima in detection will therefore occur when the $(1 - \cos)$ term equates to zero, i.e. at

$$\frac{kL}{2} = 2n\pi, \quad (4.9)$$

$$L = \frac{4n\pi}{k} = 2n\lambda. \quad (4.10)$$

These minima have a similar intuitive explanation as for the linear coils, as shown in figure 4.1, where a coil with a width of 2λ will always cancel to give zero amplitude for all wave phases. Again, as with the linear case, the maxima are less clear as the phase impacts whether the signal will cancel or not, as shown for $L = \lambda/2$ and $L = \lambda$ in figure 4.1.

Figure 4.2a) shows the solution to the absolute value of equation 4.8 for $v = 2906$ m/s (Rayleigh wave velocity in aluminium), for frequencies of $f = 0$ to 20 MHz, and a coil width of $L = 1.5$ mm. This clearly shows the first two minima are as expected, at 3.9 and 7.8 MHz. Without the $1/k$ term this would give symmetric peaks between the minima, however, the decay term shifts the peaks to slightly lower frequencies. In this example the first peak occurs at 1.44 MHz, suggesting this as the optimal frequency for operation. Figure 4.2b) shows the solution to the absolute value of equation 4.4 for the same parameters as a reference for linear coil behavior.

This analysis gives a useful prediction of the behaviour of a coil of a chosen

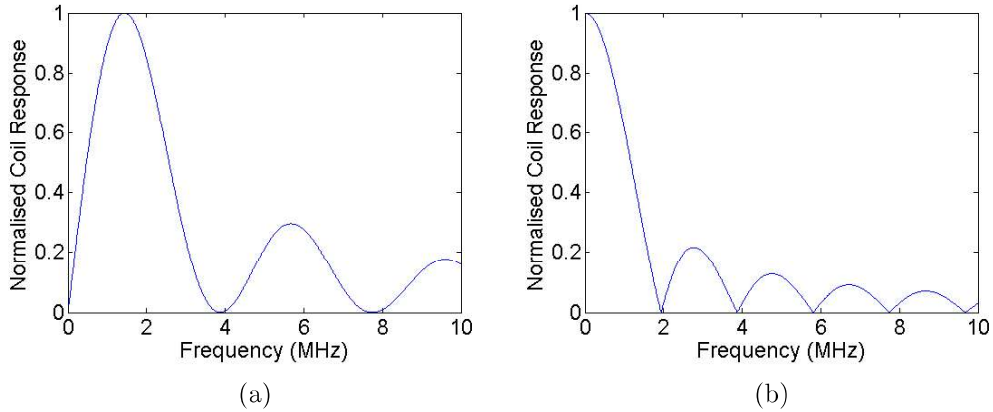


Figure 4.2: a) theoretical coil response for a racetrack EMAT coil of width 1.5 mm, detecting a wave with a velocity of 2906 m/s. b) theoretical coil response for a linear EMAT coil of width 1.5 mm detecting the same wave.

width L . However, experimental observations [4] found that a racetrack coil with a width of 1.5 mm used on aluminium had optimal signal generation when a 3 cycle, 1 ± 0.3 MHz signal was used to drive the coil, which is below the predictions of this simple model. Further consideration must be made of the other factors which will affect the frequency behaviour of an EMAT.

4.2 Experimental Results

Characteristics conditions that might affect the frequency response of a coil include the electrical impedance of the coil and the whole system, the lift-off between the coil and the sample, and the accuracy of the coil width during production. The racetrack coils used were: two sets of focused, 1.5 mm width coils (figure 3.7), the second being an attempt at an identical repeat to see if inconsistencies in production cause much variation in the output frequencies; one identical focused set except with the coil width reduced to 0.75 mm; and two unfocused racetrack pairs, (figure 3.6), one set being 6 mm longer than the other to see if the large increase in wire length, and therefore resistance, had any effect on the output frequencies. A three cycle sinusoid was used to excite all racetrack designs; further details on the focused design can be found in chapter 6.

All coils used in the experimental work are hand wound using 0.08 mm diameter wire, as wire gives a better current density than printed circuit board, and hence variations in geometry can occur. As such, the widths of all the racetrack coils were measured under an optical microscope. Three measurements were taken

per coil along their length and the average taken, to account for minor variations in the width. Table 4.1 gives the measured widths of both the generation and the detection coil, separated by commas, from the optical microscope in the column ‘Measured Coil Width’. Two 1.5 mm designed width racetrack coils were made to test reproducibility. The expected optimum frequency for the strongest generated signal from the analytical calculations outlined in section 4.1, based on the measured width of each coil, is given in the column ‘Theoretical Frequency Peak’ of table 4.1, assuming a Rayleigh wave in aluminium. The largest discrepancy from the designed width of 1.5 mm is 0.31 mm thinner than intended, which would lead to an increase in frequency peak of 0.5 MHz in aluminium. Some variation in peak frequency is therefore expected from variations in the coil widths, however, they are mostly under the designed width which should increase the peak frequency compared to the designed value assuming a 1.5 mm coil. All racetrack coils were found to have electrical resonant frequencies of around 40 MHz as they create an L-R resonant circuit. This is much higher than the driving frequencies considered, and so resonant effects will not affect the operation.

An example set of A-scans from the original set of focused coils, designed to operate at 1.45 MHz, are shown in figure 4.3 with varied driving frequencies. The noise from the driving signal can be seen starting at $3.8 \mu\text{s}$ which is the time delay of the Ritec used for generation; the noise is erratic in shape as it saturates the signal amplifier being used. The Rayleigh wave is seen starting at $\approx 15 \mu\text{s}$. The Ritec driving frequency was varied incrementally and the peak to peak amplitude of the Rayleigh wave was measured for each frequency. The maximum peak to peak signal strength of each Rayleigh wave packet, after a high pass filter has been applied to remove the low-frequency background variations, is plotted as a function of the driving frequency in figure 4.4a). It was expected to give a maximum signal when the driving frequency is close to the designed coil frequency, 1.4 MHz. It can clearly be seen from 2 MHz and above how the wave packet starts to distort, showing stronger leading and trailing edges.

Overall, the driving frequencies that gave the strongest peak to peak signals ranged from 1.1 MHz to 1.4 MHz for the different 1.5 mm width racetrack coils. These are listed for comparison in table 4.1, in the column, ‘Driving Frequency for Maximum Signal’. It can be seen that these are consistently lower than predicted by the analytical model.

Figure 4.4a) also includes the frequency profile for the unfocused racetrack coil pair using a pair of cuboidal magnets (length 20 mm, width 10 mm, height 20 mm, N45). The data outlined in the table used the same ring magnet as the

Coil Type	Designed Coil Width (mm)	Measured Coil Width (mm)	Theoretical Frequency Peak (MHz)	Driving Frequency for Maximum Signal (MHz)	Detected Frequency of Max Signal (MHz)	Cut-off Frequency (MHz)	Driving Frequency at Cut-off (MHz)
Meaderline	6 x 1.5	-	1.9	1.8	1.6	1.8	Fairly consistent
Focused Meaderline	6 x 1.5	-	1.9	1.9	1.7	1.8	Fairly consistent
Focused	1.5	1.46, 1.53	1.48, 1.41	1.1	1	2	2.25
Racetrack	1.5 (rep)	1.54, 1.43	1.40, 1.51	1.2	0.99	1.93	2.50
	0.75	0.70, 0.62	3.08, 3.48	2.25	2.23	3.96	4.5
Racetrack	1.5	1.33, 1.19	1.62, 1.81	1.4	1.25	1.71	2.25
	1.5 long	1.43, 1.52	1.51, 1.42	1.4	1.02	1.69	2.25
Focused Linear	0.75	-	0	0.6	0.57	1.8	2

Table 4.1: EMAT designs and frequency response behaviour. ‘Measured Coil Width’ gives both the generator and the detector coils. The ‘Theoretical Frequency Peak’ gives the frequency at which a maximum is predicted by the analytical calculations in section 4.1. The ‘Driving Frequency for Maximum Signal’, is the frequency at which a maximum peak to peak signal output was found. The ‘Detected Frequency of Max Signal’, gives the frequency at which a peak is found in the FFT taken of the maximum peak to peak signal found. The peak frequencies found from the FFTs of all the signals have a maximum frequency despite higher driving frequencies, this is given as the ‘Cut-off Frequency’. The ‘Driving Frequency at Cut-off’ is the driving frequency at which this maximum peak frequency is found.

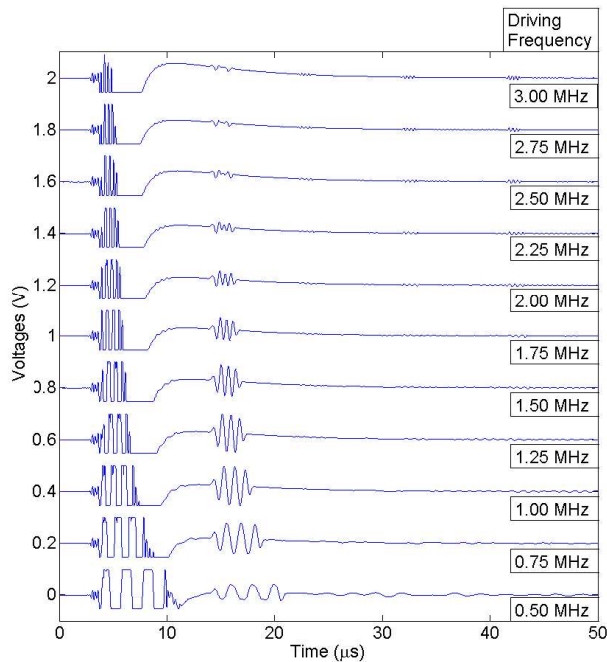


Figure 4.3: Detected signals from the 1.5 mm width, focused transmission coils pair, with a driving signal of 3 cycles and varied driving frequencies.

focused coils for all tests, (shown in the schematics in figure 3.6) to try and maintain similar magnetic field strength. However, the cuboidal magnets give a better comparison of a consistent magnetic field orientation with respect to the coils over the full length of the unfocused coils. The driving frequency of the peak in the cubic spline fit for this was not included in the table as the fit is poor; however, it is roughly consistent with the peaks found using a cylindrical magnet, but weaker and noisier due to a reduction in magnet volume.

The current output by the Ritec during the focused racetrack measurements was monitored by attaching a set of parallel resistors to the return ground in the coaxial cable and measuring the voltage drop over them. The resistors made a 1Ω load, and so the current output in Amps is equal to the measured voltage in Volts within the 10% tolerance of the resistors (this was the availability at the time). Example data for the focused racetrack pair is shown in figure 4.4b). This shows that the Ritec output increases as the frequency is increased, indicating that the peaks measured for the coil (figure 4.4a)) should actually be lower than the peaks found. However, the slope of the data is gradual, so it does not make a large difference. The frequency response of the amplifiers used in conjunction with the EMAT detectors was also checked and found to have no variation until well above

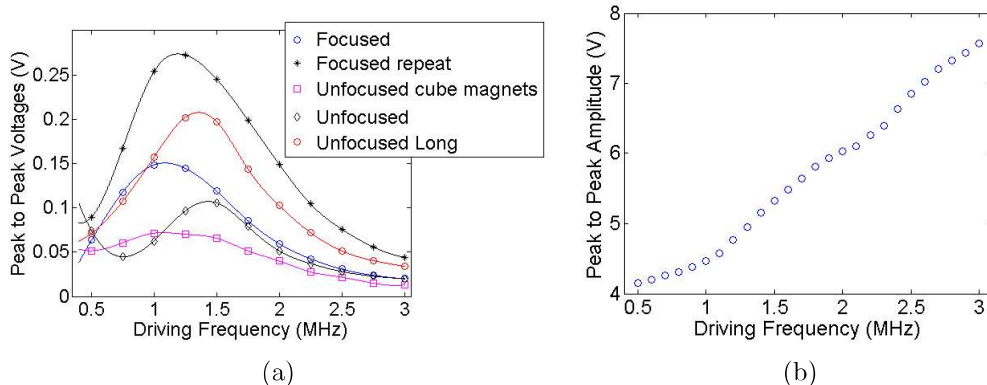


Figure 4.4: a) Output maximum peak to peak signal found for multiple 1.5 mm width racetrack coils. b) Current monitoring by measuring the voltage drop over a 1 Ω load on the ground to the coil during the focused data scan in a).

the frequency range being used.

As the driving frequency was increased from 0.5 to 1.0 MHz, the Rayleigh wave generated had a peak in its fast Fourier transform (FFT) amplitude at a frequency that matched the driving frequency, as shown in figure 4.5a) for the focused racetrack coil pair. However as the driving frequency was increased beyond 1 MHz, the frequency of the peak output from the FFT started to fall short of the driving frequency. The relation between the driving frequency and the frequency at which a maximum is found in the FFT amplitude for the racetrack coils is shown in figure 4.5b). The frequency of the generated Rayleigh wave, calculated from the peak in the FFT when the driving frequency is set such that the signal amplitude is at a maximum, is also included in the column, ‘Detected Frequency of Maximum Signal’ in table 4.1.

It can be seen in the example profiles in figure 4.5b) that the profiles have side lobes which do not increase in amplitude as the main peak increases. This means that as the signal becomes weaker these side lobes can dominate the profile. At driving frequencies above about 2.25 MHz for the 1.5 mm wide racetrack coils the signal becomes too weak and the detected maximum magnitude of the FFT becomes dominated by these lower frequency side lobes, as can be seen in figure 4.5b). At the driving frequency of 2.25 MHz the frequency of the peak in the signals’ FFT is close to 2 MHz for all the 1.5 mm width racetrack coils. This frequency is defined as the cut-off frequency for the coil, and is given individually as the ‘Cut-off Frequency’ in table 4.1. This can be seen in the A-scan data, figure 4.3; at a 2 MHz driving signal the wave packet can be seen to distort, and by 3 MHz it no longer appears as a three cycle wave of one frequency. Clearly the frequency behaviour of the racetrack

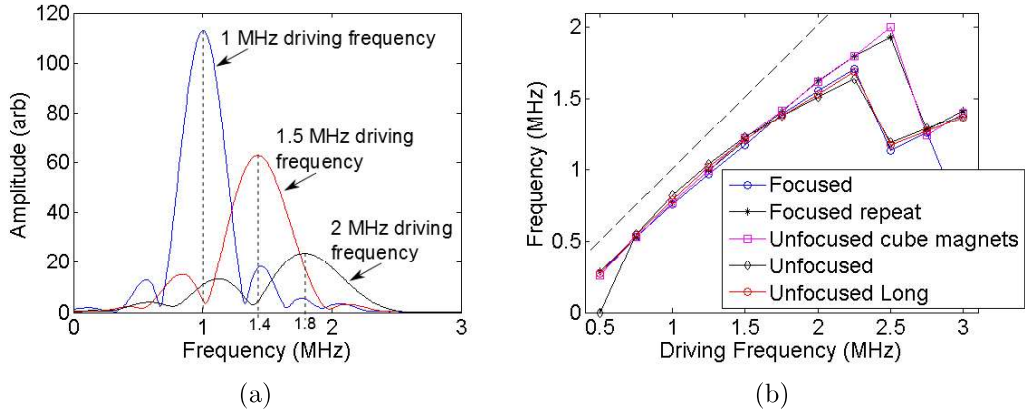


Figure 4.5: a) The frequency content of three example signals shown in figure 4.3 for the original focused racetrack coil pair, with the frequency locations of the maximum amplitudes labelled. b) The frequency locations of the maximum amplitudes, as labelled in a) dependence on the driving frequency of the coils. The dashed line indicates where the axes are equal.

coils is not behaving as simply as giving a maximum signal at odd factors of the wavelength (1.9 MHz) and minima at even factors of the wavelength (3.9 MHz).

Figure 4.6a) shows the peak to peak signals for the thinner racetrack coil, which is nominally 0.75 mm in width, and the same for a thin linear coil, also nominally 0.75 mm in width. Their strongest peak to peak signals are found at 2.25 and 0.6 MHz respectively. For the racetrack at this width, a maximum is expected at 3.9 MHz from the analytical theory. The linear coil, however, is close to consistent with the analytical theory as its signal should increase with lowering frequency (figure 4.2b)) except for very low frequencies which are outside the operational range of the Ritec. The thin racetrack coil has a correspondingly higher cut-off frequency of 3.96 MHz at a driving frequency of 4.5 MHz, as can be seen in figure 4.6b). The linear coil is consistent with the behaviour of the 1.5 mm racetrack coils, with a cut-off frequency of 1.8 MHz at a driving frequency of 2 MHz, which is to be expected as linear coils only contain a single wire direction, similar to one half of a racetrack coil.

The data from a pair of reflection meanderline coils can be seen in figure 4.7a), for a focused design and an unfocused design. They have been tuned with capacitors to have an electrical resonance as close to 1.9 MHz as could be reached within the tolerance of the capacitors. A seven cycle wave was used to excite the meanderline coils and further details can be found in reference [3] and chapter 5. The meanderline coils generate signals which have a peak in the FFT at the same frequency

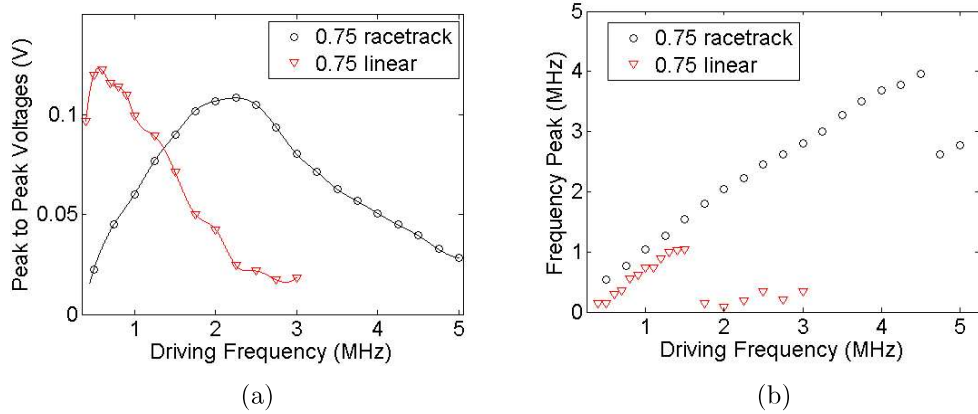


Figure 4.6: a) Output maximum peak to peak signal found for two 0.75 mm width coils, one racetrack and one linear. b) The frequency locations of the maximum amplitude found in the FFT analysis of the data from two 0.75 mm width coils, one racetrack and one linear.

regardless of the frequency of the driving signal, shown in figure 4.7b), due to their resonant frequency and the meanderline design. The average frequency location of the peak of the FFT of the Rayleigh waves generated by the meanderline coils across all driving frequencies is given in the column, ‘Detected Frequency of Maximum Signal’ in table 4.1. This falls short of the expected 1.9 MHz to 1.6 MHz and 1.7 MHz for the unfocused and the focused coils respectively. This is likely due to inaccuracies of the capacitors, which are manufactured with a 10% error in the capacitance, and inconsistencies in hand-winding the designs.

These experimental results show that the driving frequency which gives the strongest detected signals for the racetrack coils is consistently falling short of the expected optimum frequency based on the analytical model, and that this cannot be due to manufacturing error in the coils, electrical resonance, or changes in impedance between different coils. Two remaining factors to consider are the lift-off of the coils from the sample, and effects from the signal phase which is neglected in the analytical predictions. Both of these factors will now be analysed using modelling techniques.

4.3 Modelling

4.3.1 Lift-off Behaviour

The distance between the EMAT coils and the sample surface has been minimised for the experiments shown here. As the coils are encapsulated in a layer of insulating tape, the lift-off from the sample is about 0.1mm. The electromagnetic field profile

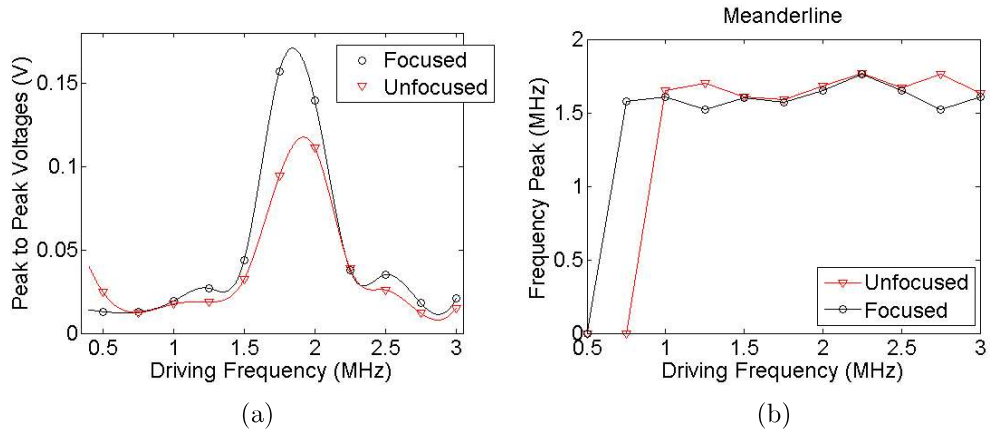


Figure 4.7: a) Output maximum peak to peak signal found for two meanderline reflection EMATs, tuned to 1.9 MHz. b) The frequency locations of the maximum amplitude found in the FFT analysis of the data from two meanderline reflection EMATs, tuned to 1.9 MHz.

seen by the sample will therefore be wider than the coil width, as the electromagnetic field extends beyond the coils. The vector potential, A , generated in a two layer sample by a coil formed of a ring of wire has been calculated by Dodd and Deeds [33]. Assuming only one substrate ($\alpha_1 = \alpha_2$ in the notation used by Dodd and Deeds) the theory simplifies to the expression:

$$A(r, z) = \mu I r_0 \int_0^\infty \mathcal{B}_1(ar_0) \mathcal{B}_1(ar) e^{-\alpha l} a \left(\frac{e^{\alpha z}}{a + \alpha} \right) da, \quad (4.11)$$

where r is the radial position from the center of the coil, r_0 is the radius at which the coil is located, z is the vertical distance from the coil, μ is the permeability of the substrate, I is the magnitude of the current pulse in the coil, \mathcal{B}_1 is a first order Bessel function, $\alpha = \sqrt{a^2 + j\omega\mu\sigma}$, ω is the angular frequency of the current pulse in the coil, σ is the electrical conductivity of the substrate. This can be used to approximately predict the lift-of behaviour of an EMAT coil.

The effect of a whole set of concentric rings, approximating a pancake EMAT coil, can then be found by summing the effects from multiple such equations at different locations. Neglecting self-field generation (experimentally found to be negligible) and neglecting magnetic edge field effects, the vector potential is proportional to the eddy current density, which is proportional to the current induced in the sample (equation 2.43). An example current density profile underneath a coil and into the sample is shown in figure 4.8a). Summing this throughout the skin depth (equation 2.54) of the sample gives a surface profile proportional to the current in the sample surface, with the half under the opposing coil direction taken to be neg-

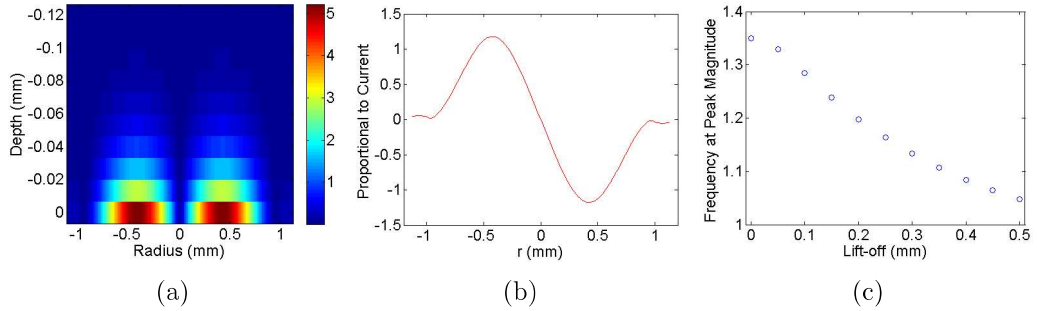


Figure 4.8: a) Example current density profile in an Aluminium substrate, 0.1 mm below a pancake coil of radius 0.75 mm with a continuous AC of frequency 1.285 MHz (color bar values are proportional to the current density). b) the surface current profile from the same coil. c) the frequency at which a peak is found in the magnitude of the FFT of profiles such as the one in b) with varied separation from the pancake coil.

ative, figure 4.8b). Taking the FFT of this profile gives another theoretical measure of the frequency content from the coil spatial profile. While this method was developed for a pancake coil, the 2D cross-section through the coils will look similar for a racetrack coil. A 1.5 mm diameter coil creates a profile with a peak in the FFT magnitude at 1.35 MHz at zero lift-off from the sample. At 0.1 mm lift-off this drops to 1.29 MHz, as shown in figure 4.8c). It is therefore possible that lift-off effects partly account for the lower frequencies seen. However, it is not enough of a drop to account for the experimental drop observed, especially when the effects of the coils being narrower than designed and the increase in Ritec output current with frequency are added.

4.3.2 Spatial Frequency Model

The detected signal from an EMAT coil should be the convolution of the frequency of the signal it is trying to detect, and the frequency profile arising from the spatial width of the coil. Considering purely the detector coil, a basic spatial model for a racetrack coil, assuming equal detection capabilities across its full width, is a square wave, where the wave amplitude represents the current flow in the coil. This has been modeled for a 1.5 mm coil with a nominal current of +1 over the range 0 to 0.75 mm, and -1 over the range 0.75 mm to 1.5 mm, corresponding to current flowing in the opposite direction, shown in black in figure 4.9a). A more extreme model is to assume detection is only at the center of the sets of wire containing parallel current, i.e. a pair of delta spikes, +1 at 0.375 mm and -1 at 1.125 mm, shown in blue in figure 4.9a). A compromise between the two models is a single cycle

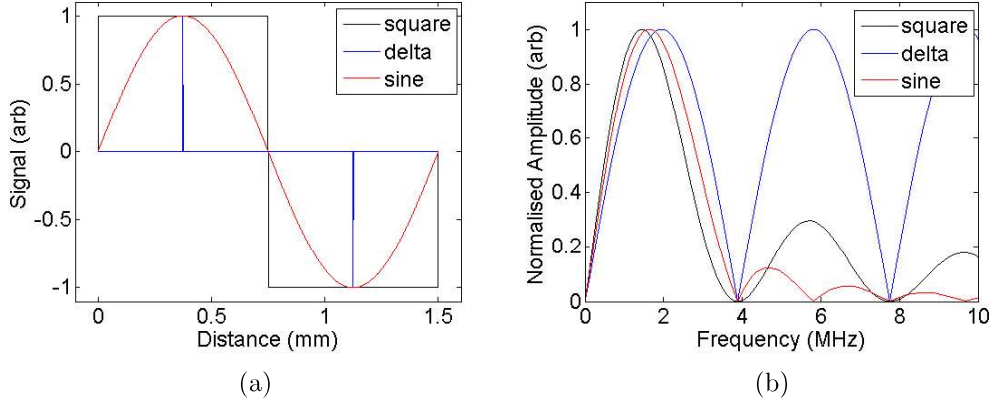


Figure 4.9: a) shows a single cycle square wave, a single cycle sinusoid, and a pair of delta spikes, all spaces for a 1.9 MHz signal, with b) showing their actual frequency content.

of a sinusoid across the same spatial range, shown in red in figure 4.9a), modeling optimal detection towards the center of each set of wires.

Taking the FFT of these waves, and using a Rayleigh wave velocity of 2906 m/s in aluminium to convert spatial response to frequency response, gives the profiles shown in figure 4.9b). The first frequency maxima for the 1.5 mm coil are at 1.9 MHz for the delta spikes, 1.7 MHz for the sine wave, and 1.5 MHz for the square wave. All give a minimum at 3.9 MHz which is in agreement with the analytical model of section 4.1. The square wave modeled is in agreement with the original analytical calculations in section 4.1.

Re-calculating the frequencies for the square wave FFT profile to match different coil widths gives a consistent relationship between the square wave width and the maximum output frequency from the FFT of the data:

$$f_p = 0.761 \frac{v}{L} \quad (4.12)$$

where f_p is the peak frequency, v is the surface wave velocity, and L is the full width of the square wave, or the full width of the racetrack coil. This allows an upper frequency limit to be calculated, however, as with the analytical calculations, it is too high to explain the experimental results.

4.3.3 Time Evolution

To study the effect of time variation and different signal shapes on detection, a synthetic wave, G , is generated using:

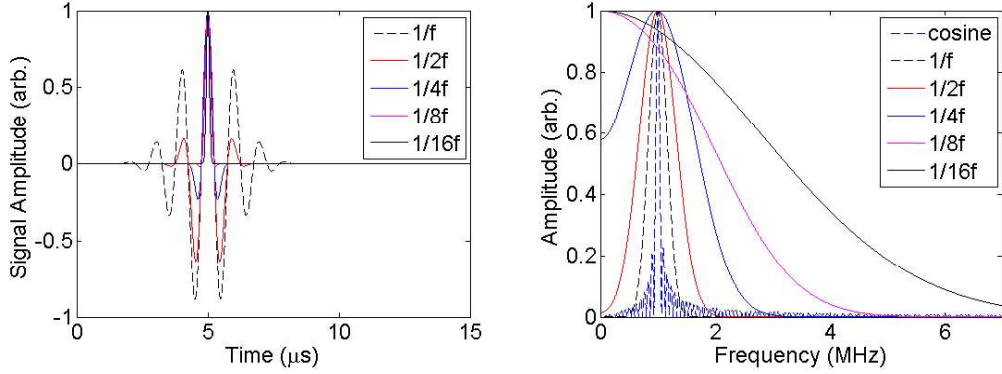


Figure 4.10: Example data with a desired frequency of 1 MHz and an envelope width (a) varied as indicated by the legend. a) shows the generated signal G , excluding the continuous wave signal for clarity. b) shows the FFT data from the signals in the top graph, now including the continuous wave for reference. The signals have all been individually normalised.

$$G = \text{Re} \left[e^{\frac{-(t-t_0)^2}{2a^2}} e^{2i\pi f(t-t_0)} \right] \quad (4.13)$$

where f is the frequency, t_0 is the time at which the center of the signal packet occurs, and a is the width of the signal in the time domain. This wave is evaluated over a time range from 0 to 15 μs with $t_0=5 \mu\text{s}$. f is varied from 0.4 to 10 MHz in steps of 0.1 MHz. To test a signal close to a continuous wave the entire first exponential term that creates the wavepacket was removed, leaving just a cosine signal, i.e. the condition where $a = \infty$. The only reason this is not actually a continuous wave is because it is only evaluated from 0 to 15 μs . To an opposite extreme a is varied as $1/f$, $1/2f$, $1/4f$, $1/8f$, $1/16f$, making the envelope increasingly narrow, heading towards a delta spike, making the generation increasingly broadband. A value of $a = 1/f$ creates a signal with three main significant peaks, to match the experimental work (black dotted line in figure 4.10a)).

The calculated G signals for these different a values, except for the continuous wave, are shown for a frequency of 1 MHz in figure 4.10a) to show how the envelope width affects the signal shape. The a parameter is given in the legend. Figure 4.10b) shows the FFT analysis of the signals shown in a). As the signal becomes closer to a delta-like signal the frequency content moves to peak at 0 MHz despite the input f value, and increasing f increases the bandwidth rather than shifting the peak location.

The EMAT coil is modeled by considering a spatial range of 0 to 1.5 mm with increments of 0.1 mm, as the wire used in the EMAT designs are 0.08 mm

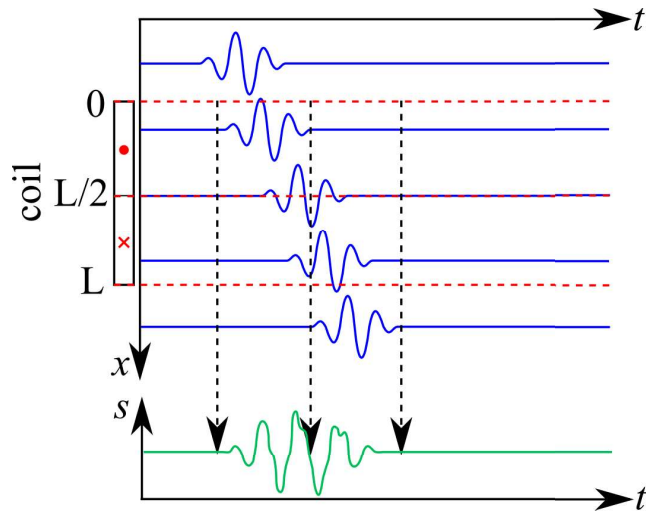


Figure 4.11: An arbitrary synthetic signal is shown in blue. As it travels in x its arrival time becomes correspondingly delayed. The actual signal detected by an EMAT coil (shown on the left) is the superposition of these signals, s shown in green.

diameter, and so 0.1 mm is a reasonable approximation to the coil winding spacing. At each spatial step the synthetic wave G was delayed by a time given by the wire spacing divided by the Rayleigh wave velocity in aluminium, 2906 m/s. This is shown schematically with exaggerated delays in the top half of figure 4.11. It was then approximated that the EMAT coil would measure the signal underneath the whole coil instantaneously, and so a single detected signal was generated by summing all the data over the positions 0 to 0.75 mm, and the data over 0.75 to 1.5 mm at each time instance. As the coil is a racetrack design, the second half was subtracted from the first half to account for the change in direction of the wire. This time staggering therefore includes the effect of the variations in the signal detected by each wire over a finite coil width at a single time, creating a simulated ‘detected’ signal from this superposition, as shown in figure 4.11.

Some example results of the relation between the input signal and the detected signal are shown in figure 4.12a), c) and e), for simulated data with $a = 1/f$, at three different frequencies; 1, 4, and 6 MHz. The 1 MHz detected signal shows very similar amplitudes to the input signal, and the 6 MHz detected signal, while smaller in amplitude, is still similar in shape to the input signal. 4 MHz, however, shows a greatly distorted signal shape, as expected for this detector width as this is a predicted minimum. Figure 4.12b), d) and e) show the FFTs of all the signals shown in a), c) and e). The 1 MHz detected data has the same frequency content as the input signal, although reduced in amplitude. The 6 MHz detected data has

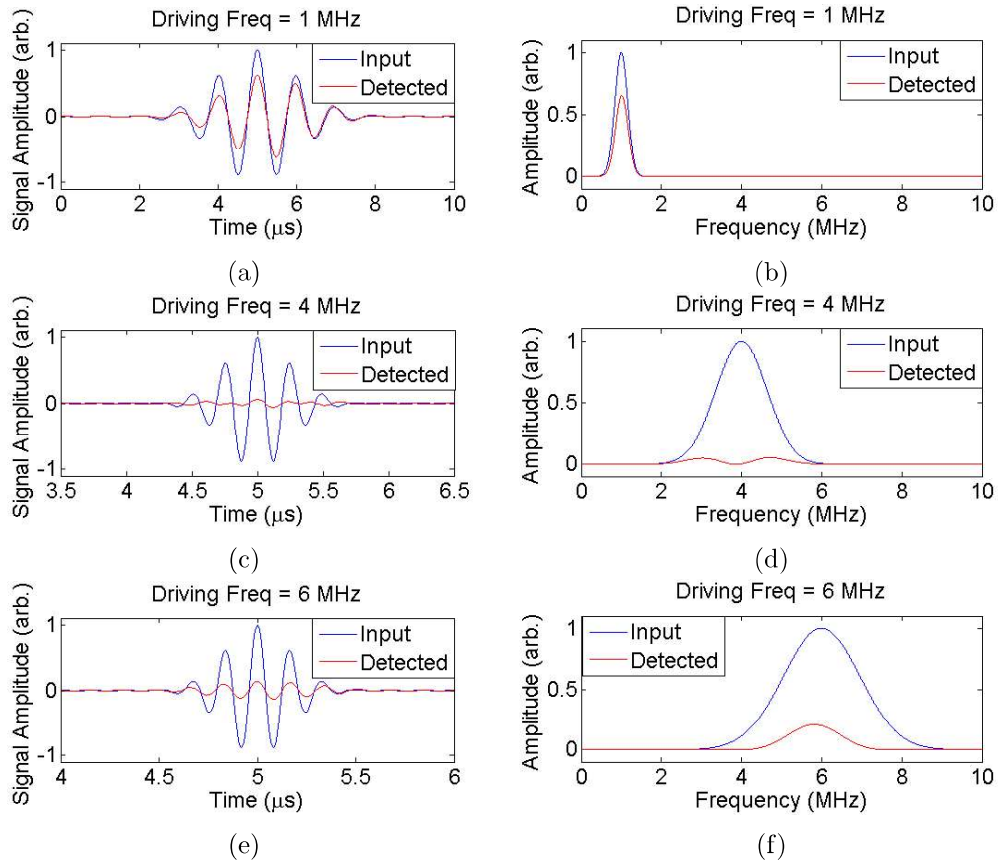


Figure 4.12: a), c) and e) show example G signals (blue) and synthetic detected signals (red) from a simulated 1.5 mm width racetrack coil with an envelope width of $a = 1/f$. a), c), and d) have input frequencies of 1, 4, and 6 MHz respectively. b), d), and f) show the corresponding FFT output data of the signals shown in a), c) and e).

a smaller bandwidth than the input signal, but the peak in amplitude occurs at roughly the same frequency as the peak in the input signal. The 4 MHz input data shows that the signal has distorted such that it has no 4 MHz signal content, and only the upper and lower portions of the frequency band remain, as expected.

Figure 4.13 shows similar data to figure 4.12 except for a bandwidth of $1/8f$. As the input signal is now close to a single delta spike there is a large amount of low frequency content, and for higher frequencies of operation the bandwidth is increased. This shows something close to the full frequency response of the coil spatial width, with little variation due to the input signal. It can be seen that in both c) and e) the detected signals have the same duration in time despite the input signals being different. This is because the input signal width is smaller than half the coil width in the time domain. Therefore the spatial width of the coil is

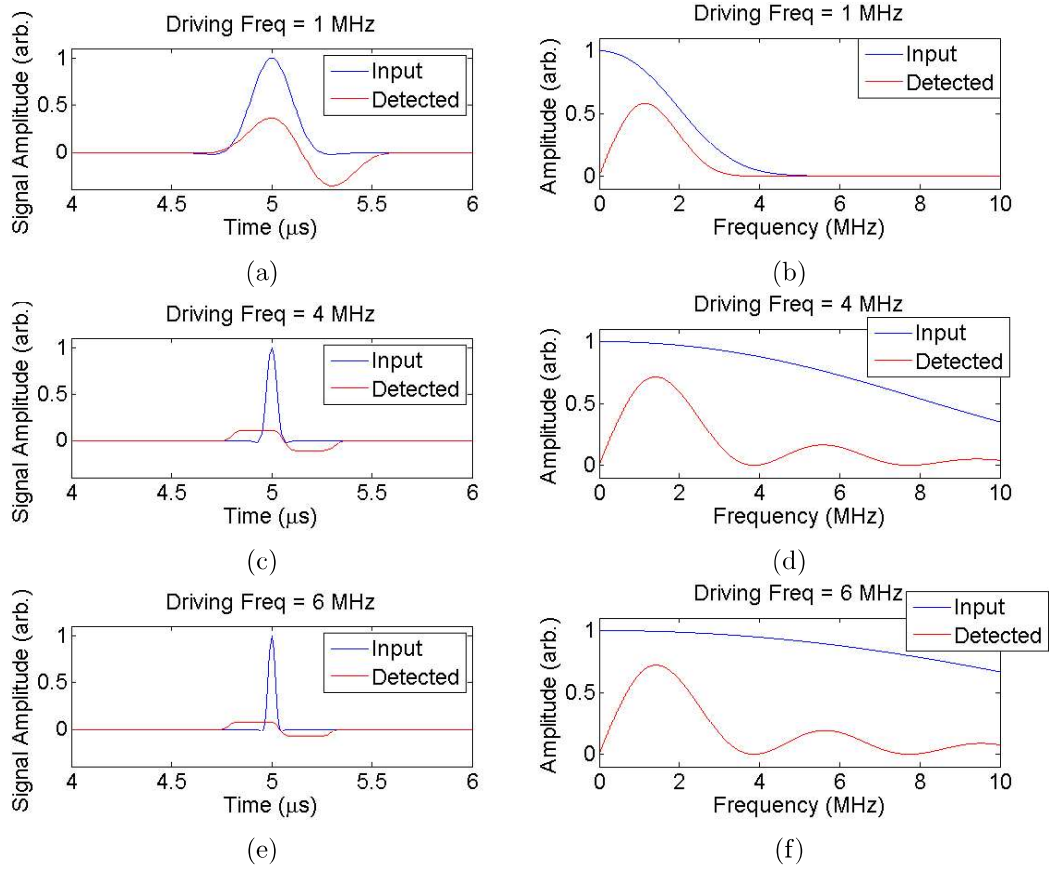


Figure 4.13: a), c) and e) show the input G signal (blue) and the synthetic detected signals (red) for input frequencies of 1, 4 and 6 MHz respectively, with an envelope width of $1/8f$. c), d) and f) show the corresponding FFT output data from the signals shown in the left hand graphs.

dominating the detected signal rather than the frequency of the input signal. d) and f) both show detected frequency responses close to the profile predicted by the analytical model. Therefore, even if a higher input frequency is used, the frequency lobe in the FFT profile between 0 and 4 MHz dominates the frequency response.

To compare the differences caused by varying both f and a , figure 4.14a) shows the maximum peak to peak signal of this synthetic detected signal s (the red signals in parts a), c) and e) of figures 4.12 and 4.13), for each value of f input into the equation for G , all normalised with respect to the maximum peak to peak signal from the continuous wave (cosine) data for comparison. It should be noted that the input frequency does not necessarily reflect the actual peak frequency produced by the initial G signal, as seen in figure 4.10b). The two narrowest wave packet signals for G , $a = 1/8f$ and $a = 1/16f$, have peaks at 0 MHz, and are increasingly broadband.

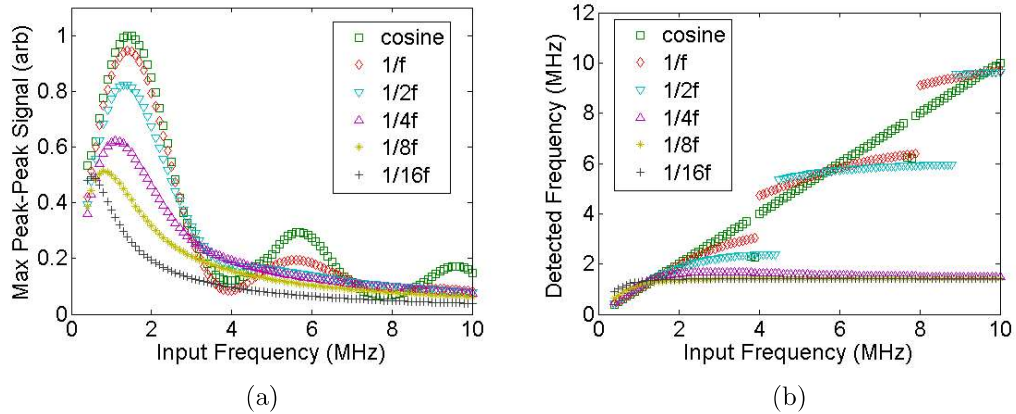


Figure 4.14: a) normalised, maximum peak to peak signal of the detected wave as a function of the set frequency input into the synthetic signal for a 1.5 mm width racetrack coil. b) the peak output frequency of the modelled detected signals plotted against input frequency.

Figure 4.14b) shows the frequencies at which a maximum amplitude is found in the FFT data of the detected signals, i.e. the peak locations of the red signals in parts b), d) and f) of figures 4.12 and 4.13. It should be noted that these peaks are also plotted against the value of f input into the equation for G , equation 4.13.

The continuous wave data has a peak at 1.5 MHz (figure 4.14a) green squares) in agreement with the analytical calculations and the simple square wave analogy shown in figure 4.9. However, as the signal packet shrinks from the continuous wave, the peak shifts to the lower frequencies, with the $1/4f$ data having a peak at 1.1 MHz. The minima are in agreement with the analytical calculations, but the time averaging effect causes the central peak to be more asymmetric towards lower frequencies. The detected frequency is firstly convoluted with the frequency profile from the coils' square wave spatial profile, and then as signal packets decrease in length as a is changed, the frequency is 'blurred' to a lower value by the time averaging effect. As the signal becomes close to a delta spike there is always a strong input frequency content between 0 and 4 MHz, meaning that this part of the coils frequency profile remains dominant over the high frequency peaks. Therefore, the curves for the $1/4f$, $1/8f$, and $1/16f$ data seen in figure 4.14a) have no distinct minima at 4 and 8 MHz, but simply a gradual decrease in amplitude.

The frequency profile of the continuous wave data (Figure 4.14b) green squares) shows the expected response: a straight line of gradient 1, with gaps at 4 and 8 MHz corresponding to 2λ and 4λ , where the signal cancels. As the signal wave packets are decreased in length, and so become broader band, the response

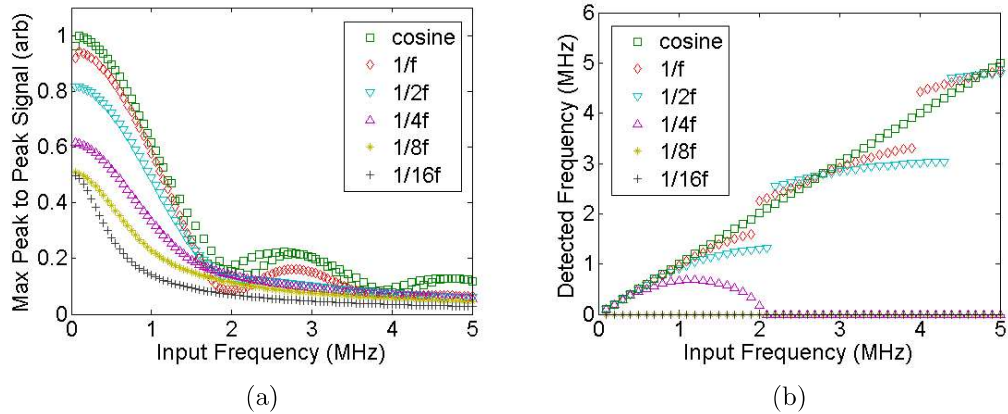


Figure 4.15: a) normalised, maximum peak to peak signal of the detected wave as a function of the set frequency input into the synthetic signal for a 1.5 mm width linear coil. b) the peak output frequency of the modelled detected signals from a linear coil detector plotted against input frequency.

shown in figure 4.14 moves increasingly further away from a straight line. This is due to more signal content at both lower and higher frequencies than the input peak, (figure 4.12d)), allowing a stronger distorted signal to remain even when the main input frequency is cancelled out by the coil geometry. However, the discontinuities at 4 and 8 MHz remain for most wave packets. For the three widest band profiles the frequency location of the maximum amplitude remains dominated by the first lobe of the FFT, as seen in figure 4.13, and so the data plateaus at this frequency, converging towards 1.5 MHz for all higher input frequencies, in agreement with the square wave profile of section 4.3.2.

The same program has been run considering instead a linear coil, where all data between 0 and 1.5 mm is summed at each instant in time. A similar effect is seen, but with minima at every integer value of the wavelength, corresponding to frequencies of 0, 2, 4, 6 etc. MHz. This is shown in figure 4.15. The frequency range used for this work was 0.05 to 5 MHz in increments of 0.05 MHz. This is as expected from the analytical calculations, and shows that this model is valid. It does not predict the drop of at very low frequencies seen experimentally in figure 4.6, however this drop is due to the lower limit of the Ritec generator being reached.

This effect partially explains the low frequency peaks observed experimentally, however the drop predicted for $a = 1/f$ is still too small to explain all the data. A sufficiently large drop is given by narrower input signals, but these have not been tested experimentally. It is possible that this model is too simplified still, and that this effect is stronger than the model predicts. However, considering the

frequency drop created by the coil lift-off, these effects together can mostly explain the frequency drop. These models, however, have not considered the effects of the generation coil. It is possible that the generation coil is creating a signal which is already lower than the Ritec driving frequency, which is then compounded by the detection bias of the detection coil. Furthermore, multiple coils that were tested contained geometric curvature. There is no theoretical reason for this to effect the frequency content, however it could effect the signal phase [147].

4.3.4 Finite Element Modelling

The analytical model outlined in the previous section considers a generic wave packet and does not consider differences between wave amplitude and wave velocity. It also neglects effects from the finite width of the generation coil, and only considers the detector coil. The experimental results obtained using the original focused racetrack coil pair also had geometric curvature, shown in figure 3.7. A 3D finite element model was developed using the software PZFlex to see if the same frequency lowering effect is seen when considering wave velocity, to look for influence from the finite width of the generator coil, and what effect geometric focusing might have. All of the models had an element size of $34 \mu\text{m}$, making them much higher resolution than the analytical models, a requirement to model the high frequency wavelengths accurately. For generation, a 3 cycle sinusoid wavefront was applied from every element within the 1.5 mm coil width, with the waveform applied as negative in the second half of the coil to represent the opposite wire direction. The driving frequencies of the wavefront applied were varied from 0.3 to 3 MHz in increments of 0.1 MHz for the focused designs, and from 0.5 to 3 MHz in increments of 0.5 MHz for the unfocused designs to check for consistency.

Figure 4.16 shows an example of the simulated x-velocity data recorded at 16.5 mm horizontally away from the generation coil back edge along the centre line for a focused simulation with a driving frequency of 1 MHz. This location is at the designed focal point of the curved design. Figure 4.17a) shows the maximum peak to peak signal found at that location for all the different driving frequencies used for both the focused and the unfocused design, and also for the simulated z-displacement data. Y-velocity data is not considered as along the centerline of the design the motion is purely in the x- and z-directions, with no y-component. The peaks found are at 2.1 MHz for the x-velocity focused simulations, 1.6 MHz for the z-displacement focused simulations, 2 MHz for the x-velocity unfocused simulations, and 1.5 MHz for the z-displacement unfocused simulations. This shows there is some discrepancy between the focused and unfocused simulations, with a slight tendency

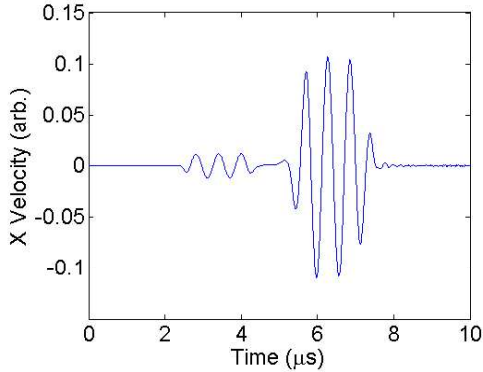


Figure 4.16: Example A-scan of the FEM simulated x-velocity data at 16.5 mm away from the coil back edge, for a driving frequency of 1 MHz. The strongest, later arriving, signal is the three cycle Rayleigh wave, the smaller, earlier arriving wave is a surface skimming longitudinal wave.

towards lower frequencies in the unfocused simulations. Discrepancies are likely due to the spreading of the unfocused wavefront as opposed to the coherent wavefront seen at the focal point of the focused design, leading to variations in phasing as the wave reach each wire the coil [147]. In both cases the peak is seen at about 2 MHz for the x-velocity data, suggesting the generation is in keeping with the analytical models first outlined, while the z-displacement data is closer to the lower peaks expected from the spatial width of the coil. It is unclear why they differ.

To simulate the racetrack detector, for simplicity just the centerline, $y = 0$, data was considered. The same method as for the time evolution model was then used to simulate a racetrack detector coil; the data between 31.5 and 32.23 mm was summed, and then the sum of the data between 32.25 and 33 mm was subtracted from the first sum to account for the opposing coil directions. The maximum peak-to-peak signal found from this simulated signal is plotted as a function of the driving frequency in the right hand graph in figure 4.17. The peaks for all of these are roughly coincident at 1.5 MHz, with a slight bias towards the lower frequency content in the z displacement data. This indicates that, despite the higher frequency peak seen at the focal point in the x-velocity data, the spatial effect of the detector coil dominates the frequency location of the maximum signal detected by the whole system, and is in agreement with the continuous wave scenario considered in the previous section.

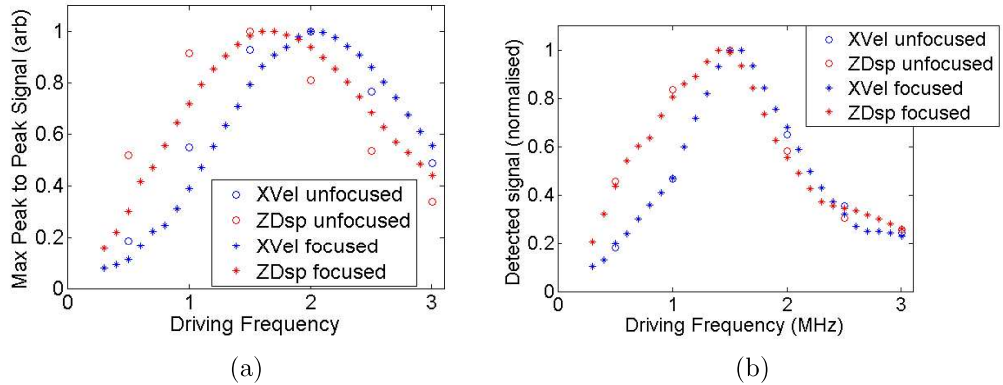


Figure 4.17: a) maximum peak to peak signal found at the focal point, or equivalent position for the unfocused coils, as a function of the driving frequency used from a 1.5 mm racetrack spatial profile. XVel indicates the x direction velocity and ZDsp indicates the z, or out-of-plane displacement. b) maximum peak to peak signal found simulating a racetrack detector at the model centerline as a function of the driving frequency used from a 1.5 mm racetrack spatial profile.

4.4 Conclusion

Experimental data from a range of 1.5 mm width transmission racetrack EMAT coils has been presented and the driving frequency which gives the strongest peak to peak detected signal ranges from 1.1 to 1.4 MHz. A simple analytical solution for the detector coils is presented using the velocity of the wave equation, as an extension from previous work on linear coils [137], which would indicate a peak frequency should be detected at 1.44 MHz, showing this calculation is overly simplified. The continuous wave excitation of a racetrack coil can be modeled as a square wave spatial profile, giving a maximum detection at $0.761^v/L$, where v is the Rayleigh wave velocity and L is the full coil width. A Matlab time evolution model was developed, giving a range of peaks between 1.1 and 1.5 MHz depending on the envelope width of the excitation signal, consistent with the experimental data. The time evolution model predicts minima in the detected signal at every even integer multiple of the wavelength, unless a fairly broadband signal is used, which eliminates the minima. The zero minima show that racetrack coils act as DC filters. The same model shows that linear coil detectors are more efficient the lower the frequency is, with minima at every integer multiple of the wavelength, again, unless a broadband signal is used, eliminating the minima.

It can be concluded that time averaging causes the actual frequency peak location for a finite wave packet to ‘blur’ the signal to a slightly lower frequency, down

to as low as 1.1 MHz for a 1.5 mm racetrack coil. The maximum peak frequency that can be generated by the coils is 2 MHz for a 1.5 mm width coil, approximately the theoretical peak frequency from the coil width, but is only obtained using a higher driving frequency of 2.25 MHz, and is a very weak signal due to the time averaging effect. Increased coil lift-off has also been shown to lower the central frequency produced by the same coils by 0.06 MHz for a 0.1 mm increase in lift-off using analytical calculations, adding to the other effects. Focusing is shown through FEM to have negligible effect on the detected frequencies. The FEM also shows that detected frequencies are dominated by detector effects, and not the generation coil. Analysis of a single point from simulated racetrack generation gives a peak in the simulated x-velocity data close to 2 MHz, as predicted by the simple analytical solution first presented, but the time averaging of the detection coil causes the signal to blur to a peak at 1.5 MHz, which is consistent with the continuous wave model first presented.

$f_p = 0.761 \frac{v}{L}$ can be used to give a rough guide for the optimum frequency of operation for a racetrack coil when long excitation pulses are used if a coil design needs to be created for a specific frequency of operation. However, if shorter excitation pulses are used it has been shown that the optimum frequency of operation will be lowered. The Matlab time evolution model presented offers a way to individually calculate the expected operation frequency depending on the input signal used. Operation at lift-off also lowers the optimal frequency of operation. It is recommended that for optimal EMAT signal strengths all coils should be tested with a driving frequency sweep in their desired operation set-up to find the exact optimal operation frequency of the whole unit.

Chapter 5

Characterisation and Defect Detection Capabilities of Focused and Unfocused Pseudo-Pulse-Echo Meanderline EMAT Designs

For the improved detection of small surface breaking cracks, focused surface waves are investigated. Geometric focusing in the EMAT coil design is used to create a focusing effect. This chapter details the behaviour and capabilities of the pseudo-pulse echo meanderline EMAT detailed in section 3.1.1, with the coil design pictured in figure 3.3. A standard, unfocused EMAT as detailed in section 3.1.1, figure 3.1, is first presented and used for comparable defect detection scans to show the improvements from the focused design. The technique presents as a pulse-echo technique, however two separate coils are used in close proximity instead as this allows for isolation between the coils, and hence the term ‘pseudo-pulse-echo’.

5.1 Wavefield Imaging

The out-of-plane displacement of an ultrasound wave generated in a sample by an EMAT can be mapped using a laser vibrometer over an area to create an image of its beam profile, as outlined in section 3.2. This section studies the wavefields produced by the unfocused meanderline coils, and the focused meanderline coils, as discussed in section 3.1.1, to give a comparison of how the change in geometry

affects the wavefield shape created. Pseudo-pulse-echo mode uses two coils in close proximity so that the two coils are isolated and can be individually tuned to a resonance frequency, as discussed in section 3.6.2. As such, the behaviour of both the generation and the detection coil must be understood to fully characterise the EMAT unit. The frequency analysis in chapter 4 forms part of this characterisation, but in addition, for focused designs the focal behaviour must be understood. The cross-correlation technique, outlined in section 3.4, was used to find the signal power from the EMAT at each X-Y location on the sample surface.

Figure 5.1 shows the results from the unfocused design and figure 5.2 shows the results from the focused design. Figure 5.1a) and b) and figure 5.2a) and b) shown two time snap shots from the EMATs, the first at 11 μs and the second at 26 μs after the EMAT pulser triggers. The colour scales have been normalised with respect to the strongest signal seen during each scan, with red indicating the strongest signal, blue the weakest signal, excluding noise outliers. No direct comparison is made here between the signal strengths of the two coils due to variations in set up, in particular the focus of the laser beam, making a numerical comparison obsolete.

To give a single, time independent, image showing the spread of energy over the whole sample, the signal power was summed from 0 to 50 μs at each x-y position and then re-normalised to give the final profile c) shown in figure 5.1, unfocused design, and figure 5.2, focused design. This will show the maximum power (red) when the ultrasonic wave is strongest, and so should show the focal position of the curved EMAT design. Some positions did typically show more noise spikes than others due to variations in surface roughness leading to the speckled variation in signal within the beam profile. The magnet placement, shown by the circular effects in the time independent images, contains a large quantity of noise in the focused scan, because the change in height of 20 mm to the surface of the magnet puts the beam of the vibrometer used out of focus. This effect does not occur on the unfocused scan due to a different set up of the laser focus, causing a loss of signal at this increased height instead. The x-axis zero position has been set at the back edge of the generation coil for both scans. Figure 5.2c) shows the focus at 43 mm from the coil back edge.

The unfocused beam is approximately symmetric on either side of the magnet with waves propagating in both directions, with a vertical extent clearly larger than the 20 mm extent of the coil. The shape appears to be stronger at the edges, at around 5 and 25 mm on the vertical axis; this is due to the curved ends of the wire as it turns between meanders, figure 3.1, creating a near field effect. The

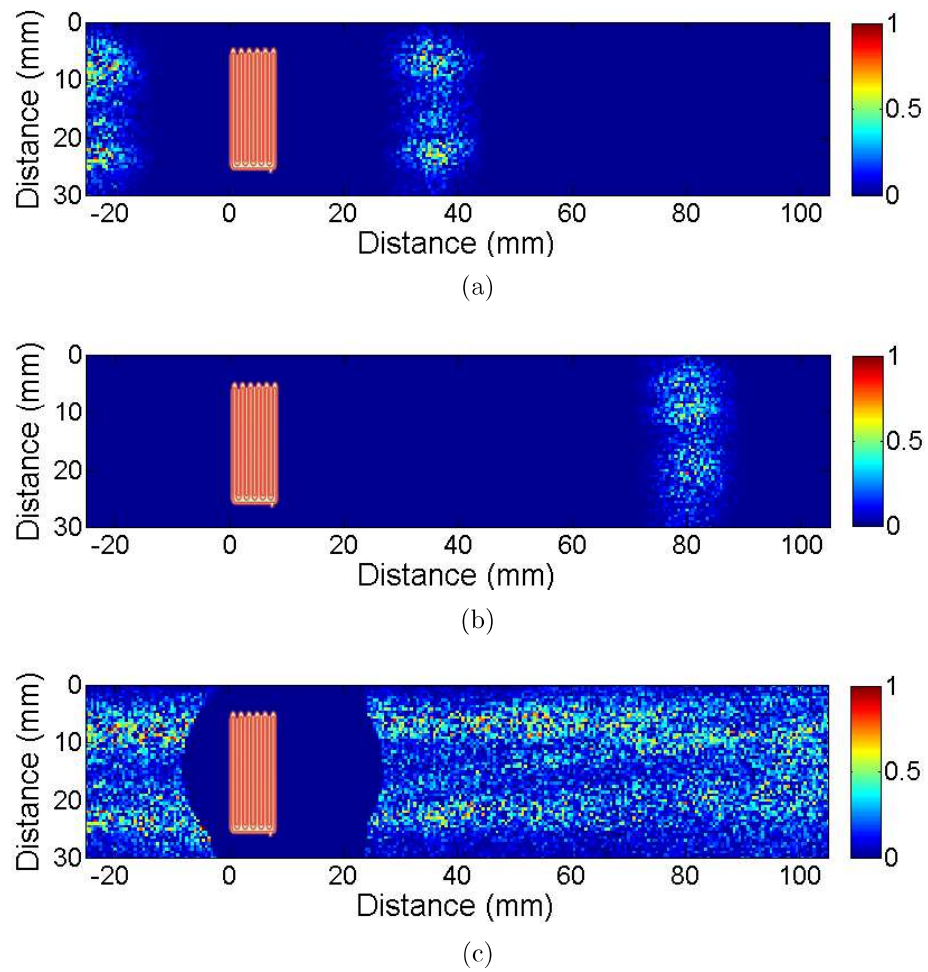


Figure 5.1: a): normalised signal power as detected by a laser vibrometer at $11 \mu\text{s}$ after the generation coil is triggered, the x zero position indicates the back edge of the generation meanderline coil. b): the same plot as the top graph except $26 \mu\text{s}$ after the coil fires. c): the full beam profile, summed between 0 and $50 \mu\text{s}$ and renormalised. The coil location has been superimposed in red/white for reference.

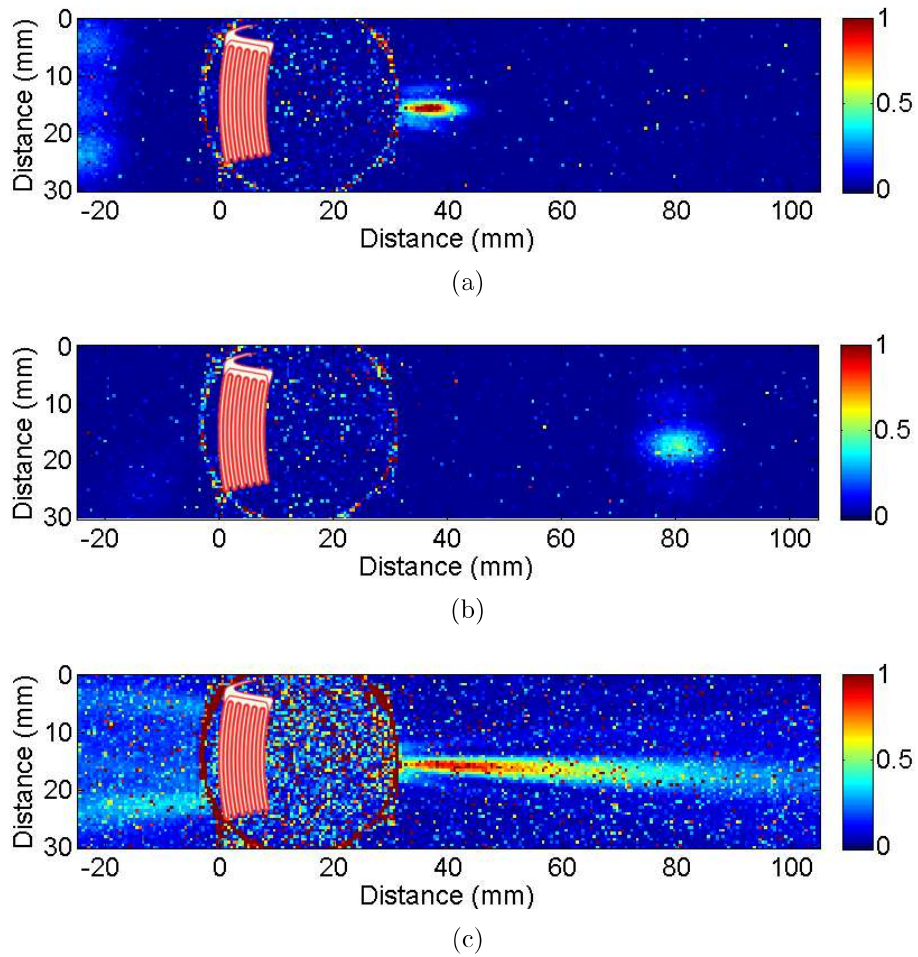


Figure 5.2: a): normalised signal power as detected by a laser vibrometer at $11 \mu\text{s}$ after the coil fires, the x zero position indicates the back edge of the generation meanderline coil. b): the same plot as the top graph except $26 \mu\text{s}$ after the generation coil is triggered. c): the full beam profile, summed between 0 and $50 \mu\text{s}$ and renormalised. The coil location has been superimposed in red/white for reference.

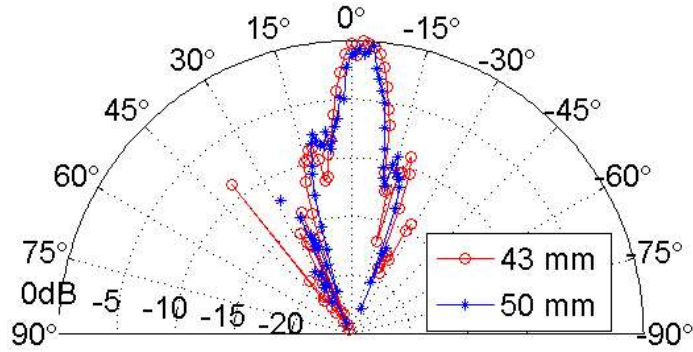


Figure 5.3: Directivity plot of the signal in dB from the focused meanderline EMAT.

wave energy appears more evenly spread throughout the beam width by the time the beam has reached 100 mm from the zero position. The profile is fairly noisy, however, and this y-axis variation in intensity is not significant enough to draw any further conclusions from. The focused coils show a clear difference in wavefield, with the wave transmitted to the left hand side of the magnet propagating outwards and diverging, and the wave on the right hand side focusing to a stronger, tight profile. Peak signal strength is reached at 43 ± 1 mm from the back edge of the generation coil. This is 7 mm shorter than the designed focal point at 50.6 mm (figure 3.3) due to the small aperture angle of the generation coil, as discussed in the next section. The vertical extent of the beam, or the beam width, at this position is 3 ± 1 mm, significantly narrower than the coil extent.

To further analyse the focusing effect, figure 5.3 shows the focused signal in dB as a function of angle at two different distances, 43 and 50 mm, as measured from the back edge of the generation coil. 0° gives the data directly in the beam path, i.e. the data at 43 and 50 mm away from the back edge of the coil along the x-axis. 90° is defined as the positive y-axis direction from the back edge of the coil, 90° from the focal axis, and -90° correspondingly as the negative y-axis direction from the back edge of the coil. At a radius of 43 mm the signal is stronger at 0° , but does in fact have a slightly broader angular extent than the signal at a radius of 50 mm (close to the designed focal point). Plotting the data in dB (i.e. a log scale) shows the presence of side lobes which are not picked up in the power image in figure 5.2.

5.2 Aperture Effect

The shortening of the measured ultrasonic focal point from the designed geometric focal point is due to the aperture angle of the coil. This is demonstrated experi-

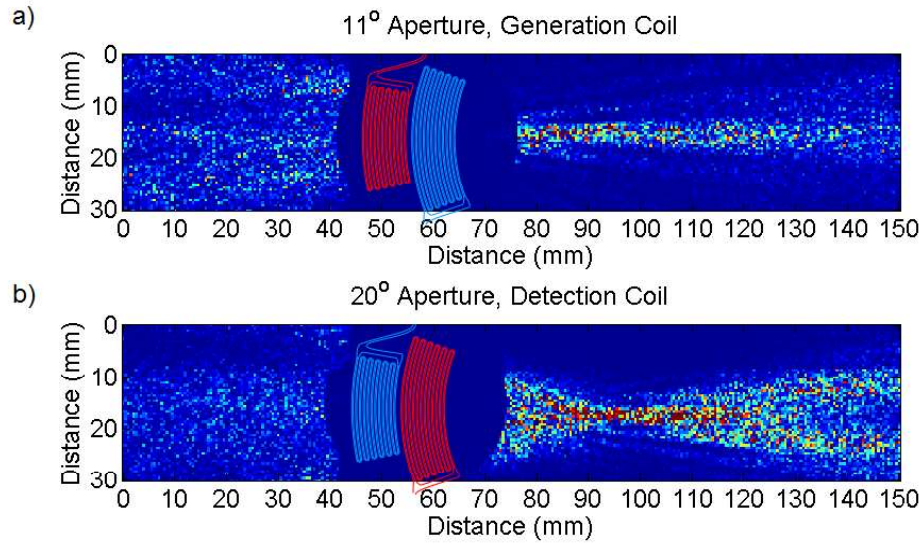


Figure 5.4: Focused meanderline beam profile comparisons, using either a) the generator or b) the detector coil as a generation coil to image its behaviour, the active coil has been superimposed in red, and the other coil in blue for reference.

mentally through a comparative pair of vibrometer scans, run sequentially, changing from using the generation coil, to using the detection coil to generate the ultrasound, with results shown in figure 5.4. The generation coil has an aperture angle of 11° , and the detection coil has an aperture angle of 20° , as labelled in figure 3.3, so this allows for a comparison of the ultrasonic focal points between two coils with different apertures. The only difference between the two coils in design is their aperture angle. Due to their different positions the generation coil has a geometric focal length of 51 mm, and the detection coil has a geometric focal length of 41 mm, so that their geometric focal points are aligned, as shown in figure 3.3. The vibrometer focus was not altered between the scans, and the exact same sample and positioning was used. The two scans have been plotted on the same, normalised colour scaling in figure 5.4. The x-axis data between the two scans do not quite line up due to drift in the x-y stage used for imaging when resetting the equipment between scans. This is duly compensated for in focal length measurements. The data is noisier than the previous scan, figure 5.2, due to difficulties with the beam focusing of the vibrometer. However, it is clear that the focal points are not the same.

For a more detailed study of the focal position, a two-wave mixer laser interferometer was used, with the detection point scanned along the $y=15$ mm centerline, along the focal axis of the beam, again using both coils alternately as generators. This system has a single direction stepping stage, so full wave field images could not

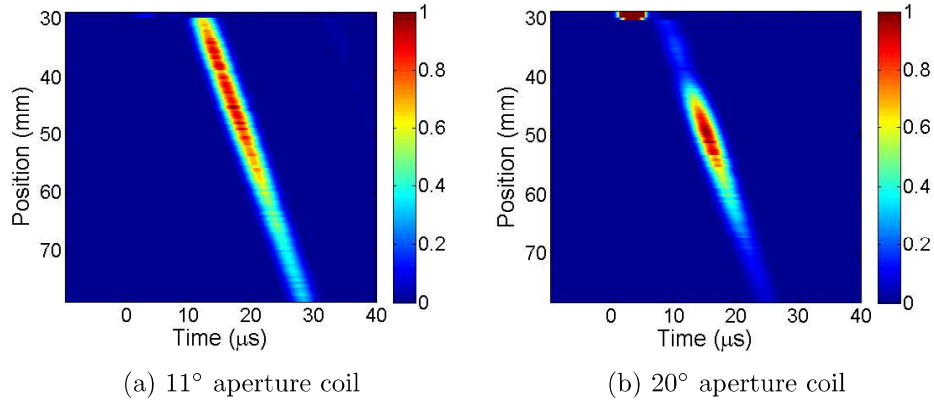


Figure 5.5: B-Scan data of normalised signal power from (a) the narrow aperture generation coil and (b) the wider aperture detection coil of the focused meanerline EMAT. Blank or noisy data at 30 mm shows where the laser beam caught the edge of the magnet.

be made. However, this detection system has much better time and spatial resolution, and has been designed to perform better on rough surfaces, giving better signal to noise ratios [148]. The associated B-scans can be seen in figure 5.5, with time on the x-axis, and position on the y-axis, corresponding to the same position direction as used for the x-axis data in figure 3.3, with the zero position set to the generation coil central back edge. The data has been individually normalised to a maximum amplitude of 1. Figure 5.5a) corresponds to the centerline of the vibrometer data in the top image of figure 5.4, with a peak at 43 mm. Figure 5.5b) corresponds to the centerline of the vibrometer data in the bottom image of figure 5.4, and shows a signal peak at 50 mm, at about the designed focal point. The wider aperture coil (detector) also shows a much tighter focal length, the signal having become almost completely dispersed by the end of the scan, unlike the signal shown in a).

It is found that the 11° aperture angle coil had a focal offset of 8 mm from the designed focal point, and the 20° aperture angle coil had a focal offset of less than 1 mm from the designed focal point. The larger detector coil gives rise to a stronger signal, as expected and can be seen in figure 5.4, and the wider aperture gives a tighter focal spot, followed by a faster spread of the signal. The narrower aperture angle gives a longer beam profile for the focal point, which is often more desirable for ultrasonic scanning as it means defects can be detected regardless of how close they are to the focal point. It can clearly be seen that the two coils are not focusing to the same spatial position despite being designed to do so.

Finite element analysis using the software PZFlex, was used to simulate the

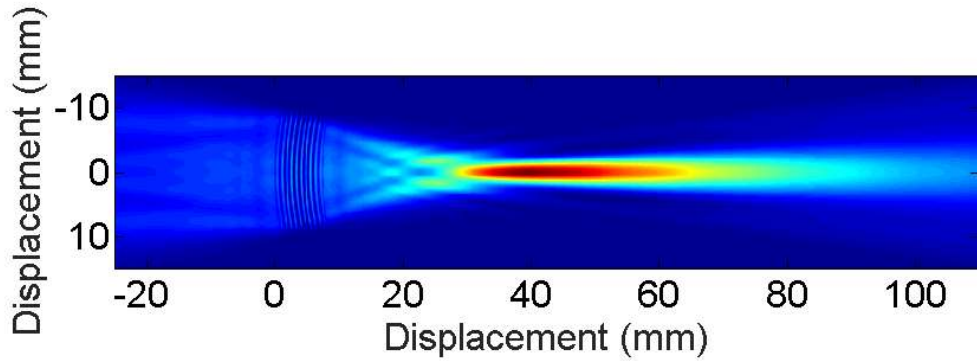


Figure 5.6: Finite element model of the beam profile for a focused meanderline EMAT with an aperture angle of 11° , as shown in figure 5.2.

Rayleigh wave produced by the EMAT and then to vary the aperture angle of the simulated coil to study its effect. The EMAT, was modelled by assuming a radial, consistent, in-plane pressure within the material surface at right-angles to the coil. The actual value of the pressure was neglected as the results of interest are comparative changes, rather than numerical. Following identical signal processing to the experimental data, the simulated, time-summed, beam profile for the modelled generation coil is shown in figure 5.6. This predicts a focal position of 40 mm, and the profile shape is roughly in agreement with the experimental measurements from the laser vibrometer. The laser vibrometer measures the out of plane displacement of the surface, whereas the EMAT detection coil measures in-plane velocity, however, simulations were run to study both the out-of-plane displacement and the in-plane velocity, and the profiles were found to be very similar, with the focal points appearing in the same location.

Coil models were generated with aperture angles varying from 10° to 20° . Figure 5.7 shows some example data, plotting signal power measured along the focal axis from the time-summed signal power profiles for three different aperture angles. All the coils have been designed to focus at 51 mm, as marked on the figure, but the profile peaks fall increasingly short of this as the aperture angle decreases. The beam depth along the x-axis is also seen to increase with decreasing aperture angle, as seen in the wave field images from the two coils (figure 5.5) and the peak height decreases as the depth increases as the beam profile is more spread out. The measured focal point has almost converged to the designed focal point by 20° .

As the detection coil has a designed focal length of 41 mm (figure 3.3) due to its different placement position, the same modeling was also run for a set of coils with apertures angles from 10° to 20° but a designed focal position of 41 mm. To

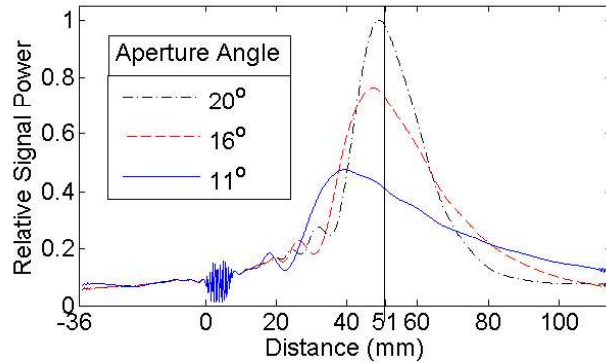


Figure 5.7: Focal axis profiles along $y = 0$ for coils with three different aperture angles, all designed to focus at 51 mm.

compare the results from the two different designed focal points, the focal position found for each model is subtracted from the designed focal position to give a focal offset, therefore showing how far the found focal point is away from the designed focal point. This is plotted in figure 5.8 as a function of aperture angle. The two different curves represent the two different designed focal lengths as indicated in the legend. Both curves are very similar in shape, with slight variations due some small oscillating patterns showing up in the beam profile, which can be seen on close inspection of figure 5.8, particularly in the smaller aperture designs, causing the peak to vary in a few places. The FE model predicts a focal offset of 11 mm for the 11° aperture coil, which is an overestimate from the experimental offset of 8 mm, however, it predicts an offset of 1 mm for the 20° aperture coil, in close agreement with the experimental offset of just under 1 mm. It can be concluded that for aperture angles of 20° or more, the actual focal point position will be within an error of 1 mm from the geometric, designed focal point.

Having analysed the two coils separately they need to be tested as a single unit, since they are designed to work as a pair, with one generating the focused beam profile and the other detecting the curved wave front reflected back from an EMAT. This was done by scanning the EMAT pair towards an ‘infinite depth defect’, in this case the end of a 5 by 50 mm cross-section aluminium bar. The strongest reflection was detected by the detection coil at 51 mm, the designed focal point and the focal point of the detector coil, as shown in figure 5.9. This indicates that the focal point of the detector coil dominates the system. This can be understood from considering the extent of the beam spots of both coils along their focal axis, as shown in figure 5.5. While the 11° coil has its strongest generation point at 41 mm, there is very little signal generated by the 20° coil at this position. It can therefore be assumed that

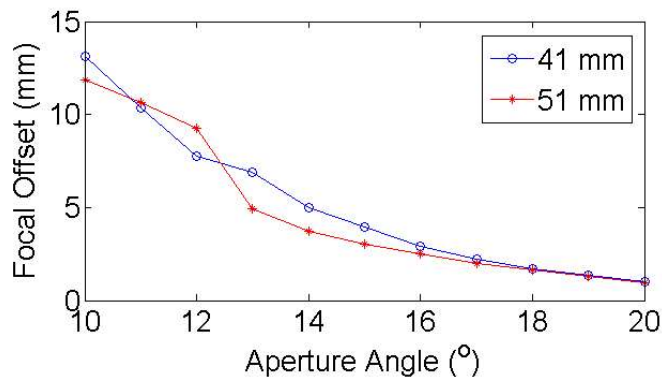


Figure 5.8: The change in focal position of the EMAT with respect to the designed focal position (or focal offset) as a function of the coil aperture angle. The two different designed focal lengths are indicated in the legend.

the 20° coil has correspondingly poor detection capabilities at 41 mm. At 51 mm the 20° coil can be assumed to have optimum detection in correspondance with its generation capabilities, as shown in figure 5.5. For the generation coil at 51 mm, while it is not the optimum point of generation, there is still a significant amount of signal generated due to its longer beam length, and so this is preferentially detected.

Figure 5.9 shows the $y=0$ focal axis profiles from the laser vibrometer scan, the FE model for an 11° aperture, and the EMAT-EMAT scan against the aluminium end wall, all aligned to a zero displacement position at their respective focal points to compare the beam profiles. The EMAT-EMAT data has a double focus, as the generator coil and the detector coil are both focused, and so the FE and the laser data have been squared to allow for the focusing effect in detection that neither considers. The profiles are in good agreement, however, the FE model underestimates the attenuation over distance.

All this shows that consideration needs to be made of the coil design, particularly the aperture angle, when designing a focal point. A new set of focused meanderline coils were made, with aperture angles ranging between 15 and 19°, shown in figure 5.10. This means that the focal point of the generator and detector coils will be much closer aligned, allowing for both coils to be operating at their optimum focal point. The coil apertures were made to fit to the magnet shape to maximise the use of the space under the magnet. The design is shown in figure 5.10.

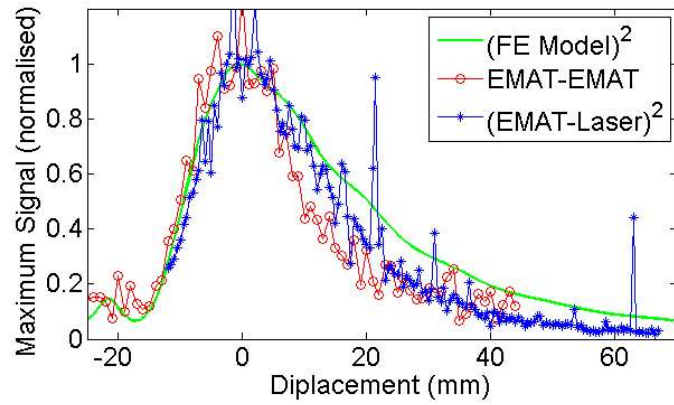


Figure 5.9: Signal profile comparisons down the focal axis of the coil, as measured with the other EMAT coil, and the laser vibrometer, and the simulation of the laser vibrometer.

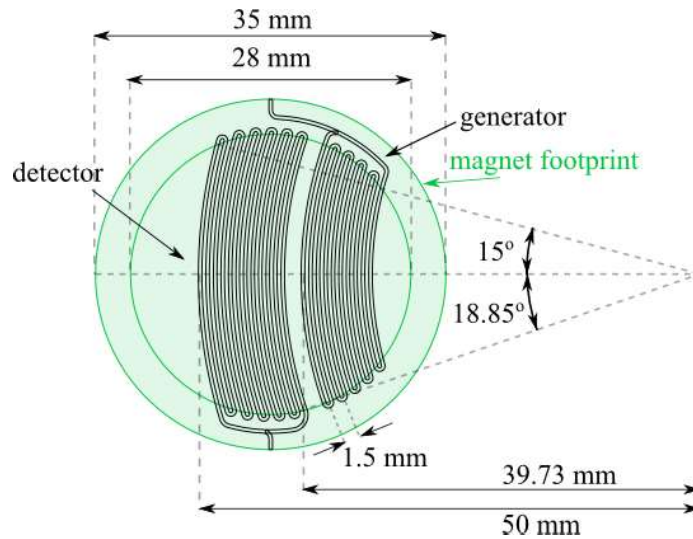
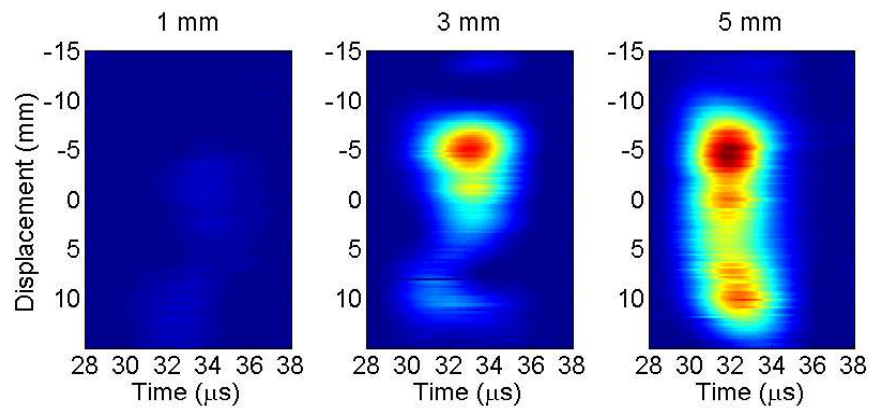
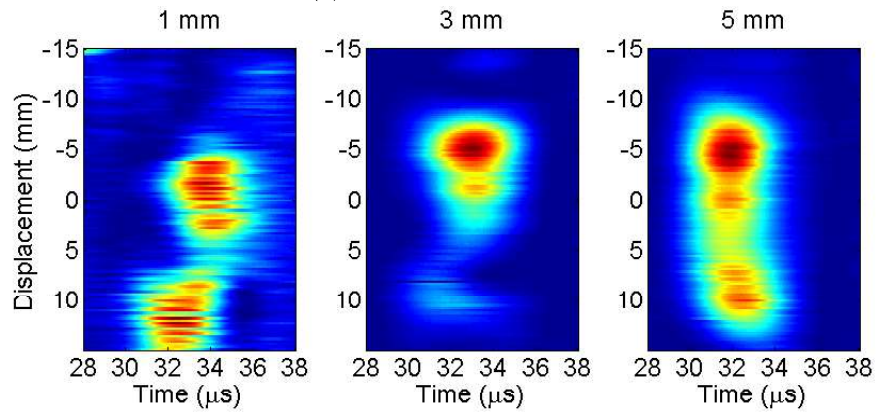


Figure 5.10: Focused meanderline coil schematic, with less disparity in the aperture angles to improve the focal point alignment. The green outer circle indicates the magnet placement. The green inner circle indicates the edge to which the meanders extend.



(a) Overall normalisation



(b) Individual normalisation

Figure 5.11: Meanderline inline scans of a set of slot defects, all 1 mm in depth, and 1 mm in widths, lengths given in the headers. Red indicates maximum detected signal, blue indicates no signal. a) the top row of graphs are normalised collectively to the maximum signal found in the top right hand graph, the 5 mm length defect. b) the lower three graphs have been individually normalised with respect to the maximum signal detected within each graph.

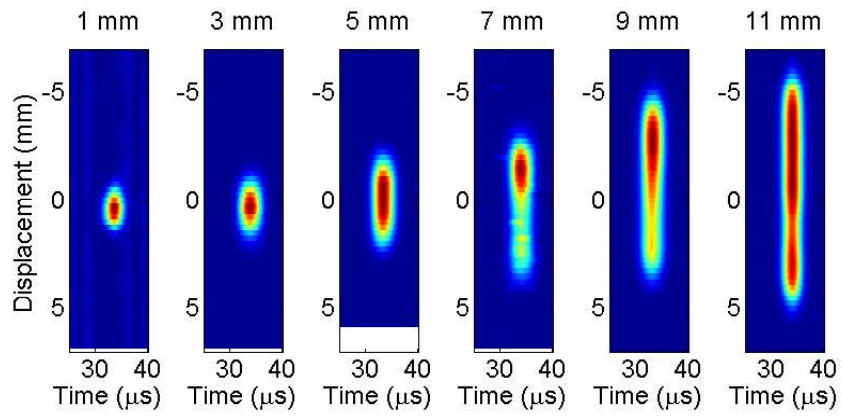
5.3 Defect Detection

Both the unfocused meanderline EMAT pair, and the new design focused EMAT pair shown in figure 5.10, were employed to scan the machined slot defects detailed in section 3.3. The scanning set up is shown in figure 3.11, with the back edge of the generator coil at a distance of 51 mm from the defect leading edge, scanning in the transverse direction. This leads to an expected arrival time of the Rayleigh wave of approximately $32 \mu\text{s}$. Figure 5.11 shows some example data from the unfocused EMAT represented as brightness scans (or B-scans). The data is presented twice as the first set (a) shows the data normalised to the overall maximum found for all defects (shown in the third scan of the 5 mm length defect), and the second set (b) shows the data individually normalised to the maximum found within each scan. The y-axis shows the displacement of the center of the detector coil from the center of the sample (and hence the center of the defects) as it is scanned across the sample parallel to the long edge of the defect. The x-axis shows the time, and the colour data shows the normalised signal power detected by the EMAT at that position and time, with red indicating a detected reflection, and blue indicating no reflection.

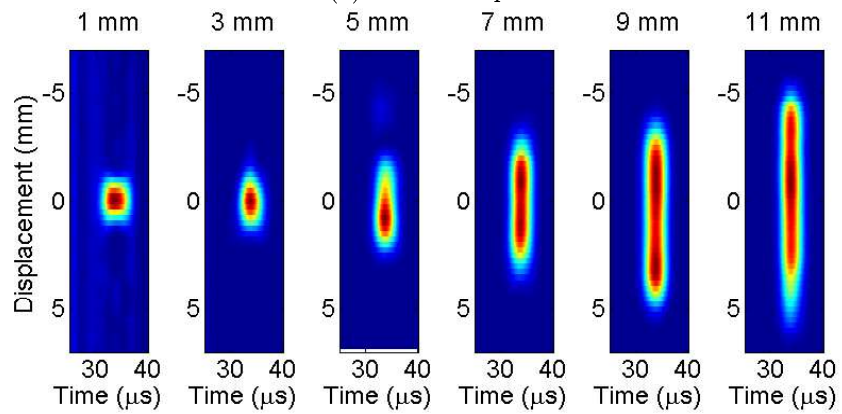
The unfocused EMAT does detect all of the defects, however, the signal for the smallest, 1 mm depth, 1 mm diameter drilled hole is weak and noisy compared to the others. The extent of the detected signals does not appear to have any correlation with the defect length, with all three scans showing reflections over a similar distance, which corresponds to the beam width (figure 5.1) and therefore the coil length (figure 3.1). The same scans were run for similar defects but with depths of 1.5 and 2 mm, with very similar results, showing that an increase in depth does not provide increased spatial resolution; defects smaller than the beam width will show strong reflections regardless of where they are incident within the beam width.

The focused EMAT pair was also used to scan all of the billet defects outlined in the methodology. The lengths of the defects were varied from 1 to 11 mm in increments of 2 mm, all at depths of 0.5, 1.0, 1.5, and 2 mm, making for a total of 24 different defects. Figure 5.12 shows the scans from the 0.5 mm and 1.5 mm depth defects. The white space at the end at some of the scans is where no data was taken as the scans were shorter than other scans. All of the defects are detected with up to 30 dB signal to noise ratios, despite all data being taken as single shot, with no averaging. The images have been individually normalised to their peak signals, as with the data in figure 5.11b) for the unfocused EMAT.

At each displacement position in figure 5.12, the maximum reflected signal power was measured, and this is plotted for the 0.5 mm depth defects in figure 5.13,



(a) 0.5 mm depth



(b) 1.5 mm depth

Figure 5.12: Focused meanderline B-scans of a set of slot defects, all 1 mm in width, lengths given in the headers, depths given in the captions.

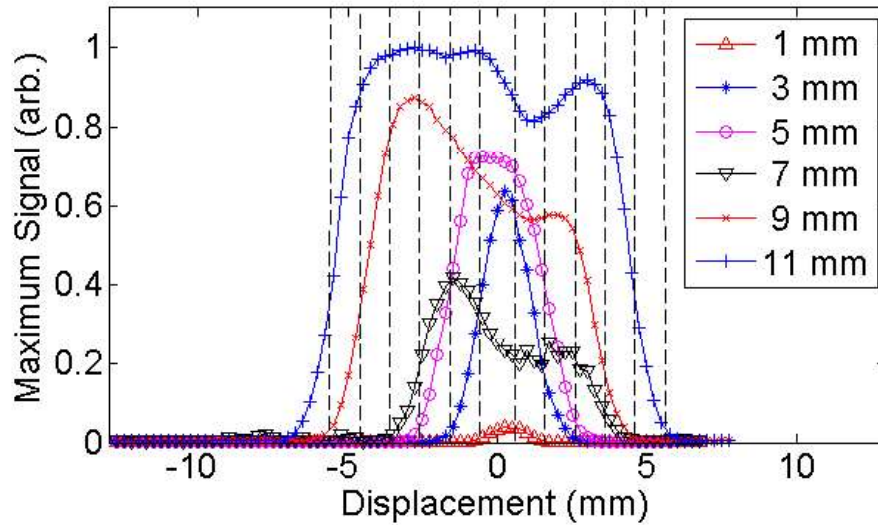


Figure 5.13: The maximum signals detected from the B-scan data shown in figure ??, lengths given in the legend, all at a depth of 0.5 mm. The dotted vertical lines show the expected locations of the defects.

with all the signals normalised with respect to the strongest overall signal so that the profiles can be compared. As expected, the strongest signals are returned from the largest defect, and the weakest from the smallest defect. The reflection from the 1 mm length defect is particularly weak because the defect is significantly smaller than the 3 mm beam width of the Rayleigh wave at the focal point, however, it is still detectable. The 7 mm defect has a surprisingly weak reflected signal, weaker than both the 5 and the 3 mm length defects. This is due to variations in the EMAT lift-off. The set-up was designed such that the EMAT should be scanned in contact with the sample surface, however, with the automated scanning system that was used, this can cause it to catch on the sample surface, and the pressure of the contact was variable. The inconsistencies in peak signal strength along the length of the defects individually, especially noticeable on the 7 and the 9 mm length defects, might also be an effect of the EMAT catching on the sample, or variations in the roughness of the defects and the sample. An industrial scanning system would mitigate some of these variations.

The finite width of the beam profile, 3 mm, means that each defect shows a rising edge as the beam moves from partially impinging on the defect, to fully incident. The rounded ends of the defects from the cylindrical milling also add to this effect. As such there is not a precise edge which can be used to identify the defect location. Instead, the defects were considered individually, normalising the signal

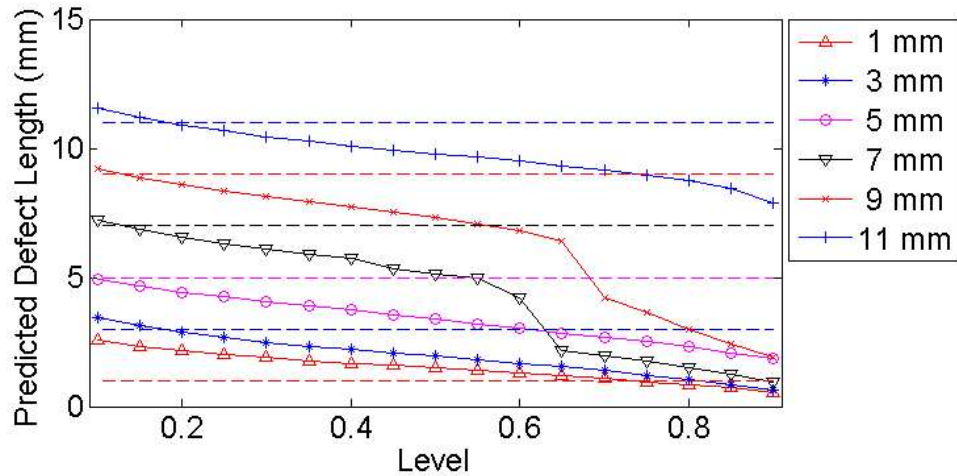


Figure 5.14: Predicted defect lengths for the 0.5 mm depth defects as dependent on the signal level as a fraction of the maximum signal used for the measurement. Dotted lines indicate the actual defect lengths.

maximum to 1 for each separate defect. An arbitrary threshold signal level was then chosen, ranging from 0.1 to 0.9 of the signal maximum, and the position at which the signal crossed that level defined as the end of the defect. These defined ends were then used to give a predicted defect length, which is plotted in figure 5.14. The dotted lines show the actual defect lengths. It can be seen that for all of the defects, except for the smallest, 1 mm cylindrical hole defect, the predicted length only matches the actual defect length when the threshold is set at a very low level, between 0.1 and 0.2. The level that gives a correct prediction for the 1 mm defect, conversely, is around 0.7, due to the fact that it is significantly smaller than the beam profile, therefore behaving as a specular scatterer. This analysis was performed additionally for all the other depth defects, all of which showed similarly low thresholds.

A typical change used in ultrasound to define a detectable signal is a change of 6 dB [17]. This corresponds to a change in power of 0.5 as a fraction of the maximum. It can be seen from figure 5.14 that this will underestimate all the defect lengths. The signal level at which the predicted length matches the actual defect length was found for all defects, including the depths of 1, 1.5, and 2 mm which are not pictured. Finding the levels which gave the actual defect length for all the defects scanned, and then taking the average of all of these, gives 0.3 as a suitable threshold.

Figure 5.15 shows the difference between the measured defect length, and the

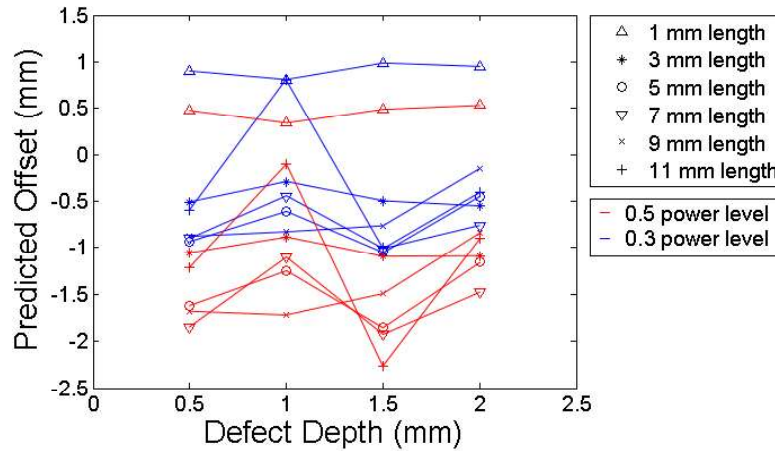


Figure 5.15: The error in the predicted defect length measurement, found by subtracting the predicted value from the actual value, depending on the change in signal level used to indicate the presence of a defect.

actual defect length (the predicted offset) as a function of the defect depth for both a 0.5 signal change (in red), and the calibrated 0.3 signal change (in blue), for all defects measured. The calibrations are skewed by the 1 mm, cylindrical hole defects, which are consistently under-estimated in size. This is because they are smaller than the beam profile and act as a point scatterer for the ultrasound, causing the strong discrepancy from the other defects. Despite this, using the calibrated level of a 0.3 change in signal all of the defect lengths are predicted with an accuracy ± 1 mm, and the measurements are not affected by the depth of the defect, despite some of them being significantly shallower than the 1.5 mm wavelength of the ultrasound. This indicates that if an initial length measurement of a defect is made using the 0.5 power level and then this initial prediction is used to choose the correct calibration level, the error can be reduced to ± 0.5 mm.

5.4 Conclusion

A standard meander-line coil design has been presented, with a 1.5 mm pitch, showing that the beam profile has a wavefront length approximately equal to the length of the coils, with no dispersion. It has been employed with a second standard meander-line coil in a pseudo-pulse-echo configuration to detect surface defects down to a 1 mm depth, 1 mm diameter drilled hole in aluminium, but cannot be used to size these defects. A focused version of the coil pair has also been presented. The focal position and size of the beam is dependent on both the curvature of the coils and

the size of the aperture angle used. It has been found through experimental data and FEA that aperture angles under 20° focus closer to the coils than is expected from just the geometric curvature, but by 20° the focal point is within error of the geometric focal point. The beam at the focal point has a width of 3 ± 1 mm (perpendicular to the focal axis), which is much smaller than the coil extent of over 20 mm. This focused design has been shown to detect surface defects down to a 0.5 mm depth, 1 mm diameter drilled hole, and to be able to predict defect lengths with an accuracy of ± 0.5 mm with accurate calibration. This could be used to size defects which are hard to measure visually, e.g. under a paint layer.

Chapter 6

Characterisation and Defect Detection Capabilities of Focused and Unfocused Pitch-Catch Racetrack EMAT Designs

A variety of transmission EMATs have been designed and built using a generator and detector coil separated by a distance on the order of 10's of mm, and used to study the transmission of surface waves over these set distances. The transmission technique allows for placing the EMAT coils further apart from each other than the designs in the previous chapter, reducing the interference found between the coils. This can be done with the previous meander designs, but that would require a long travel distance for the ultrasound wave, subjecting it to more material attenuation, to keep the two coils sufficiently far apart. The transmission designs used instead, based on racetrack or linear coil designs, decrease the total distance travelled for the wave, while also moving the coils further apart, because the designs are more compact. Transmission designs also allow for the additional measurement of the changes in amplitude and frequency content of the transmitted signal which can be used to measure the depth of a defect [121, 138].

The racetrack and linear coil designs were used in this work to simplify coil construction, as opposed to the complex meander line designs of the previous section, and with a view to finding designs with improved lift-off capabilities, as explored later in chapter 8. They also give a wider bandwidth of frequencies, allow-

ing for better analysis of the changes in transmitted frequency content due to the defects [121, 138]. For the sake of maximising signal strength, most of the following designs were built intending to put the coils as close together as permissible by the dead time interference. In the case of the racetrack designs this allowed them to maintain the advantage of remaining under the same magnet as this facilitates simpler scanning and alignment. The frequency response of the coil profiles has already been explored in chapter 4.

6.1 Unfocused Racetrack Coil Designs

Racetrack designs are broader band than meanderline coils. The typical frequency of operation is influenced by the width of the coil, as discussed in chapter 4, with higher frequencies requiring narrower width coils and consequently giving reduced signal strength. Figure 6.1 shows the laser vibrometer wave field image (see Methodology) generated by the unfocused racetrack design (outlined in figure 3.6a)), used in conjunction with a 25 mm long, 10 mm wide, 20 mm height, cuboidal magnet, with a 1 MHz, 3 cycle driving signal. The $X=0$ mm position in the scans is just onto the edge of the magnet. The coil center is positioned off the left of the scan at -3 mm. The Y extent of the coil is slightly off center, with the coil center at approximately 22 mm. The Y extent of the coils is 24 mm, and it can be seen that the Y extent of the generated wavefront is approximately the same as the coil length, covering from $Y=10$ to 32 mm. However, the Y extent of the signal power does become a little more concentrated to the center of the beam by the final image shown at $27 \mu\text{s}$. The signals for this EMAT are weaker than the meanderline EMATs, and the higher noise level made a time summed image, such as those presented in section 5.1, too noisy to be of use. Figure 6.1d) e) and f) show the cross-correlations of the data shown in a) b) and c), showing the positions of the signal wave packet.

This is as expected for an unfocused coil. The signals can be used for defect detection, however any defect within the vertical range of $Y=10$ to 32 mm will return a reflection, giving poor spatial resolution. Defects with a Y extent much smaller than the wave front will also only block a very small proportion of the wave front, leading to difficulty in detecting the change in transmitted signal. Focusing of the beam profile should lead to improved Y resolution and also better SNR for small defects due to the concentration of the wave front.

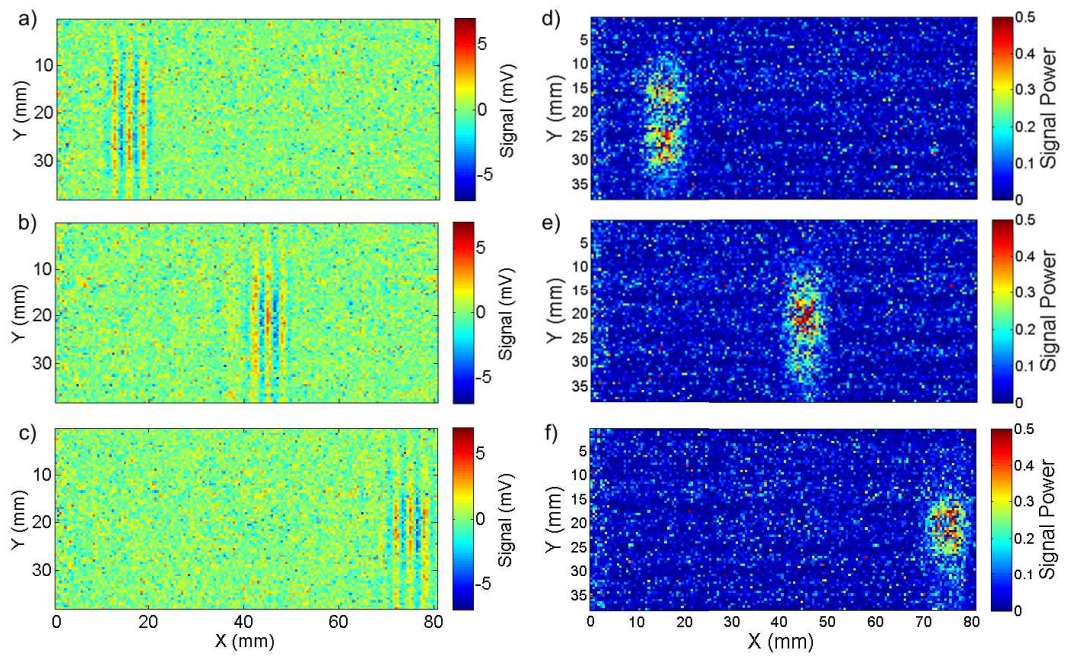


Figure 6.1: Unfocused racetrack beam profile, driven at 1 MHz. a), b), and c) show the detected signals, d), e) and f) show the signal power. a) and d) show the data $7 \mu\text{s}$ after signal generation, b) and e) $17 \mu\text{s}$ after, and c) and f) $27 \mu\text{s}$ after signal generation.

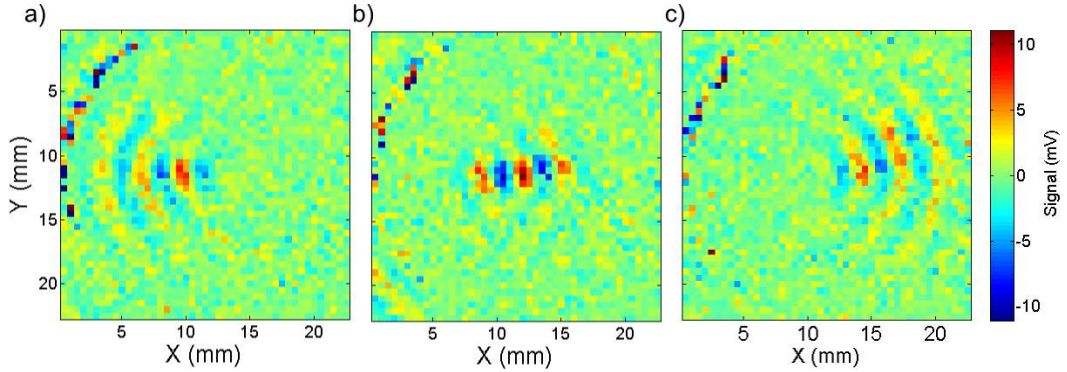


Figure 6.2: Focused racetrack beam profile within the 23 mm magnet hole, driven at 1 MHz. a) $3.7 \mu\text{s}$ after signal generation, b) $5.4 \mu\text{s}$ after signal generation, c) $7.1 \mu\text{s}$ after signal generation.

6.2 Focused Racetrack Coil Designs

This section covers the focused racetrack design shown in figure 3.7, section 3.1.2.

6.2.1 Wavefield Imaging

The coil pair first built (repeat constructions were used in some later work) was found to have a maximum detected signal when a 1 MHz driving signal was used. The beam created by this coil at 1 MHz has also been imaged with the laser vibrometer. The results are shown in figure 6.2. This was done in conjunction with a ring magnet with a larger inner diameter than the one detailed, figure 3.7, so that more of the profile could be imaged. The magnet had the same outer diameter, 35 mm, and the same height, 25 mm, however, it had a larger inner diameter of 23 mm, so that a 23 mm diameter area in the center can be imaged. The inner edge of the magnet can be seen, in particular in the top left of the images, where the angled magnet edge and change in height changes the focus of the vibrometer. There are no noticeable side lobes to the beam profile. The beam depth (X extent) at the focal point is $7.6 \pm 0.3 \text{ mm}$, and the beam width is $2.7 \pm 0.3 \text{ mm}$ (Y extent).

The coil pair were employed for defect scanning using a 2 MHz driving signal to improve the sensitivity to small defects, despite the reduction in signal strength. The wavefield was therefore also imaged with this driving signal, and also with the larger magnet used with the 10 mm central hole, to find the beam profile incident with the defects. This magnet is the same grade (N50) as the previous one, which a large increase in volume, hence a stronger field. The results are shown in figure 6.3. Although the EMAT system as a whole was found to generate a stronger signal at

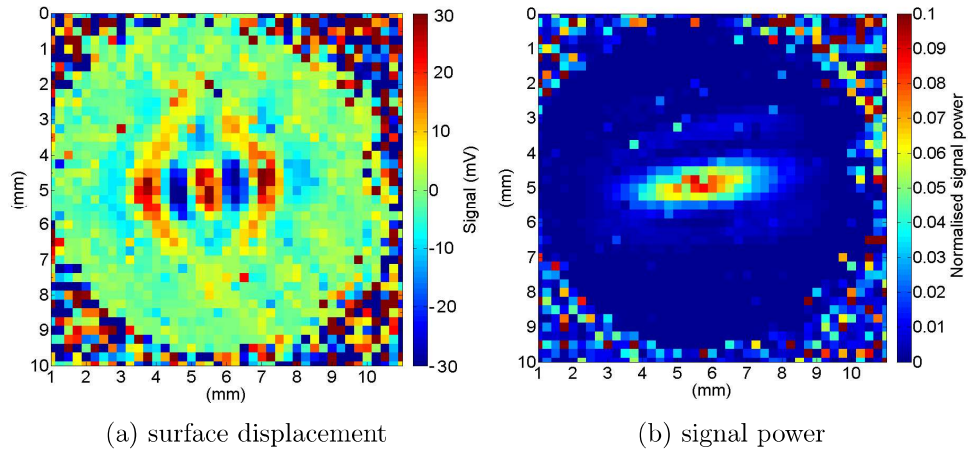


Figure 6.3: Focused racetrack beam profile within the 10 mm magnet hole, at $5.4 \mu\text{s}$ after pulse generation, driven at 2 MHz. a) shows the surface displacement, b) shows the signal power, as found by the appropriate cross-correlation and processing.

a 1 MHz driving signal, the wavefield image signals for the 1 MHz driving signal are weaker than those found for the 2 MHz driving signal. This is due to the large reduction in the volume of magnet used for the 1 MHz image which would correspondingly reduce signals generated and detected, and also differences in the laser alignment. The beam depth (X extent) at the focal point for the 2 MHz generation is 3.7 ± 0.3 mm, and the beam width is 1.3 ± 0.3 mm. The beam depth of the 2 MHz signal is roughly half the beam depth of the 1 MHz signal because the ultrasound wavelength is half that at the higher frequency. The beam width is also roughly halved, despite the fact that the aperture angle of the coils is the same, which is the main controlling factor of the focal effect. This shows that the ultrasound frequency is just as important a consideration as the geometry of the coils.

6.2.2 Defect Detection

A driving function of three cycles at 2 MHz, giving a 1.5 mm wavelength in aluminium, was chosen to give suitable frequency content for reliably detecting sub-millimetre depth defects, while still having a reasonably strong and undistorted signal (see chapter 4). The defect profiles are shown in figure 3.12 and the scanning directions are shown in figure 3.11b). Defects were artificially produced using a 1 mm diameter milling piece, giving rounded ends and a constant opening width of 1 mm. The lengths were varied as 1, 3, 5, 7, 8, and 11 mm, and the depths were varied as 0.5, 1, 1.5, and 2 mm, giving a total of 24 simulated defects. The

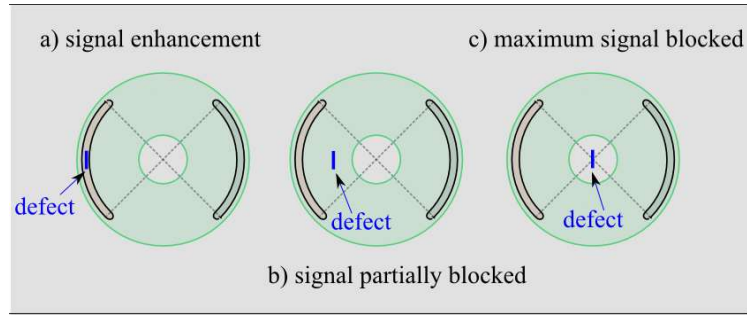


Figure 6.4: Schematic of in-line scanning of a defect using the focused transmission EMAT design.

lengths include the 1 mm diameter curved edge; the 1 mm length defects are hence cylindrical milled holes. A set of scans were performed, with two scan directions used; transverse (perpendicular to the focal axis) and in-line (along the focal axis), labeled in figure 3.11b). All data is taken in single shot (no averaging).

Figure 6.4 shows the three main stages of the in-line scan of a defect: a) the position where signal enhancement is seen (as discussed in section 2.1.4, figure 2.5), b) the transition through from a) to c) where the amount of signal being blocked gradually increases, and the c) the position where the maximum amount of signal is blocked. The second half of the scan then mirrors the first, as signal increases again, followed by enhancement as the other coil moves over the defect.

Figure 6.5 shows some examples of B-scans from in-line scans of three different length, 2 mm deep, defects. The B-scans show scanning position along the x-axes, time along the y-axes, and the colour scale shows the signal power. Each image has been normalised to the maximum power during that scan. When there is no defect between the two coils a strong signal power will be measured. However, when a defect is present the power transmitted will be reduced, and if the defect is of sufficient size and in the correct position no signal will be transmitted. This effect is shown clearly in the figure; for the 1 mm length (cylindrical) defect even at the focal point there is still some transmission around the defect as it is smaller than the beam width, nevertheless, the defect is still detected by a reduction in transmission. For the longer defects, a region of minimum signal power is found with the length of this region dependent on the length of the defect relative to the focal beam area. Deep defects wider than the transducer width will block all signal once it is between the coils (seen later in chapter 7).

When the generator or detector coils pass over the defect, signal enhancement can be seen; This is the interference pattern and enhancement of signal power close to the defect (e.g. between 10-15 mm on the scan of the 5 mm length defect,

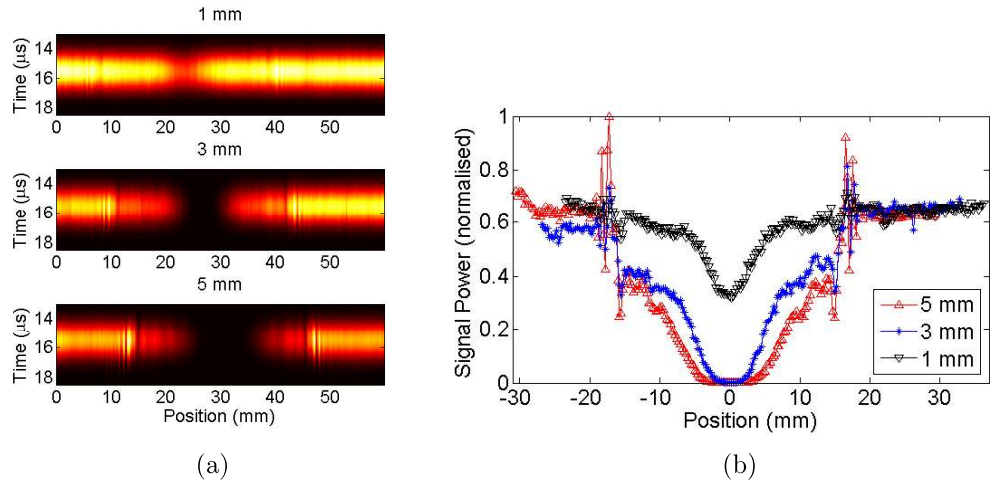


Figure 6.5: a) In-line scans of three different length, 2 mm depth defects. Lengths indicated in the headers. Each scan has been individually normalised to its own maximum. b) Maximum signals from the in-line scans of three different length, 2 mm depth defects, from the data in part a). Lengths indicated in the legend.

figure 6.5a). This effect has been studied in several works [51, 50]; the enhancement is due to interference between the incident Rayleigh wave and the reflected and mode-converted waves from the defect. For the 5 mm length defect the enhancement is much stronger than for the shorter lengths, as it is reflecting more of the incident waves, and covers a larger length when it is underneath the coils.

The maximum signal power within the expected Rayleigh wave arrival time was measured at each scan position of figure 6.5a and is shown in figure 6.5b, with a scan position of 0 mm now set when the focal beam is at the center of each defect. This shows the enhancement, with sharp signal spikes around ± 15 mm from the central position when the coils are incident over the defect, and the gradual blocking of the signal in the center. Longer defects do block more of the signal earlier in the scan, and this effect could be used for defect sizing. However, this effect is largely dominated by the width of the focal point, and so is not the most accurate way to size the defects. It also does not make optimal use of the focusing effect.

Once a defect is found, transverse scans (depicted in figure 3.11b)) can be done to ensure that the focal point is always aligned with the defect, giving optimal contrast for sizing. Example B-scans are shown for 0.5 mm depth defects in figure 6.6, with position now shown on the y-axes to indicate the change in scan direction. No signal enhancement is expected for these as the coil never passes over the defects. Again, the data has been cross-correlated and individually normalised

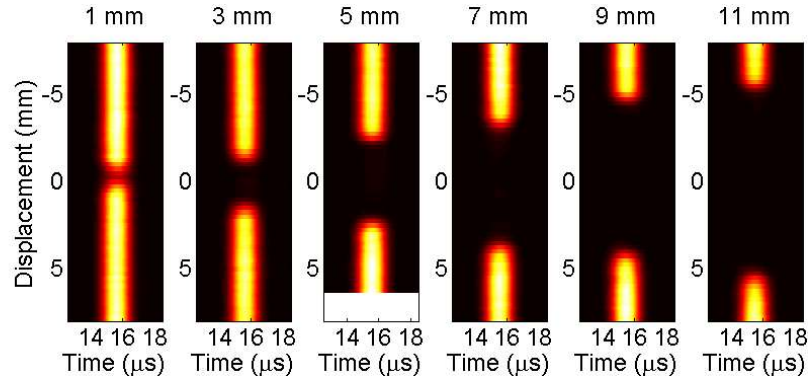


Figure 6.6: Transverse scans of six different length (indicated in the headers) 0.5 mm depth defects. Scans are individually normalised. The 5 mm length scan has a shorter scan length and the white segment at the end of the scan represents the area where no data was taken.

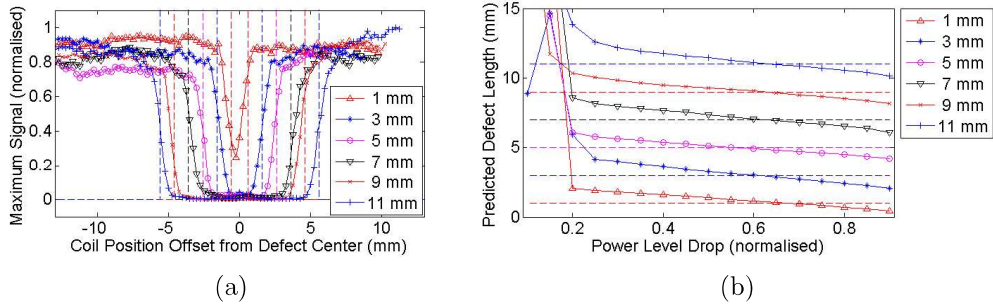


Figure 6.7: a) Maximum detected signal power for six different length 0.5 mm depth defects. b) Predicted defect lengths depending on the signal level drop defined as sufficient to indicate the presence of a defect.

to the maximum signal in each plot, and all defects are detected. Figure 6.7 a) shows the maximum signal power measured in the Rayleigh wave arrival time window at each position, normalised to the maximum signal for all scans. Vertical dotted lines show the actual defect lengths. As can be seen, all of the defects block almost all of the signal at the center except for the 1 mm diameter defect which still allows some noticeable transmission, as it is narrower than the beam width. There is still transmission beneath these shallow defects, as would be expected from the ultrasound wavelength, however the cross-correlation technique adds a strong preferential enhancement to stronger signal, making it difficult to measure this transmission using this signal processing technique.

A drop in normalised signal power of 0.5 corresponds to a 6 dB drop, the usual threshold for ultrasonic signal detection [17]. However, as before, as the defects

have rounded ends and the beam does not have a point-like focus, a 6 dB signal drop (or half power point) is not necessarily the best for measuring defect lengths. A calibration is done similar to that outlined in the previous chapter (section 5.3), except that the power level drop is defined as one minus the maximum signal plotted in figure 6.7a), instead of looking for a rise in signal power. The relationship between an arbitrary threshold and the consequential calculated defect length is shown in figure 6.7b). The actual defect lengths are indicated by the dotted lines. It is clear that, unlike the reflection testing where a low threshold (0.3) was needed, requiring such a small drop will lead to a noisy measurement and higher rate of false calls. However, requiring a large drop in signal power before a defect is indicated will give an underestimate of the length.

To compare data using this method from all the different defects scanned, the power level drops at which the predicted lengths match the actual lengths (where the data lines in figure 6.7b) intersect with the dotted lines) have been interpolated from the data and are shown in figure 6.8a. The 0.5 mm depth defects have a consistently lower optimum power level drop; for these shallow defects, some signal is always transmitted, giving reduced power level drops compared to the deeper defects. However, the figure indicates that a 0.7 power level drop would give reasonably accurate predictions for all defects without assuming any knowledge of the defect depths. This corresponds to $1 - 0.3$, the threshold found for reflection detection in the previous chapter. Figure 6.8b shows a direct comparison of the difference between the actual length and the predicted length of the defect (the y-axis, labelled predicted offset) when power level drops of either 0.5 (red) or 0.7 (blue) are used to estimate the lengths. It can be seen explicitly that a 0.5 level drop consistently overestimates the defect length for every measurement, and there is a rising trend with the defect depth, with the deeper defects showing the most inaccuracy. The 0.7 power level drop underestimates the lengths of the 0.5 mm deep defects, and slightly overestimates the lengths of the 1-2 mm deep defects, however, the consistency is improved, and the overall spread of error is reduced to within ± 0.4 mm.

6.2.3 Frequency Depth Calibration

At 2 MHz, even for the shallowest defect, there is only small amplitude transmission under or around the defects, as can be seen from the almost complete loss of signal power in figure 6.6. This is highly beneficial for ensuring defect detection, but for depth gauging some transmitted signal needs to be measured [138], otherwise all that can be said is that the defect depth is greater than the main ultrasound wavelength. The EMAT was used to scan the defects using a three cycle, 1 MHz driving signal,

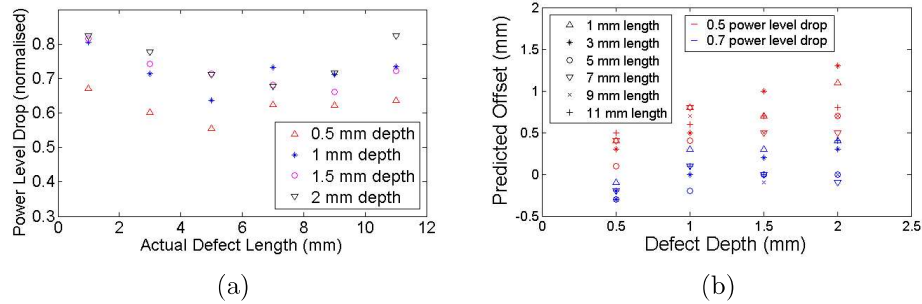


Figure 6.8: a) power level drop at which the predicted defect length matches the actual defect length for a range of defects. b) The difference between the actual defect length and the measured defect length (predicted offset) when either a 0.5 or a 0.7 power level drop is used, plotted as a function of defect depth.

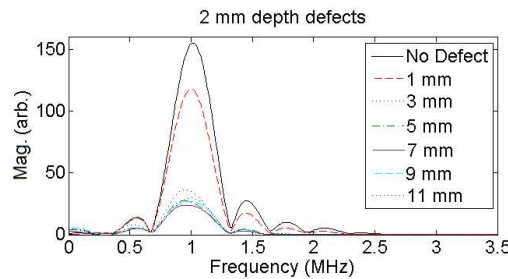


Figure 6.9: Frequency content of the detected signals after transmission under a variety of defects of depth 2 mm. The defect lengths are shown in the legend.

as this not only gives a much stronger signal, but is also more likely to be partially transmitted underneath the defects due to its longer ultrasonic wavelength. This was done using the largest ring magnet presented earlier for maximum signal. Data were taken at a single position for each defect with the focal point aligned to the center of the defect, and 16 averages were used.

Example frequency content from some of the resulting signals can be seen in the fast Fourier transforms (FFTs) in figure 6.9 for defects of depth 2 mm. There is significant transmission around the 1 mm defect, but for the longer defects a near-constant frequency content is measured. The overall shape of the FFTs with their set of peaks are due to the finite length of the signal being analysed. Analysis looked at the peak magnitudes in three of the frequency ‘lobes’; low frequency (0.35 - 0.67 MHz), main lobe (0.67 - 1.33 MHz), and high frequency (1.33 - 1.65 MHz), as a function of defect depth.

The shortest defects, 1 mm and 3 mm, are smaller than, or close to, the size of the beam width (~ 3 mm at 1 MHz) and so were excluded for calibration. The reference signal (no defect) was used to normalise the data in each frequency lobe.

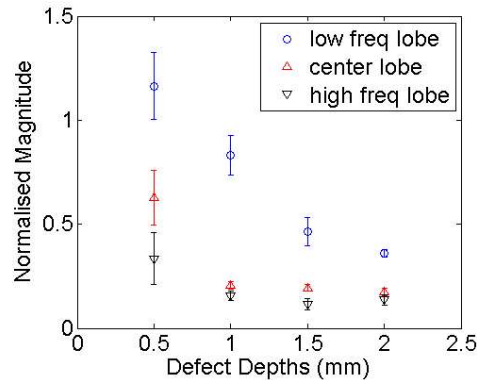


Figure 6.10: Relative change in frequency location of maximum magnitude for the low frequency, center frequency, and high frequency lobes. The magnitudes were normalised to that for ‘no defect’.

The maximum magnitude for each frequency lobe was then found for each defect. Defect length was found not to affect the transmitted frequency content for defects of 5 mm and longer. As such, the magnitude data from all defects of the same depth but different lengths was averaged to give a single magnitude in each frequency range for a single defect depth. The maximum magnitude in each frequency region (low, central, and high frequency lobes) for each defect depth is plotted as a function of depth in figure 6.10. As expected, all of the frequency peaks are increasingly attenuated with increasing defect depth. The high frequency lobe shows the most attenuation, while the low frequency has the least relative attenuation. This could be used as calibration curves to predict defect depths [121, 138].

6.3 Focused Four Coil Racetrack Design

With some types of defect and samples (such as RCF in railway tracks) the mechanism that causes the defect also dictates the orientation of its growth. However, this is not always the case. If a narrow, crack-like defect happens to be orientated end-on to the transducer beam, it may not be detectable, even if the defect has significant spatial extent in the other dimensions. Typically, crack-like defects are detectable from straight-on to the transducer up to around 45° at best, depending on the size of the defect. One solution is to perform at least two scans with the transducer rotated 90° between scans to ensure that reflections or changes in transmission are achieved, and improve the chances of a favorable defect orientation. This is, however, a time consuming solution, especially as for full coverage more than two orientations of the transducer are necessary.

Figure 3.8 shows the schematic for a four coil version of the EMAT design presented in the earlier sections of this chapter, with all coils equivalent. It can be used as two separate transmission coil pairs, to perform the equivalent to scanning in two different orientations but without the need for a separate second scan. It can also be used as a single generator with three detector coils. To see how the latter arrangement performs with different orientations of defect, the EMAT was set up with the focal point at the center of a small, 0.2 mm width, 2 mm length, 1.5 mm depth, laser machined slot defect and then rotated to see the effect of crack orientation on the signals on each of the three detector coils. A 1 MHz driving frequency was used in this case for improved signal strength.

The scanning set up is shown in figure 6.11, with 0° defined as having the wave propagation direction parallel to the defect. The blue arrows represent some of the expected wave paths. Detector 2 will show full signal transmission at 0° and 180° as it is end-on to the narrowest part of the defect, but will lose signal gradually until the detected signal is at its weakest at 90° , when the longest extent of the defect is across the beam width. Detectors 1 and 3 should not receive any transmission, however, when the propagation direction is at 45° to the defect, detector 1 should pick up a reflection. It is also possible that there will be some diffraction from the defect. Detector 3 from 90 to 180° should mirror the signal from detector 1 for 0 - 90° , as detectors 1 and 3 are effectively switched over in this angular range.

The signal power measured by the three different detector coils is plotted in figure 6.12 as a function of orientation angle. Part (a) shows the data as a B-scan with the colour scaling showing normalised signal power from 0 (black) to 1 (yellow), the x-axes show the signal arrival time, and the y-axes show the angle of rotation. Part (b) shows the maximum signal detected during a time window of 15-18 μ s, matching the predicted arrival time of the Rayleigh wave, plotted as a function of angle.

The data from each detector has been individually normalised in both parts of figure 6.12. The transmitted signals measured by detector 2 are much stronger than the reflection / diffraction signals measured by detectors 1 and 3. For reference, the maximum signal in the raw data for each scan is 17.5, 67.1, and 16.3 mV for detectors 1, 2 and 3 respectively.

Detector 2 (transmission) behaves as expected; the strongest, unimpeded signal is measured at 0° and 180° , and the weakest signal is seen at 90° when the longest spatial extent of the defect is directly across the beam width. The strongest signals measured by detectors 1 and 3, arriving at around 45° for detector 1 and 135° for detector 3, are Rayleigh wave reflections from the defect, while the weaker

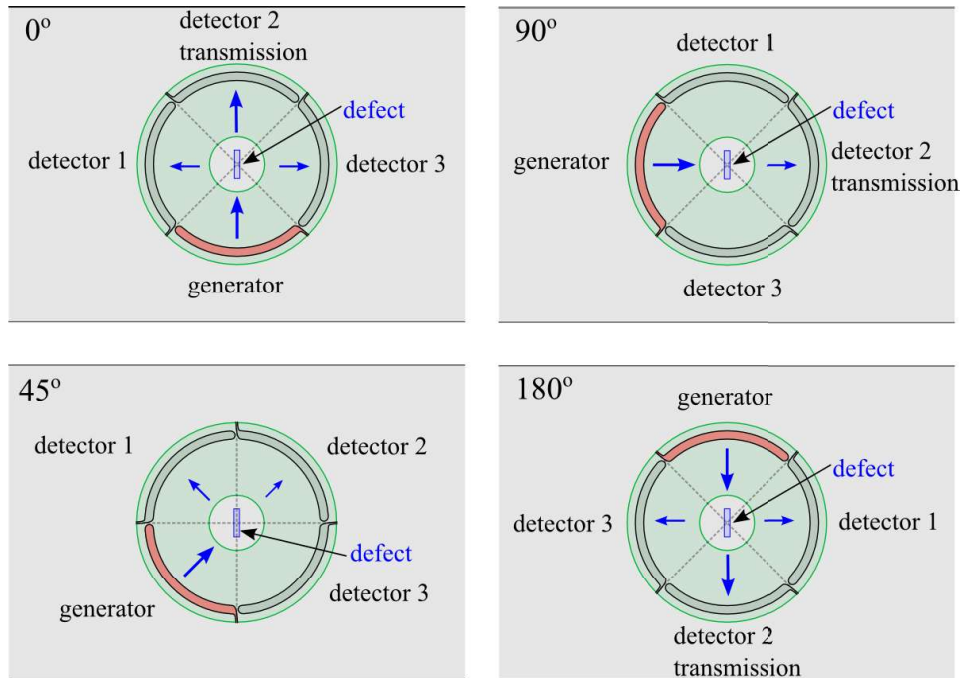


Figure 6.11: Rotational scan set up. The blue arrows indicate the expected wave paths. Green indicates the magnet placement. Red indicates the generator position.

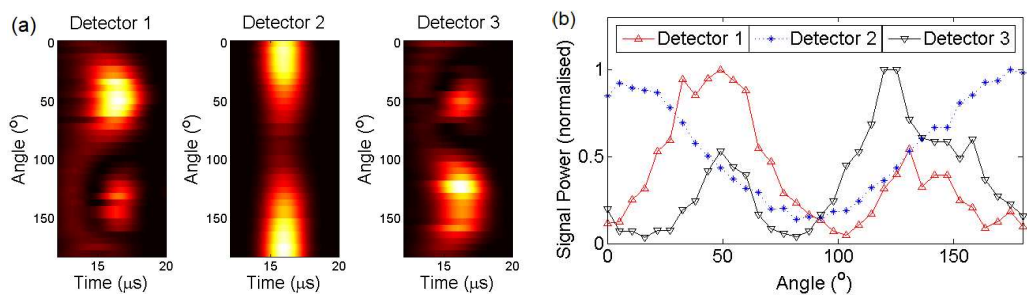


Figure 6.12: Rotational scan of a laser-micromachined defect, 0.2 x 2 x 1.5 mm. a) shows the Bscan images from the three detector coils, and b) shows the maximum signals extracted from the time sections shown in a). All data has been individually normalised to the maximum output from each individual detector coil.

signals, appearing at around 135° for detector 1 and 45° for detector 3, are likely due to reflection or tip diffraction from the defect end. The 45° angle has been simulated with PZFlex FEA to confirm the origin of this third signal.

Similar to the previous chapter, the generation coil was modelled by assuming a uniform magnitude force underneath the coil footprint, with the force vector applied perpendicular to each coil element. Figure 6.13 shows the out of plane displacement of the sample surface for the simulation at two instances in time, a) with the signal interacting with the defect, and b) just after the interaction clearly showing the three distinct signals that are detected. In a) the reflected wave off the defect is constructively interfering with the incident wave, creating a signal enhancement. The third interaction clearly occurs from the end of the crack closest to the generator, labeled in purple in both a) and b).

The angular ranges at which these signals are detected in the FEA data are in rough agreement with the experimental, even when only using a single point as a detector. Figure 6.14 shows the signal detected in the center of each detector coil (as shown in figure 6.13) over a range of 90° as the simulated defect is rotated in the center of the simulation. Detectors 1 and 3 show the Y velocity (vertical in figure 6.13) of the signal and detector 2 shows the X velocity (horizontal in figure 6.13) as these are the directions the EMAT detectors are most sensitive in those locations, as detector 2 is 90° rotated with respect to detectors 1 and 3. This agrees very well with the experimental data.

Similarly to the length measurements, the exact angular ranges over which a defect is reliably detectable and also sizable is dependent upon how much signal variation is classed as significant. Using the 70% power level drop used previously for length gauging (corresponding to a drop in the signal power from 1 to 0.3), the transmitted signals give a detectable defect over a 70° range centered on 90° . Using a 0.5 power level drop increases this range to 87° , however, the amplitude reduction will no longer give accurate sizing, as seen in the previous section. Reducing the power level drop further will give a better range if detectability is prioritised over sizing, but will be liable to a higher number of false positives.

The signals measured by detectors 1 & 3 can increase the angular detection range for detectability by applying a further constraint on the level of the reflected signal; for example, by defining an increase to a power level of 0.3 on these detectors as being sufficient to identify a defect, the range of detectability is increased to 16° to 170° over the range from 0° to 180° . This is sufficiently above the noise level to indicate that signals are reliably being detected, and in practice one would set a threshold on signal power above which an indication is given, to remove the

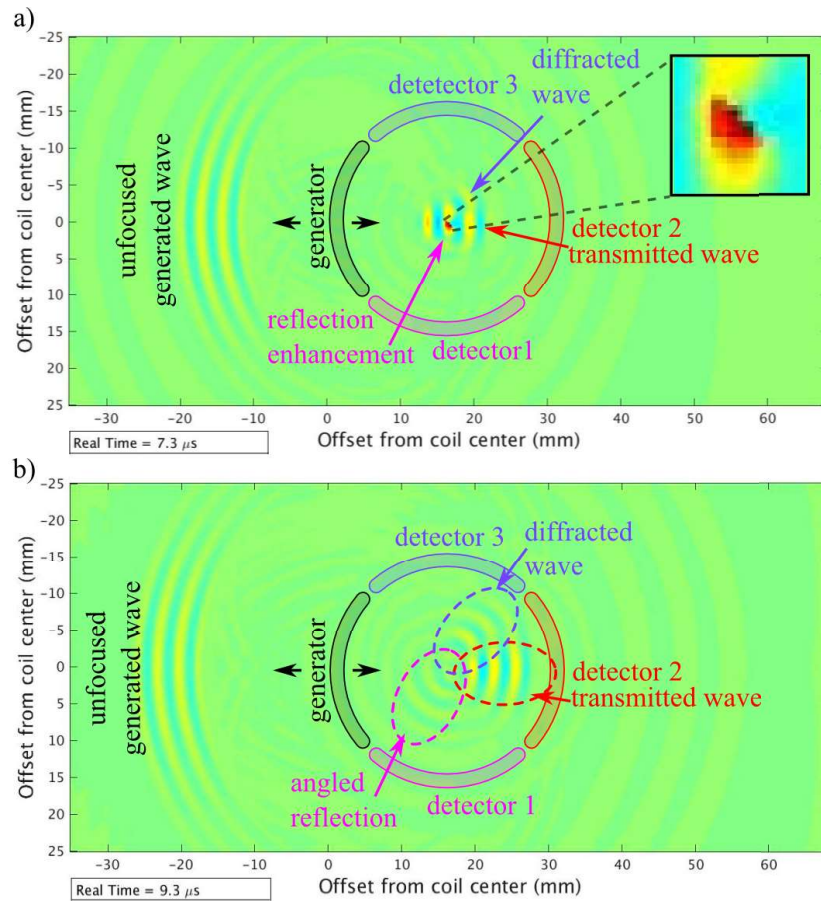


Figure 6.13: The FEA out-of-plane surface displacement of an aluminium block with a 0.2 mm width, 1.5 mm depth, 2 mm length surface breaking defect at the ultrasound focal point. The generator coil location is shown in black. The three detector coil positions are showing in pink, red and purple. a) is after $7.3 \mu\text{s}$ and the inset shows the inclination of the defect of 45° to the generator coil. b) shows the displacement after $9.3 \mu\text{s}$.

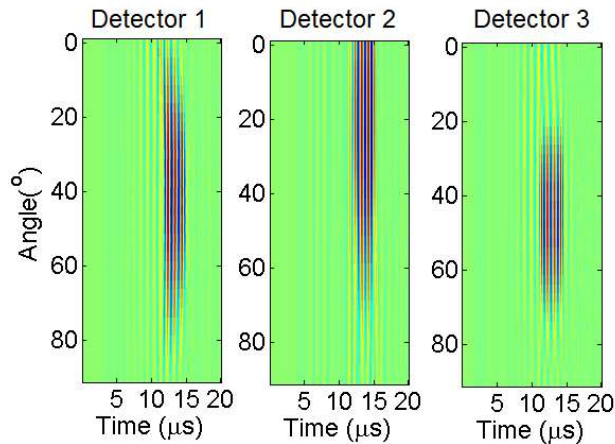


Figure 6.14: Simulated rotational scan of the experimental scan shown in figure 6.12. Detectors 1 and 3 show Y velocity, and detector 2 shows X velocity. The data is taken from just the center point of the expected detector locations (as shown in figure 6.13).

requirement for normalisation. Even within these detectable ranges, the signal drop for detector 2 will not reflect the true severity of the defect except close to 90° . However, considering also the information from the side detectors will indicate if the defect is likely to be at an angle other than 90° , and hence its severity is greater than measured. Rough surfaces and variations in lift-off can effect the signal transmitted, but can be identified by monitoring the current flow in the generation coil, and correspondingly compensated for [149].

A possibly more accurate 2D scanning technique could be to monitor the signals observed by detectors 1 and 3, and when significant signal is seen a rotation could be performed to find the point of weakest transmission to detector 2, giving the orientation of the defect and identifying the correct set-up for scanning to measure the length. The relative strength of detector 1 and 3 also gives a indication of which way the defect is orientated, so a full rotation need not be necessary. An alternative faster scanning technique still giving full angular coverage would be to scan using detector 1 and then detector 2 or 4 as generation coils, effectively performing the same scan twice at 90° , and only a 90° physical rotation of the transducer would be needed to create a 180° image. A five coil set could potentially be used, putting a fifth racetrack coil behind the generation coil to detection reflected signals as well as the transmission. Duplexing of the generation coil to act as another detector also was attempted, however the dead time from the generation noise was too long for any reflected signals from the focal point to be detected. A five coil set has not been trialled as the fifth coil will likely need to be significantly far away from the

generation coil to leave the dead time and the transducer will become quite large.

6.4 Conclusion

A standard racetrack EMAT is presented with a width of 1.5 mm. The beam produced is shown to have a wavefront length similar to the length of the coils, with no dispersion, similar to the standard meander-line design presented in the previous chapter. A focused design is then presented, using a 45° aperture angle, aiming for a small spot size, assuming a similar aperture dependence as found using FEA for the meanderline coil in the previous chapter. This has a beam spot with a width (perpendicular to the focal axis) of 2.7 ± 0.3 mm for a 1 MHz signal, and 1.3 ± 0.3 mm for a 2 MHz signal. The beam length along the focal axis is 7.6 ± 0.3 mm and 3.7 ± 0.3 mm for the 1 and 2 MHz signals respectively. Two focused coils in close proximity under a ring magnet in transmission were used to detect surface defects down to a 0.5 mm depth, 1 mm diameter milled hole, and to size defect lengths with an accuracy of ± 0.4 mm using accurate calibration. The transmitted signals show a frequency dependence with the defect depth which could be used as a calibration curve to measure defect depths. A four coil design is presented and shown to be able to detect a thin, 0.2 mm width, 2 mm length, 1.5 mm depth laser micromachined crack from any angle to the defect if two coils are used alternately as generators. Using three coils as detectors can also be used to compensate for the defect angle for defect sizing. Further work to investigate more coils with smaller aperture angles for higher resolution imaging and orientation predictions is recommended.

Chapter 7

Scanning Real Defects

Up until now the transducers presented have only been tested on well known, machined defects. For industrial implementation it is important that their capability on realistic defects is assessed. Real defects typically have rough internal surfaces, causing reflected signals to have less coherence. Real defects often have a more complex geometry, such as clusters of cracks and crack branching. An additional challenge is presented if the defects are partially closed, with the two surfaces pressed tight together with no air gap, often allowing ultrasound to transmit directly through the interface with little detectable effect. Defects of industrial interest to this work can be hidden beneath a metallic paint coating. The test of these new NDT techniques is to find such defects.

The focused meanderline reflection EMAT design (as figure 5.10) and the focused racetrack transmission EMAT design (as figure 3.7) were assembled into 3D printed cases and attached to automated X-Y stepping stages. 2D scans were then performed on a variety of real surface defects to test how they perform with rough defects, and hidden defects, testing the methods investigate with visible, ideal defects in chapters 5 and 6. Several different cracked samples are discussed within this chapter. The first section details all the samples and the nature of the cracks, and the following sections detail the scans done and their results.

It was found that both the reflection meanderline coils (presented in chapter 5) and the transmission racetrack coils (presented in chapter 6) were capable of mapping out a real pair of cracks in an aluminium billet, however the meanderline pair showed better resolution where the cracks were overlapping. The transmission technique is better suited to finding small (less than the distance between the coils, 25 mm) isolated cracks, as it cannot resolve multiple cracks within the beam profile. The meanderline coil pair was found to be unsuitable for scanning for small cracks

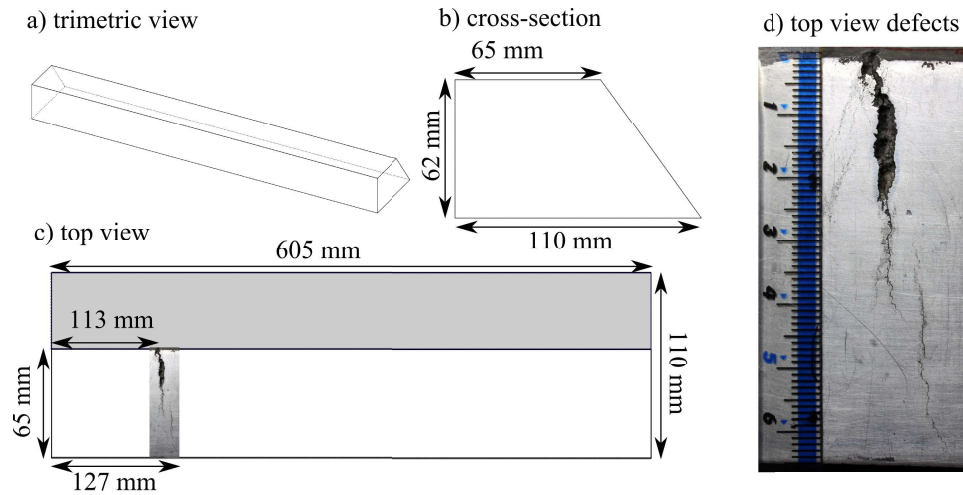


Figure 7.1: a) shows a to scale trimetric view of the billet, b) shows the cross section, c) shows the top view of the billet and d) shows a photograph of the defects taken from above, in the same orientation as c). The photograph from d) has also been superimposed into diagram c) to show the defect locations. Measurements are approximate, varying by a few mm across the length of the sample as it is not perfectly square.

in metallic steel due to the difficulty in aligning the transducer correctly against the sample attraction. The transmission pair performed well on a set of small (largely sub-mm) cracks in metallic steel, however not all of the cracks were detected due to damage in the samples, and the observations of a signal arrival time delay proved more accurate than observing signal reduction at a crack.

7.1 Surface Cracked Samples

Surface cracks were noticed by the company Alcoa in a large pillow shaped slab of aluminium prior to rolling. It was sectioned, and a sample was given to the University of Warwick Ultrasonics group for study. The top of the sample has been milled to be approximately flat, creating a good surface for inspection. The billet details are shown in figure 7.1. Alternating Current Potential Drop (ACPD) measurements were performed prior to this work, with the results reproduced in figure 7.2, the original measurements published by Dixon et. al. [125]. The ACPD measurements were performed by an untrained user. It is not certain how accurate these measurements are, despite the error bars given, as a by eye measurement of the crack depth at the two ends of the billets suggests that they are either shallower than the ACPD suggests, or they become so closed as to not be visible by eye.

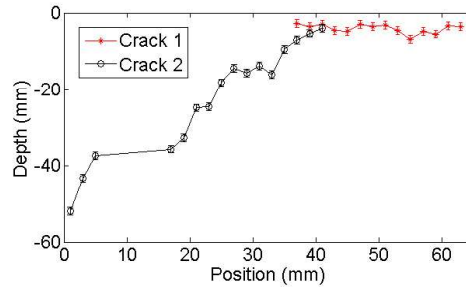


Figure 7.2: ACPD depth measurements of the aluminium billet cracks shown in figure 7.1 [125]. Position axis roughly corresponds to the distances shown by the ruler in figure 7.1d).

Further samples were provided as part of a collaborative project between Rolls Royce and the University of Warwick. A set of ferritic steel samples were provided by Rolls Royce containing realistic surface defects grown using thermal fatigue cracking by the company True Flaw [150]. The samples were all 200 mm long, 10 mm in depth, and widths were either 50 mm or 100 mm, as shown in figure 7.3. A set of four fatigue cracks were grown on each sample, roughly spaced out across the width, at a fairly consistent y value of either 100 mm (the sample center) or 50 mm (the sample quarter line) as indicated by the dotted lines in figure 7.3. The actual locations of the defect centers, and rough estimates of the defect lengths, are given in table 7.1. These defects were imaged using dye penetrant by True Flaw, with the images shown in figures 7.4-7.8 (note that the images provided are not to the same scalings). The cracks show up where the green fluorescent dye has been drawn into the cracks by capillary action, as detailed in section 1.2.1. It should also be noted that besides the cracks, sample damage can be seen as dark regions around the cracks, and red rust spots can also be seen. The surface was also not abraded prior to the dye penetrant inspection to avoid the risk of closing or eliminating the grown cracks, and there is significant surface roughness.

After cracking, all the samples except for one were then coated in a 40-60 μm thick metallic paint. This paint coating makes the use of contact ultrasonics such as piezoelectrics difficult due to the acoustic impedance mis-match between the paint and the metal, and the two layer behaviour, and its metallic nature causes issues for high frequency electromagnetic techniques such as eddy currents (where high frequency operation is typically required to image small defects on the sub-mm scale but high frequencies are then skin depth limited to the coating). Potential problems with the samples for EMAT inspection include the possibility of the coating not bonding correctly to the sample as the surface was not abraded prior to its

Sample	Coating	Width (mm)	X location (mm)	Y location (mm)	Length (mm)
W1128	coated	50	11.5	101	3.9
			21	99	2.7
			30	99.5	1.5
			39.5	103.5	5
W1129	coated	50	9.5	50	1.2
			20	49	4.5
			30	48.5	0.7
			40	48.5	0.8
W1130	uncoated	100	20	100.5	2
			40	98	1.1
			60	100	1
			79	103	6.1
W1131	coated	100	21.5	53.5	3.3
			40	49	1
			60	49	1
			80	48.5	4.6
W1133	coated	100	20	50	1.2
			41	50	5.3
			60	49	2.5
			81	48	1

Table 7.1: Summary of the ferritic steel samples (see figures 7.5 to 7.8), indicating whether or not they are coated, their widths (sample lengths and depths do not vary, figure 7.3), the X and Y locations of all their defects and the reported defect lengths from dye penetrant imaging. The defect depths are estimated to be half of the defect length, but no measurements were provided. All data provided by True Flaw.

application, and the possibility of the coating filling up the cracks, neither of which scenario is representative of a real crack situation. Un-bonded paint will cause variations in the lift-off of the EMATs, although current measurements can be used to monitor this. Cracks filled by the paint could cause the ultrasonic surface waves to partially transmit directly through the cracks, as the mismatch in impedance between the paint and the steel is not as large as the mismatch between steel and air.

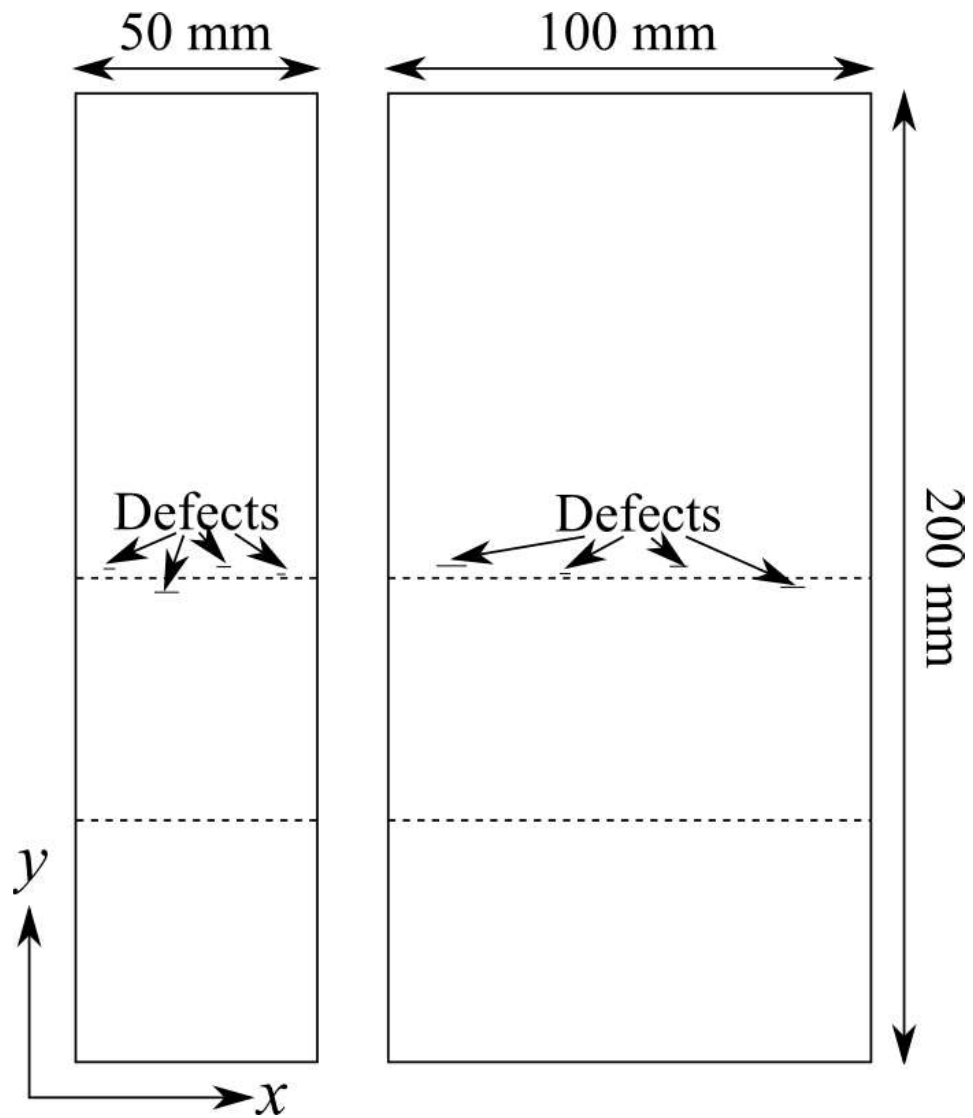


Figure 7.3: Schematic of the top view of two example ferritic steel samples. X labeling is used for positions across the sample widths, and Y labeling is used for positions along the sample length. The dotted lines represent the y positions over which the defects are spread. For some samples this is half way along the length, as shown here, and for some it is in the bottom quarter, where the second dotted lines are.

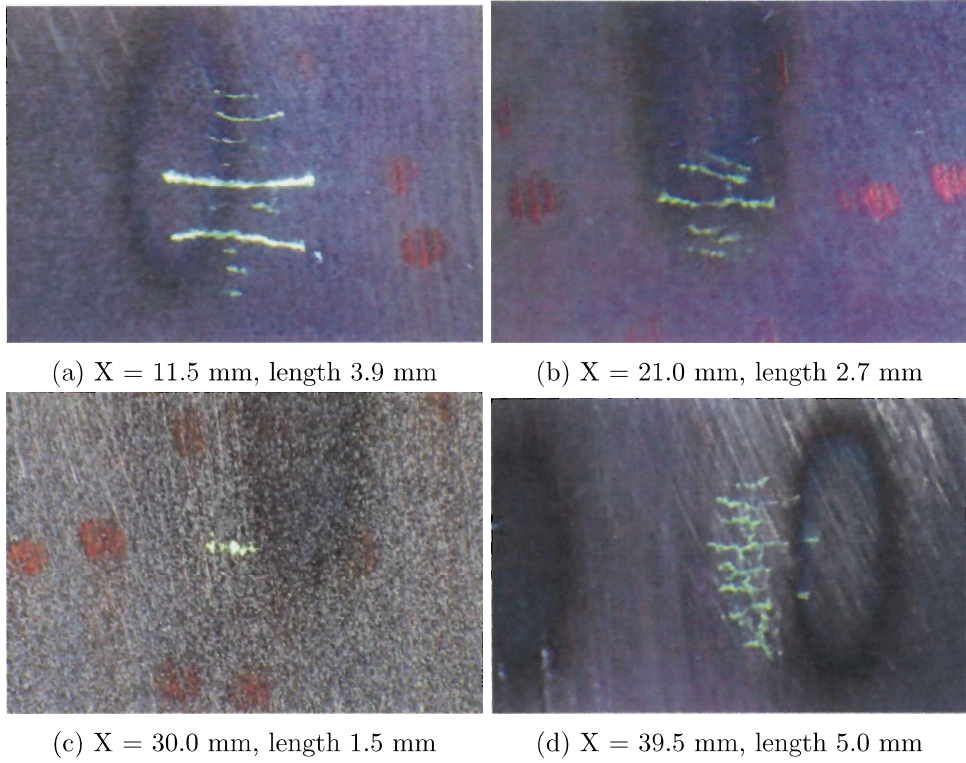


Figure 7.4: Sample W1128

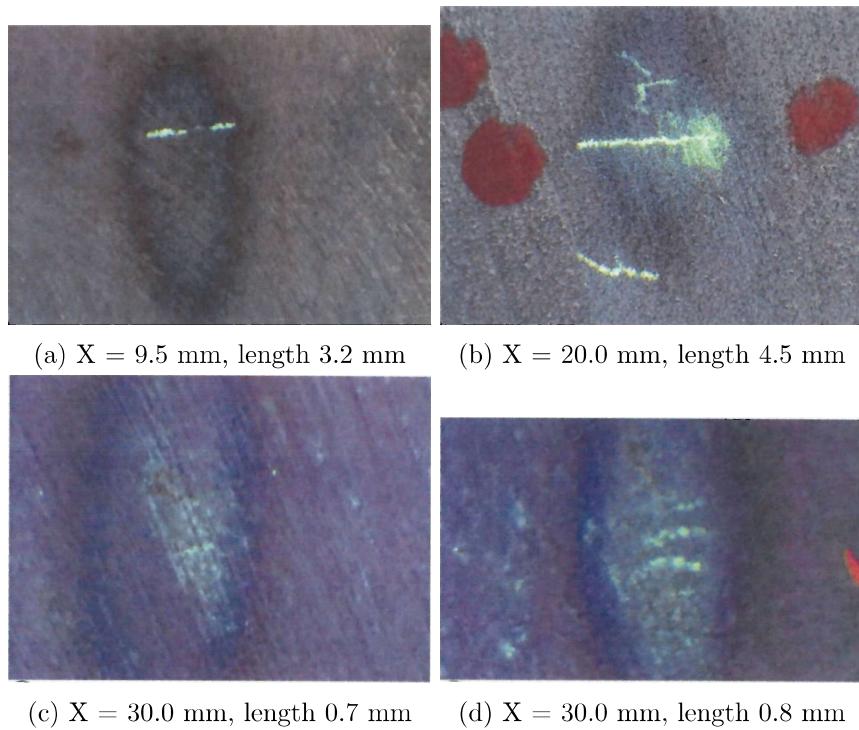


Figure 7.5: Sample W1129

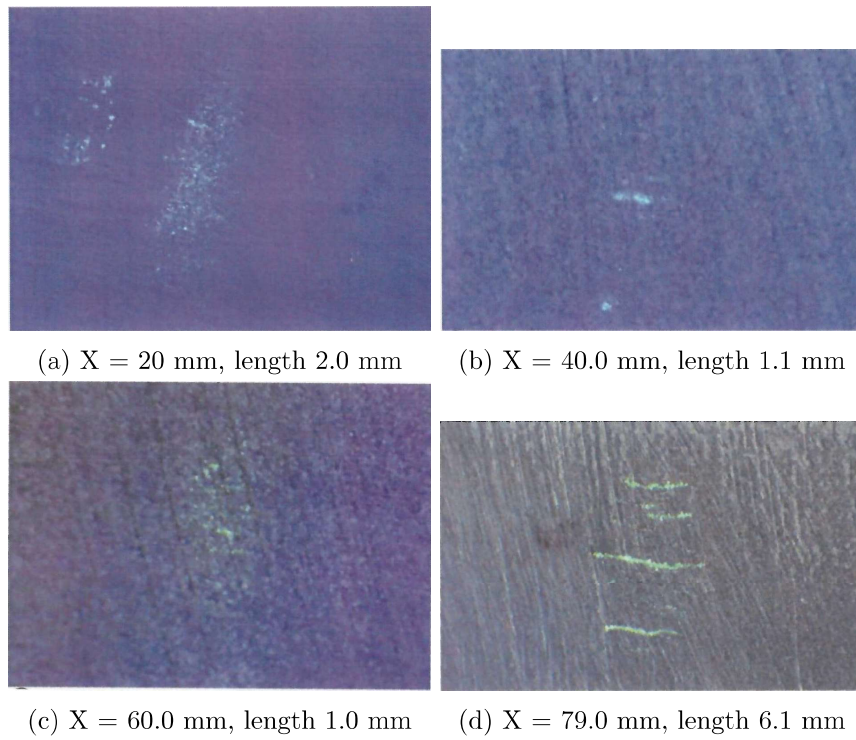


Figure 7.6: Sample W1130 (uncoated)

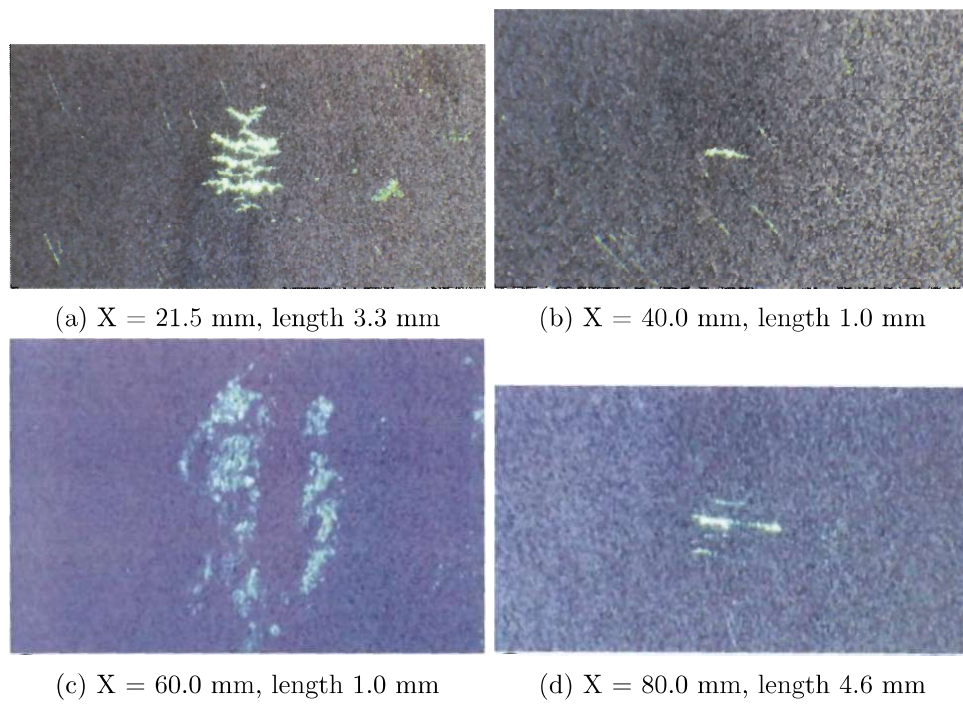


Figure 7.7: Sample W1131

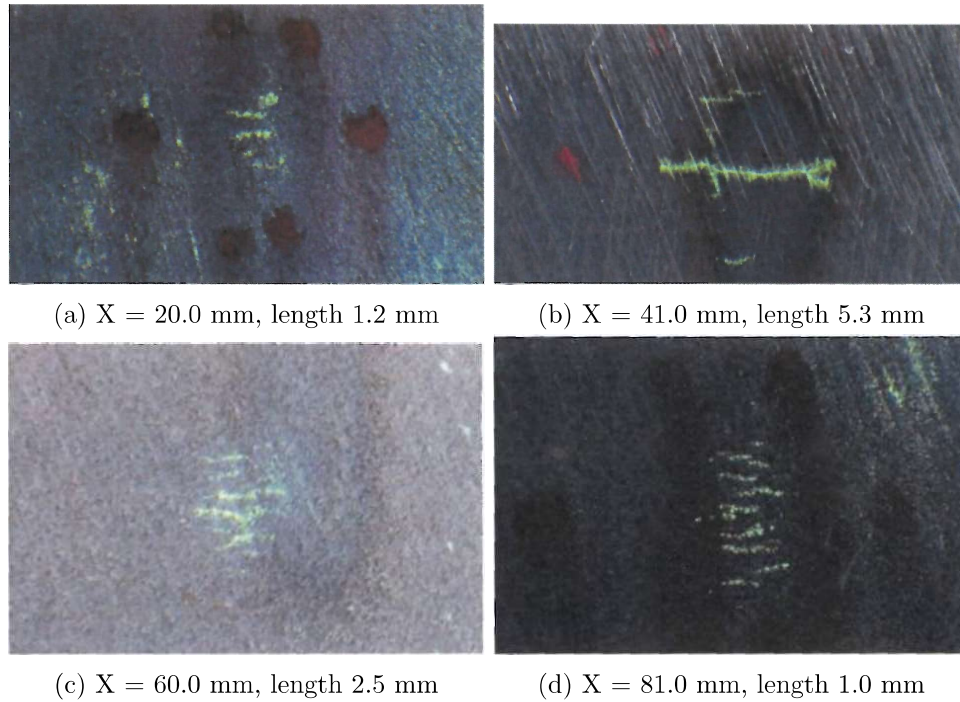


Figure 7.8: Sample W1133

7.2 EMAT Scanning on Cracked Aluminium Billet Sample

The aluminium billet sample (figures 7.1, 7.2) has been scanned using both the confocal meanderline EMAT in reflection (figure 5.10), and the focused transmission racetrack EMAT (figure 3.7). All scans are single shot with no averaging. The scan dimensions are shown in figure 7.9, scanning in 2D in the region bounded by the dashed lines for a full map of the defect surface. Only a small segment of the crack is scanned with the meanderline EMAT, restricted to keep the full EMAT footprint on top of the sample so as to avoid signal loss as the EMAT leaves the sample. The area scanned by this EMAT is 30 by 20 mm, starting by moving the EMAT towards the cracks in increments of 0.25 mm, indicated by the red arrow in figure 7.9a). Once a single line has been scanned across the defects, the EMAT is brought back to the start position, and then stepped 0.25 mm along the defect length (vertical in the figure), and then a new line scan is made across the defects. The focused racetrack pair are scanned similarly, but across a larger range using increments of 1 mm. The scan runs for this EMAT almost up to the defect edges to see if the defect can still be detected despite signal loss as the EMAT leaves the sample. A driving signal of 6 cycles at 2 MHz is used for the reflection meanderline EMAT,

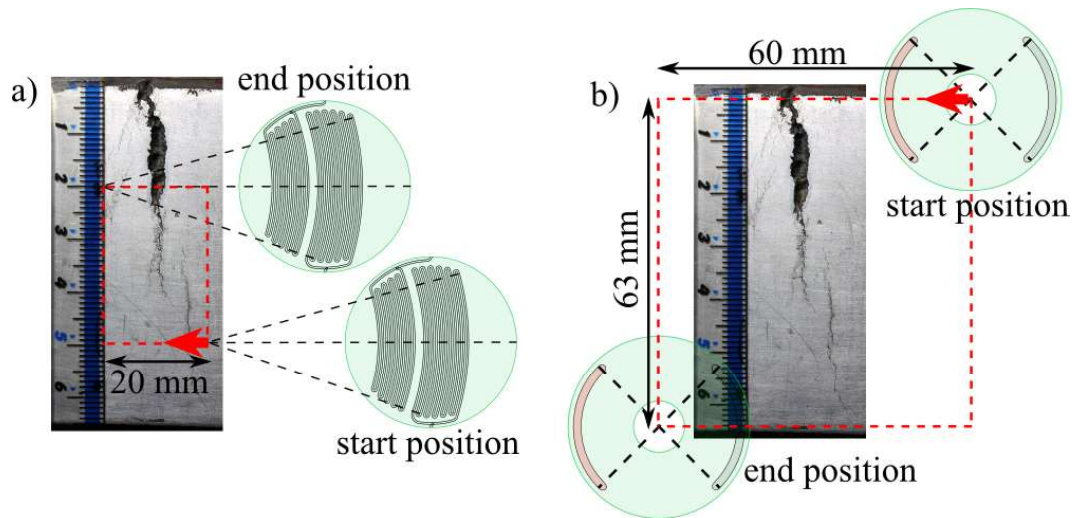


Figure 7.9: Scale diagrams of the scans performed on the cracked aluminium billet (figure 7.1). a) shows the scan performed with the meanderline EMAT. The smaller coil was used as the generator and the larger coil as the detector. b) shows the scan performed with the racetrack EMAT, the coil shaded in red was used as the generator, the gray as the detector. The magnet footprints are shown in green.

and two separate scans at 2 MHz, and then 1.2 MHz, with a 3 cycle signal, were done for the transmission racetrack EMAT. 1.2 MHz is the frequency found to give the strongest signal for this transmission EMAT, however, 2 MHz is also used due to its sensitivity to shallower defects, and to compare the difference in transmitted signals with the 1.2 MHz signal.

Two automated scripts were written to process the data from the two different types of scan. The reflection data is all cross-correlated with a reference signal (see section 3.4). A detectability threshold of 0.015 times the maximum detected signal is set, and the arrival time of any signal above this threshold is recorded. The arrival time measured at the maximum of the cross-correlated signal is then used to calculate the location of the defect returning the reflection relative to the EMAT. The known scan position of the EMAT is then used to find the defect position with respect to the start position of the scan. This EMAT has a long (figure 5.2) focal length, and so the cracks are detectable over a range of positions giving better reliability. The locations of these detected signals are shown in figure 7.10 superimposed on the photograph of the area scanned. The colours of the dots indicating reflections shows the signal power of the reflection, red indicating the strongest and blue the weakest. Varying the detectability threshold varies the accuracy of the image. A threshold of 0.015 was chosen as it gives a lower number of outliers and still maps

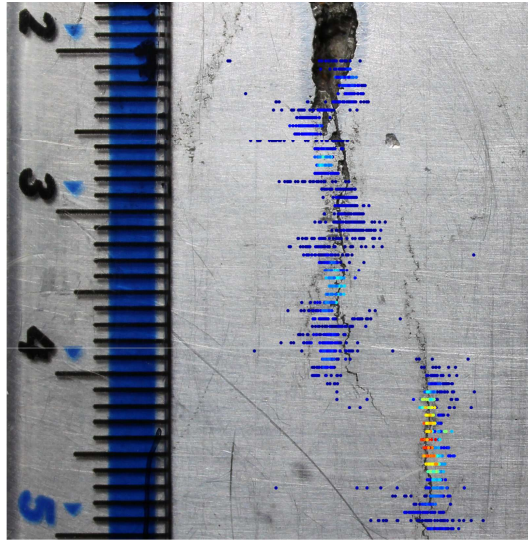


Figure 7.10: The coloured dots mark the locations of detected signals found using the focused meanderline EMAT, figure 3.3. The colour of the dots indicates the strength of the detected reflection, with red showing the strongest reflections and dark blue the weakest reflections.

the majority of the crack. It is so low compared to calibration work in chapter 5 as the red reflections seen in the image were abnormally strong compared to the rest of the reflections. This is due to variations in the inner roughness and angle of the defects [124]. Where the two defects overlap, more of the shallowest defect is detected when a lower threshold is used, but then a large number of false positives begin to appear. Figure 7.10 shows that this technique is able to detect and position a real, rough-faced, variable depth defect.

Figure 7.11 shows the maximum peak-to-peak signal strength detected at every scan position by the transmission EMAT, using both a 2 MHz and a 1.2 MHz driving signal. The 1.2 MHz driving signal gives a less noisy scan as the signals have a higher SNR. Strong signal (red) is seen when the coils are both on one side of the crack or the other and the wave can travel directly between the coils. The signal is blocked (blue) when the crack is between the two coils. The variation in signal strength when the defect is not between the coils is due to variation in the surface of the billet which is not perfectly flat, causing variations in the EMAT lift-off. Higher frequencies are more susceptible to this effect, and the 2 MHz scan correspondingly shows more variation. At 0 and 63 mm in the Y direction the signal is completely lost as too much of the EMAT is off the sample edge. The signal for the 2 MHz scan is completely blocked when any of the cracks are between the two coils. The 1.2 MHz scan shows some transmission under the smaller crack.

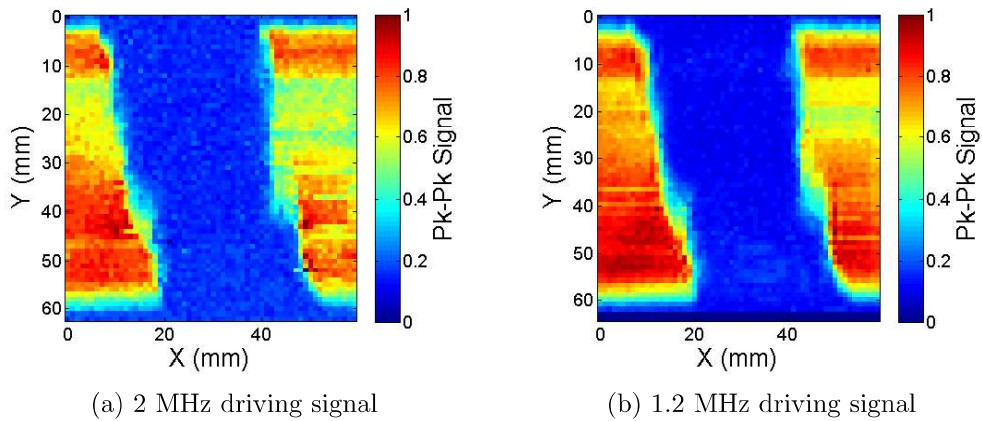


Figure 7.11: Normalised maximum peak to peak signals detected by the transmission focused racetrack EMAT at each scan location of the cracked aluminium billet sample.

These transmission scans by themselves do not map the defect position, as the cracks are large compared to the EMAT. To estimate the defect position, the center of each line scan in X ($Y = \text{constant}$ within each line scan) where the signal is blocked was found. The maximum peak-to-peak signal is then found for each X position (see figure 7.12 for example data at $Y = 54$ mm), and from these a maximum and a minimum signal is found (as labeled in red on the figure). A ‘half’ signal value exactly half way between this maximum and minimum is then defined (red). The X positions on either side of where the peak signal transitions through this half signal value are then found, and then linear interpolation is used to estimate the X position at which this exact value would be reached. This gives two locations, the point where signal is lost, and the point where signal is regained (labeled in green on figure 7.12). The defect location is defined to be exactly half way between these positions. These estimated locations are plotted in figure 7.13, for both the 2 MHz and the 1.2 MHz driving signals. The two different frequency data are slightly staggered in x position as the scans were run sequentially, and drift was seen in the realignment of the X-Y stage between the two scans. There is no drift in the y position as the defect edges were used to compensate for the drift.

From figure 7.13 it can be seen that the resolution in both directions is very good, within a few mm of the actual defect location, except where the two defects overlap. At the overlap the defect is estimated to be roughly between the two cracks. This is because the two defects are closer together than the two EMAT coils in the X direction. This could be resolved by rotating the transducer through 90° , however, that would put the rest of the defect below parts of the coil, which will prevent

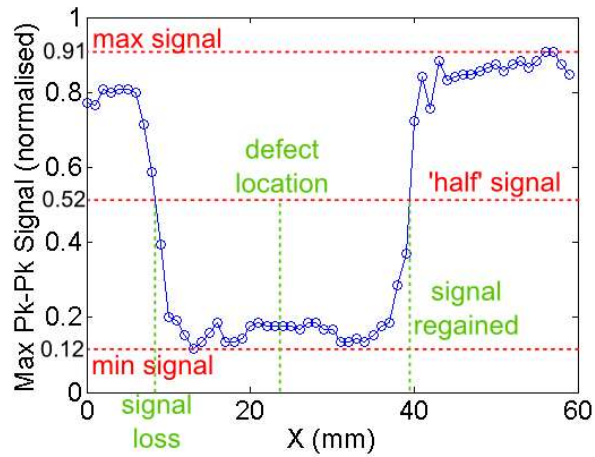


Figure 7.12: Example data for the $Y = 54$ mm line scan, showing how a defect location is chosen from the scan data. The y-axis shows the maximum peak to peak signal found at each X location. This data was using a 1.2 MHz driving signal.

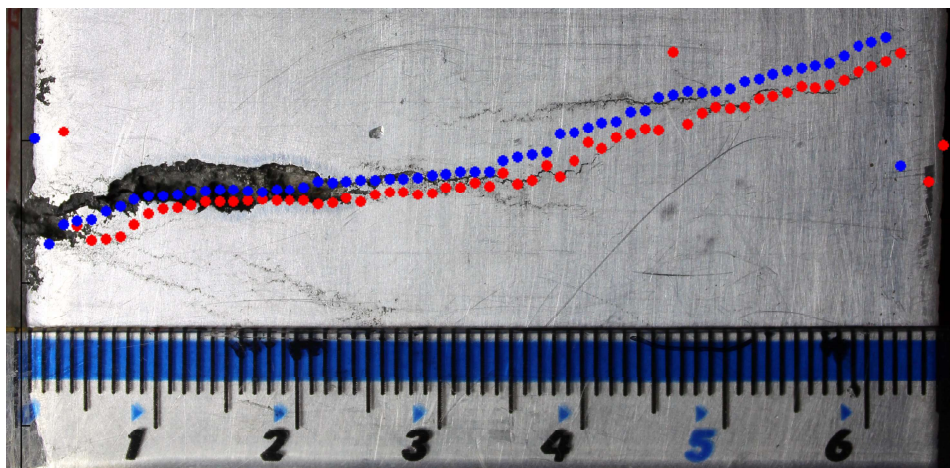


Figure 7.13: Predicted crack locations overlaid on the photograph of the cracks. Blue dots are the predicted locations from the 1.2 MHz driving frequency, and red dots from the 2 MHz driving frequency, using the focused racetrack transmission EMAT coil pair.

some of the signal being generated or detected. While the EMAT deals remarkably well with such a large pair of defects, it was designed for resolving cracks smaller than the distance between the two EMAT coils in all dimensions, but larger than the beam size at the focal point.

Figure 7.14 shows an example scan along the X direction at Y=54 mm again, but this time showing the raw data on a B-scan, with the defect clear by the loss of most of the signal amplitude between X = 10-40 mm. However, a weak transmitted signal can still be seen over this X range. Weak reflections from the crack can also be seen starting at approximately 17 μ s, initiating at 8 and 40 mm and branching away from the main signal. A delay is also observed in the transmitted wave arrival time when a defect is present. The time range 15.15 to 15.72 μ s was chosen to analyse the arrival time of a single peak from the Rayleigh wave packet. The arrival times of the maximum signal at each X location found within this time window for the Y = 54 mm line scan are shown in figure 7.14b). The change in arrival time is $0.3 \pm 0.1 \mu$ s. If the delay is purely due to a change in path length, for a Rayleigh wave velocity of 2906 m/s [16] this suggests an increase in path length of 0.7 ± 0.3 mm. If the wave is propagating along the crack faces this would suggest a crack depth of 0.4 ± 0.1 mm. From the ACPD measurements, however, this crack location is known to be between 4.5 and 6.8 mm deep. It is likely the crack is partially closed at the bottom, as at a 1.2 MHz frequency the Rayleigh wavelength is 2.4 mm, and so it is surprising that any transmitted signal is seen. If, however, the crack is largely closed and the depth the ultrasound wave ‘sees’ is 0.4 ± 0.1 mm deep this explains the observed strength of the transmitted signal and the small time delay. A similar delay is seen in the next section with the ferritic steel samples and further discussed there, considering also changes in velocity related to stress variations in the material.

Transmitted signal frequencies can be analysed to predict crack depths (section 2.1.4), however, due to the large depths of the cracks compared to the wavelengths used, the transmitted signals seen with this crack are so weak that the frequency content was too noisy to analyse. A minimum crack depth can still be given, as the 2 MHz signal is entirely blocked by the cracks, giving a minimum depth of 1.5 mm. Interestingly, this disagrees with the ACPD depth measurements, giving support to the theory that the cracks are partially closed.

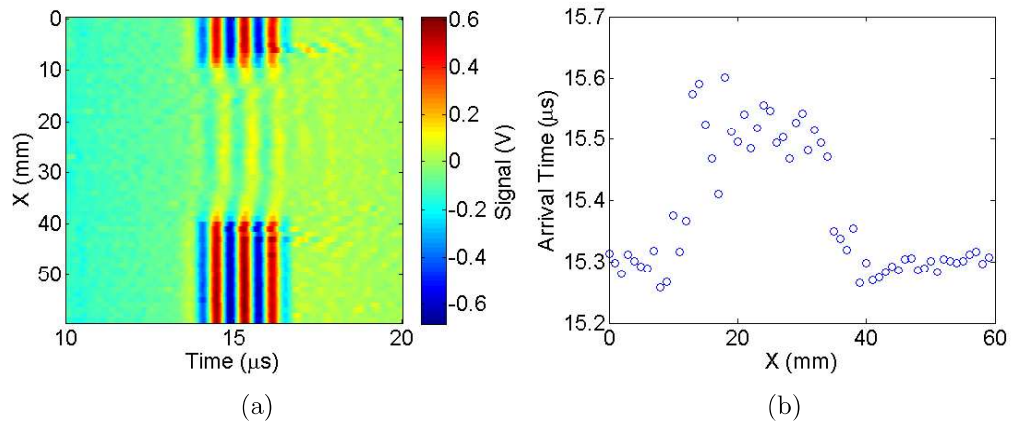


Figure 7.14: (a) Example B-scan data for $Y=54$ mm using the 1.2 MHz driving frequency, on the cracked aluminium billet with the transmission focused racetrack EMAT. (b) the arrival time of the peak found between 15.15 and 15.72 μs .

7.3 EMAT scanning on Thermal Fatigue Cracked Samples

Two pairs of focused, racetrack, transmission EMATs (see figure 3.7 for details), with coil widths of 1.5 mm and 0.75 mm, were used on several of the ferritic steel samples (figures 7.4-7.8), scanning the EMATs across the width of the sample with the focal point aligned to pass over the defect region. A schematic of the scans is shown in figure 7.15 a). The defects are roughly distributed along a line across the width of the sample, labeled the ‘defect line’, in figure 7.15a). There is some variation in the defect positions away from the defect line used. Defects that do not coincide exactly within the focal point of the transducer can appear to be shallower than they really are as they do not block the full width of the signal, as can be seen by comparing figure 7.15b) and c). They will also affect transmission over a longer distance and hence appear longer, as can be seen by comparing figure 7.15 b) with part c). In both parts of the figure, the defect is at the same height with respect to the EMAT beam width (displayed as the vertical position in the figure), however, only in b) is the defect incident in the beam path, whereas in c) it is not, as it is displaced horizontally from the focal point. As such the defect in b) will be detected by a reduction in transmitted signal strength, but in c) it will not be detected until closer to the true vertical location of the defect. As such, offset defects will appear shallower and broader.

Detection and sizing issues could be circumvented by taking a full 2D scan of the area, as done in the previous section, scanning the focal point over all positions.

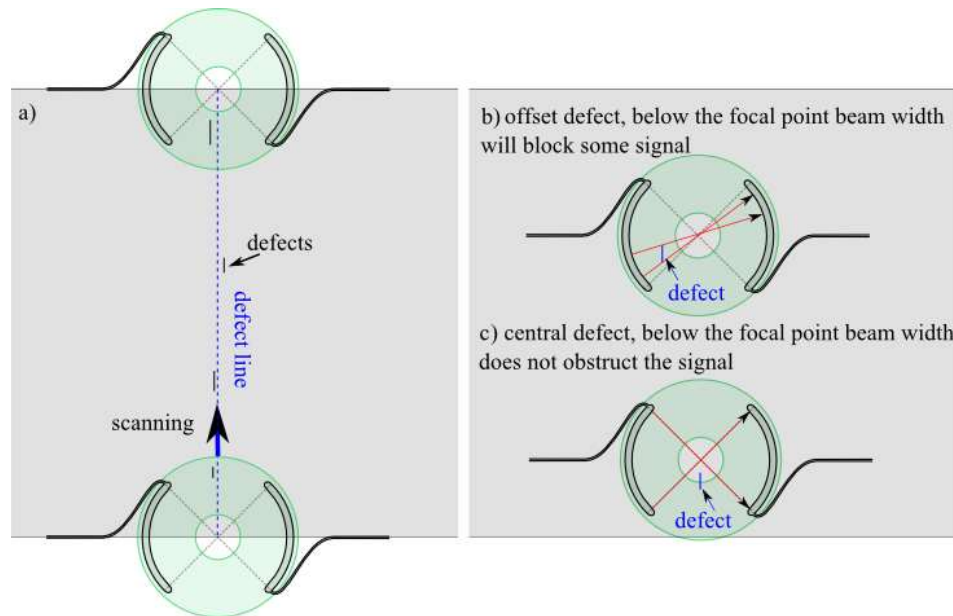


Figure 7.15: a) Schematic of the scanning set up for transmission detection of defects. Right: schematic of the broadening effect that can be seen when a defect is not in the center line of a scan. b) shows how a defect below the focal point can still block signal by being offset. c) shows how a central defect at the same height does not impinge upon the beam path.

However, with hand held scanning of a ferritic steel sample such images would have a large inaccuracy due to issues positioning the EMAT, because of the strong NdFeB magnet it contains and its strong attraction to the sample. In these samples the deviations of the defects from the scanning line are all less than 3 mm, which is the length of the focused beam spot for the 2 MHz signal, meaning inaccuracies from the mis-alignment should be minimal. From the images provided of the defects before coating, figures 7.4-7.8, many of the defects have a large amount of secondary cracking in parallel to the main defect, which would lead to a similar broadening effect to the position effects.

Several of the samples provided contained defects which are close to the sample edge, and so in the following scans the effect of the sample edge on the detected signals needs to be accounted for. In the long run this project work is intended for inspecting pipe shafts or other large samples which will not have this issue. To give an idea of the typical background variation expected in the detected signal due to sample edge effects, the transducer was scanned from a position where the focal point was incident directly on the sample edge of W1128 to a position where it was incident directly on the opposite edge, shown in figure 7.15 a), for a section of

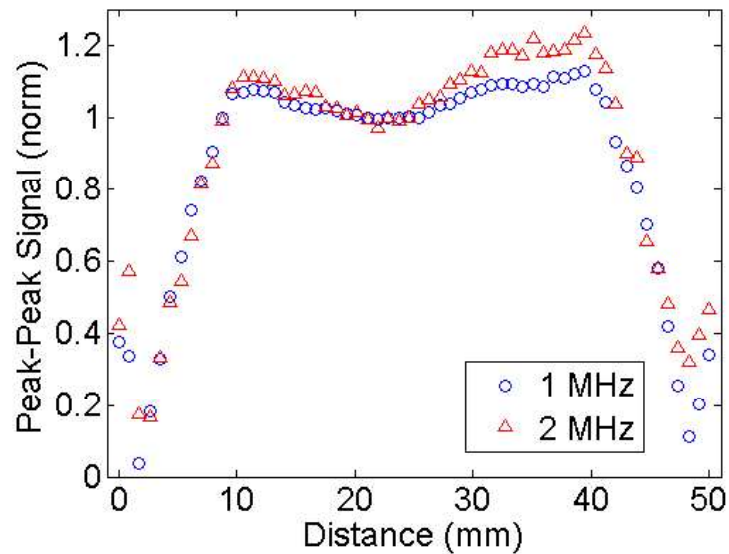


Figure 7.16: reference scan across the full width of W1128, away from any defects, to demonstrate the typical background signal shape. Peak signal has been normalised to 1 at the center of the scans for comparison.

the sample containing no defects. Two different generation frequencies were used, 1 and 2 MHz, using the 1.5 mm width coils. To improve positional consistency between the two sets of data, they were measured during the same scan, so the two frequencies for these samples are measured at identical transducer positions.

The maximum peak to peak signal detected at each scanning position for each frequency is plotted in figure 7.16. Between scanning distances of 10 and 40 mm the transducer is fully on the sample. As this section contains no defects a consistent transmitted signal would be expected for both frequencies. Signal strength can vary if the EMAT lift-off varies, however the EMAT is well pressed down due to the attraction between the magnet and the steel. The paint coating likely varies slightly in thickness (quoted as 40-60 μm), however, the signal variations cannot be due to the paint coating alone, as similar variations are seen in scans of the uncoated sample W1130 (section 7.3.3). The variations in generated signal could be due to variations in the material properties of the steel. The samples were subjected to strong localised heating to create the defects, which could alter the ultrasound wave velocity [151]. This should not affect the peak-to-peak amplitude of the transmitted signal, but changes in the steel from this heating, or possible variations in the steel composition, could change how the magnetic field is shaped by the steel, and so change the generation of the ultrasound when using an EMAT.

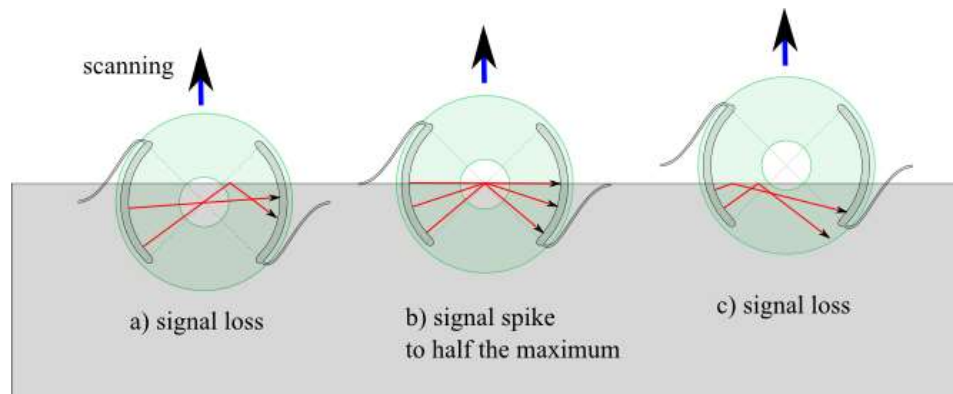


Figure 7.17: schematic of simplified ray tracing to explain the variations in signal found as the transducer leaves the edge of a sample.

Variations in surface roughness could also be a factor. While Rayleigh waves are non-dispersive, increased surface roughness causes more attenuation [48]. Surface roughness will affect higher frequencies more strongly than lower frequencies as the higher frequencies are concentrated closer to the surface (section 2.1.3) and features will be of closer size to the wavelength. The 2 MHz generation does show more variation than the 1 MHz signal suggesting surface roughness effects are likely.

At the scan edges, 0-10 mm and 40-50 mm, the effect of the transducer moving on and off the edge of the sample can be seen. Close to 10 and 40 mm there is a short section where the magnet is slightly off the edge of the sample, however, the EMAT coil is fully over the sample. Ferritic steel shapes the magnetic field (exploited for transducer designs [135, 63, 152]), and so some variation might be expected here. Between 0 mm and 10 mm the coil transitions over the sample edge, showing a rising signal from 0, with the reverse process seen between 40 mm and just before 50 mm. As shown in part a) of figure 7.17, at these positions there is less coil able to generate ultrasound, and some of that signal will be deflected from the sample edge and might not create a coherent signal at the detector or even reach the detector. At 0 and 50 mm a strong edge effect is seen. At these positions half of both the generator and detector coils are off the sample, however, the signal from the half that is still on the sample has a coherent reflection through the focal point to the detector coil, as depicted in figure 7.17 b), leading to a signal spike back up to 50% of the original signal. This can be seen experimentally in figure 7.16 at 0 and 50 mm. It then rapidly drops off again as the coil leaves the sample, shown in as figure 7.17 c), however, this is outside of the scan range performed experimentally (figure 7.16).

Samples W1128, W1129, W1133 and the uncoated sample W1130 were scanned

with the wider (1.5 mm) width coil at frequencies of 1 and 2 MHz. W1131 was scanned with the thinner (0.75 mm) width coil at 2 and 3 MHz, to see if higher frequencies improved the detection ability. Scan increments are 1 mm per step, but performed by hand due to the difficulty of scanning large magnets on ferritic steel, so there is a high inaccuracy of at least 0.5 mm at each position. The error is not fully cumulative however, as the start and end positions of the scan are known with less than 0.5 mm error, and hence the number of steps required is known.

7.3.1 W1128

Figure 7.4 shows the dye penetrant images for W1128 provided before the sample was coated, and the expected size and location of each defect as given by True Flaw are given in the table 7.1. The largest three cracks show significant secondary cracking in parallel with the main crack. Figure 7.18 shows the B-scan from the 1 MHz data. The saturated signal starting at 3.8 μ s is the noise from the signal generation. $t=0$ occurs before signal generation, dependent on the trigger mechanism of the Ritec. The curved shape between 10 and 12 μ s is the end of the noise from the generation, with the variation in time indicating some change in the sample properties or the effect of the sample edges. The signal starting at approximately 14 μ s is the Rayleigh wave.

To create a comparative plot for both frequencies at which the inspection was performed, the maximum peak to peak signal strength of the Rayleigh wave was found at each position and plotted as a function of the scan distance, shown in figure 7.19 a). The main overall shape, with strong signal loss at the edges coupled with spikes at 0 and 50 mm, matches the expected edge effects profile from the calibration scan in figure 7.16. In the 1 MHz signal (blue circles), distinct signal loss compared to the expected profile can be seen at 11 and 39 mm. This indicates the presence of defects partially blocking the transmitted signal between the EMAT coils. There is also a possible signal loss shape at just over 30 mm, however the shape is shallower and so is potentially a background effect, especially as that location has a very small defect which is unlikely to be detectable. There is a similar drop in the 2 MHz data but ranging across 30 to 35 mm, making a wider shape, much too large to be the 1.5 mm defect. However, within the shape there are two localised drops at 30 and 35 mm, so they could be similar features to the 1 MHz data but on a different background shape, but the variations are too small to be conclusive. Conversely, in the 2 MHz signal, strong signal spikes are seen at 11 and 40 mm, which is unexpected as the presence of a defect should block signal, and not enhance it. However, both of these spikes occur close to the interference effects at the sample edge, so they also

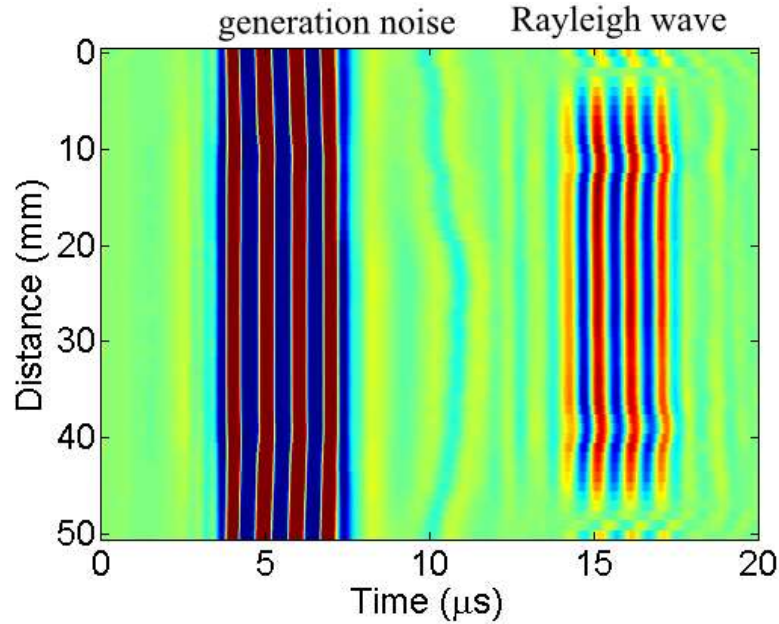


Figure 7.18: A B-scan of the received data when scanning across the sample defect line of W1128. Red indicates a positive velocity, blue indicates a negative velocity, and green indicates a zero velocity.

show edge effects. Further analysis is need to ascertain which signal shapes indicate defects and which are background variations.

It was noticed that the transmitted signals also exhibit variations in the signal arrival time at certain positions, as can be seen in figure 7.18. To track the arrival time, a narrower time range was chosen for analysis to isolate only one peak of the three cycle signal, and the arrival time of the maximum signal in that time range at each position was measured. The peaks chosen to isolate were those exhibiting the strongest signals in order to minimise the noise in the data. The measured arrival time is plotted in figure 7.19 b). In this plot delays at 11 and 39 mm are easily distinguishable at both frequencies, indicating the presence of defects.

A surface defect can increase the path length for Rayleigh waves and so delay the arrival time of a transmitted signal [124]. The time delays range from $0.09 \mu\text{s}$, to $0.14 \mu\text{s}$ for the four peaks seen (two for each defect at the different frequencies). If the wave is entirely Rayleigh, with a velocity of roughly 3000 m/s , this would indicate an increase in path length of 0.27 to 0.42 mm . To be traveling under a defect, therefore, it would have to have a depth of half this, i.e. 0.114 to 0.21 mm in depth. This is too shallow to have been picked up by this transducer, at wavelengths of $1.5\text{-}3 \text{ mm}$, with the visible signal drops in the peak to peak signal in the 1 MHz data (figure 7.19 a)). It is also expected that the defects have depths which are

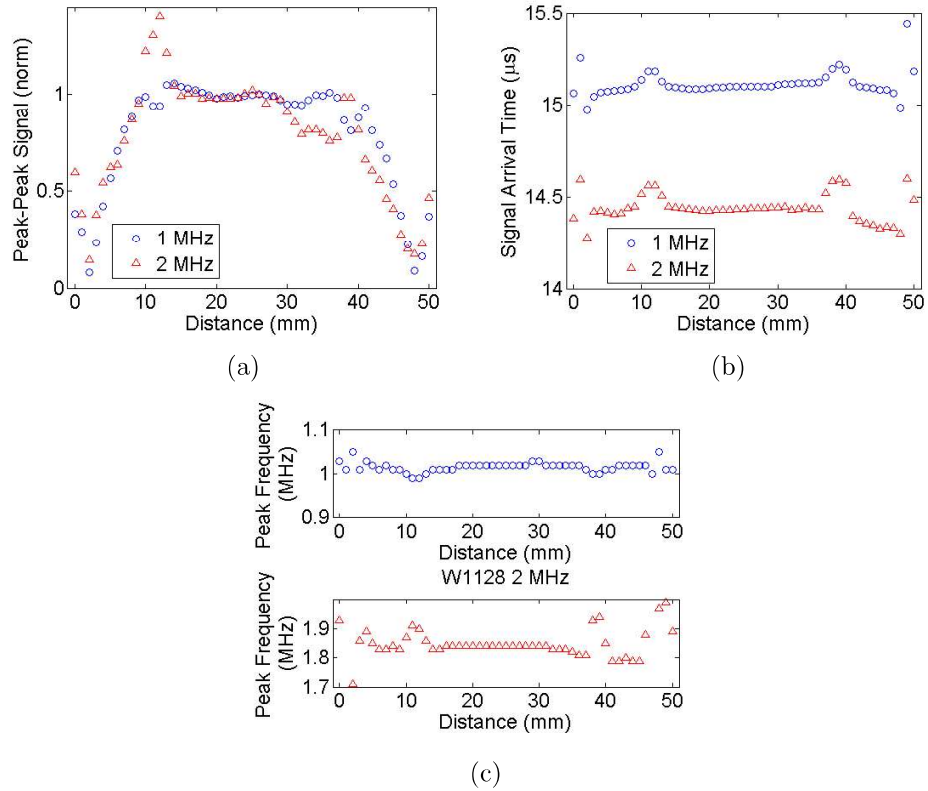


Figure 7.19: W1128 results, with a) showing peak to peak signal variation scanning across the defect line of W1128, normalised to the central signal, avoiding edge effects, b) showing the arrival time of these signals, and c) showing their peak frequency content.

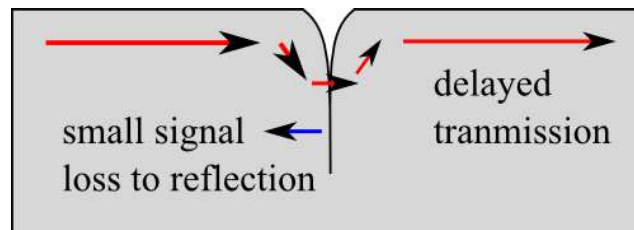


Figure 7.20: Possible defect geometry and ray tracing to explain the small time delay of the transmitted Rayleigh wave at a defect.

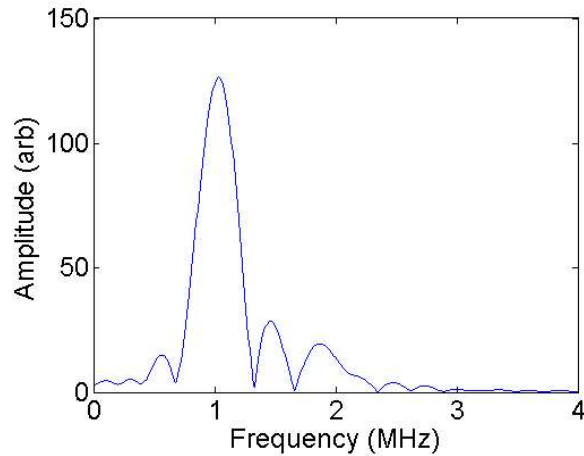


Figure 7.21: An example FFT output of the data in the center of the scan shown in figure 7.18.

approximately equal to half of their lengths, suggesting depths of 1.9 and 2.5 mm for the defects at $X = 11$ and $X = 40$ mm respectively, making it unlikely that this delay is simply from traveling underneath the defects. It is possible that the defects are partially closed, so the surface wave is only traveling part of the way down the crack before transmitting through it, as shown in figure 7.20. However, it must be noted that this ray tracing behaviour is over simplified, as it neglects the bandwidth of the signal. Some of the signal, particularly the lower frequencies, will pass straight under the crack, and will be measured in combination with the delayed higher frequencies. Another possible explanation is changes in the steel due to the thermal cycling to create the cracks has reduced the velocity of the ultrasound in the defect region slightly [151].

Transmission under defects is often frequency dependent in nature [114], and so the frequency content of each transmitted wave was studied. Figure 7.21 shows an example FFT output from the measurement taken at the center of the scan for the 1 MHz data, i.e. the centerline data shown in figure 7.18. To ensure no effects from other waves are included the data is windowed over the Rayleigh wave. The defects typically reduce the higher frequency content of the wave transmitted, which could cause the main frequency lobe to become asymmetric. This shape comparison is a complex comparison to make reliably [4], and so instead the frequency at which the maximum amplitude in the FFT occurs is recorded. The data is plotted in figure 7.19c). The edges of the data, 0-8 mm and 42-50 mm, can be ignored as the transmitted signal is too weak, and so the frequency data is very noisy. The 1 MHz data shows a small shift in the peak to lower frequencies at the defect locations,

however, the shift is within the noise levels of the full data. The 2 MHz data shows a clear shift to higher frequencies at the defect locations, This is initially surprising, as typically surface breaking defects predominantly block higher frequencies more than lower frequencies. However, this does not necessarily affect the peak in frequency, just the overall shape of the frequency content. A broader band signal would give much more reliable results when using this technique. This frequency behaviour cannot be an effect of the coating as the same effect is seen on the uncoated sample, W1130, figure 7.23.

7.3.2 W1129

Figure 7.5 shows the dye penetrant images for the defects in W1129. The first crack at 9.5 mm is a singular crack, not a cluster. The second crack at 20 mm shows some secondary cracking but less significant compared to that seen in W1128. The final two defects are very small and may just be scratches, and are unlikely to be detectable.

The same scan as on W1128 was performed, using both 1 and 2 MHz signals, with the results shown in figure 7.22. In the peak to peak transmitted signal a sharp signal loss can be seen for both frequencies at 20 mm, but again the end defects are hidden in the edge effects on the amplitude. However, both of the larger defects (expected at 9.5 and 20 mm) very clearly show up as delays in the signal arrival time, figure 7.22 b). Once again, there is an increase in peak frequency at the defects at 9.5 mm and 20 mm in the 2 MHz data, figure 7.22 c), and possible frequency decrease in the 1 MHz, but the latter is rather noisy. The time delay and high frequency spike seen on the first crack at 9.5 mm shows that this cannot be due to having a cluster of cracks, as this is clearly a single flaw in the pre-coating images. Additionally, the fact that the same behaviour is seen for both defects shows that this is definitely not an effect from the samples edges.

7.3.3 W1130

The same scan was run for W1130. This sample is uncoated, allowing for optical imaging. On observation of the dye penetrant images (figure 7.6) and also new images taken using an optical microscope, the 6.1 mm crack at 79.0 mm is the only significant defect, this also being a cluster of cracks in parallel. Figure 7.23 shows the results of the scan. While there is a large amount of variation in the peak to peak signal of the transmitted data over the whole scan, figure 7.23 a), the large defect at 79 mm clearly shows as a large signal drop present at both frequencies.

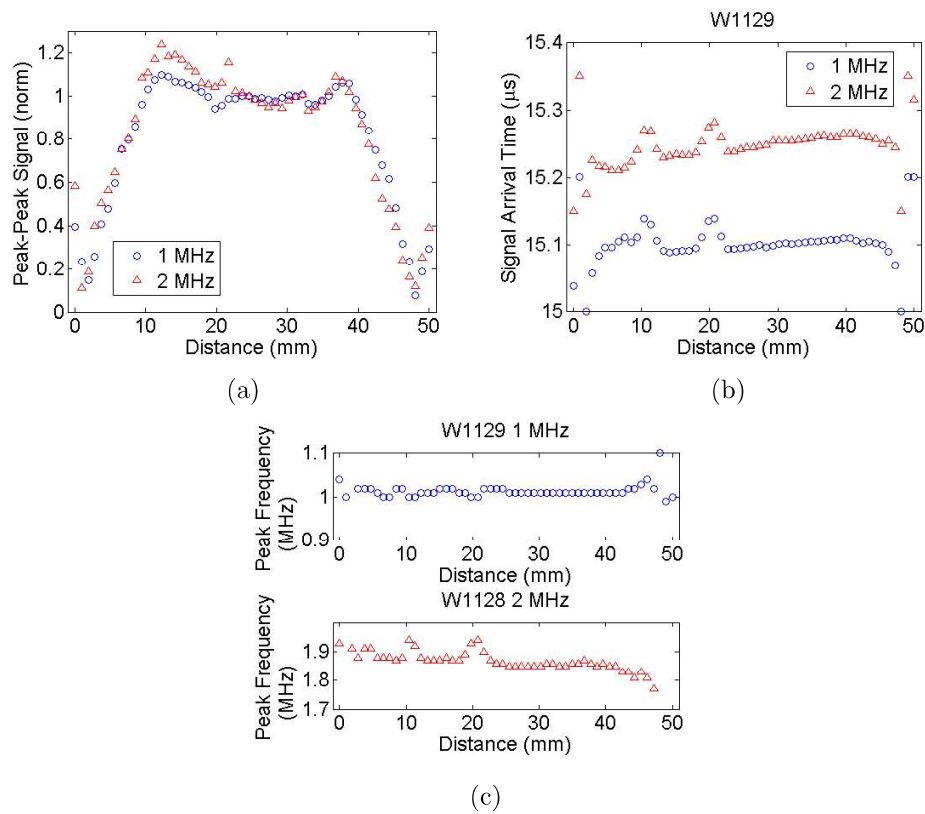


Figure 7.22: W1129 results, with a) showing peak to peak signal variation scanning across the defect line of W1129, normalised to the central signal, b) showing the arrival time of these signals, and c) showing their peak frequency content.

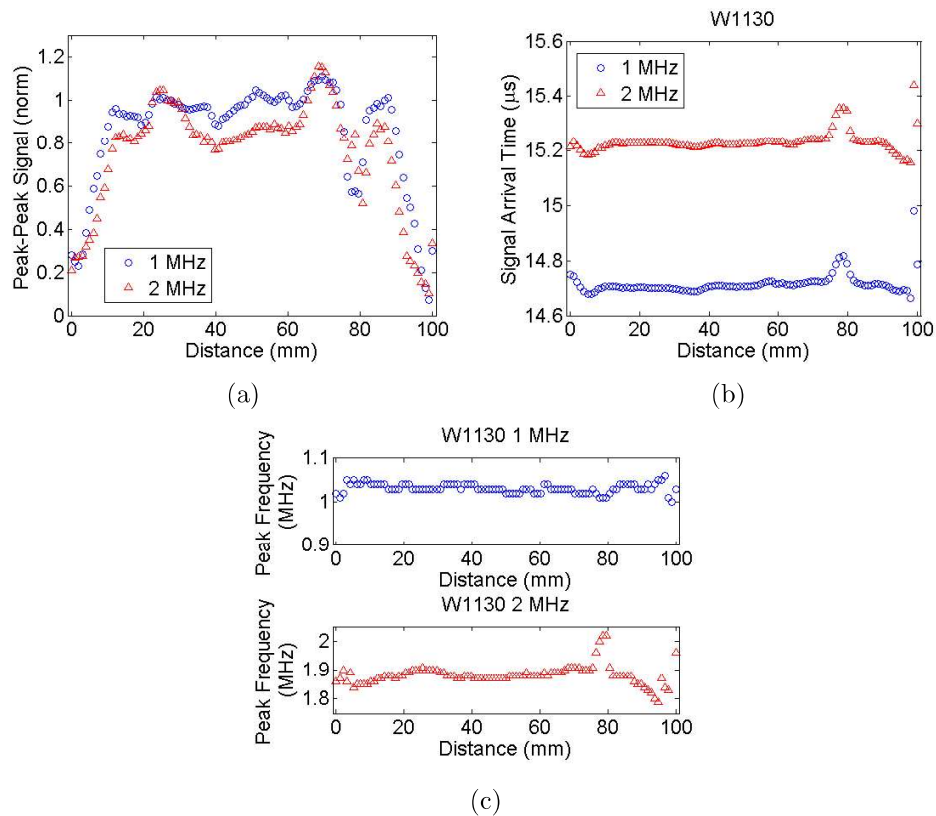


Figure 7.23: W1130 results, with a) showing peak to peak signal variation scanning across the defect line of W1130, normalised to the central signal, avoiding edge effects, b) showing the arrival time of these signals, and c) showing their peak frequency content.

Interestingly, the 2 MHz data appears to have a double dip profile to the defect, and prior to the drop there is a marked increase. This could be part of the background variation seen in all scans, but could indicate interaction of the Rayleigh wave with the defect.

A marked delay in arrival time is also seen at both frequencies, figure 7.23 b), at 79 mm. An increase in frequency is also observed in the 2 MHz data, figure 7.6 c), similarly to the previous two scans, indicating that this effect cannot be an artifact of the sample coating. There is a potential variation at 40 mm that shows up at both frequencies in the peak to peak data, and a small variation in the arrival time at this position, however it is much smaller than seen for all other defects and could just be noise. All other defects are too small or too closed to detect.

7.3.4 W1131

The same scan was run for W1131 and the dye penetrant images before coating are shown in figure 7.7. The defect at 21.5 mm shows as a cluster of defects, while the others only show minor secondary cracking, and the smallest, figure 7.7 bottom left, appears very small and may just be a scratch. This sample experienced some damage to the opposing side, at the opposing end to where the final reported defects are located. This damage was due to an initial attempt to create defects but it was reported that a machine malfunction cause the sample to overheat. While this is far removed from the scanning location of the final defects, it is possible that this has caused larger variations in the steel properties across the whole sample.

Results are shown in figure 7.24. The peak to peak transmitted signals show a lot of variation, figure 7.24a), and there is also a lot of variation in the signal arrival time, figure 7.24b). It is likely this is due to the heating damage reported affecting the ultrasound velocity in the sample. Whilst W1133, in the next section, also shows more variations in the signal arrival times, it is not as significant as W1131, and the variations are likely due to the use of an EMAT with narrower coils for higher frequency generation.

At 70 mm there is a large reduction in transmitted peak to peak signal and a corresponding delay in the signal arrival time, but it is a much broader feature than previous defects, ranging almost from 60 mm to 80 mm. The detected frequencies of the 1 MHz data do show a slight increase in the frequency, however there is no change in the 2 MHz data. It seem unlikely that this is a true detection of a defect, although there is a large defect located at 80 mm. In the signal arrival time a consistent delay can be seen at 21 mm, the expected location of the largest defect cluster, despite it being difficult to distinguish a corresponding drop in the peak to peak signal. The detected frequencies of the 1 MHz data show an increase in frequency at closer to 30 mm, preceded by a slight dip at 21 mm which might correspond to a defect, however no change is seen in the 2 MHz data. The similarity of the time delay at 21 mm to previous results suggests this is detecting the defect, but the variations in material properties mean that results on this sample are unreliable.

7.3.5 W1133

The defects contained in this sample prior to coating are shown in figure 7.8. This sample was scanned using the narrow width, 0.75 mm, coil using both 2 MHz and 3 MHz frequencies. These higher frequencies are more surface sensitive, so may show more variation due to the defects, however it also makes them more sensitive

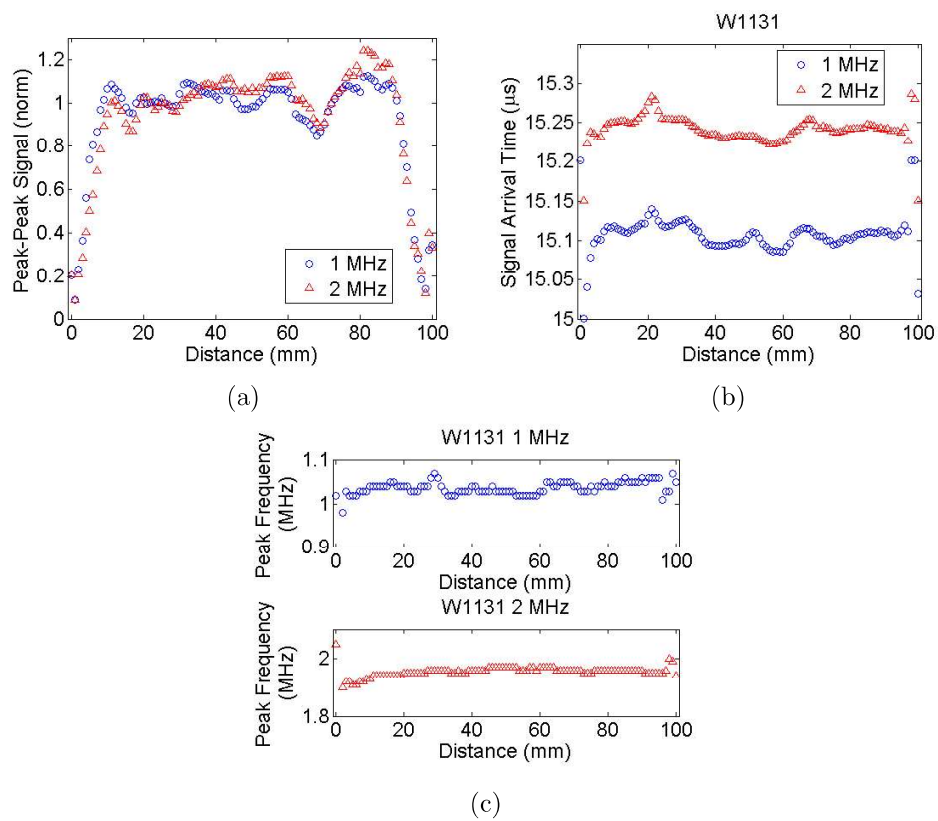


Figure 7.24: W1131 results, with a) showing peak to peak signal variation scanning across the defect line of W1131, normalised to the central signal, b) showing the arrival time of these signals, and c) showing their peak frequency content.

to variations in surface roughness, and the narrower coil width makes the signals much weaker, and therefore noisier. The two frequency data sets were also taken in separate scans, not in conjunction. Scanning across the central width of the sample containing the defects of W1133 found no obvious signal drops or significant variations in signal arrival time. This scan was stopped just before the coil itself left the sample surface, and so the strong spikes at the scan edges (figure 7.25 a)) are likely the effects from the changing magnetic field, and the signal drop offs are not visible in this scan. No clear signal drops or spikes are seen, no significant variations in the arrival time of the Rayleigh wave were visible, figure 7.25 b), and no noticeable frequency variations are seen, figure 7.25c). It is possible there is some defect-like signal loss around 20 mm, however it is not possible to tell if it is just noise without removing all background effects. The combination of signal drop, frequency shift and time delay indicates that defects are not reliably detected. However, this is expected due to the reduced signal amplitude when using this coil.

7.4 Conclusion

In summary, Table 7.2 lists all of the different scans performed in this chapter, and the defect detectability detectability.

The focused reflection and the focused transmission EMATs can be used to map large defects. The reflection provides the most detailed spatial map when the crack is longer than the focal point, and when there are multiple cracks in close proximity. The transmission EMAT, however, also provides a minimum depth measurement. The cracking in the aluminium billet inspected is also concluded to be partially closed below the surface, causing a small time stagger in the transmitted wave.

For the inspection of very small cracks the transmission EMAT provides the most useful information. The attempts on these samples with the reflection EMAT have not been presented as it is too difficult to align on the ferritic steel when scanning by hand. The largest two defects on samples W1128 and W1129 can be detected using the delays in arrival time of the transmitted wave. Looking for dips in the amplitude of the transmitted signal does work in the 1 MHz data, but is more noisy than the arrival time delay data, especially when incident in the edge effects of the samples. The largest crack on the uncoated sample W1130 is clearly visible in both amplitude loss and time delay. No defects are detected in W1133 despite the presence of a large single crack, however this sample has undergone damage creating noise from variations in the material properties. The reason for the arrival

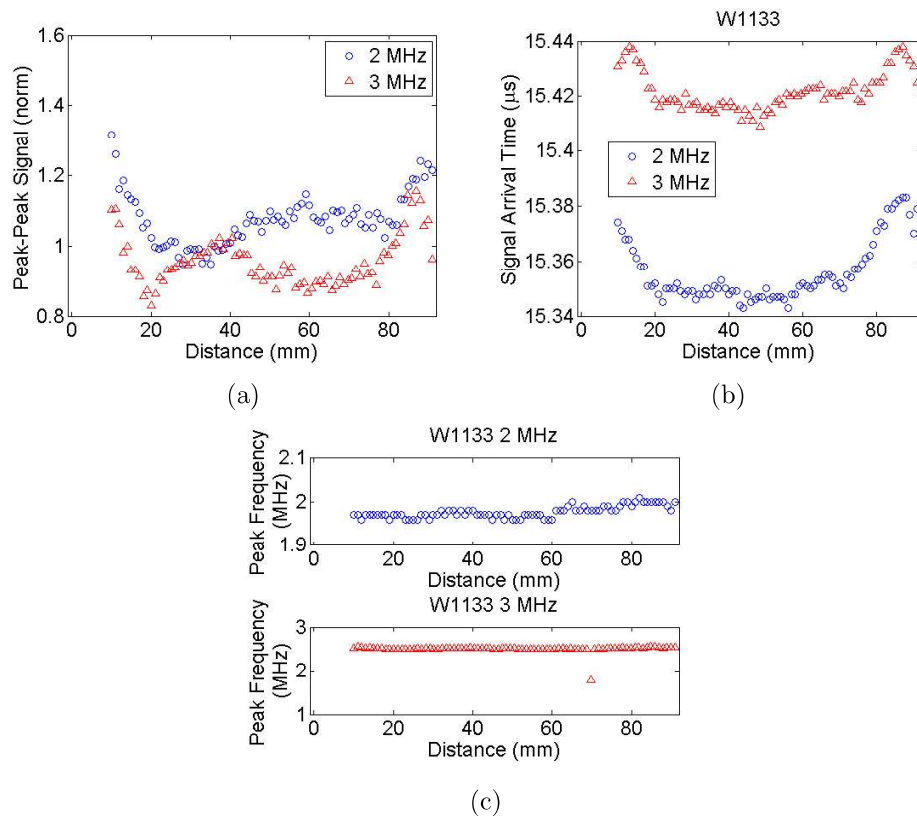


Figure 7.25: W1133 results, with a) showing peak to peak signal variation scanning across the defect line of W1131, normalised to the central signal, avoiding edge effects, b) showing the arrival time of these signals, and c) showing their peak frequency content.

Sample	Coating	Length (mm)	Coil type	Frequency (MHz)	Detectability
Aluminium Billet	uncoated	64	Meanderline	2	2D mapping
		and 27	Racetrack	1	Cannot map overlap
			“	2	“
					can also depth gauge
W1128	coated	3.9	Racetrack	1 and 2	yes
		2.7	“	“	no
		1.5	“	“	no
		5	“	“	yes
W1129	coated	1.2	“	“	yes
		4.5	“	“	yes
		0.7	“	“	no
		0.8	“	“	no
W1130	uncoated	2	“	“	no
		1.1	“	“	no
		1	“	“	no
		6.1	“	“	yes
W1131	coated	3.3	“	“	maybe
		1	“	“	no
		1	“	“	no
		4.6	“	“	no
W1133	coated	1.2	“	2 and 3	no
		5.3	“	“	no
		2.5	“	“	no
		1	“	“	no

Table 7.2: Summary table of all the real defect tests performed in this chapter

time delays and the frequency behaviour of the transmission cannot be an artifact of the edge effects, or an effect of the coating, or an effect of multiple cracking. The time delays alone could be explained by partially closed cracks but this does not explain the frequency variations. It is therefore concluded that the time delays are probably caused by a combination of partially closed cracking and reduction in the ultrasound velocity due to thermal fatigue, and the variations in material properties are correspondingly altering the transmitted frequencies [151].

It is proposed that, for small cracks, a data fusion technique between the three different measurements, peak-to-peak amplitude, signal arrival time, and frequency content, should be employed for optimum defect detection [42, 43, 153]. All three analysis techniques are noisy, but the probability of detection increases by combining the results. A proposed technique is to defect a detection threshold for each of the three analysis techniques, and at least two out of the three must be over their detection threshold at the same scan position for it to be reported as a defect. The potential for defect sizing is increased if both transmission and reflection techniques are used, as the reflection technique has better resolution, particularly with overlapping and large cracks, but the transmission technique is needed to give an indication of depth. Robotic implementation will also improve the reliability of results, as more accurate alignment can be used, and the lift-off can be controlled [66]. An efficient system would begin with coarse scanning to identify problem areas with the reflection technique. In-depth measurements with both the reflection and the transmission technique can then be used for accurate surface mapping and defect depth gauging.

Chapter 8

EMAT lift-off capabilities

One advantage of EMATs over piezoelectric transducers is their capability to work out of contact with a material. This chapter presents the lift-off performance of the geometric focused EMATs already characterised and employed for NDE in the previous chapters. Three unfocused, transmission, calibration designs are then presented, designed so that the generator and detector coils can be lifted off from the sample separately and combinations of different generators and detectors can be used, so that generator and detector effects can be distinguished for different coil types.

8.1 Focused EMATs

Figure 8.1a) shows the maximum peak-to-peak signal amplitude generated by multiple EMAT designs as they are moved out of contact with the sample (increased lift-off). Thin sheets of plastic were used to create consistent incremental lift-offs, creating an artificial ‘air gap’ between the coils and the sample. The signals have been individually normalised to 1 at the zero lift-off position so that the different lift-off behaviours can be compared, regardless of the relative strengths of the signals generated by each design. The reflection mode meander-line EMAT, shown in figure 3.3, was aligned with the end of an aluminium sample to give a maximum reflected signal to study. A driving frequency of 2 MHz was used as this is the optimal frequency for this design, and the results are shown by the blue circles in figure 8.1.

Similarly, the transmission EMATs were placed in the center of a large aluminium sample away from defects or edges so the maximum transmitted signal can be analysed. Two different focused racetrack designs have been lift-off tested, one

with a racetrack width of 1.5 mm and one with a racetrack width of 0.75 mm, both with designs as shown in figure 3.7. The 1.5 mm width pair was tested at two different driving frequencies as both have been used in previous chapters: 2 MHz is shown by the red stars, and 1 MHz by the black triangles in figure 8.1. The 0.75 mm race track pair has only been used at one driving frequency (2 MHz) and is shown by the pink triangles in figure 8.1. One focused linear transmission design has also been tested, with a coil width of 0.75 mm, with the design shown in figure 3.9. This was also tested at two different driving frequencies: 0.6 MHz, as this was found to generate the strongest detected signals, shown by the pink crosses, and 1 MHz for a comparison to the 1 MHz focused racetrack coils, shown by the blue squares in figure 8.1.

It should be noted that at ‘zero’ lift-off the actual distance from the coils to the sample is approximately 0.1 mm for all designs due to a layer of insulating kapton tape over the bottom of the coils. However, as this is as close to the sample as can safely be obtained by any design this is referred to as the ‘zero’ lift-off position in this section.

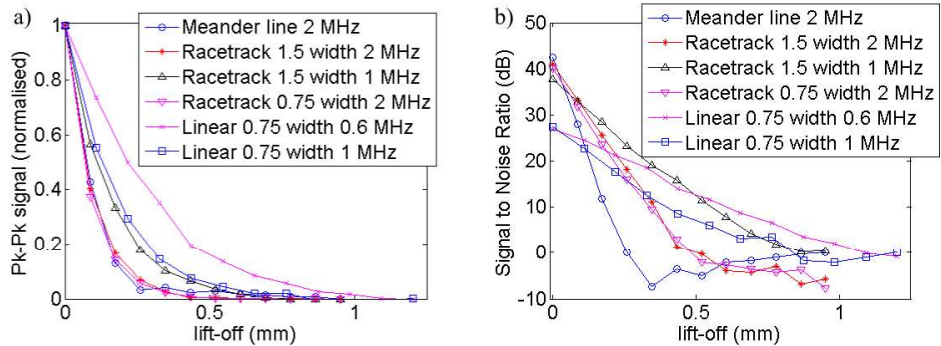


Figure 8.1: a) Maximum peak to peak signal detected by the focused EMAT designs (figures 3.3, 3.7, and 3.9) as the separation between the EMAT and the sample is increased. b) The signal shown in a) is converted to a signal to noise ratio (SNR). The frequencies given in the legend are the driving frequencies used for the generator coils.

Figure 8.1b) shows the signal to noise ratios (SNR) of the lift-off data shown in figure 8.1a), calculated by taking $20 \times \log_{10}(\text{signal}/\text{noise})$ [17]. The ‘noise’ estimate was obtained by finding the maximum and the minimum signals detected before the wave is generated, taking the absolute value of the minimum and adding it to the maximum, so it is comparative to the peak-to-peak value taken for the signal.

The meander-line EMAT (blue circles) clearly shows the worst SNR performance with lift-off, dropping to zero SNR at 0.3 mm lift-off from the sample. The

linear coils, although they start with a lower SNR when in contact with the sample, show the slowest decrease in their signal with lift-off, with signals above the noise level almost up to 1 mm lift-off. The racetrack coils exhibit behaviour part way between the two. It is suggested that the meander-line EMAT coil has such poor lift-off performance due to the creation of close proximity opposing magnetic dipoles from the sections of neighboring wire containing opposing current flow. At a distance from the coil these magnetic dipoles will cancel out, leading to poor signal generation. The racetrack coils will likely also see a similar effect but less pronounced as they only contain one pair of opposing dipoles. The linear coils do not contain any opposing dipoles and so have the least SNR drop off with increased lift-off. Full electro-magnetic field modelling is needed to test this theory.

The lift-off profiles are affected by the frequencies of operation. When operating the same linear coil pair at 0.6 MHz (pink crosses) and at 1 MHz (blue squares) it can be seen that the lower frequency performs the best at high lift-off. A similar effect is seen in the racetrack coils (red stars verses black triangles). Additionally, the coils do not all produce the same frequency signal that they are driven with. For example, the 1.5 mm racetrack coil pair, when driven with a 2 MHz driving signal, have a maximum magnitude in the FFT of the detected signal at 1.8 MHz, as shown in chapter 4. It has been shown in chapter 4 that the signal produced by the Ritec AC source actually increases with frequency and so this effect cannot be due to simply having a stronger current source.

It is well known that the eddy currents generated by a single coil will have a deeper penetration into a sample if they are lower frequency, as given by the skin depth (equation 2.54), however, this does not consider variations in the distance of the field source from the sample. It seems likely that this will lead to lower frequencies showing less effects from lift-off as observed but more modelling is needed.

8.2 Unfocused EMAT Calibration

Three unfocused, pitch-catch (transmission mode) EMATs were created to separate the effect of frequency from the effect of coil design on lift-off behaviour; one pair of 1.5 mm width racetrack coils (figure 8.2), one pair of 1.5 mm width linear coils (figure 8.3), and one pair of 0.75 mm width linear coils. The signals generated are weaker than the focused designs due to the use of smaller magnets and the lack of geometric focusing. The EMAT pair frequency response to different driving signals was first ascertained.

Figure 8.4a) shows the maximum peak-to-peak signal strength of the Rayleigh

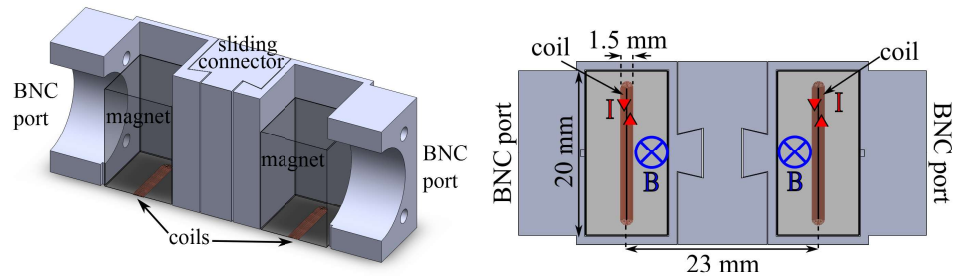


Figure 8.2: Calibration, unfocused racetrack EMAT transmission set-up, showing the cross-section and the bottom view.

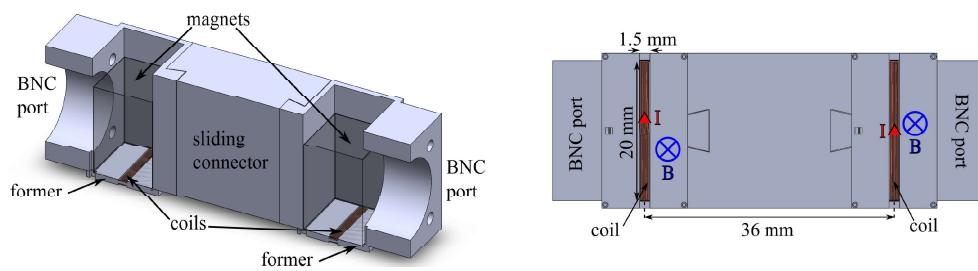


Figure 8.3: Calibration, unfocused linear EMAT transmission set-up, showing the cross-section and the bottom view.

wave generated and detected in aluminum by the racetrack design as the driving signal is changed in frequency with ‘zero’ lift-off. Both a single cycle, and a three cycle driving signal are used, as indicated in the legend. The single cycle has a wider bandwidth than the three cycle. The response when in contact with the sample is consistent with the findings of chapter 4, with the smoothing spline fit peaks occurring at 1.3 MHz for the 1 cycle data, and 1.4 MHz for the 3 cycle data. Figure 8.4b) shows the same test, with an addition of 0.2 mm of plastic beneath the whole EMAT. This gave peaks of 1.1 MHz for both the 1 cycle and the 3 cycle data. This drop is also consistent with the calculations made in chapter 4.

Figure 8.5 shows the same results at ‘zero’ lift-off for the calibration linear coil pairs. The data is much noisier as the amplitude of the generated signal is much weaker, making it difficult to pin point an accurate peak location, but the 0.75 mm width coils have a peak in efficiency close to 1 MHz, and the wider, 1.5 mm width coils are clearly generating preferentially below 1 MHz. The existence of a peak, rather than a gradual increase towards low frequencies does not match the theory discussed in section 4, but is consistent with the experimental data found with the focused linear coils in chapter 4 and the behaviour of the Ritec used for generating the signals.

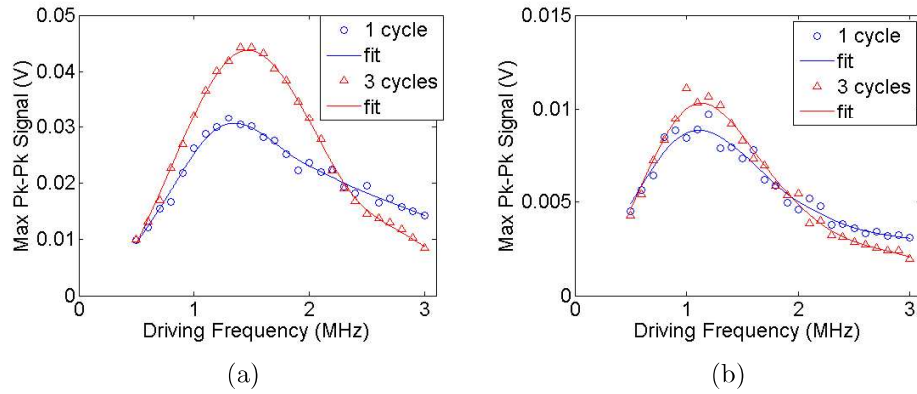


Figure 8.4: Frequency response of the unfocused racetrack pair shown in figure 8.2. a) as close to sample contact as the casing allows. b) 0.2 mm lift off added below both EMAT coils. 64 averages used. Fits shown are 0.99 smoothing spline fits.

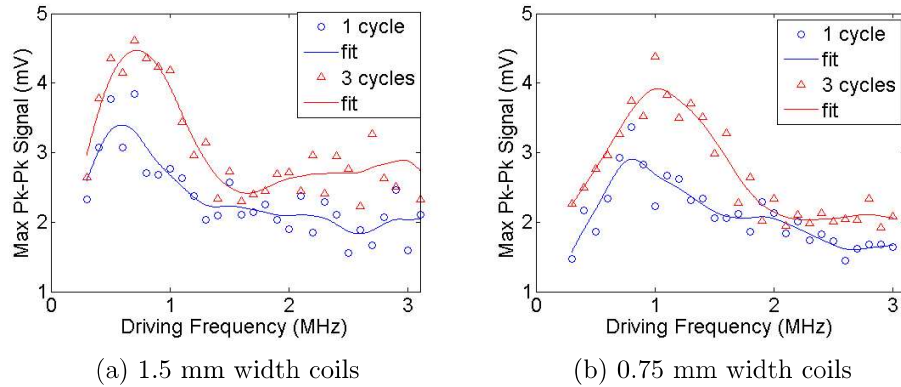


Figure 8.5: Frequency response of a) the unfocused linear pair shown in figure 8.3, and b) a similar pair but 0.75 mm in width, all taken as close to sample contact as the casing allows. 64 averages used. Fits shown are 0.99 smoothing spline fits.

Example lift-off behaviour at different frequencies is shown in figure 8.6 a) for the racetrack, and b) for the linear coils, for the case of adding lift-off under both the generator coil and the detector coil at the same time. This is representative of the presence of different thicknesses of coatings on a sample. Additionally, tests were done where the generator or detector were lifted off from the sample individually with the other remaining in contact. No difference was seen between lifting off just the generator vs lifting off just the detector, and the drop off was exactly half that of the drop off seen when both the generator and the were lifted off. The effect of both simply compounds the signal loss, and so only this final data is presented. It can be consistently seen that higher frequencies have worse performance at lift-off than lower frequencies for both coil designs.

All coils are found to produce a detectable signal when a 1 MHz excitation signal is used, and the FFT data also all give a maximum magnitude close to 1 MHz. The 1 MHz data is therefore used to compare the lift-off behaviour, plotted as an SNR in figure 8.6c). Some linear fits have been added to the data to aid the visual comparison of the different data plots. The linear coil data rapidly becomes very noisy and so it is difficult to differentiate at what point the data should be neglected as noise. However, regardless of the possible fits chosen, the linear coil data is found to have a slower decline in SNR than the racetrack coil data. An improved way of using or making the linear coils could therefore be beneficial.

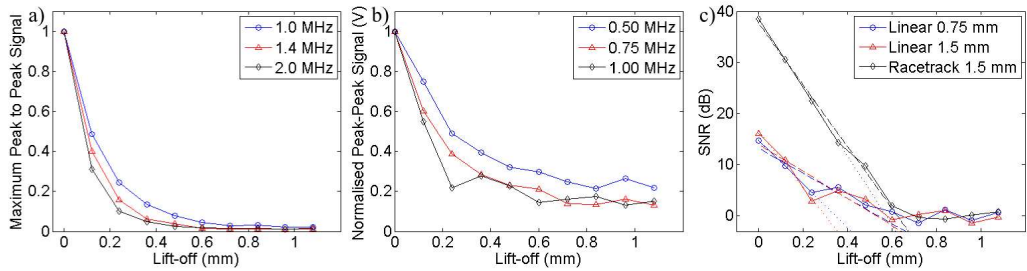


Figure 8.6: Maximum detected signal response as the coils are lifted from the sample for a) 1.5 mm unfocused racetrack coils, and b) 1.5 mm unfocused linear coils,. c) shows a comparison of the SNR from a), b), and a similar 0.75 mm width linear coil pair for a 1 MHz driving signal at 1 MHz. Some proposed linear fits have been added to the data to aid visualisation.

8.2.1 Generator versus Detector Effects

To investigate the dominant effects of the coil design on generated frequency and lift-off, a composite EMAT was produced using parts of the EMATs shown in the previous section. This composite EMAT has either a racetrack coil as a generator and a linear coil as a detector, or vice-versa. The 1.5 mm racetrack coil and the 0.75 mm linear coil both have frequency profiles centered around 1 MHz and so these widths were used for the composite EMAT. Figure 8.7 shows the 1 and 3 cycle data from changing the generation frequency for this composite system, once with the racetrack coil as the generator and the linear coil as the detector, and once with the linear coil as the generator and the racetrack coil as the detector.

It can be seen that both systems peak around 1 MHz, as would be expected, but their behaviour, particularly at higher frequencies, varies slightly. Some variation may be due to noise, however the profiles are still clearly distinct. The pair with a linear generator and a racetrack detector have a narrower profile in frequency,

with the detected signal dropping off faster above and below 1 MHz, than the profile with a racetrack generator and linear detector. As seen in the previous section, figures 8.4 and 8.5, the linear coil has a lower performance than the racetrack at high frequencies. This suggests that the generator coil behaviour is dominant in the composite EMAT. However, this comparison is purely qualitative as the data from the purely linear EMAT (figure 8.5) has low SNR.

It should also be noted that, despite the use of one linear coil, the amplitudes of the maximum signals detected by the composite EMAT are almost as strong as those detected by the two racetrack coil EMAT, with the maximum peak-to-peak signal of the composite EMAT falling just under 40 mV and the fully racetrack EMAT signal going up to just over 40 mV. This is surprising as the fully linear EMAT system peak-to-peak signals are lower than 5 mV, and a composite system would be expected to fall between the two, around 23 mV. This suggests that no matter which coil is employed as generator or detector, in the composite system the behaviour of the racetrack coil is dominating the signal strength detected. These voltages are laid out in table 8.1.

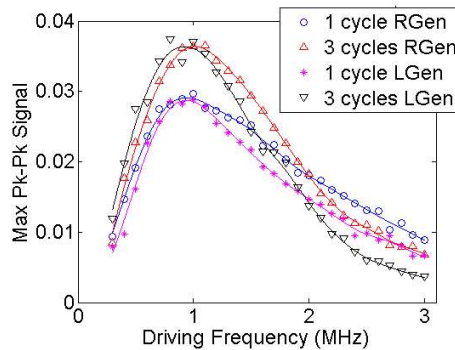


Figure 8.7: Frequency response of an unfocused composite EMAT pair. The legend entry ‘RGen’ indicates a 1.5 mm racetrack generator with a 0.75 mm linear detector. LGen indicates a 0.75 mm linear generator, and a 1.5 mm racetrack detector. 64 averages were used. Fits shown are 0.99 smoothing splines.

Figure 8.8 shows the lift-off behaviour of this composite EMAT, in comparison with the original purely racetrack and purely linear set-ups. Linear fits have again been added to the SNR data in figure 8.8b) to help show the relative gradients of the different data sets. It is found that the SNR variation with lift-off of the composite system is unchanged by swapping the generator and the detector around, and brings it approximately central between the purely racetrack and the purely linear system with regards to its lift-off behaviour. This indicates that in both systems the effects for the generator and the detector coils are equal, with the linear coils

Cycles	Generator	Detector	Maximum Pk-Pk Signal (mV)
1	Racetrack	Racetrack	30
	Racetrack	Linear	28
	Linear	Racetrack	28
	Linear	Linear	3
3	Racetrack	Racetrack	44
	Racetrack	Linear	37
	Linear	Racetrack	37
	Linear	Linear	4

Table 8.1: Summary table of the different peak-to-peak voltages found for different combinations of the 1.5 mm width racetrack coils and the 0.75 mm width linear coils in transmission.

being the least affected by increasing lift-offs despite their weaker signals. It can be concluded that the linear coil designs have the most potential for performing at high lift-offs. However, linear coils produce lower frequencies than the racetrack design for the same size coil, which reduces their ability to detect small defects. Their design needs optimizing for higher frequency signals.

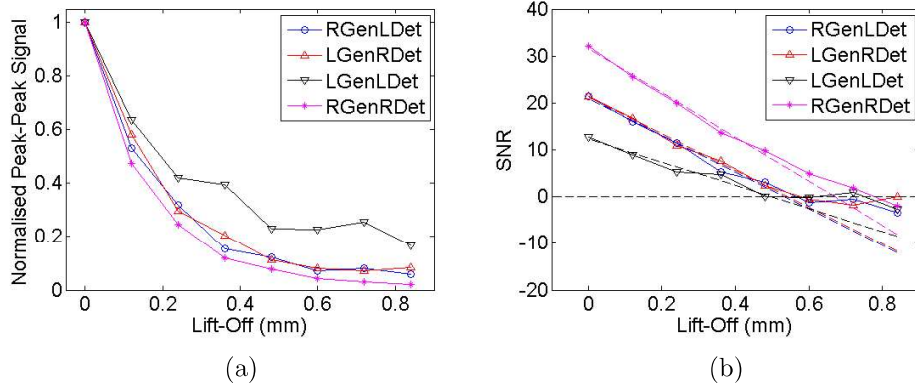


Figure 8.8: The lift-off behaviour of a composite racetrack-linear EMAT coil, in comparison with the behaviour of the racetrack-racetrack and the linear-linear coil behaviour. Legend values; ‘R’ indicates a racetrack coil, ‘L’ indicates a linear coil, ‘Gen’ indicates the generator coil, and ‘Det’ indicates the detector coil. a) shows the normalised peak to peak signals. b) shows the signal to noise ratio, with linear fits to the first five data points above the noise threshold.

8.3 Phased Linear Coils

The meander-line coils presented in chapter 5 show the strongest SNR when in contact with the sample. They also have the best capabilities to generate high frequencies without signal loss as a large coil can still be used, unlike racetrack and linear coils which have to decrease in width to function at higher frequencies (section 4). However, their poor lift-off performance makes them only applicable for close contact applications. It is believed that the reason the meander-line behaves so poorly with lift-off is because it creates opposing magnetic dipoles from opposing wire directions, required to force the ultrasound wave to the desired wavelength. However, at lift-off these magnetic dipoles cancel out, rapidly reducing the applied force in the sample. The linear coils presented in this chapter clearly show less SNR drop off with increased lift off and it is suggested that this is due to the lack of any opposing dipoles as all the wire elements have parallel current flow. However, linear coils have much weaker SNRs and a 2 MHz coil is not achievable.

Figure 8.9 shows a proposed phased EMAT design combining aspects of both the meander line EMAT and the linear EMAT design. The separate coil sets are linear in nature and so should have the best lift-off capability out of the different surface wave designs tested when used individually. The design shown in figure 8.9 is proposed to space the coils elements by $3\lambda/2$, and then to excite them with a corresponding time delay, so the opposing currents will not be active at the same time. This should create a meander-line style wavelength selection to give an increased signal strength, without the opposing current dipoles being active at the same time. A further improvement would be to include geometric focusing for higher signal strengths. A prototype design has been produced and is undergoing testing, using an specialist pulser system giving a phased output. Preliminary results suggest it is working as expected.

8.4 Conclusion

Meander-line designs improve the high frequency content of the wave generated but at the expense of lift-off capabilities, partially because higher frequencies intrinsically suffer more with the lift-off, and partly due to the occurrence of opposing magnetic dipoles in the meander-line design, although the latter needs to be modelled for confirmation. Linear designs are shown to have the best lift-off capabilities but the weakest overall signals. A phased design is proposed to retain the high frequency nature of the meander-line designs, but with improved lift-off capability

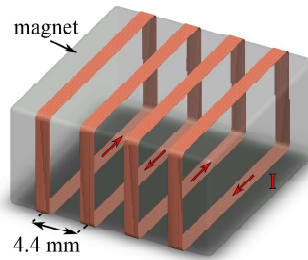


Figure 8.9: A proposed linear coil design to improve the high frequency capabilities of a linear EMAT. Coils are spaced by $3\lambda/2$ and will be fired with a time delay so the opposing forces from the opposing current directions are not active at the same time.

as the phasing eliminates the opposing magnetic dipoles. This is under study by a new PhD student.

It is still not known why the linear coils perform better with lift-off, nor why the racetrack coils dominate in a composite racetrack/linear system. It was thought that, as detection is a simpler mechanism than generation, a racetrack generation coil and a linear detection coil would create a good compromise, however this is not the case, and commuting the generation and detection coils makes no measureable difference, and is in fact much closer in signal strength to a fully racetrack system than a fully linear system. Full EMAT modelling is needed to study this. This is under further investigation from another PhD student, including COMSOL models, and experimental work at lower frequencies where the linear coils are larger with better SNR, and investigating linear coils that are wrapped fully around the magnet for further noise reduction.

Chapter 9

Conclusions and Further Work

9.1 Conclusions

This work has addressed a gap in the literature for the accurate detection and sizing of sub-mm surface breaking defects using Rayleigh wave EMATs. This work is necessary for the early stage detection of RCF and SCC type cracks using a non-contact method, allowing for fast scanning without coupling gel, using a relatively safe and inexpensive technique, with inspection on the same surface as the transducer. Similar focused EMAT shear wave techniques have been used [97], however this is for inspecting the opposite surface of a sample to the EMAT, rather than the same surface. In some situations, such as inside buried pipes, only one side is accessible, and so a Rayleigh wave technique can be needed depending on the location of defects. The main other systems used for this type of detection are piezoelectric arrays, which cannot be scanned easily or used in harsh environments, and eddy current systems. Eddy current systems do not provide the accurate sizing and orientation information which the EMAT systems used in this work give, however, in some situations they can provide higher resolution.

Three main types of coil have been used; linear, racetrack, and meanderline. Geometric focused designs of all three have been produced. Focused Rayleigh wave meanderline EMATs do appear in a standard by the American Society for Acoustic Testing [99], but have not been reported in detail in the literature. Focused racetrack and linear designs do not appear in the literature. The meanderline has only been tested in reflection and the racetrack and linear coils have only been tested in transmission, however, the generation methods are commutable. The linear design generates the weakest signals, and is the most inefficient design, however, it has the least SNR reduction as the coil is lifted-off from the sample surface. The meander-

line designs have the strongest signals but the largest SNR reduction as the coil is lift-off from the sample. Therefore in situations where the sample is known to be very flat, and so 0.1 mm lift-off or less can be used, the meander-line designs are the optimal transducer. The racetrack coil provides a good intermediary compromise between signal strength and lift-off properties, especially if used in transmission rather than reflection, so that the coils can be kept in close proximity for an increased signal strength.

The relation between focal point size and coil geometry has been detailed for both meander-line and racetrack coil generation and the designs fully characterised, so that any new designs can be made tailored to the desired focal point position, size, and frequency. Care must be taken in the design of both the meander-line and the racetrack designs. Focused meander-line designs with under 20° aperture angle have shorter focal distances from the geometric focal point than designed. The frequency content that racetrack designs can generate and detect is partly dependent on the coil geometry and on the lift-off from the sample. Simple analytical models overestimate the optimum frequency for racetrack coils, and time dependent modeling must be used. Increasing lift-off lowers the optimum frequency of operation.

The reflection, focused, meander-line EMAT design and the transmission, focused, racetrack EMAT design have been employed for surface breaking defect detection on a set of milled calibration defects, and can predict defect lengths within ± 0.5 and ± 0.4 mm respectively. The smallest calibration machined defect they have been used to detect is a 0.5 mm deep, 1 mm diameter milled hole. They have also been employed on a large overlapping pair of cracks in an aluminium billet sample, and a set of sub-mm cracks beneath a metallic paint coating in a set of flat steel samples. The transmission EMAT cannot map the overlap between the two cracks on the aluminium billet as they are closer together than the distance between the coils, however, the meander-line EMAT maps the overlap with similar accuracy to the rest of the cracks. The reflection meander-line EMAT was too difficult to position accurately by hand to scan the defects on ferritic steel, however the racetrack transmission EMAT detected the majority of the expected defects, especially when the extra information of the signal arrival time and the signal frequency content is added to the reduction in signal strength. It can be concluded that for defect features with a length extent longer than the distance between the transmission coils, or defects in closer proximity to each other than the distance between the transmission coils, more accurate surface maps can be made using the reflection meander-line EMAT. However, use of a four coil set and different generator and detector orientations can allow for mapping of more complex defect orientations than the reflection meander-

line EMAT. The transmission designs also provide defect depth information, or at least a minimum depth if the defect is much larger than the ultrasound wave length, which the transmission EMAT does not provide.

It is proposed that a composite EMAT-eddy current system would provide the best system for mapping small surface breaking defects [153, 42]. The focused meander-line and racetrack EMATs have been shown to work through thin coatings (40-60 μm thick) detecting real defects, however, more work is needed to improve their lift-off capabilities, which are 0.5 mm and less, depending on the coil and application. A variety of further designs have been proposed for this purpose.

9.2 Future Directions

Two clear areas of further work are the implementation of the focused designs presented onto pipe shafts and thin sheets. The extension from Rayleigh waves, with only one surface affecting the wave, to a thin sheet, or a pipe adding curvature, creates guided wave modes [48]. The meander-line pitch (coil spacing) could be employed to select a desired mode [48, 154]. The focal effect around a curved surface will also need to be investigated and modeled to design a suitable coil. Another clear extension is the ability of EMATs to function at high temperatures. Both of these techniques have been implemented with EMATs [77, 155, 156] but never with the designs presented in this work. These designs will give improved signal strength and SNR for the detection of smaller defects on pipe shafts, sheet materials, and at high temperatures, of interest to the oil and gas industry, steel milling, and the power industry.

A further point for investigation is coupling the scans using these transducers with eddy current techniques. The transducers presented in this work lend themselves to situations in which eddy current techniques are often employed, however, they provide information which is not as material dependent as eddy current techniques, especially when it comes to defect depth measurements. The four coil EMAT system presented in section 6.3 also gives defect orientation which eddy current coils cannot, unless they are far smaller than standard and arrays are used. It is proposed that data fusion with an eddy current coil, or set of coils, positioned at the EMAT focal point, could add sensitivity to smaller defects by using the eddy current system, but coupled with the extra information that the ultrasonic signal gives on larger defects [43, 157]. The definitive detection from the eddy current coil system could be used to eliminate false positives from the EMAT system and provide and improve defect map, and vice-versa.

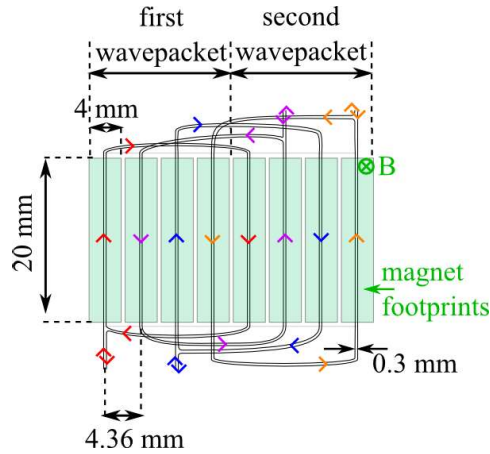


Figure 9.1: Proposed phased nested four coil EMAT design.

The next two sections propose further EMAT designs building on the work presented here, and the preliminary work performed to indicate that these designs could be beneficial.

9.2.1 Four Coil Phased Designs

A four coil, phased design has already been proposed in section 8.3. This presented a set of four linear coils, spaced $3\lambda/2$ apart, so that a single cycle sine current impulse can be sent to each coil with corresponding time delays such that the Rayleigh wave generated by each coil will re-enforce the wave generated by the next coil. This generates a stronger signal than one coil can generate, operating at higher frequencies than a single, larger coil. Linear designs have been found to have the best performance with increasing lift-off, however, the more wire is being actively used to generate ultrasound, the more efficient the design is. It is plausible that the reason for the better performance of the linear coils with lift-off is their lack of opposing dipoles. Therefore, a phased, nested four coil loop design is proposed. This will actively use the majority of the wire to generate ultrasound, making it more efficient, while at the same time spreading out the sections of wire which have opposing dipoles if activated at the same time.

The proposed schematic is shown in figure 9.1. Neighboring wire segments will be fired after a time delay (again, spaced as $3\lambda/2$) so no neighboring opposing dipole will be active at the same time. This should give it lift-off capabilities similar to that of a linear coil design. A separate magnet is used over each wire segment to reduce interference between the coils, and prevent a traveling wave in the bottom of the magnet reaching other coil loops, as was observed in earlier designs. This design

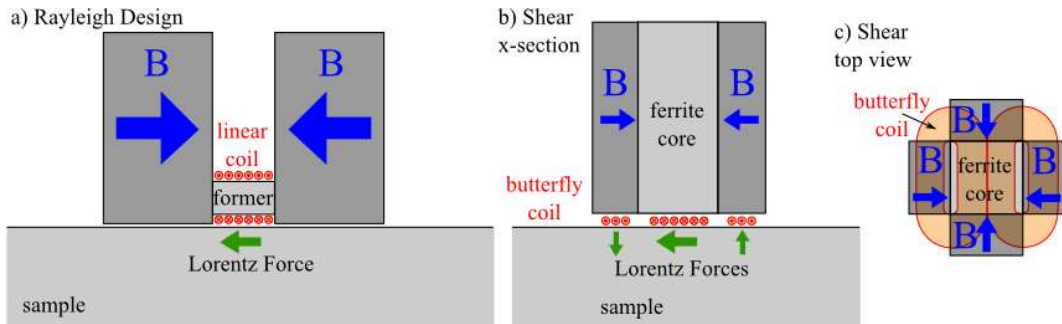


Figure 9.2: Edge field EMAT designs for a) Rayleigh wave detection, presented by Dutton et. al. [144], c) and c) shear waves, presented by Isla et. al. [152].

will create two wave packets, one generated by the first half of each coil loop, and one generated by the second half of each loop. This dual wave packet nature can also be exploited using a cross-correlation technique to improve signal detection, such as has been done before with chirp signals [2]. This will, however, reduce the lateral resolution of the EMAT as the signal becomes extended in time. This design has been constructed but not tested.

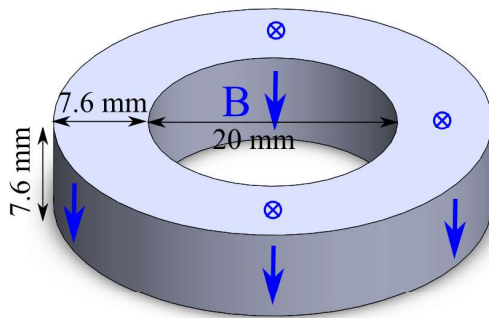
A further improvement to the spatial resolution of both the linear and the loop phased designs would be to then incorporate geometric focusing.

9.2.2 Magnetic Edge Field Designs

It has been reported by Dutton et. al. [144], and Isla et. al. [152] that placing an EMAT coil in between two magnets which are north-north aligned can improve the EMAT performance at lift-off. Figure 9.2a) shows the design created by Dutton et. al. for Rayleigh wave detection, b) and c) show the design from Isla et. al. designed for shear wave detection. Both exploit the fact that the opposing magnetic fields force the field to become vertical in between the two magnets, within a confined space, creating a concentrated vertical field. Both works report stronger magnetic fields between the coils than when using a single magnet. However, the experimental comparisons made by Dutton et. al. did not account for the large increase in magnet volume that their edge field design contains, compared to the single magnet, traditional linear EMAT design. Isla et. al. used FEA to compare multiple designs using comparative magnet sizes, and still found the edge field concentration, when including ferrite in the gap to further constrict the magnetic field lines, to give the strongest fields.

To create a similar edge field for the focused racetrack coil designs used, ideally two ring magnets would be used, with the inner one having a radial polar-

a) single ring magnet



b) unphysical concentric ring magnets

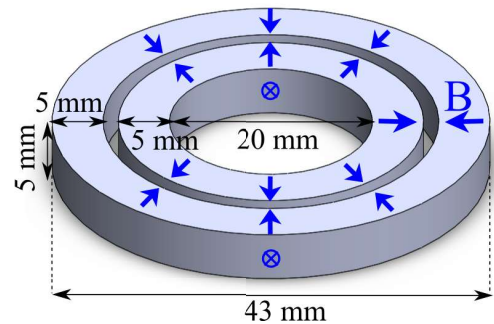


Figure 9.3: Magnets built in COMSOL to compare magnetic fields created. a) is a reference ring magnet similar to those used in previous sections, designed to have the same volume as the two magnets in b). b) shows the design that would be required for an edge field design with the focused designs used in previous work.

isation outwards, and the outer ring magnet having a radial polarisation inwards, figure 9.3b). These magnets are unphysical, as radial fields like this cannot be created, however it can be approximated with multiple smaller magnets, as shown later in figure 9.5. This has been modeled in COMSOL for a pair of rings, as shown in figure 9.3b), and also for a reference single ring, as sketched in figure 9.3a), calculated to have approximately the same volume of magnet (5000 mm^3) as the design in b) for a fair comparison. This was modeled using rotational symmetry about the central axis. A radial position of 15.75 is therefore directly between the two rings in the concentric design, and the center of where the EMAT coil would be positioned. A position of 15 mm, under the outer edge of the inner ring magnet, is also considered. These positions are compared with the field at a radial position of 13.8 mm in the single ring design, this being central under the ring magnet.

Figure 9.4 shows the vertical component of the magnetic field for radial positions of 15 and 15.75 mm in the concentric ring design, and 13.8 mm for the single ring design. The horizontal field component is close to zero for the concentric ring design and so is neglected here. The horizontal axis shows vertical position, so between 0 and 5 mm is within the magnet height range for the concentric ring designs, and between 0 and 7.6 mm is within the body of the ring magnet for the single ring design. The negative positions on the horizontal axis are below the magnets, and so shows the field that will interact with any sample to be studied. It can be seen that while the field values are similar at 0 mm, and the field drop off for the single large ring is slower than the field for the concentric rings. This suggests that a single large ring has just as strong a vertical field as the new design at the surface, and the single ring in fact has a stronger field beneath the coil than

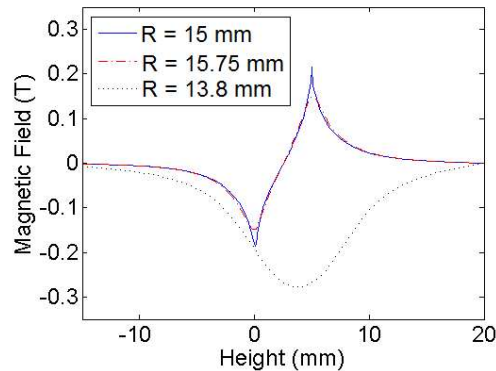


Figure 9.4: A comparison of the vertical component of the magnetic field for radial positions of 13.8 mm in the single ring design (as figure 9.3 a)), and 15 and 15.75 mm in the concentric rings designs (as figure 9.3 b)).

beneath the concentric ring pair.

However, despite the unfavorable model results, decreasing the magnet field in the sample is of interest to improve the ability to scan ferritic samples. An edge field design might therefore still give a strong field right at the sample surface, but with less overall interaction with the sample, allowing it to be moved more easily. The field concentrating effects of the ferrite sample need to be modeled. Figure 9.5 shows a design to combine the focused racetrack coils already presented in this work with the edge field design presented by Dutton et. al. It has been built but has not been characterised. The volume of magnet used has been greatly decreased compared to the designs used in previous chapters, however it is hoped that the design will still give strong signals at the surface due to the field arrangement. If edge field work shows further promise, it can be incorporated with the nested phased design shown in figure 9.1 by fitting edge field magnets between the wire elements instead of directly above them.

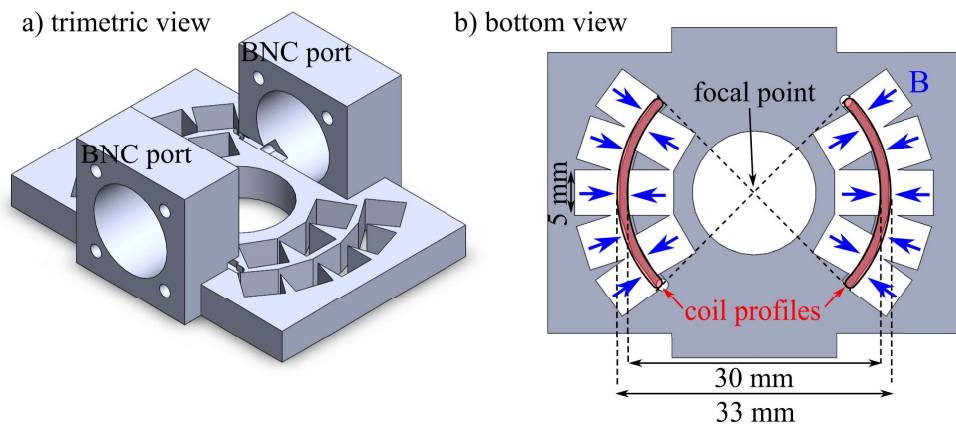


Figure 9.5: a) trimetric view of the 3D printed holder created for a focused edge field EMAT design. b) bottom view of the holder with the coil positions and the magnetic field directions added. The magnets are 5 mm cuboidal, N50, NdFeB.

Bibliography

- [1] P Thayer. RCNDE industrial members vision for the future requirements for NDE. *Insight*, 54:124–127, 2012.
- [2] H. Hirao, M. Ogi. *EMATs for Science and Industry Noncontacting Ultrasonic Measurements*. Kluwer Academic Publishers, Boston, 2003.
- [3] C. B. Thring, Y. Fan, and R. S. Edwards. Focused Rayleigh wave EMAT for characterisation of surface-breaking defects. *NDT and E International*, 81:20–27, 2016.
- [4] C. B. Thring, Y. Fan, and R.S. Edwards. Multi-coil focused EMAT for characterisation of surface-breaking defects of arbitrary orientation. *NDT & E International*, 88:1–7, 2017.
- [5] C. B. Thring, S. J. Hill, S. Dixon, and R. S. Edwards. The Effect of EMAT Coil Geometry on the Rayleigh Wave Frequency Behaviour. 2018.
- [6] P.E. Bold, M.W. Brown, and R.J. Allen. Shear mode crack growth and rolling contact fatigue. *Wear*, 144(1):307–317, 1991.
- [7] J W Ringsberg. Life prediction of rolling contact fatigue crack initiation. *International Journal of Fatigue*, 23:575–586, 2001.
- [8] S L Grassie. Rolling contact fatigue on the british railway system: treatment. *Wear*, 258:1310–1318, 2005.
- [9] D.F. Cannon and H. Pradier. Rail rolling contact fatigue Research by the European Rail Research Institute. *Wear*, 191(1-2):1–13, 1996.
- [10] D. F. Cannon, K. O. Edel, S. L. Grassie, and K. Sawley. Rail defects: An overview. *Fatigue and Fracture of Engineering Materials and Structures*, 26(10):865–886, 2003.

- [11] G. N. Haidemenopoulos, P. I. Sarafoglou, P. Christopoulos, and A. D. Zervaki. Rolling contact fatigue cracking in rails subjected to in-service loading. *Fatigue and Fracture of Engineering Materials and Structures*, 39(9):1161–1172, 2016.
- [12] K R Tretheway. Some observations on the current status in the understanding of stress-corrosion cracking of stainless steels. *Materials and Design*, 29:501–507, 2008.
- [13] Yichao Fan. *The analysis of surface defects using the ultrasonic Rayleigh surface wave*. PhD thesis, University of Warwick, 2008.
- [14] Y Fan, S Dixon, R S Edwards, and X Jian. Ultrasonic surface wave propagation and interaction with surface defects on rail track head. *Non-Destructive Testing and Evaluation International*, 40:471–477, 2007.
- [15] P A Petcher, M D G Potter, and S Dixon. A new electromagnetic acoustic transducer (EMAT) design for operation on rail. *Non-Destructive Testing and Evaluation International*, 65:1–7, 2014.
- [16] Kaye and Laby. *Tables of Physics and Chemical Constants*. National Physical Laboratory.
- [17] J Blitz and G Simpson. *Ultrasonic Methods of Non-destructive Testing*. Chapman and Hall, London, 1996.
- [18] S. Kenderian, B. B. Djordjevic, and R. E. Green. Point and line source laser generation of ultrasound for inspection of internal and surface flaws in rail and structural materials. *Research in Nondestructive Evaluation*, 13(4):189–200, 2001.
- [19] R. N. Parkins. Stress Corrosion Spectrum. *British Corrosion Journal*, 7(1972):15–28, 1972.
- [20] K. Sieradzki and R.C. Newman. Stress-corrosion cracking. *Journal of Physics and Chemistry of Solids*, 48(11):1101–1113, 1987.
- [21] F. Hernandez-Valle, A. R. Clough, and R. S. Edwards. Stress corrosion cracking detection using non-contact ultrasonic techniques. *Corrosion Science*, 78:335–342, 2014.
- [22] F. Hernandez-Valle, B. Dutton, and R. S. Edwards. Laser ultrasonic characterisation of branched surface-breaking defects. *NDT and E International*, 68:113–119, 2014.

- [23] C. Manfredi and J. L. Otegui. Failures by SCC in buried pipelines. *Engineering Failure Analysis*, 9(5):495–509, 2002.
- [24] Dr. R. A. Cottis. Guides to Good Practise in Corrosion Control: Stress Corrosion Cracking. Technical report, Corrosion and Protection Centre, National Physical Laboratory, 2000.
- [25] ASTM. Standard practice for evaluating stress-corrosion cracking resistance of metals and alloys in a boiling magnesium chloride solution. *Annual book of ASTM standards*, 0302(G36-9:123–8, 1996.
- [26] Gene Mathers. Welding of austenitic stainless steel. Part 2. Technical report, The Welding Institute, TWI Ltd., 2015.
- [27] Barry Hull and Vernon John. Liquid Penetrant Inspection. In *Non-Destructive Testing*, pages 7–17. Macmillan Education UK, London, 1988.
- [28] Louis Cartz. *Nondestructive testing: radiography, ultrasonics, liquid penetrant, magnetic particle, eddy current*. Materials Park, OH : ASM International, 1995.
- [29] Gwan Soo Park and Eun Sik Park. Improvement of the sensor system in magnetic flux leakage-type nondestructive testing (NDT). *IEEE Transactions on Magnetics*, 38(2 I):1277–1280, 2002.
- [30] M J Lovejoy. *Magnetic particle inspection: a practical guide*. Springer Science & Business Media, 2012.
- [31] Uwe Ewert, Kurt Osterloh, and Bernhard Redmer. *Handbook of Technical Diagnostics*. 2013.
- [32] Ioannis Valavanis and Dimitrios Kosmopoulos. Multiclass defect detection and classification in weld radiographic images using geometric and texture features. *Expert Systems with Applications*, 37(12):7606–7614, 2010.
- [33] C. V. Dodd and W. E. Deeds. Analytical solutions to eddy-current probe-coil problems. *Journal of Applied Physics*, 39(6):2829–2838, 1968.
- [34] Robert Rhys Hughes. *High-sensitivity eddy-current testing technology for defect detection in aerospace superalloys*. PhD thesis, 2015.
- [35] J Blitz. *Electrical and Magnetic Methods of Non-destructive Testing*. Chapman and Hall, London, 1997.

- [36] Jay A Bieber, Cheng-chi Tai, and John C Moulder. Quantitative assesment of corrosion in aircraft structures using scanning pulsed eddy current. pages 315–322, 1998.
- [37] Gui Yun Tian, Ali Sophian, David Taylor, and John Rudlin. Multiple sensors on pulsed eddy-current detection for 3-D subsurface crack assessment. *IEEE Sensors Journal*, 5(1):90–96, 2005.
- [38] M. Mina, S. S. Udpa, L. Udpa, and J. Yimx. A new approach for practical two dimensional data fusion utilizing a single eddy current probe. In *Review of Progress in Quantitative Nondestructive Evaluation*, volume 16, pages 749–755, 1997.
- [39] Bruce W. Drinkwater and Paul D. Wilcox. Ultrasonic arrays for non-destructive evaluation: A review. *NDT and E International*, 39(7):525–541, 2006.
- [40] Raimond Grimberg, Lalita Udpa, Adriana Savin, Rozina Steigmann, Valerian Palihovici, and Satish S. Udpa. 2D Eddy current sensor array. *NDT and E International*, 39(4):264–271, 2006.
- [41] H.A. Wheeler. Formulas for the Skin Effect. *Proceedings of the IRE*, 30(9):412–424, 1942.
- [42] R. S. Edwards, A. Sophian, S. Dixon, and G. Y. Tian. Data fusion for defect characterisation using a dual probe system. *Sensors and Actuators, A: Physical*, 144(1):222–228, 2008.
- [43] X. E. Gros, J. Bousigue, and K. Takahashi. NDT data fusion at pixel level. *NDT and E International*, 32(5):283–292, 1999.
- [44] R. Hughes, Y. Fan, and S. Dixon. Near electrical resonance signal enhancement (NERSE) in eddy-current crack detection. *NDT and E International*, 66:82–89, 2014.
- [45] Nicola Bowler. Theory of four-point alternating current potential drop measurements on a metal half-space. *Journal of Physics D: Applied Physics*, 39(3):584–589, 2006.
- [46] H. Saguy and D. Rittel. Flaw detection in metals by the ACPD technique: Theory and experiments. *NDT and E International*, 40(7):505–509, 2007.

- [47] Farhang Honarvar, Farzaneh Salehi, Vahid Safavi, Arman Mokhtari, and Anthony N. Sinclair. Ultrasonic monitoring of erosion/corrosion thinning rates in industrial piping systems. *Ultrasonics*, 53(7):1251–1258, 2013.
- [48] J L Rose. *Ultrasonic Waves in Solid Media*. Cambridge University Press, 1999.
- [49] A. P. Cracknell. *Ultrasonics*. Wykeham Publication (London) Ltd., 1980.
- [50] R. S. Edwards, X. Jian, Y. Fan, and S. Dixon. Signal enhancement of the in-plane and out-of-plane Rayleigh wave components. *Applied Physics Letters*, 87(19):1–3, 2005.
- [51] R. S. Edwards, S Dixon, and X Jian. Enhancement of the Rayleigh wave signal at surface defects. *Journal of Physics D: Applied Physics*, 37(16):2291–2297, 2004.
- [52] Amir Manbachi and Richard S.C. Cobbold. Development and application of piezoelectric materials for ultrasound generation and detection. *Ultrasound*, 19(4):187–196, 2011.
- [53] Walter Heywang, Karl Lubitz, and Wolfram Wersing. *Piezoelectricity Evolution and Future of a Technology*. Springer-Verlag Berlin Heidelberg, 2008.
- [54] S. C. Minne, S. R. Manalis, and C. F. Quate. Parallel atomic force microscopy using cantilevers with integrated piezoresistive sensors and integrated piezoelectric actuators. *Applied Physics Letters*, 67(1995):3918, 1995.
- [55] Timothy Galante, Jeremy Frank, Julien Bernard, Weiching Chen, George A. Lesieutre, and Gary H. Koopmann. Design, modeling, and performance of a high force piezoelectric inchworm motor, 1999.
- [56] Jian Li, Ramin Sedaghati, Javad Dargahi, and David Waechter. Design and development of a new piezoelectric linear Inchworm. *Mechatronics*, 15(6):651–681, 2005.
- [57] SE Burrows, KL McAughey, RS Edwards, and S Dixon. Solgel prepared bismuth titanate for high temperature ultrasound transducers. *RSC Advances*, 2(9):3678, 2012.
- [58] Atsushi Baba, Clifford T. Searfass, and Bernhard R. Tittmann. High temperature ultrasonic transducer up to 1000 c using lithium niobate single crystal. *Applied Physics Letters*, 97(23):2–5, 2010.

- [59] M. Castaings. The generation, propagation, and detection of Lamb waves in plates using air-coupled ultrasonic transducers. *The Journal of the Acoustical Society of America*, 100(5):3070, 1996.
- [60] Gordon Dobie, Rahul Summan, S. Gareth Pierce, Walter Galbraith, and Gordon Hayward. A noncontact ultrasonic platform for structural inspection. *IEEE Sensors Journal*, 11(10):2458–2468, 2011.
- [61] Firas Akasheh, Todd Myers, John D. Fraser, Susmita Bose, and Amit Bandyopadhyay. Development of piezoelectric micromachined ultrasonic transducers. *Sensors and Actuators, A: Physical*, 111(2-3):275–287, 2004.
- [62] David W. Schindel, Lichun Zou, Michael Sayer, and David A. Hutchins. The Design and Characterization of Micromachined Air-Coupled Capacitance Transducers. *IEEE Transactions on Ultrasonics, Ferroelectrics, and Frequency Control*, 42(1):42–50, 1995.
- [63] Tobias J.R. Eriksson, Michael Laws, Lei Kang, Yichao Fan, Sivaram N. Ramadas, and Steve Dixon. Experimental evaluation of three designs of electrodynamic flexural transducers. *Sensors*, 16(9):0–9, 2016.
- [64] Tomás E. Gómez Álvarez-Arenas. Air-coupled piezoelectric transducers with active polypropylene foam matching layers. *Sensors (Switzerland)*, 13(5):5996–6013, 2013.
- [65] Lei Kang, Andrew Feeney, Riliang Su, David Lines, Axel Jager, Han Wang, Yavor Arnaudov, Sivaram Nishal Ramadas, Mario Kupnik, and Steve Dixon. Two-dimensional flexural ultrasonic phased array for flow measurement. *IEEE International Ultrasonics Symposium, IUS*, pages 3–6, 2017.
- [66] G.I.I. Dobie, a. Spencer, K.C. Burnham, S.G. Pierce, K. Worden, W. Galbraith, and G. Hayward. Simulation of ultrasonic lamb wave generation, propagation and detection for an air coupled robotic scanner. 2009.
- [67] C. B. Scruby and L. E. Drain. *Laser ultrasonics : techniques and applications*. Bristol : Adam Hilger, 1990.
- [68] S Dixon, T Harrison, Y Fan, and P A Petcher. Thermoelastic laser generated ultrasound using a ring source. *J. Phys. D*, 45(175103), 2012.
- [69] S. Dixon, C. Edwards, and S. B. Palmer. Generation of ultrasound by an expanding plasma. *Journal of Physics D: Applied Physics*, 29(12):3039–3044, 1996.

- [70] Marvin B. Klein, G. David Bacher, Anders Grunnet-Jepsen, Daniel Wright, and W. E. Moerner. Homodyne detection of ultrasonic surface displacements using two-wave mixing in photorefractive polymers. *Optics Communications*, 162(1):79–84, 1999.
- [71] J. P. Monchalin, J. D. Aussel, R. Héon, C. K. Jen, A. Boudreault, and R. Bernier. Measurement of in-plane and out-of-plane ultrasonic displacements by optical heterodyne interferometry. *Journal of Nondestructive Evaluation*, 8(2):121–133, 1989.
- [72] I Baillie, P Griffith, X. Jian, and S Dixon. Implementing an ultrasonic inspection system to find surface and internal defects in hot, moving steel using EMATs. In *45th Annual British Conference on NDT*, 2006.
- [73] R J Dewhurst, C Edwards, and S B Palmer. Noncontact detection of surface-breaking cracks using a laser acoustic source and an electromagnetic acoustic receiver. *Applied Physics Letters*, 49(7):374–376, 1986.
- [74] X Jian, I Baillie, and S Dixon. Steel billet inspection using laser-EMAT system. *Journal of Physics D: Applied Physics*, 40:1501–1506, 2007.
- [75] X Jian, S Dixon, and S B Palmer. In-plane and Out-of-plane Particle Velocity Measurement Using Electromagnetic Acoustical Transducers. *IEEE Ultrasonics Symposium*, 2:1276–1279, 2005.
- [76] Francisco Hernandez-Valle and Steve Dixon. Initial tests for designing a high temperature EMAT with pulsed electromagnet. *NDT and E International*, 43(2):171–175, 2010.
- [77] N. Lunn, S. Dixon, and M. D.G. Potter. High temperature EMAT design for scanning or fixed point operation on magnetite coated steel. *NDT and E International*, 89:74–80, 2017.
- [78] K. S. Ho, D. R. Billson, and D. A. Hutchins. Inspection of drinks cans using non-contact electromagnetic acoustic transducers. *Journal of Food Engineering*, 80(2):431–444, 2007.
- [79] C. Holmes, B. W. Drinkwater, and P. D. Wilcox. Post-processing of the full matrix of ultrasonic transmit-receive array data for non-destructive evaluation. *NDT & E International*, 38:701–711, 2005.

- [80] Jie Zhang, Bruce W. Drinkwater, and Paul D. Wilcox. The use of ultrasonic arrays to characterize crack-like defects. *Journal of Nondestructive Evaluation*, 29(4):222–232, 2010.
- [81] David Reilly, Gordon Hayward, and Senior Member. A model to predict the transient radiation from segmented annular rings radiating into solid media. 43(2), 1996.
- [82] Shi-Chang Woo and Yijun Shi. Influence of phased array element size on beam steering behavior. *Ultrasonics*, 36:737–749, 1998.
- [83] J. Isla and F. Cegla. EMAT phased array: A feasibility study of surface crack detection. *Ultrasonics*, 78:1–9, 2017.
- [84] K. Sawaragi, H. J. Salzburger, G. Hübschen, K. Enami, A. Kiriigashi, and N. Tachibana. Improvement of SH-wave EMAT phased array inspection by new eight segment probes. *Nuclear Engineering and Design*, 198(1):153–163, 2000.
- [85] Y. Ohara, T. Oshiumi, H. Nakajima, K. Yamanaka, X. Wu, T. Uchimoto, T. Takagi, T. Tsuji, and T. Mihara. Ultrasonic phased array with surface acoustic wave for imaging cracks. *AIP Advances*, 7(6), 2017.
- [86] W A K Deutsch, A Cheng, and J D Achenback. Self-Focusing of Rayleigh Waves and Lamb Waves with a Linear Phased Array. *Research in Nondestructive Evaluation*, 9(2):81–95, 1997.
- [87] B G Kim, J O Lee, and S Lee. New design and analysis for point-focusing of surface waves in contact testing. *IEEE Transactions on Ultrasonics, Ferroelectrics, and Frequency Control*, 40(2):162–166, 1993.
- [88] W A K Deutsch, A Cheng, and J D Achenback. Focusing of Rayleigh waves: simulation and experiments. *IEEE Transactions on Ultrasonics, Ferroelectrics, and Frequency Control*, 2A(2):333–340, 1999.
- [89] P Cielo, F Nadeau, and M Lamontagne. Laser generation of convergent acoustic waves for materials inspection. *Ultrasonics*, 23(2):55–62, 1985.
- [90] Xiao Wang, Michael G. Littman, John B. McManus, Mohsen Tadi, Young Sik Kim, Attila Askar, and Herschel Rabitz. Focused bulk ultrasonic waves generated by ring-shaped laser illumination and application to flaw detection. *Journal of Applied Physics*, 80(8):4274, 1996.

- [91] T Stratoudaki, J A Hernandez, M Clark, and M G Somekh. Cheap optical transducers (CHOTs) for narrowband ultrasonic applications. *Measurement Science and Technology*, 18(3):843–851, 2007.
- [92] Ahmet Arca, Jon Aylott, Leonel Marques, Matt Clark, Mike Somekh, Richard Smith, Steve Sharples, Teti Stratoudaki, and Xuesheng Chen. CHOTs optical transducers. *Nondestructive Testing and Evaluation*, 26(3-4):353–366, 2011.
- [93] R J Gutfeld, D R Vigliotti, C S Ih, and W R Scott. Thermoelastic hologram for focused ultrasound. *Applied Physics Letters*, 42:1018, 1983.
- [94] H Kim, K Jhang, M Shin, and J Kim. A noncontact NDE method using a laser generated focused Lamb wave with enhanced defect-detection ability and spatial resolution. *Nondestructive Testing and Evaluation International*, 39(4):312–319, 2006.
- [95] G A Alers and D T Maclauchlan. High frequency, angle beam EMATs for weld inspection. *Review of Progress in Quantitative Nondestructive Evaluation*, 2A(5):271–281, 1983.
- [96] H Ogi, M Hirao, and T Ohtani. Line-Focusing Electromagnetic Acoustic Transducers for the Detection of Slit Defects. *IEEE Transactions on Ultrasonics, Ferroelectrics, and Frequency Control*, 46(2):341–346, 1999.
- [97] Takashi Takishita, Kazuhiro Ashida, Nobutomo Nakamura, Hirotsugu Ogi, and Masahiko Hirao. Development of shear-vertical-wave point-focusing electromagnetic acoustic transducer. *Japanese Journal of Applied Physics*, 54(7S1):07HC04, 2015.
- [98] S Wang, R Su, X Chen, Kang L, and G Zhai. Numerical and experimental analysis of unidirectional meander-line coil electromagnetic acoustic transducers. *IEEE Transactions on Ultrasonics, Ferroelectrics, and Frequency Control*, 60(12):2657–2664, 2013.
- [99] American Society for Testing and Materials. Standard practice for ultrasonic examinations using Electromagnetic Acoustic Transducer (EMAT) techniques, 1996.
- [100] P J Latimer and D T MacLauchlan. EMAT inspection of welds in thin steel plates of dissimilar thicknesses, 2000.
- [101] P J Latimer and D T MacLauchlan. EMAT probe and technique for weld inspection, 1998.

- [102] B. A. Auld. *Acoustic Fields and Waves in Solids*. Krieger Publishing Company, 1990.
- [103] R. Truell, C. Elbaum, and B. B. Chick. *Ultrasonic Methods in Solid State Physics*. Academic Press (London), 1969.
- [104] I. A. Viktorov. *Rayleigh and Lamb Waves Physical Theory and Applications*. Plenum Press, New York, 1967.
- [105] J D Achenback. *Wave propagation in elastic solids*. Elsevier Science Publishers B. V., 1999.
- [106] J. P. Morrison, S. Dixon, M. D G Potter, and X. Jian. Lift-off compensation for improved accuracy in ultrasonic lamb wave velocity measurements using electromagnetic acoustic transducers (EMATs). *Ultrasonics*, 44(SUPPL.):1401–1404, 2006.
- [107] Andrzej Ambroziak, Roman G. Maev, Marcin Korzeniowski, and Paweł Kustron. Ultrasonic quality control methods for spot-welded joint. *Welding International*, 25(12):927–932, 2011.
- [108] J. E. Gubernatis, E. Domany, J Krumhansl, and M. Huberman. The Born approximation in the theory of the scattering of elastic waves by flaws. *Journal of Applied Physics*, 48(7):2812, 1977.
- [109] F. R. S. Rayleigh. Investigations in optics, with special reference to the spectroscope. *Philosophical Magazine Series 5*, 8(49):261–274, 1879.
- [110] A. A. Maznev and O. B. Wright. Upholding the diffraction limit in the focusing of light and sound. *Wave Motion*, 68:182–189, 2017.
- [111] F Simonetti. Multiple scattering: The key to unravel the subwavelength world from the far- field pattern of a scattered wave. *Physical Review E*, 73(3):1–13, 2006.
- [112] F. Simonetti. Localization of pointlike scatterers in solids with subwavelength resolution. *Applied Physics Letters*, 89(9):1–4, 2006.
- [113] Christophe; Bescond, Jean-Pierre Monchalín, Daniel; Lévesque, Adam; Gilbert, Richard; Talbot, and Makoto Ochiai. Determination of Residual Stresses Using Laser-Generated Surface Skimming Longitudinal Waves. In *Proceedings of SPIE. Nondestructive Evaluation and Health Monitoring of*

Aerospace Materials, Composites, and Civil Infrastructure IV, pages 175–186, 2005.

- [114] R. S. Edwards, S. Dixon, and X. Jian. Depth gauging of defects using low frequency wideband Rayleigh waves. *Ultrasonics*, 44(1):93–98, 2006.
- [115] Leonard J Bond. Surface cracks in metals and their characterization using Rayleigh waves. *Center for Nondestructive Evaluation Theses and Dissertations*, 1978.
- [116] L. J. Bond. A computer model of the interaction of acoustic surface waves with discontinuities. *Ultrasonics*, 17(2):71–77, 1979.
- [117] J Blake and J Bond. Rayleigh wave scattering from surface features : wedges and down-steps. 28:214–228, 1990.
- [118] L. J. Bond and J. Taylor. Interaction of Rayleigh waves with a rib attached to a plate. *Ultrasonics*, 29(6):451–458, 1991.
- [119] R.J. Blake and L.J. Bond. Rayleigh wave scattering from surface features: up-steps and troughs. *Ultrasonics*, 30(4):225–265, 1992.
- [120] Masahiko Hirao, Hidekazu Fukuoka, and Yosuke Miura. Scattering of Rayleigh surface waves by edge cracks: Numerical simulation and experiment. *The Journal of the Acoustical Society of America*, 72(2):602–606, 1982.
- [121] X. Jian, Y. Fan, R. S. Edwards, and S. Dixon. Surface-breaking crack gauging with the use of laser-generated Rayleigh waves. *Journal of Applied Physics*, 100(6), 2006.
- [122] M. Ochiai. Laser-induced surface acoustic wave technique for precise depth measurement of stress corrosion cracking. *Journal of Physics: Conference Series*, 278(1), 2011.
- [123] Y. C. Angel and Jan D. Achenbach. Reflection and Transmission of Obliquely Incident Rayleigh Waves By a Surface-Breaking Crack. *Journal of the Acoustical Society of America*, 75(2):313–319, 1984.
- [124] B. Dutton, A. R. Clough, M. H. Rosli, and R. S. Edwards. Non-contact ultrasonic detection of angled surface defects. *NDT and E International*, 44(4):353–360, 2011.

- [125] S Dixon, B Cann, D L Carroll, Y Fan, and R S Edwards. Non-linear enhancement of laser generated ultrasonic Rayleigh waves by cracks. *Non-Destructive Testing and Evaluation*, 23(1):25–34, 2008.
- [126] R S Edwards, B Dutton, A R Clough, and M H Rosli. Enhancement of ultrasonic surface waves at wedge tips and angled defects. *Applied Physics Letters*, 99(9):94104, 2011.
- [127] R S Edwards, B Dutton, and A R Clough. Interaction of laser generated ultrasonic waves with wedge-shaped samples. *Applied Physics Letters*, 100(18):184102, 2012.
- [128] I. S. Grant and W. R. Philips. *Electromagnetism*. John Wiley & Sons, Incorporated, 1990.
- [129] S B Palmer and S Dixon. Industrially viable non-contact ultrasound. *Insight*, 45(3):211–217, mar 2003.
- [130] R Ribichini. *Modelling of electromagnetic acoustic transducers*. PhD thesis, Imperial College London, 2011.
- [131] R. Ribichini, F. Cegla, P. B. Nagy, and P. Cawley. Evaluation of electromagnetic acoustic transducer performance on steel materials. In *AIP Conference Proceedings*, volume 1335, pages 785–792, 2011.
- [132] X. Jian, S. Dixon, K. T V Grattan, and R. S. Edwards. A model for pulsed Rayleigh wave and optimal EMAT design. *Sensors and Actuators, A: Physical*, 128(2):296–304, 2006.
- [133] Dirk Rueter. Induction coil as a non-contacting ultrasound transmitter and detector: Modeling of magnetic fields for improving the performance. *Ultrasonics*, 65:200–210, 2016.
- [134] T Nishinaga. *Handbook of Crystal Growth: Fundamentals*. Elsevier Ltd, 2014.
- [135] Jose Francisco Hernandez-Valle. Pulsed-electromagnet EMAT for high temperature applications. *the University of Warwick, Ph.D. Thesis*, 2011.
- [136] S Dixon, C Edwards, and S B Palmer. Electromagnetic Acoustic Transducers for Testing Power Station Boiler Tubes. *Review of Progress in Quantitative Nondestructive Evaluation*, 18:1995–2000, 1999.

- [137] S. Dixon, S. E. Burrows, B. Dutton, and Y. Fan. Detection of cracks in metal sheets using pulsed laser generated ultrasound and EMAT detection. *Ultrasonics*, 51(1):7–16, 2011.
- [138] R. S. Edwards, S. Dixon, and X. Jian. Characterisation of defects in the railhead using ultrasonic surface waves. *NDT and E International*, 39(6):468–475, 2006.
- [139] E. G. Steward. *Fourier Optics an introduction*. Ellis Horwood Limited, 1987.
- [140] J. Whiteley. *Finite Element Methods. Mathematical Engineering*. Springer, Cham, 2017.
- [141] Alan Morris. *A Practical Guide to Reliable Finite Element Modelling*. John Wiley & Sons Ltd, Chichester, PO19 8SQ, 2008.
- [142] Richard Challis, Vladimir Ivchenko, and Raied Al-Lashi. Ultrasonic attenuation measurements at very high SNR: Correlation, information theory and performance. *Journal of Physics: Conference Series*, 457:012004, 2013.
- [143] Peter Enders. Huygens’ principle and the modelling of propagation. *European Journal of Physics*, 17(4):226–235, 1996.
- [144] B. Dutton, S. Boonsang, and R. J. Dewhurst. A new magnetic configuration for a small in-plane electromagnetic acoustic transducer applied to laser-ultrasound measurements: Modelling and validation. *Sensors and Actuators, A: Physical*, 125(2):249–259, 2006.
- [145] S. A. Boctor. *Electric Circuit Analysis*. Prentice-Hall International, London, 1987.
- [146] Shujuan Wang, Lei Kang, Zhichao Li, Guofu Zhai, and Long Zhang. Mechatronics 3-D modeling and analysis of meander-line-coil surface wave EMATs. *Mechatronics*, 22(6):653–660, 2012.
- [147] S. Dixon, T. J. Harrison, and P. A. Petcher. Phase changes of ultrasonic bulk waves through focusing measured using a noncontact ultrasonic method. *Applied Physics Letters*, 97(5):2008–2010, 2010.
- [148] Andrew Richard Clough. A study on the near-field interactions of ultrasonic surface waves with surface-breaking defects. *Ph.D. Thesis*, page 252, 2013.

- [149] X. Jian, S. Dixon, R. S. Edwards, and J. Morrison. Coupling mechanism of an EMAT. *Ultrasonics*, 44(SUPPL.):653–656, 2006.
- [150] Iikka Virkkunen, Mika Kempainen, Henner Ostermeyer, Raimo Paussu, and Tony Dunhill. Grown cracks for NDT development and qualification. *Insight: Non-Destructive Testing and Condition Monitoring*, 51(5):271–275, 2009.
- [151] K. Ravi-Chandar and E. Schneider. Ultrasonic detection and sizing of plastic zones surrounding fatigue cracks. *Research in Nondestructive Evaluation*, 5(3):191–209, 1994.
- [152] Julio Isla and Frederic Cegla. Optimization of the bias magnetic field of shear wave EMATs. *IEEE Transactions on Ultrasonics, Ferroelectrics, and Frequency Control*, 63(8):1148–1160, 2016.
- [153] R. S. Edwards, A. Sophian, S. Dixon, G. Y. Tian, and X. Jian. Dual EMAT and PEC non-contact probe: Applications to defect testing. *NDT and E International*, 39(1):45–52, 2006.
- [154] Masahiko Hirao and Hirotugu Ogi. An SH-wave EMAT technique for gas pipeline inspection. *NDT & E International*, 32(3):127–132, 1999.
- [155] M. D G Potter and S. Dixon. Ultrasonic texture measurement of sheet metals: An integrated system combining Lamb and shear wave techniques. *Nondestructive Testing and Evaluation*, 20(4):201–210, 2005.
- [156] Matthew Clough, Matthew Fleming, and Steve Dixon. Circumferential guided wave EMAT system for pipeline screening using shear horizontal ultrasound. *NDT and E International*, 86:20–27, 2017.
- [157] Shejuan Xie, Mingming Tian, Pan Xiao, Cuixiang Pei, Zhenmao Chen, and Toshiyuki Takagi. A hybrid nondestructive testing method of pulsed eddy current testing and electromagnetic acoustic transducer techniques for simultaneous surface and volumetric defects inspection. *NDT and E International*, 86(September 2016):153–163, 2017.